

Dissertation
submitted to the
Combined Faculties for the Natural Sciences and for Mathematics
of the Ruperto-Carola University of Heidelberg, Germany
for the degree of
Doctor of Natural Sciences

presented by

Jervis Vermal Thevathasan BSc(MedBioSci)(Hons)

born in Singapore

Oral examination: October 15th 2019

**Establishing single-molecule localization
microscopy as a quantitative tool towards
structural cell biology**

Referees: Prof. Dr. Carsten Sachse
Prof. Dr. Bernd Bukau

Parts of the work described in this thesis have been published:

Thevathasan, J. V.*, Kahnwald, M.*, Cieśliński, K., Hoess, P., Peneti, S. K., Reitberger, M., ... Ries, J. (in press, 2019). Nuclear pores as versatile reference standards for quantitative superresolution microscopy. *Nature Methods*, Accepted.

Abstract

In my PhD, I set out to establish single molecule localization microscopy (SMLM) as a complementary technique to answer questions in structural cell biology. The strengths of SMLM are resolution in the nanometer regime, molecular specificity and the ability to record dynamic information.

In this thesis, I report on two independent projects:

1. The use of nuclear pores as a versatile reference standard for quantitative superresolution microscopy.
2. Visualizing the self-assembly of alpha-synuclein fibril polymorphs.

In the first project, we introduced to the field nuclear pore complexes (NPC) as a reference standard for quality control in superresolution microscopy. To this end we generated, four CRISPR cell lines with nucleoporin96 (Nup96) endogenously tagged with labels SNAP, Halo, mEGFP and mMaple. The success of NPCs as a reference standard is owed to its well characterized structural organization and composition. Nup96 is present as 32 copies divided equally over the cytoplasmic and nuclear ring of the NPC. It's stereotypic arrangement facilitates the visualization of the NPC's radial eightfold symmetry under SMLM. The overall dimensions of the NPC positions fluorophores at relevant distances for 2D and 3D resolution calibration and quality control. Knowledge of the absolute number of underlying labels present in each NPC allowed us to calculate the effective labeling efficiency of each labeling strategy. Having a defined number for fluorophores also allowed for counting of protein copy numbers within complexes using both diffraction-limited and superresolution microscopy.

In the second project, I established a correlative transmission electron microscopy (TEM) and single molecule localization microscopy (SMLM) method to study the dynamic self-assembly of amyloid fibril polymorphs. Amyloid fibril polymorphism has been found in distinct neurodegenerative disease phenotypes . The ability to exist as different polymorphs has been a stumbling block towards understanding disease etiology. To address this need, I first established an imaging assay that enabled the visualization of the self-assembly process of single amyloid fibrils in real-time. To visualize individual fibrils, I used the point accumulation for imaging in nanoscale topography (PAINT) imaging strategy with fluorogenic amyloid binding dyes. This strategy allowed for imaging with unmodified protein monomers while achieving high labeling densities on fibrils permitting the characterization of respective fibril self-assembly. From my dynamic PAINT measurements, I have identified that fibrils exhibit growth characteristics specific to the solution conditions they are in. The unique opportunity of analyzing the

polarization of the emitted fluorescence of each binding event enabled me to visualize fibril ultrastructure. To further validate observed structural features, I performed correlative TEM tomography and dynamic PAINt. Such multiparametric correlative imaging enables the description of fibril growth kinetics with respect to its underlying structure, which would otherwise not be possible.

Zusammenfassung

Meine Doktorarbeit etabliert Einzelmoleküllokalisationsmikroskopie (engl. Single-molecule localization microscopy, SMLM) als komplementäre Technik zur Beantwortung von Fragen in der Strukturbiologie. Zu den besonderen Stärken von SMLM zählen ihre Auflösung im Nanometer-Bereich und die molekulare Spezifität, sowie die Möglichkeit, Dynamiken zu erfassen.

In meiner Dissertation bearbeite ich zwei unabhängige Gebiete:

1. Kernporen als einen vielseitigen Referenzstandard für quantitative, supraauflösende Mikroskopie
2. Visualisierung der Selbstassemblierung von alpha-Synuclein in polymorphen Fibrillen

Im ersten Projekt führen wir Kernporen als einen Referenzstandard zur Qualitätskontrolle in supraauflösender Mikroskopie ein. Hierzu wurden vier CRISPR-Zelllinien generiert, in denen jeweils Nucleoporin96 (Nup96) mit SNAP, Halo, mEGFP oder mMaple endogen markiert wurde. Kernporen eignen sich aufgrund ihrer umfassend charakterisierten Struktur und Zusammensetzung besonders gut als Referenzstandard. Nup96 liegt in 32 Kopien gleichmäßig verteilt über den zytoplasmatischen und nukleoplasmatischen Ring der Kernporen vor. Seine stereotype Anordnung führt zur Visualisierung mit radialer, achtfacher Symmetrie in SMLM. Die Dimensionen einer Kernpore positionieren die Fluorophore in relevanten Abständen zur Kalibrierung der Auflösung in 2D und 3D, sowie zur Qualitätskontrolle in supraauflösender Mikroskopie. Die exakte Kenntnis der Anzahl der vorhandenen Markierungsstellen in jeder Kernpore ermöglicht es, die erreichte Effizienz der fluoreszenten Markierung zu ermitteln. Das Vorliegen einer definierten Anzahl an Fluorophoren ermöglicht es außerdem, die Anzahl von Proteinen innerhalb von Komplexen sowohl in beugungsbegrenzter wie auch in supraauflösender Mikroskopie zu bestimmen.

Im zweiten Projekt etabliere ich eine Methode der korrelativen Transmissionselektronenmikroskopie (TEM) und Einzelmoleküllokalisationsmikroskopie, um die dynamische Selbstassemblierung von alpha-Synuclein in polymorphen Fibrillen zu untersuchen. Amyloidfibrillenpolymorphismus wurde in verschiedenen Phänotypen neurodegenerativer Erkrankungen entdeckt. Das Auftreten verschiedener Polymorphe ist ein Hindernis in der Erforschung der Ursachen dieser Krankheiten.

Zunächst etabliere ich einen bildgebenden Assay, welcher die Visualisierung des Selbstassemblierungsprozesses einzelner Amyloidfibrillen in Echtzeit ermöglicht.

Hierzu nutze ich die Technik der Punktakkumulation zur Bildgebung in Nanoskalen-Topographie (engl. point accumulation in nanoscale topology, PAIN) mit fluorogenen Farbstoffen, welche an Amyloide binden. Diese Strategie ermöglicht die Bildgebung mit unmodifizierten Proteinmonomeren bei Erreichen hoher Markerdichten, welches die Charakterisierung der jeweiligen Selbstassemblierung einer Fibrille erlaubt. Die dynamischen PAIN Messungen zeigen, dass die Wachstumscharakteristiken der Fibrillen von spezifischen Bedingungen der Lösungen abhängen, in denen sie wachsen. Das Auslesen der Polarisation der emittierten Fluoreszenz jedes Bindungsereignisses ermöglicht es, die Ultrastruktur der Fibrillen zu visualisieren. Zur Validierung der beobachteten strukturellen Merkmale werden korrelative TEM-Tomographie und dynamische PAIN-Messungen eingesetzt. Diese multiparametrische, korrelative Bildgebung ermöglicht das Wachstum der Fibrillen in Bezug auf ihre zugrundeliegende Struktur zu beschreiben, was andernfalls nicht möglich wäre.

Acknowledgements

Great is His faithfulness! (Lam 3:23). I thank the Lord my God, for sustaining me all these years. Everything that I am, and ever will be is because of the goodness and faithfulness of God. He is the source of my life, hope, wisdom and understanding.

I am thankful to Jonas Ries for providing me with this opportunity to undertake my PhD in his laboratory and at EMBL. It has truly been a privilege to have worked alongside with you. You were always generous with your time and accommodating in nature that made it easy to approach you regardless of the issue at hand. Thank you for your understanding whenever I had to devote my time to my family. You are one of the best scientists I have come to know, respect and aspire to be.

I would like to thank my PhD defence and TAC committee members, Prof. Dr. Carsten Sachse and Prof. Dr. Bernd Bukau and Dr. Alba Diz Muñoz. Thank you for your meaningful support and sincere encouragement at our meetings, especially during the many struggles I faced with my experiments. I would like to thank Prof. Dr. Matthias Mayer for kindly accepting to be a part of my PhD defence committee.

Thank you to all past (Li-Ling Yang and Konstanty Cieslinski) and present members (Yiming Li, Aline Tschanz, Lucas-Raphael Mueller, Maurice Kahnwald, Anindita Dasgupta, Robin Diekmann, Markus Mund, Joran Deschamps, Philipp Hoess, Yu-Le Wu and Ulf Matti) of the Ries lab for being a part of this journey. Yu-Le Wu, thank you for your genuine interest and help in designing and implementing the analysis pipeline for my alpha-synuclein project. Robin Diekmann, thank you for your initial help with analyzing my fibril data. It really helped to kick start and generate insights from my self-assembly assays. You are a gifted teacher and scientist, as I have learnt a lot about optics from you. Joran Deschamps, thank you for all the microscope support (during and outside office hours). I could not have gotten data of such high quality without your support. But I must say, sometimes; sometimes.. the fault does not lie with my sample. You bring a lot fun and cheer to the lab atmosphere. Philipp Hoess, I am indebted to you for your help during my thesis writing and helping me fix all the errors in my writings.

Markus Mund, you have pioneered the way for all the PhD students in the lab and you were the best person to do it. Thank you for sharing your thoughts on how to progress the project and all the encouragement you have provided. Yiming Li, you were a good office neighbour, thank you for answering all my optics related questions. Ulf Matti, Thank you for helping me with things in the lab and also with my initial move to Germany. Anindita, thank you for sharing M3 with me and helping me solve objective height problems, 2 channel alignment and explaining optics to me.

Sebastian Brosig, Thank you for helping me with German translations and showing me how things are done in Germany. You are one of the few people I know who would go the extra mile to help me with things. Thanks for listening to all my complaints about everything.

Special mention and thanks goes to Jacob Scheurich (my white brother from another mother), for the many rounds of protein purifications done together. Thank you for making all the time spent working at the bench with you fun and memorable. Thank you for your patience and willingness to go through with all my trouble shooting and optimization. Although there was a lot of inertia from your end, you always accommodated and helped me the best you could. Maybe I will bring some chocolates. Kim Remans, thank you for always keeping your door open to me, allowing me to work alongside Jacob in the PEPCORE and for listening to all my scientific and unscientific hypotheses regarding alpha-synuclein. Nikolay Dobrev, in the short time I have known you, you have been a good friend and have inspired me to hold myself to higher standards. Thank you for all the help you have rendered during my thesis writing. We will someday change the world for the better together. I would also like to thank Henry Werner from the mechanical workshop for helping me cut the 100's of PCR tubes for my imaging chamber.

I want to thank all the Master's students whom I have worked with on the NPC project, Daniel Heid, Sudheer Kumar and especially Maurice Kahnwald. Maurice, it was truly a pleasure to have had the opportunity to work with you. We could not have finished the paper without your diligent and conscientious work. Thank you for your hands, your brains, your humour and frequent rides home. "Its Gggooooodddd!"

Thank you to my family at Life Church, Heidelberg. Thank you to Sam and Friederike, Michael and Temi, Johannes, Kyle, Eppie and Sherrie and for every person who has faithfully stood in the gap on my behalf, before the Lord. Your prayers carried me through, and filled me with hope when I had none myself.

Finally,

To my dearest Hasini, my wife, life companion and best friend, you always bring out the best in me. Words cannot express how thankful I am for all the sacrifices you have made. I could not have done this PhD without your consistent love and patience. Thank you for always encouraging me with the word of God and reminding me that I am always exactly where God intended me to be. You have shown me by example what it means to be compassionate as you shared my struggles during the most difficult times of this journey. In the past four years, we have moved countries, set up a home together, embarked on a PhD and doubled in our family size. I never for once, imagined that all of this could be possible. Your selfless sacrifice of putting your career aside, to take care of our family is

something I can never repay. I ask that the Lord our God will bless you with all your heart's desires. This PhD is not something I accomplished but it is something WE accomplished. I love you very much!

To my parents, Appa and Amma, Thank you for my whole life. For believing in me and doing everything in your power to give me the best opportunities in life. I am deeply grateful for your labour of love, for every sacrifice, for every prayer, and words of encouragement that you pour in to my life. I am blessed to have you as my parents. You have set an example of perseverance and unwavering trust in the Lord; both lessons have carried me through this entire PhD. You truly embodied what it means to be joyful in hope, patient in affliction and faithful in prayer. Thank you, from the bottom of my heart. I love you.

To my brothers, Kevin Annae, Morven & Naveen, Thank you for being the best brothers in the world. For continually supporting me on this journey. For all the sacrifices you have had to make for me, while I was studying overseas. Thank you for all the joy and laughter you bring into my life. For visiting me in Germany, and loving my kids the way you do. Your visits always came at the right time, and gave me the rest I needed. The memory of our silly adventures always brought a smile to my face, especially on the hard days. The best is yet to be!

To my sons, Samuel Elias and Nathanael Ezra, I thank the Lord for blessing me with the both of you. You are both very precious to me. You are what I am most proud of, the sweetest gift that I have ever received. Samuel, thank you for the love you so freely give. I will always cherish the moments of your innocent joy as you rush to greet me everytime I return home from the lab. Thank you for making every day better. You made me forget the hardships, and made me smile through it all. I love you, Samuel.

Nathanael, You are absolutely adorable. I will never forget our early morning meetings. Secretly, I would hope that you would wake up before I left for the lab, so that I could get at least 15 mins with you before rushing off to the lab or to write this thesis. Thank you for faithfully waking up for our secret sessions. Let's not tell mummy. I love you, Nathanael.

Contents

Abstract	vii
Zusammenfassung	ix
Acknowledgements	xi
Contents	xv
1 Introduction	1
1.1 Tools and techniques for structural studies	1
1.2 Light and diffraction	3
1.3 Structured illumination microscopy	4
1.4 Stimulated emission depletion microscopy	5
1.5 Single molecule localization microscopy	6
1.5.1 Localization precision and accuracy	7
1.5.2 Sampling and labeling density	8
1.5.3 3D information	10
1.5.4 Instrumentation	12
1.6 Single molecule localization microscopy for structural cell biology .	13
I Nuclear pores as versatile reference standards for quantitative superresolution microscopy	15
2 Aims	17
3 Introduction	19
3.1 Quantitative microscopy	19
3.1.1 Microscope performance	19
3.1.2 Sample preparation	20
3.1.2.1 Choice of fluorophore	20
3.1.2.2 Labeling strategies	23
3.1.3 Imaging conditions	27
3.1.3.1 Buffer Conditions	27
3.1.3.2 Acquisition conditions	28

3.2	Reference standard for SMLM	29
3.3	The nuclear pore complex (NPC)	30
3.3.1	Structure of the NPC	30
3.3.2	The Y-complex and Nup96	31
4	Results	33
4.1	Generation and validation of cell line	33
4.2	The NPC as a 2D & 3D resolution standard	35
4.2.1	Resolving capabilities of imaging modalities	35
4.2.2	Quantifying 'Linkage Error'	35
4.2.3	Correction of depth-dependent aberration	35
4.3	Labeling efficiency standard	38
4.3.1	Analysis pipeline	38
4.3.2	Quantifying effective labeling efficiencies	39
4.3.2.1	Self-labeling enzymes	39
4.3.2.2	Nanobodies and antibodies	39
4.3.2.3	Photoactivatable protein, mMaple	39
4.3.2.4	Imaging buffer composition	40
4.4	Counting protein copy numbers	43
5	Discussion	45
5.1	Cell line validation	45
5.2	Ease of use & reproducible	46
5.3	2D & 3D calibration	46
5.4	Quantifying effective labeling efficiencies	47
5.4.1	Labels	47
5.4.2	Fluorophores	47
5.4.3	Buffer conditions	48
5.4.4	Oxygen scavenging system	49
5.5	Counting protein copy numbers	49
6	Future outlook	51
7	Materials & Methods	53
7.1	Generation of CRISPR cell lines	53
7.1.1	Genome editing plasmids	53
7.1.2	Southern blotting of Nup96	53
7.1.3	siRNA silencing of Nup96	54
7.1.4	Western blotting of Nup96	54
7.2	Cell culture maintenance	55
7.3	Sample preparation	55
7.3.1	Coverslip preparation and cell seeding	55
7.3.2	SNAP-tag labeling	56

7.3.3	Nanobody labeling of Nup96-mEGFP fusion proteins	56
7.3.4	Indirect immunostaining of Nup96-mEGFP fusion proteins	57
7.3.5	Halo tag labeling in fixed cells	57
7.3.6	Halo tag labeling in live cells	57
7.3.7	Fixation of Nup96-mMaple	58
7.4	Microscopes	58
7.4.1	SMLM microscope	58
7.4.2	Pixel size calibration	59
7.4.3	Confocal microscopy	59
7.4.4	Airy-scan microscopy	61
7.4.5	STED microscopy	61
7.4.6	Ratiometric dual-color SMLM	61
7.4.7	Astigmatic 3D SMLM	62
7.5	Data analysis	62
7.5.1	Fitting	62
7.5.2	Post-processing	62
7.5.3	Segmentation	63
7.5.4	Geometric analysis	63
7.5.5	Analysis of profiles	63
7.5.6	Radius of NPC	63
7.5.7	Distance between cytoplasmic and nucleoplasmic rings in 2D data	64
7.5.8	Distance between cytoplasmic and nucleoplasmic rings in 3D data	64
7.6	Determination of effective labeling efficiencies	64
7.6.1	Probabilistic model for effective labeling efficiency	65
7.6.2	Determination of number of localizations per fluorophore .	65
7.7	Counting protein copy numbers	65
7.7.1	Counting in diffraction-limited microscopy using Nup96-mEGFP as a reference	65
7.7.2	Counting in mammalian cells using Nup96-mMaple as a reference	66
II Visualizing the self-assembly of alpha-synuclein polymorphs		67
8	Aims	69
9	Introduction	71
9.1	Alpha-synuclein in Parkinson's disease	71
9.2	Alpha-synuclein's native structure	72
9.3	Alpha-synuclein mutations and post-translational modifications . .	73
9.4	Alpha-synuclein's physiological role	74

9.5	Alpha-synuclein in disease	74
9.6	Conformations of alpha-synuclein during aggregation	75
9.7	Alpha-synuclein fibrils	76
9.8	Measuring the self-assembly of fibrils	79
9.9	Studying self-assembly of single fibrils	84
9.10	Characterization of self-assembly kinetics	84
9.11	Superresolution imaging of amyloid fibrils	85
9.12	Inferring fibril features from optical signatures	86
9.12.1	Spectral properties of dyes	86
9.12.2	Polarization dipole of dyes	88
10	Results	91
10.1	Protein purification and characterization	91
10.2	Super resolution imaging of alpha-synuclein fibrils	93
10.2.1	Visualization of alpha-synuclein fibrils	93
10.2.2	Finding the optimal conditions for PAINting with pFTAA	96
10.2.2.1	Optical filter configuration	96
10.2.2.2	Buffers	96
10.2.2.3	pFTAA spectral properties	97
10.3	Differentiating different alpha-synuclein polymorphs	99
10.3.1	Localizations emission spectrum	99
10.3.2	Localizations distribution and polarization	101
10.4	Visualizing the self-assembly of alpha-synuclein fibrils	106
10.5	Measuring the self-assembly under different conditions	111
10.6	Measuring the self-assembly with a solution change midway	117
10.7	Correlative SMLM/EM of amyloid fibril self-assembly assay	119
11	Discussion	123
11.1	Visualizing and differentiating individual fibril polymorphs	123
11.1.1	Differentiating fibrils	123
11.2	Visualizing the self-assembly of alpha-synuclein fibril	126
11.2.1	Identifying ideal conditions for fibril elongation	126
11.2.2	Fibril elongation consists of intermittent stop and growth phases	127
11.3	Fibril elongation characteristics in different solution conditions	128
11.4	Fibril elongation is dependent on solution conditions	130
11.5	Correlative SMLM/EM for validation of structural features observed in SMLM	131
12	Future outlook	133
13	Material & Methods	135
13.1	Alpha-synuclein expression and purification	135

13.1.1	Alpha-Synuclein expression	135
13.1.2	Periplasmic extraction	136
13.1.3	Ion-exchange chromatography (IEX)	136
13.1.4	Hydrophobic-interaction chromatography (HIC)	137
13.1.5	Size-exclusion chromatography	138
13.2	Alpha-synuclein fibril formation	138
13.3	Alpha-synuclein seed generation	139
13.4	Fibril formation of beta-amyloid (1-42)	139
13.5	Fibril formation of Tau	139
13.6	Sample preparation for spectral imaging	139
13.7	Spectral imaging on the Zeiss LSM 780	140
13.8	Imaging fibrils on glass coverslip	140
13.9	Construction of chambers for seeded aggregation assays	140
13.10	Fibril elongation assay	140
13.10.1	Imaging chamber construction	140
13.10.2	Seed adsorption to the coverslip	141
13.10.3	Protein monomer solution for fibril elongation assay	141
13.11	Fibril elongation assay with change in solution conditions	142
13.12	Correlative electron microscopy	142
13.12.1	Resin embedding	142
13.12.2	Resin sectioning and Imaging	143
13.13	SMLM Microscope setup	143
13.14	Data acquisition	144
13.15	Data analysis	144
13.15.1	Fitting localizations	145
13.15.2	Filtering and rendering localizations	145
13.15.3	Intensity calculation (2 channel – polarization)	145
13.15.4	Polarization calculation	145
13.15.5	Registering 2 channels	146
13.15.6	Drift correction	146
13.15.7	Fibril segmentation	146
13.15.8	Straightening fibrils	146
13.15.9	Descriptive analysis of fibrils	147
13.15.10	Analysis of kymographs	147

Bibliography

List of Figures

1.1	Spatial scale of biomolecules	2
1.2	Generation of Moiré fringes	4
1.3	Stimulated emission depletion microscopy	5
1.4	Single molecule localization microscopy	7
1.5	Localization precision and accuracy	7
1.6	Sampling effects on image quality	9
1.7	PSF engineering for 3D localization microscopy	10
1.8	Different modes of illumination	13
1.9	Illumination effects on fluorophore photophysics	14
3.1	Jablonski Diagram	21
3.2	Effect of fluorophore photophysics on image quality	22
3.3	Different modes of photoswitching in organic dyes	23
3.4	'Linkage error'	24
3.5	Self-labelling enzymes SNAP and Halo tag	25
3.6	Structure of the nuclear pore complex	30
3.7	The Y-complex within the NPC	32
4.1	Validation of cell line homozygosity with Southern and Western blotting	34
4.2	Gallery of Nup96 cell lines acquired across different imaging modalities	36
4.3	Quantifying 'Linkage Error'- NPCs as a 2D resolution standard	36
4.4	Correcting depth-dependent aberrations - NPCs as a 3D resolution standard	37
4.5	Analysis pipeline for determining ELE	38
4.6	Effective labeling efficiencies of labeling strategies	41
4.7	Diffraction-limited counting	43
4.8	SMLM counting	44
9.1	An illustration of the regions and structure of alpha-synuclein.	73
9.2	Alpha-synuclein oligomer formation	76
9.3	Amyloid fibril core structure and organization	77

9.4	Molecular structure of alpha-synuclein fibrils	78
9.5	Alpha-synuclein fibril polymorphism	78
9.6	Molecular structures of alpha-synuclein polymorphs	80
9.7	Interaction of extrinsic dyes with fibrils	82
9.8	Self-assembly process of amyloid fibrils	83
9.9	PAINTing alpha-synuclein fibrils	86
9.10	Spectrally-resolved PAINT	87
9.11	Dipole moment of dyes	88
9.12	Different polarization optical setups and respective readouts	89
10.1	Protein purification of alpha-synuclein	92
10.2	Fluorescence emission spectrum of various dyes	94
10.3	PAINTing with various dyes	95
10.4	Bulk emission spectra of dyes staining different amyloids	98
10.5	SMLM reconstruction of fibril polymorphs	99
10.6	Dual-channel emission spectrum PAINT	100
10.7	Dual-channel polarization	103
10.8	Characterization of fibril morphology	104
10.9	Distribution of fibril morphology	105
10.10	Illustration of the self-assembly assay	106
10.11	Alleviating phototoxicity	108
10.12	Snapshots of self-assembly assay	109
10.13	Kymographs to describe fibril self-assembly	110
10.14	Kymograph analysis	110
10.15	Growth characteristics of fibrils in the presence and absence of salt	113
10.16	Growth characteristics of fibrils in different monomer concentrations	114
10.17	Growth characteristics of fibrils in 400 μ M monomer compared to no salt conditions	115
10.18	Autocorrelation amplitude against periodicity	116
10.19	Schematic of experimental workflow for change of buffer	117
10.20	Growth characteristics of fibrils when the solution condition is changed	118
10.21	Resin embedding and TEM imaging of fibrils grown on coverglass	120
10.22	Correlative SMLM/EM of fibril self-assembly assay	121

List of Tables

4.1	Various imaging conditions and analysis	42
7.1	Buffers used for sample preparation	56
7.2	Acquisition parameters	59
7.3	Composition of imaging buffers used	60
10.1	Summary of the different filter settings and its respective S/N ratio recorded	96
10.2	Summary of pFTAA performance in different buffer conditions	97
11.1	Summary of reported WT alpha-synuclein fibril growth rates	129
13.1	Buffers used for protein purification	136

List of Abbreviations

$(\text{NH}_4)_2\text{SO}_4$	Ammonium sulfate
MgCl_2	Magnesium chloride
2D	2-dimensional
3D	3-dimensional
AA	Ascorbic acid
AD	Alzheimer's disease
ADU	Analog-digital unit
AF647	Alexa Flour 647
AFM	Atomic force microscopy
ATP	Adenosine triphosphate
BALM	Binding activated localization microscopy
BC	O ₂ -benzylcytosine
BCA	bicinchoninic acid
BFP	Back focal plane
BG	Background
BG	Benzylguanine
BME	Beta-mercaptoethanol
BME	beta-mercaptoethanol
BSA	Bovine serum albumin
C-term	Carboxy-terminal
CAT	Catalase
CC	Cytoplasmic connector
CD	Circular dichroism
CLEM	Correlative light (fluorescence) and electron microscopy
CMA	Chaperone-mediated autophagy
COT	Cyclooctatetraene
CR	Congo-red
CRISPR	Clustered regularly interspaced short palindromic repeats
Cryo-EM	Cryogenic electron microscopy
DLB	Dementia with lewy bodies
DLS	Dynamic light scattering
DMEM	Dulbecco's Modified Eagle's Medium

DNA	Deoxyribonucleic acid
dSTORM	Direct stochastic optical reconstruction microscopy
DTT	Dithiothreitol
EDTA	Ethylenediaminetetraacetic acid
EGTA	ethylene glycol-bis(beta-aminoethyl ether)-N,N,N,N-tetraacetic acid
ELE	Effective labeling efficiency
EM-CCD	Electron multiplying charge-coupled device
EM	Electron microscopy
esiRNA	Endoribonuclease-prepared siRNA
FAB	Fragment antigen binding
FACS	Fluorescent-activated cell sorting
FB	Fixation buffer
FF	Fast flow
FOV	Field of view
FP	Fluorescent protein
FT	Flow through
FTD	Frontotemporal dementia
G	Glycine
GFP	Green fluorescent protein
GLOX	Glucose oxidase
GLOXC	Glucose oxidase / catalase
GPU	Graphic processing unit
gRNA	Guide ribonucleic acid
GSH	Glutathione
HCl	Hydrochloric acid
HEK	Human embryonic kidney cells
HIC	Hydrophobic interaction chromatography
HILO	Highly inclined laminated optical sheet
ICCM	Inner cytoplasmic core module
ICYC	Inner cytoplasmic Y-complex
IEX	Ion exchange chromatography
IF	Immunofluorescence
IgG	Immunoglobulin G
INCM	Inner nuclear core module
INM	Inner nuclear membrane
INYC	Inner nuclear Y-complex
IPTG	Isopropyl beta-D-1-thiogalactopyranoside
ISC	Inter-system crossing
JF	Jenelia Fluor
KAc	Potassium acetate
KD	Knockdown
L-DOPA	L-3,4-dihydroxyphenylalanine

LB	Lewy bodies
LB	Lysogeny broth
LCO	Luminescent conjugated oligothiophenes
LCP	Luminescent conjugated polymers
LL	Log likelihood
LN	Lewy neurites
LUV	Large unilamellar vesicles
MC	Misfolded conformation
MEA	Mercaptoethylamine
mEGFP	Monomeric enhanced green fluorescent protein
MES	2-(N-morpholino)ethanesulfonic acid
mMaple	Monomeric photoconvertible green-to-red fluorescent protein
MOPS	3-(N-morpholino)propanesulfonic acid)
mRNA	messenger ribonucleic acid
MSA	Multi system atrophy
mTOR	Mammalian target of rapamycin
MW	Molecular weight
N-term	Amino terminal
NA	Numerical aperture
NAC	Non-beta amyloid component
NaCl	Sodium chloride
NC	Nuclear connector
NEAA	Non-essential amino acid solution
NMR	Nuclear magnetic resonance
NPC	Nuclear pore complex
Nups	Nucleoporins
OCCM	Outer cytoplasmic core module
OCYC	Outer cytoplasmic Y-complex
OD	Optical density
ONCM	Outer nuclear core module
ONM	Outer nuclear membrane
ONYC	Outer nuclear Y-complex
PA	Photoactivatable
PAFP	Photoactivatable fluorescent protein
PAGE	Polyacrylamide gel electrophoresis
PAINT	Point accumulation for imaging in nanoscale topography
PALM	Photoactivatable localization microscopy
PB	Permeabilization buffer (in the context of sample preparation (Part 1 of thesis))
PB	Phosphate buffer (in the context of buffer for aggregation (Part 2 of thesis))
PBS	Phosphate buffered saline
PCR	Polymerase chain reaction
PD	Parkinson's disease

PEG	Polyethylene glycol
PEPCORE	Protein expression and purification core
PET	Positron-emission tomography
PFA	Paraformaldehyde
pFTAA	Penter-formyl thiophene acetic acid
PI3K-SH3	Phosphatidylinositol 3-kinase Src homology 3
PMS	F Phenylmethylsulfonylfluorid
POX	Pyranose oxidase
POXC	Pyranose oxidase / catalase
PSF	Point spread function
PSFP	Photoswitchable fluorescent protein
PVDF	Polyvinylidene difluoride
QD	Quantum dots
QS	Quenching buffer
RESOLFT	Reversible saturable optical fluorescence transition
RIMF	Refractive index mismatch factor
ROI	Region of interest
ROS	Reactive oxygen species
RT	Room temperature
S₀	Singlet ground state
S₁	Singlet excited state
sCMOS	Scientific-grade complementary metal-oxide-semiconductor
SDS	Sodium dodecyl sulfate
SEC	Size-exclusion chromatography
SIM	Structured illumination microscopy
SiR	Silicon rhodamine
siRNA	Small interfering ribonucleic acid
SLM	Spatial light modulator
SMAP	Single-molecule analysis platform
SMLM	Single-molecule localization microscopy
SNCA	Synuclein Alpha
SNpc	Substantia nigra pars compacta
SNR	Signal to noise ratio
sPAINT	Spectrally-resolved PAINT
ssNMR	Solid-state nuclear magnetic resonance
STD	Standard deviation
STED	Stimulated emission depletion
STORM	Stochastic optical reconstruction microscopy
T₁	Triplet excited state
TBA	Transport buffer with BSA
TBS	Tris buffered saline
TEM	Transmission electron microscopy

ThT	Thioflavin T
TIR	Total internal reflection
TIRF	Total internal reflection fluorescence
TIRFM	Total internal reflection fluorescence microscopy
TRB	Transport buffer
tRNA	Transfer ribonucleic acid
U2OS	Human osteosarcoma cell line
UAA	Unnatural Amino Acid
UC	Unfolded conformation
UV	Ultra-violet
VAMP2	Vesicle-associated membrane protein 2
WT	Wild-type

For Hasini

1 | Introduction

Cell biology involves the study of structure and function of a cell; the basic unit of life. A cell comprises of numerous concerted cellular processes that are primarily facilitated by individual proteins, protein complexes and higher molecular assemblies. The structure, composition, organization and subcellular localization of these protein machineries are crucial for the proper operation of cellular function. The well-orchestrated and regulated interplay between the different protein assemblies is a requirement to prevent cellular malfunction which leads to disease. Hence, characterization of protein complexes involved in vital cell processes helps us to understand its underlying biology and identify potential avenues for developing novel therapeutics.

1.1 Tools and techniques for structural studies

There are specific tools and techniques available to characterize certain aspects of protein complexes (Dobson, 2019). X-ray crystallography is a powerful technique which enables characterization of the structure, composition and organization of protein complexes at atomic resolution. However, crystallization of proteins can be hindered by protein heterogeneity, internal flexibility and requirements of protein complex partners for successful reconstitution. In addition, with increasing size and complexity structural determination becomes challenging. Recent advances in cryogenic electron microscopy (Cryo-EM) together with single particle averaging has overcome these challenges to facilitate the structure determination of high kilodalton and megadalton cellular machineries such as ribosome, spliceosome and RNA polymerases (Kühlbrandt, 2014). In the last couple of years, using this method, structure determination of individual proteins in a lower kilodalton range, were obtained with near atomic resolution (Liu et al., 2019; Khoshouei et al., 2017). However, both techniques require isolated and purified proteins with high homogeneity, which precludes the study of proteins in their native environment. Furthermore they are unable to inform on protein dynamics and transient interactions. In this regard, nuclear magnetic resonance (NMR) spectroscopy enables the study of dynamic protein conformations in solution and solid state NMR (ssNMR) allows the study of protein conformations in membranes

and in aggregated states. However, NMR structural studies require purification of isotope labelled proteins and are typically limited to small proteins (Marion, 2013). Advancements in cryo-electron tomography (cryo-ET) have unlocked the ability to achieve molecular resolution of protein assemblies within their cellular context. Cryo-ET is currently limited to thin sections (300 nm) of sample, lacks molecular specificity and is unable to capture dynamic information (Pfeffer and Mahamid, 2018).

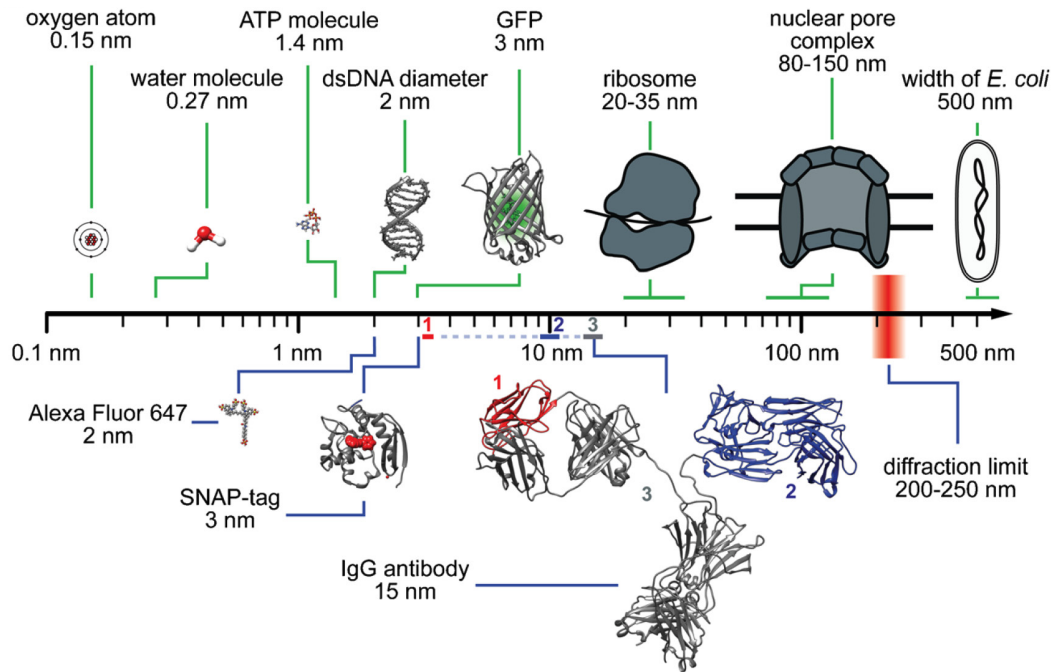


Figure 1.1: Spatial scale of biomolecules. The IgG antibody contains 2 other antigen binding structures, 1: nanobodies derived from camelids (3 nm, red), and 3: FAB fragment (10 nm, blue). This figure has been taken from (Turkowsky et al., 2016) which is distributed under Creative Commons Attribution License (CC-BY).

To help bridge this gap, correlative light (fluorescence) and electron microscopy (CLEM) is used. Molecules tagged with a fluorescent probe are first visualized under fluorescence microscopy modalities and then subjected to high resolution electron microscopy (Kukulski et al., 2011; Stepanek and Pigo, 2016). This technique has been used to investigate plasma membrane shaping during endocytosis, transport on microtubules and virus life cycle (Kukulski et al., 2012; Bykov et al., 2016; Stepanek and Pigo, 2016). Although these studies brought new insights to understanding the cellular processes involved, they have fallen short of reporting on the organization of the protein complexes that are involved. This is due to the limited resolution of fluorescence microscopy and the lack of molecular specificity in electron microscopy. As an example, endocytosis is a key cellular process facilitated by more than 50 proteins to result in the formation of 60-120 nm vesicles (Kaksonen and Roux, 2018). Fluorescence microscopy is only capable of resolving two objects separated more than 200 nm apart due to the fundamental law of diffraction (Fig. 1.1). As a consequence the organizational and compositional study of small protein complexes

such as those involved in endocytosis is not possible. However, with the advent of superresolution microscopy, such detailed study of the protein machinery involved in endocytosis is possible at the nanoscale (Mund et al., 2018). This study along with others has extended the utility of superresolution microscopy, specifically, single molecule localization microscopy (SMLM) into the domain of structural cell biology. Addressing questions regarding protein complex organization and compositions with SMLM requires stringent quality control to prevent erroneous conclusions. In the following sections, I will describe the different approaches to achieve resolution in the nanometer scale.

1.2 Light and diffraction

There are mainly two forms of optical microscopy. Firstly, 'bright-field' microscopy which is dependent on degrees of sample transparency to achieve contrast for image formation and secondly, fluorescence microscopy which usually requires specific labels that is able to absorb and emit photons at different wavelengths. A microscope essentially consists of a light source for illumination, lenses for focusing the light and a detector for image formation (Murphy and Davidson, 2012). Lenses act like a circular aperture. When light waves are transmitted through a lens, individual wavefronts are created that then start to interfere to generate a diffraction pattern. This diffraction pattern is observed as a concentric geometric pattern, also called a "point spread function" (PSF). It consist of alternating bright and dark concentric rings, with the center ring bearing the highest intensity. Simplistically, the minimum distance required to distinguish two PSF would determine the effective resolution but there are additional factors to be considered (Vangindertael et al., 2018). The size of a PSF is dependent on the wavelength and the transmission efficiency of lenses within the microscope. Therefore, a more accurate description of resolution was determined by physicist Ernst Abbe (Abbe, 1873),

$$d = \frac{\lambda}{2NA} \quad (1.1)$$

Here d , is the minimum distance between two points that can be resolved, λ is the wavelength of light used and NA is the numerical aperture of the objective (lens) used to collect light. NA is a measure of the ability of an objective to collect light. Therefore, with 550 nm emission wavelength together with a high NA objective (NA = 1.4), the resolution attainable is approximately 200 nm. This is also called the diffraction barrier. Within the past two decades, innovative methods have been applied to overcome this diffraction barrier to reach resolutions on the order of 5-10 nm. These methods work around the diffraction properties of light by either, spatially and temporally separating individual emitter PSFs or use mathematically methods to achieve a higher resolution.

1.3 Structured illumination microscopy

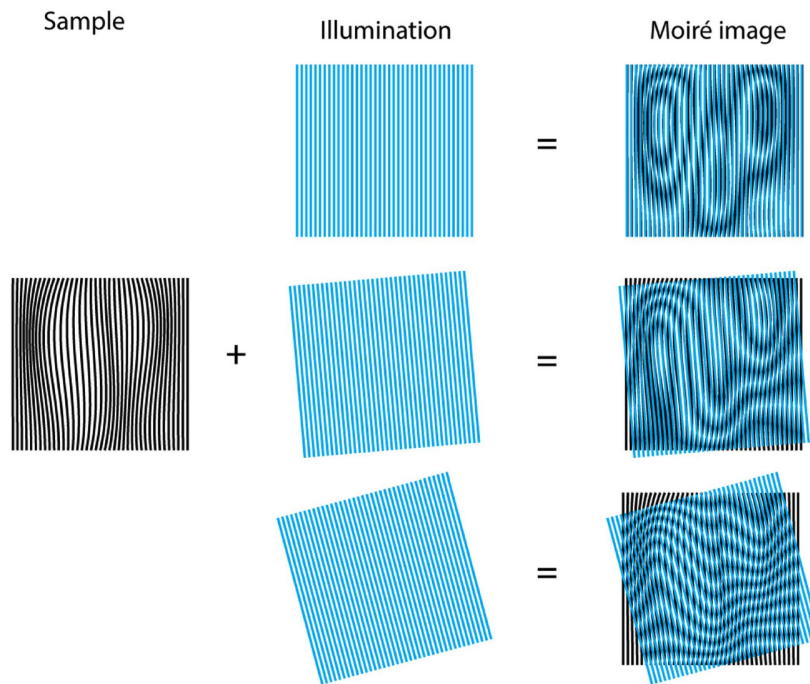


Figure 1.2: Generation of Moiré fringes. Generation of Moiré fringes. When samples with high spatial frequencies are illuminated by patterned illumination it results in the generation of Moiré fringes that contain lower frequencies. By shifting and rotating the illumination pattern with respect to the sample, different frequencies are recorded. The acquired images can then be used to mathematically recover the structure of the underlying object. This figure has been taken from (Vangindertael et al., 2018) which is distributed under Creative Commons Attribution 3.0 unported License (CC-BY 3.0).

Structured illumination microscopy (SIM) improves the achievable resolution by a factor of two by using optical elements combined with mathematical methods (Gustafsson, 2000). In SIM, samples are illuminated with a periodic excitation pattern that is created by a phase mask inserted along the excitation light path. This pattern is shifted or rotated between image acquisitions of the object. The shifting and rotating of excitation patterns result in Moiré patterns or fringes containing lower spatial frequencies of the object being imaged (Fig. 1.2). Since the pattern of excitation is known, the objects original frequencies can be mathematically recovered to reconstruct an image of the object. One of the benefits of SIM is that specific sample preparations are not required. However, SIM has a longer acquisition time as it has to acquire a series of images with a number of excitation patterns. This increases the time of illumination on the sample increasing phototoxicity. The need to acquire the same region with multiple patterns also sets a limitation to its temporal acquisition rates. To overcome this, spatial light modulators (SLM) which are able to generate different patterns of excitation light at a much higher rate are used (Fiolka et al., 2012). By adopting the lattice light-sheet microscopy illumination scheme together with use of SLM, both acquisition time and phototoxicity due to

illumination has been reduced, enabling 3D visualization of biological processes (Chen et al., 2014a).

1.4 Stimulated emission depletion microscopy

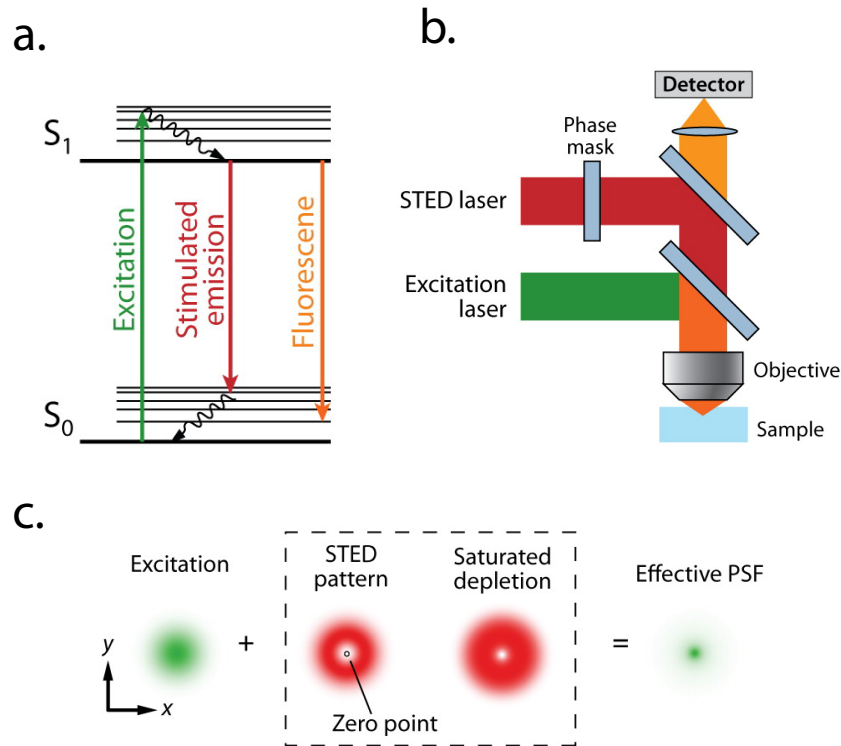


Figure 1.3: The working principle for STED microscopy. (a) Schematic of energy level transitions of a fluorophore. Fluorophores absorb energy from excitation to transition from the ground state, S_0 , to a bright state, S_1 . From S_1 fluorophores can be returned to S_0 via fluorescence decay or by absorbing energy to undergo stimulated emission. (b) An illustration of an optical STED optical setup. Both excitation and depletion laser (STED laser) are overlaid and focused onto the sample. (c) An illustration to visualize how overlaying the STED pattern over the excitation results in a smaller effective PSF. Saturation depletion is achieved by increasing the STED laser intensities. This figure has been taken from (Huang et al., 2009) with permission.

Stimulated emission depletion microscopy (STED) uses optical elements to spatially separate (coordinate targeted) individual emitters PSFs. Stefan Hell and Jan Wichmann (Hell and Wichmann, 1994) showed that shrinking the illumination volume (illumination PSF) in a laser scanning microscope would yield increased resolution. This is done by positioning a donut shaped depletion laser with a zero center on top of the excitation laser. The donut shape is achieved by inserting a phase mask in the beam path of the depletion laser. This overlay causes fluorophores on the periphery of the zero center excitation volume to be non-fluorescent (Fig. 1.3b). When a fluorophore is excited it absorbs energy from its ground state S_0 , to transition to S_1 , a higher energy level (Fig. 1.3a). By exciting a fluorophore at S_1

with a matched wavelength, it can be made to relax back to S_0 . This is called stimulated emission. The probability of a fluorophore undergoing stimulated emission scales with intensity of the depletion laser. Therefore, with sufficiently high laser powers, STED could theoretically achieve extremely high resolutions. However, extremely high depletion laser powers results in loss of fluorophores due to photobleaching and induced phototoxicity experienced by the sample. In most cases resolutions between 30–80 nm are reported (Sydor et al., 2015). For optimal STED imaging, fluorophores with increased photostability are required. Amongst all the superresolution methods, STED is the only method that does not require post-processing after image acquisition. To achieve 3D volumetric imaging, two phase masks are inserted into the depletion laser beam path (Klar et al., 2000). One creates the donut shape depletion pattern laterally and the second creates a donut intensity distribution axially. Reversible saturable optical fluorescence transitions (RESOLFT) is a variant of STED, instead of a depletion laser being used for stimulated emission of fluorophores, it is used for photoswitching fluorophores to their dark state ('off state') (Hell et al., 2004). RESOLFT is compatible only with reversibly photoswitchable dyes or fluorescent proteins, but it comes with the advantage of using much lower depletion laser intensities (Huang et al., 2009; Schnorrenberg et al., 2016).

Although the resolution limits of SIM and STED are well within the diffraction-barrier, their utility in structural cell biology has been limited to large protein complexes. MINFIELD STED, a variant of STED, has been shown to be able to resolve the eight fold radial symmetry of NPCs, however, it is limited to small fields of view and requires considerable efforts in sample preparation (Göttfert et al., 2017). The strengths of SIM and STED lie in their compatibility with live cell imaging because of the relatively faster acquisition rates compared to SMLM.

1.5 Single molecule localization microscopy

Single molecule localization microscopy (SMLM) achieves the highest resolution in comparison to the methods mentioned earlier. Under typical imaging conditions, resolutions in the order of 10–30 nm are routinely achieved (Sydor et al., 2015). Its working principle is to mathematically determine positions of single emitters PSFs that are spatially and temporally separated. The spatial and temporal separation of PSF is achieved by switching a small population of fluorophores from their dark state ('off-state') to their bright state ('on-state') in a stochastic manner while ensuring that individual PSF do not overlap (Fig. 1.4). In the field there are many names and acronyms for this technique (photoactivatable localization microscopy, PALM; stochastic optical reconstruction microscopy, STORM; direct stochastic optical reconstruction microscopy, *d*STORM), however, the core working principle is similar. They simply reflect the diverse methods that can be used to achieve

fluorophore switching between bright and dark states. This is discussed in more detail in the introduction of my first project. In the following sections, I will expound more on the working principles governing SMLM and parameters to be considered for quantitative imaging.

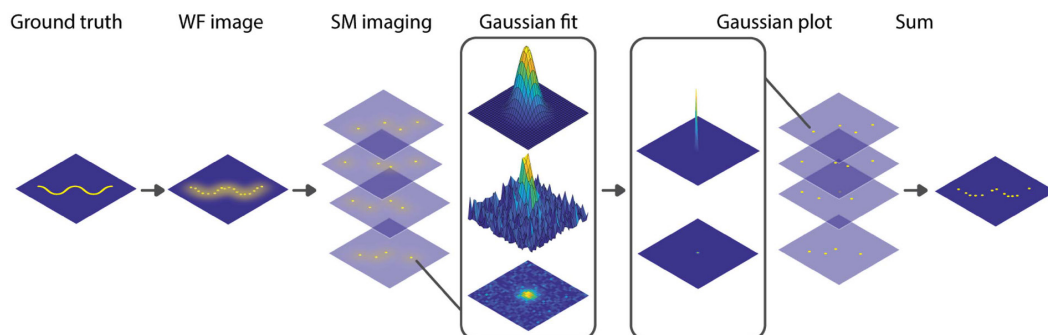


Figure 1.4: The working principle of SMLM. Under widefield conditions all the fluorophores are in their bright state simultaneously resulting in a diffraction-limited image. Under single molecule imaging conditions only a small subset of fluorophores is in its bright state in a stochastic manner. Each fluorophore's PSF is spatially and temporally separated allowing for individual PSF to be fit with a Gaussian. The centroid of the Gaussian fit is then calculated as the fluorophores position and recorded. Rendering all the recorded positions in a single image represents the underlying object with increased resolution. This figure has been taken from (Vangindertael et al., 2018) which is distributed under Creative Commons Attribution 3.0 unported License (CC-BY 3.0).

1.5.1 Localization precision and accuracy

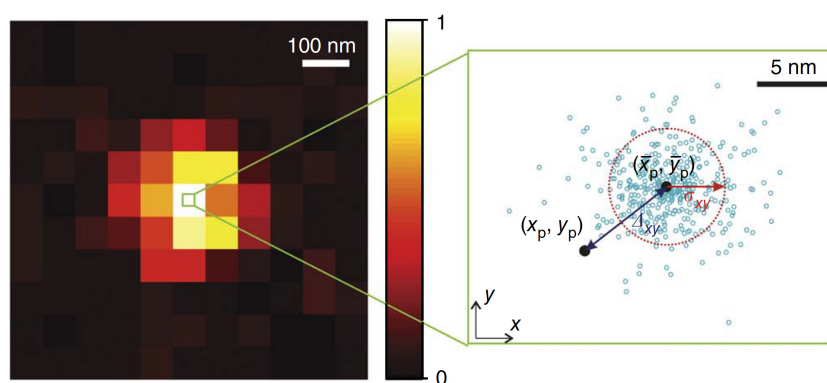


Figure 1.5: Localization precision and accuracy. The panel on the left is an example of an individual emitter recorded in a raw image. The emitters true position is denoted as (x_p, y_p) . Each blue circle denotes position estimates from different images of the same emitter. The lateral localization precision is described by (σ_x, σ_y) and the localization accuracy is described by $(\Delta_{x,y})$. This figure has been taken from (Deschout et al., 2014) with permission.

Resolution in SMLM is closely tied to two factors. The first factor is how precisely the position of each single emitter is determined. When a fluorophore is measured repeatedly, it results in a spread in position estimates. This spread (standard deviation) can be described as the localization precision (Fig. 1.5)(Deschout

et al., 2014). A small localization precision value indicates a better estimate of each single emitter's position. Localization precision in the absence of background can be described by,

$$\sigma_{x,y} \geq \frac{\sigma_{\text{PSF}}}{\sqrt{N}} \quad (1.2)$$

where (σ_{PSF}) is the standard deviation of the measured PSF and N is the number of photons that is recorded (Deschout et al., 2014; Thompson et al., 2002). This directly translates to bright single fluorophore being localized more precisely than dim fluorophore with a lower number of photons. It also highlights the importance of fluorophores being imaged directly at the focal plane. When a fluorophore is out of the focal plane its PSF size is larger, leading to a lower calculated localization precision (Deschout et al., 2014).

Localization accuracy is the deviation of the measured localization from the true position of the fluorophore. Localization accuracy is much harder to determine as it requires prior knowledge of the ground truth which may not be easily attainable. Therefore, imaging reference standards with a defined structure such as microtubules (Dempsey et al., 2011; Linde and Sauer, 2014 and DNA origamis (Zanacchi et al., 2017) have been introduced. However, the current standards in the field are suboptimal and are prone to cherry-picking resulting in overestimation of resolution measurements.

1.5.2 Sampling and labeling density

The second factor tied to resolution determination in SMLM is sampling and labeling density. This is especially important in SMLM compared to SIM or STED, because high densities of localizations are required for higher resolution. A sufficient number of fluorophores have to be localized to be able to reconstruct the underlying object. Borrowing from the field of signal processing, the Nyquist theorem specifies the need for objects to be sampled at least two times the desired resolution. For an example, to visualize a 100 nm filament, there needs to be a label every 50 nm. Therefore, the maximum resolution attainable when the localization precision is smaller than the distance between labels (Shroff et al., 2008):

$$\text{Resolution Nyquist limit} = \frac{2}{[\text{localization density}]^{\frac{1}{N}}} \quad (1.3)$$

If the localization precision is comparable or larger than the distance between labels, then the following approximation has been proposed (Legant et al., 2016):

$$\text{Overall resolution} = \sqrt{\text{localization precision}^2 + \text{Nyquist resolution}^2} \quad (1.4)$$

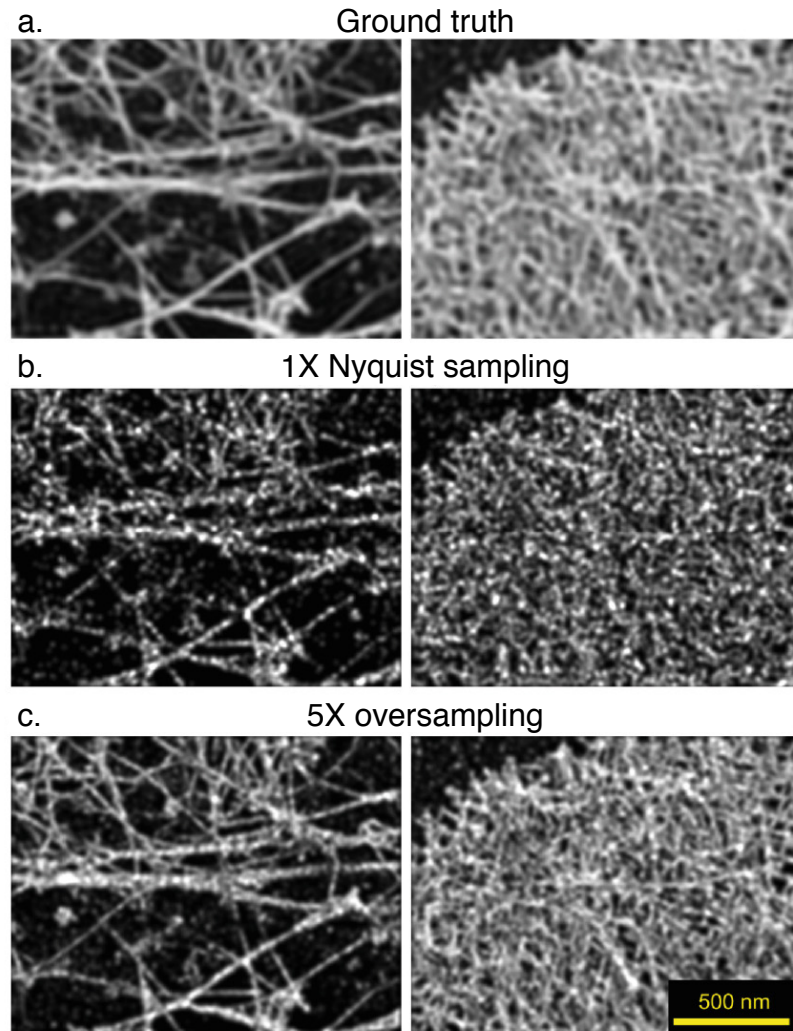


Figure 1.6: Sampling effects on image quality. (a) EM images were used as ground truth images. They were then binarized and filtered in the Fourier domain to present them at a resolution of 31 nm. (b) Simulation of SMLM images obtained from the ground truth image with 1X Nyquist sampling density. (c) Simulation of SMLM images obtained from the ground truth image with 5X oversampling. Structural details were closer to the ground truth in the 5X oversampled simulated images, displaying the need for sufficient sampling for structural imaging. This figure has been adapted from (Legant et al., 2016) with permission.

An assumption in the Nyquist theorem is that samples taken are regular and accurate descriptors of the underlying objects. This does not hold true in the context of imaging biological samples, the sampling of fluorophores is stochastic and with each event being unrelated to the specific organization of labels on the object being imaged. In addition, for most biological samples, targets may not be labeled due to limited label specificity, label inaccessibility, labels themselves not linked with

a fluorophore, nonspecific background signal and suboptimal image acquisition parameters. All these factors have a substantial impact on the measured labeling density. Therefore, for structural imaging it has been theoretically determined that oversampling by a factor of 5–10X is necessary to faithfully reconstruct the underlying sample (Fig. 1.6)(Legant et al., 2016). While this is true for continuous structures, in the case of discrete structures such as the nuclear pore complex (NPC), the increase in density of localizations would not provide more information on the structure. Instead, it depends on how well they are labeled (labeling efficiency). This emphasizes the need to optimize labeling efficiency in samples.

1.5.3 3D information

Protein complexes are three dimensional (3D) objects with specific spatial organization for their functional purpose. Therefore, it is crucial to be able to collect 3D information when performing structural imaging. The axial resolution of SMLM is around 10–75 nm (Sydor et al., 2015). There are a few methods for obtaining axial information from the measured PSF of fluorophores. PSFs are 3D ellipsoids that are symmetrical with their longest radius orientated axially to the optical axis. One approach is to measure the PSF at two separate planes (Bi-Plane). This is done by modifying the emission light to achieve signal contributions from different focal planes on each half of a camera chip. By fitting the localizations with a 3D PSF model, both lateral and axial positions of the fluorophore are determined (Juette et al., 2008; Ram et al., 2007). Developing this strategy further to obtain images from multiple focal planes has enabled imaging depths of 4 μm (Hajj et al., 2014)

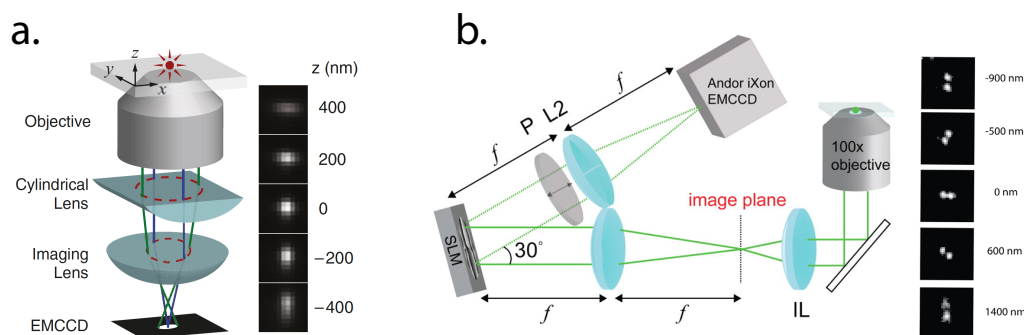


Figure 1.7: Two methods of PSF engineering to achieve 3D information in localization microscopy. (a) A schematic of PSF engineering with the use of a cylindrical lens to induce astigmatism. The PSF is stretched in opposing directions above and below the plane of focus. (b) With the use of a spatial light modulator (SLM) the PSF can be projected to two lobes that circle around each other along the different z-planes following a double helix pattern. This figure was adapted from (a) (2008) and (b) (Pavani et al., 2009) with permission.

Another approach to obtain axial information is to use special optics that allow for PSF engineering. When using a cylindrical lens to induce astigmatism, the

PSF is distorted asymmetrically along the axial optical axis. Above the plane of focus the ellipsoid PSF is stretched laterally and below the plane of focus it is stretched perpendicularly (Fig. 1.7a). The distance of the PSF from the focal plane is encoded in the size of the PSF and its shape encodes whether it is above or below the focal plane (Huang et al., 2008a). With astigmatism imaging depths of 1 μm are achieved. PSFs can also be engineered to appear as different shapes to encode for axial information. By using a SLM or phase ramp device, the PSF can be projected to appear as two lobes rotating around each other along the z-axis, like a double helix (Fig. 1.7b)(Pavani et al., 2009). A double helix PSF enables imaging up to the depth of 2 μm . Recently, this PSF engineering concept has been extended to encode for both the axial and spectral properties of various fluorophores to allow for larger z-axis ranges (tetrapod PSF). It boasts the capability multicolor imaging up to 20 μm depth in the z-axis. However, there is a trade-off between axial and spectral resolution (Shechtman et al., 2015). Currently PSF engineering methods such as astigmatism and helical PSFs are routinely used for 3D SMLM, which is due to its simplicity in implementation and post processing of data. Both methods require careful prior calibration with bead samples for correct axial assignment of recorded PSFs. It is noteworthy to mention that PSFs are susceptible to depth dependent aberrations that may result in deviations away from the calibrated PSFs. These aberrations arise mostly due to a refractive index mismatch between the glass and the sample imaged above resulting in systematic localization errors. To overcome this, a computational method has been developed to correct for these depth dependent aberrations (Li et al., 2019).

Although the methods mentioned earlier enable 3D imaging, the axial resolution is worse by a factor of 2–3 compared to the achievable lateral resolution. In this regard, interferometric approaches with the use a dual objective optical setup boast superior performance in both axial and lateral resolution. Interferometric methods rely on interference patterns that result from signal captured from both objectives. Signal from PSFs at different focal planes would have to travel through different optical path lengths thereby resulting in different interference patterns encoding for distance from the focal plane (Aquino et al., 2011; Huang et al., 2016; Shtengel et al., 2009). However, interferometric optical setups are extremely complicated and samples have to be prepared sandwiched between two coverslips to allow for imaging from top and bottom. Recent computational efforts to improve achievable axial resolutions have enabled acquisition of data quality similar to interferometric approaches on normal single objective based optical setups. By using an experimental PSF model as opposed to a 2D Gaussian for fitting PSFs, Li, Y. et al., (2018) were able to resolve the hollow structure of a microtubule using astigmatism, a feature previously only shown to be possible by interferometric methods.

1.5.4 Instrumentation

The instrumentation for SMLM is technical much simpler compared to SIM and STED. All that is needed is a highly stable microscope with a high NA objective, lasers with sufficient power and cameras capable of sensitive photon detection and fast frame rates (Vangindertael et al., 2018). High NA (1.4) immersion oil objectives are used to ensure efficient collection of photons from single molecule events. This comes at a cost of a limited working distance between 0.13 mm to 0.21 mm (Murphy and Davidson, 2012). These distances are usually sufficient to image an entire cell under epifluorescence (Fig. 1.8a). For some imaging applications, to minimize the contribution of background signals, the excitation laser beam is aligned off axis towards to the edge of the back focal plane. As a result the excitation laser beam exits the objective and hits the glass coverslip with a critical angle causing the beam to be reflected back into the objective (Fig. 1.8c). This is called total internal reflection fluorescence microscopy (TIRFM). This interaction of light with the glass coverslip results in the formation of an evanescent excitation wave that is capable of exciting fluorophores 150–250 nm above the coverslip. Fluorophores deeper in the sample are not excited, thus a higher signal to noise ratio is recorded. Another variant of TIRFM is highly inclined laminated optical sheet (HILO) illumination. Instead of the excitation laser being reflected back into the objective, the illumination is parked slightly off the axis of the objective to reduce the excitation depth thereby reducing background signal contribution (Fig. 1.8b). This raises the importance of paying attention to the behavior of fluorophores under different excitation powers.

Fluorophore photoswitching and photophysical properties are coupled to the excitation laser power being used (Bates et al., 2005; Heilemann et al., 2008). Especially, for quantitative imaging purposes, it is important to ensure that all fluorophores across the field of view are exposed to homogeneous laser intensity. Usually, lasers from single mode fibers result in an illumination with a Gaussian illumination profile. To reduce the effect of inhomogeneous illumination, the field of view that is recorded can be cropped around the peak intensity distribution of the Gaussian profile (Fig. (1.9a)). Another approach would be to use a multimode fiber together with a speckle reducer to ensure homogeneous illumination across the entire field of view (Fig. (1.9b) (Deschamps et al., 2016)). This ensures that all the localizations collected would exhibit similar photophysical properties and preclude the introduction of systematic errors or biases when analyzed (Fig. 1.9c,d).

Finally, to ensure a high signal to noise ratio (SNR), a sensitive electron multiplying charge-coupled devices (EM-CCD) cameras are used for detection. Although EM-CCD cameras have a high SNR, they are limited by their acquisition rates when the full camera chip (512x512 pixels) is being used. A workaround would be to image smaller regions, this however, reduces the throughput of an already slow method and imposes limitations on the biological questions that can be addressed

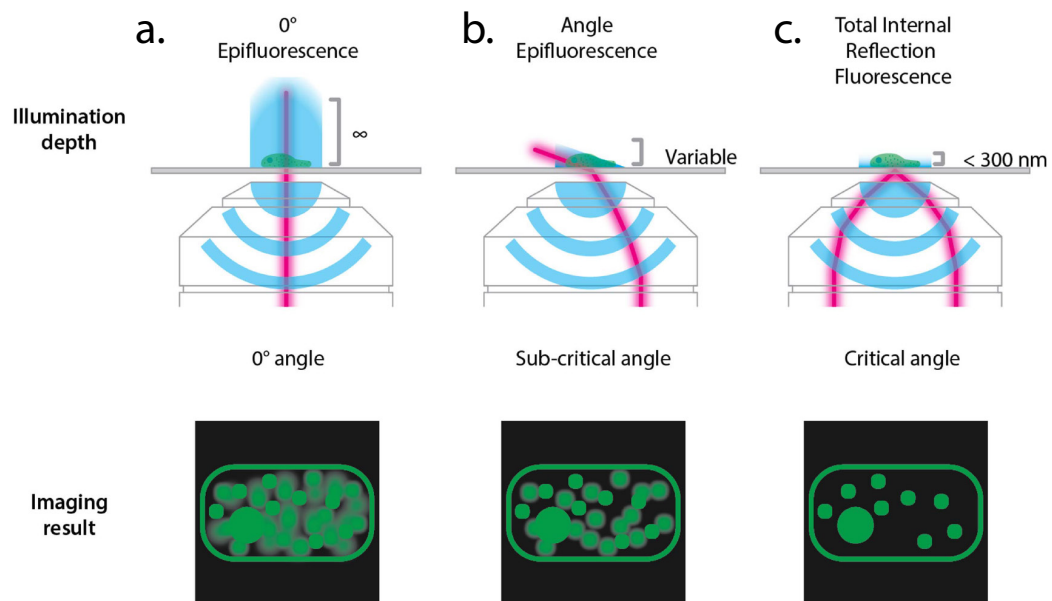


Figure 1.8: Different modes of illumination. (a) In epifluorescence mode, the entire sample is illuminated, which results in fluorophores out of the focus plane fluorescing contributing to a higher background. (b) When the laser beam is parked off axis to the objective, the laser exits the objective at a sub-critical angle thus reducing the penetrance depth of the excitation. This results in lower background fluorescence. (c) In total internal reflection (TIR) mode, the excitation laser beam is parked at the edge of the back focal plane such that when the laser exits the objective, it hits the coverglass at a critical angle resulting in the beam being reflected back into the objective. The interaction of the laser beam with the glass results in the propagation of an evanescent field with a penetrance depth of approximately 300 nm. Under TIR mode the background is very low due to the small volume of excitation. This figure has been taken from (Vangindertael et al., 2018) which is distributed under Creative Commons Attribution 3.0 unported License (CC-BY 3.0).

(Huang et al., 2013). Another class of cameras used in SMLM are scientific-grade complementary metal-oxide-semiconductor (sCMOS) cameras. sCMOS cameras have a larger field of view (2000x2000 pixels) and are capable of much faster readouts. It is important to note that the camera's architecture results in individual pixels having unique noise characteristics. This pixel dependent noise would have effects on SMLM post processing algorithm which assume a Poisson noise resulting in errors in localization determination (Huang et al., 2013).

1.6 Single molecule localization microscopy for structural cell biology

Among the three main methods for achieving nanometer resolution, SMLM as a technique is most suited for structural cell biology. It delivers the best spatial resolution with molecular specificity and the possibility of measuring dynamics. There are however, many levels at which SMLM is susceptible to systematic errors

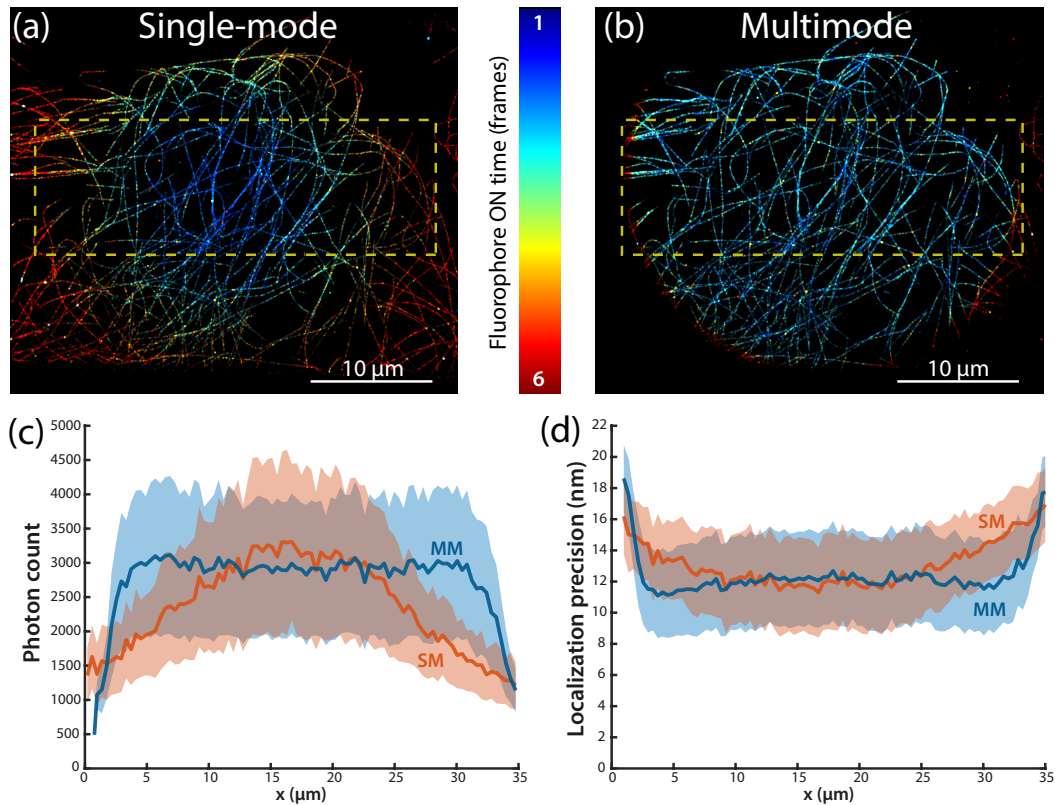


Figure 1.9: Illumination effects on fluorophore photophysics. (a) Image reconstruction of microtubules from U2OS cells immunolabeled with AF647 excited with a single mode fiber. (b) Image reconstruction of microtubules from U2OS cells immunolabeled with AF647 excited with a multimode fiber. The lookup table used in (a) and (b) denote the lifetime of each fluorophore's bright state. In (a) we observe that the recorded lifetimes of fluorophores increase moving towards the periphery of the field, reflecting the effect of a Gaussian illumination profile. This variation in life time is not observed with the use of a multimode fiber. (c) Plot of the amount of photons emitted by fluorophores across the field (within the yellow box) in (a). (d) Plot of the amount of photons emitted by fluorophores across the field (within the yellow box) in (b). Inhomogeneous illumination with the use of single mode fibers clearly has an impact on fluorophore photophysics and performance. This directly translates towards data quality. This figure has been reprinted with permission from (Deschamps et al., 2016) © The Optical Society.

and artifacts. There is a heavy dependency on performance of microscopes, quality of sample, final acquisition parameters and post processing of acquired data. To systematically ensure that the data collected is of sufficient quality for quantitative studies, a reference standard is needed for benchmarking. To address this need, in the first part of my thesis, I will introduce the use of nuclear pore complexes as versatile reference standards.

In the second part of my thesis, I will further extend the domain of SMLM in structural cell biology by introducing an assay that enables visualization of individual amyloid fibril ultra-structure and capture self-assembly process in real-time and space.

Part I

Nuclear pores as versatile reference standards for quantitative superresolution microscopy

2 | Aims

An imaging reference standard is required for quality control in quantitative single molecule localization microscopy.

We propose that the nuclear pore complex (NPC) would be an ideal reference standard. It has a well characterized stereotypic structure, composition and subcellular localization.

Our aims are to

1. Use CRISPR-Cas9 technology to generate 4 stable homozygous U2OS cell lines, with the Nup96 protein endogenously tagged with either SNAP, Halo, mEGFP or mMaple, respectively.
2. Demonstrate its capacity to function as a reference standard with assays that
 - (a) Measure labeling efficiencies of commonly used labeling strategies.
 - (b) Characterize and optimize fluorophore performance in different imaging buffer compositions.
 - (c) Determine protein copy numbers in protein complexes.

3 | Introduction

3.1 Quantitative microscopy

Single molecule localization microscopy (SMLM) as a technique is well suited for a quantitative study on organization and composition of protein complexes within their biological context. It has shed light on the organization of the NPC, neuronal synapses, the endocytic machinery, centrioles and actin rings present in neuronal axons (Dani et al., 2010; Mund et al., 2018; Szymborska et al., 2013; Xu et al., 2013; Yang et al., 2018). To achieve data quality that allows for quantitative interpretation, parameters such as microscope performance, sample preparation, image acquisition settings and data post processing have to be characterized and optimized. It is difficult to identify artifacts and judge the quality of data produced unless prior knowledge regarding the cellular localization or molecular arrangement of the protein complex is known. Albeit, it is not always possible. Therefore, it is important to have an imaging reference standard for benchmarking and calibration. In the following text I will expound on how the aforementioned parameters have an impact on data quality and interpretation.

3.1.1 Microscope performance

As mentioned in my overall thesis introduction, a microscope consists of lenses that focus light. In theory, these lenses allow light to pass through them without distortions; however, this is far from reality. Aberrations are optical faults intrinsic to lenses. Some common aberrations are spherical aberration, coma, chromatic aberration and astigmatism. These aberrations can arise from manufacturing errors due to misalignment or optical arrangement errors ("Lenses and Geometrical Optics" 2012). These distortions or aberrations have an effect on the point spread function (PSF) of single point emitters (Goodwin, 2007). Aberrated PSFs have photon distributions that lead to lower recorded intensity at the peak (centermost ring), thereby reducing the localization precision (Coles et al., 2016). Most of these aberrations originate from the lenses within the objective. Therefore, objectives are carefully designed by manufacturers to minimise these aberrations. Spherical aberrations can be minimized by means of a correction collar present on most

objectives. Fluorescent beads immobilized on a coverslip are usually used to characterize and correct for these aberrations. The next parameter important for quantitative imaging is sample preparation.

3.1.2 Sample preparation

In fluorescence microscopy, targets of interest have to be labeled with a fluorophore that absorbs energy in the form of photons and emits photons by means of fluorescence.

3.1.2.1 Choice of fluorophore

Fluorophores need to fulfill certain criteria in order to be used for SMLM. The accuracy of localization is dependent on the number of photons emitted per single dye molecule. Therefore, fluorophores with a high quantum efficiency and high photon yield are preferred. They should be stable and resistant to photobleaching as SMLM acquisitions are long and require the sample to be continuously illuminated with a laser. The ability to switch a fluorophore from a bright state ('on-state') to a dark state ('off-state') is a strict requirement for its utility in SMLM. This 'switching' is accomplished by using imaging buffer additives to modulate fluorophore photophysics, photoactivation of caged fluorophores or using fluorogenic capability upon binding to target (Dempsey et al., 2011).

Photophysics of a fluorophore can be described using a three state model (Jablonski, 1933) (Fig. 3.1). It has a singlet ground state, S_0 , a singlet excited state, S_1 , and a triplet excited state, T_1 . The fluorescence phenomena is observed when a fluorescent molecule cycles between S_0 and S_1 ('on-state'). When the fluorophore is irradiated with a photon wavelength that matches the energy level of the fluorophore's singlet ground state, S_0 , it absorbs the energy and gets excited to the first excited singlet state, S_1 . It then returns to its ground singlet state, emitting fluorescence. This transition has a short lifetime (ns). Alternatively, the fluorophore in the S_1 state can undergo intersystem crossing (ISC) to enter its triplet-excited state T_1 . T_1 has a longer lifetime (μ s), it is photochemically active and does not emit fluorescence. From T_1 , the fluorophore can then be further excited to result in photobleaching or it can be quenched via oxidation to return S_0 . This three state simplified model serves as a description of a fluorophore's photophysics. With the modulation of buffer compositions (see 3.1.3.1), fluorophores can be pushed to a dark state ('off-state') where it can be brought back to the bright state in a controlled manner (Fig. 3.1).

The interplay between the amount of photons emitted by the fluorophore in its bright state and the duration of its bright state determines how faithfully the localizations represent the imaged object. A fluorophore which emits high numbers

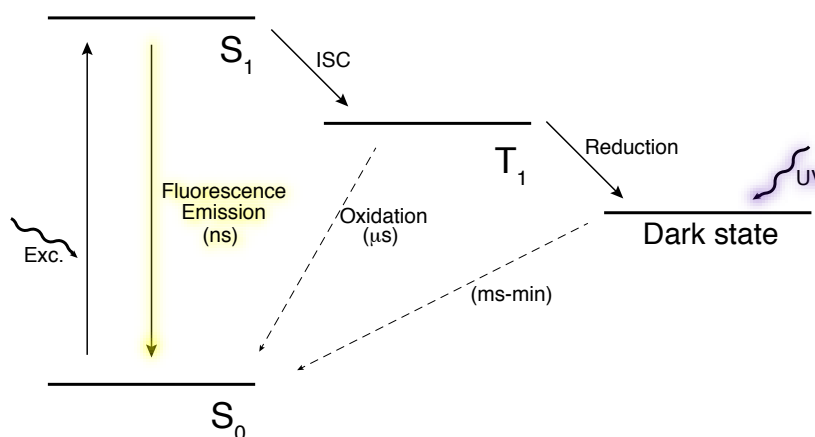


Figure 3.1: Jablonski Diagram. A diagram that illustrates the different electronic states of a fluorophore and transitions states it can occupy. Energy absorption from an excitation wavelength pushes the fluorophore from S_0 to S_1 . The return of a fluorophore from S_1 to S_0 results in fluorescence. S_1 is short lived. Alternatively, the fluorophore may undergo inter-system crossing (ISC) to enter T_1 , where it can be oxidized to S_0 or reduced to a dark state which can be excited with light that has a wavelength from 350–550 nm. The dark state of the fluorophore is long-lived enabling controlled switching of fluorophore back to the bright state using 405 nm excitation. This figure has been adapted from (Nahidiazar et al., 2016). This is an open access article distributed under the terms of the Creative Commons Attribution License.

of photons while having a short duration in the bright state allows for precise localization and high numbers of localizations that faithfully represent the imaged object (Fig. 3.2). If the fluorophore has a short duration in the bright state but emits few photons, even though many localizations are captured, they do not represent the imaged object. Finally, if a fluorophore has bright states with a long duration, due to multiple emitters being in the bright state simultaneously, it would result in fewer localizations and they would be mislocalized.

Due to these requirements, dyes from the xanthene and cyanine group are used for SMLM. Within the cyanine group, Alexa Fluor 647 (AF647), a variant of Cy5, is the dye of choice for many SMLM studies due to its high photon count per switching event. The absorption of UV switches dark state AF647 to its bright state (Fig. 3.3a) (Dempsey et al., 2011; Heilemann et al., 2005). This allows for high localization precision; therefore, it is routinely used to study organization within protein complexes. AF647 is a charged dye molecule thus rendering it cell membrane impermeable (Lavis and Raines, 2008). Cells are usually fixed prior to introduction of the dye preventing its use for live-cell imaging or labeling. This is an important factor when considering its utility in pulse chase experiments. The excitation and emission spectrum of AF647 also makes it compatible with another cyanine dye, CF680, for ratio-metric dual-color imaging. This enables mapping organization of protein assemblies (Hoess et al., 2018).

From the xanthene class of organic dyes, rhodamines, have been extensively

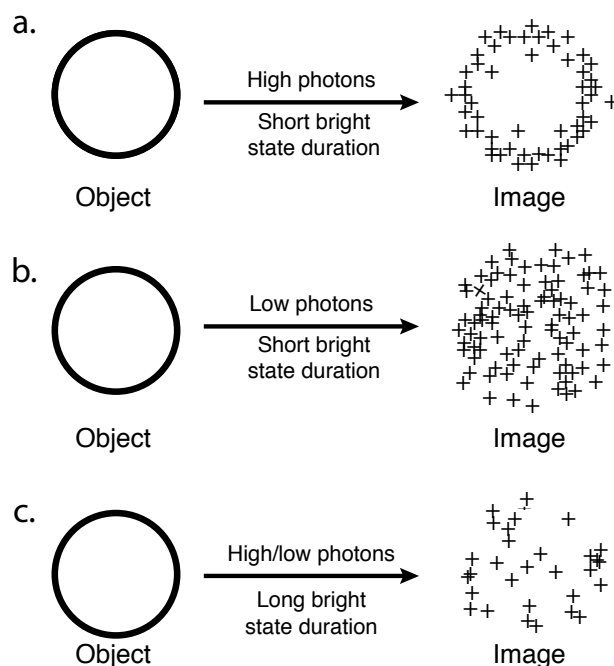


Figure 3.2: Effect of fluorophore photophysics on image quality.(a) A fluorophore with a high photon yield and short bright duration, would result in more localizations localized at high precision, thus better object reconstruction. (b) If a fluorophore has low photon yield, even with short bright durations, the localizations would not be localized with precision resulting in mislocalization and inability to reconstruct the underlying object. (c) If a fluorophore has long bright durations, it would result in fluorophores being bright simultaneously resulting in a reduced number of localization and mislocalizations. This figure has been adapted from (Dempsey et al., 2011) with permission.

modified to create Janelia Fluor (JF) dyes with spectral properties spanning the visible spectrum (Grimm et al., 2017). Placing a silicon, Si, in position 10 of the xanthene chromophore, resulted in the creation of silicon rhodamine (SiR) which are cell permeable and possess infra-red spectral properties (Koide et al., 2011). Modified rhodamines are fluorogenic as they exist in an equilibrium between the nonfluorescent lactone forms and fluorescent zwitterionic forms (Grimm et al., 2017; Lukinavičius et al., 2013). Upon binding to the protein that is being labelled, it favors formation of the fluorescent zwitterion to enter the bright state (Fig. 3.3b). Once in the bright state the dyes are able to photoswitch to facilitate SMLM. Another way to modulate switching of these dyes would be to attach a photolabile chemical group, such that the dye is produced in its off-state. Illumination with 405 nm, removes or modifies the photolabile chemical group to result in the dye's bright state (Fig. 3.3c) (Grimm et al., 2016; Grimm et al., 2013; Lukinavičius et al., 2013). Photoactivatable organic dyes are especially useful for studying target copy numbers as these dyes do not usually photoswitch more than once, thus preventing the issue of overcounting. However, they also result in lower labeling efficiency if a prebleach step is added before acquisition.

Organic dyes are available across the visible spectrum and new dyes are

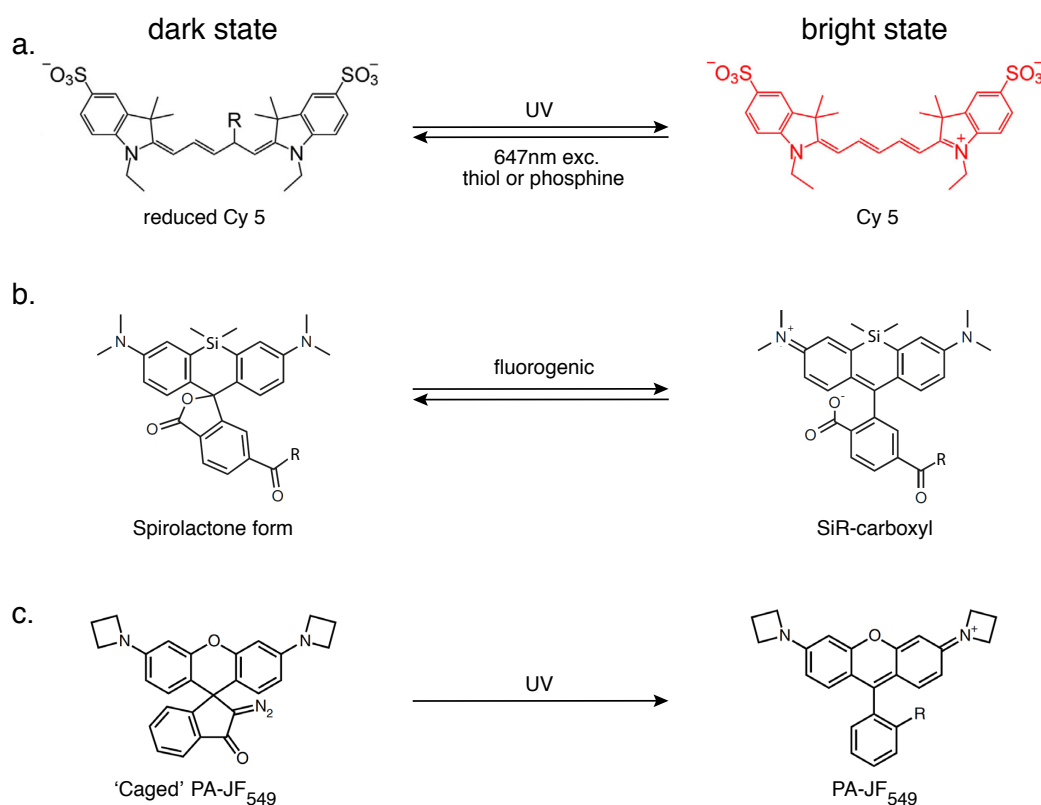


Figure 3.3: Different modes of photoswitching in organic dyes. (a) Cyanine dyes like Cy 5 or AF647 can be pushed to the dark state when excited with 647 nm in the presence of thiols. Reduced Cy 5 (dark state) can be returned to bright state when excited with UV (405 nm). (b) The transition from the spirolactone form of Silicon Rhodamine to its zwitterionic form is fluorogenic in nature. (c) Excitation with UV results in photo cleavage of the masking group to result in fluorescent JF549. This figure has been adapted from (a) (Chozinski et al., 2014), (b) (Lukinavičius et al., 2013) and (c) (Grimm et al., 2016) with permission.

published frequently. Future technological advances in SMLM would most likely stem from the area of fluorescent probe development. Therefore, it is important to have a robust imaging reference standard that is able to benchmark characteristics such as photon count, duration of bright states and number of photoswitching cycles of these new probes.

All probes need to be attached or directed to the target of interest. In the next section, I will discuss different labeling strategies to facilitate introduction of probes to the desired target.

3.1.2.2 Labeling strategies

In diffraction-limited microscopy, the size of the label being attached to the target did not matter due to the diffraction spot (> 200 nm). However, in SMLM, with resolution limits down to 10–20 nm, the physical size of label becomes a factor to be considered. This is factored in as ‘linkage error’ when measuring the physical

dimensions of the target (Fig. 3.4). Labeling strategies are classified broadly into two groups, namely, direct and indirect labeling. Direct labeling attaches a dye molecule (unnatural amino acids) or protein tag (self-labeling enzymes and fluorescent proteins) covalently to the target. Indirect labelling is performed with proteins that bind with specificity and affinity (antibodies, nanobodies and binding partners) onto the target.

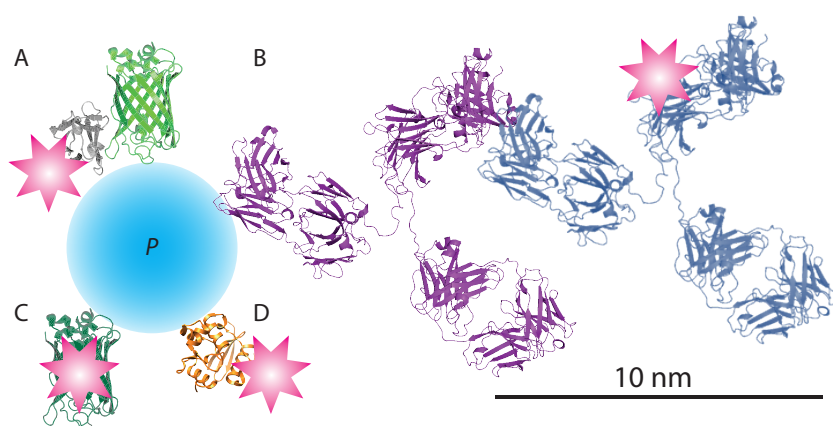


Figure 3.4: Schematic of 'linkage error'. (a) A nanobody against GFP labelled with a fluorophore. (b) Indirect immunolabeling with fluorophore labelled secondary antibodies. (c) Photoactivatable protein. (d) self-labelling enzymatic labels. The stars represent fluorophores. P represents the protein that is being detected. This figure has been taken from (Mund et al., 2014) with permission.

Unnatural amino acid labeling. This technique inserts an unnatural amino acid (UAA) with a functional group, which allows covalent linking of dyes via 'click chemistry' into the protein's primary sequence. To incorporate an UAA, an amber stop codon is inserted into the gene of interest. An orthogonal tRNA synthetase-tRNA pair is introduced into the cell to facilitate the translation of the modified gene (Lang and Chin, 2014). UAA labelling has the smallest linkage error, albeit the technique is not straightforward when compared with other labelling techniques (e.g. using fusion proteins). It requires the coexpression of tRNA synthetase, tRNA and the protein of interest. The expression levels may also vary due to inefficient expression. There is also an added limitation of high unspecific background resulting from incorporation of UAAs into non-target proteins and free UAAs in the cell.

Self-labeling enzymes The most commonly used commercial self-labeling enzymes are SNAP-tagTM, CLIP-tagTM and Halo-tag[®]. SNAP-tag is derived from human DNA repair protein O6-alkylguanine-DNA alkyltransferase that reacts specifically with benzylguanine (BG) (Fig. 3.5a) (Keppler et al., 2003). With a molecular weight of 20 kDa, SNAP-tag is the smallest self-labeling enzyme.

CLIP-tag was engineered based on SNAP-tag but with a substrate specificity for O²-benzylcytosine (BC). Halo-tag is a bacterial haloalkane dehalogenase that reacts with primary chloroalkane (Fig. 3.5b) (Los et al., 2008). Halo-tag has a molecular weight of 33 kDa. Synthetic dyes (described above under 3.1.2.1) can then be attached to the ligands for labeling of the tags. Depending on the dye permeability, labelling and imaging can be performed on live cells.

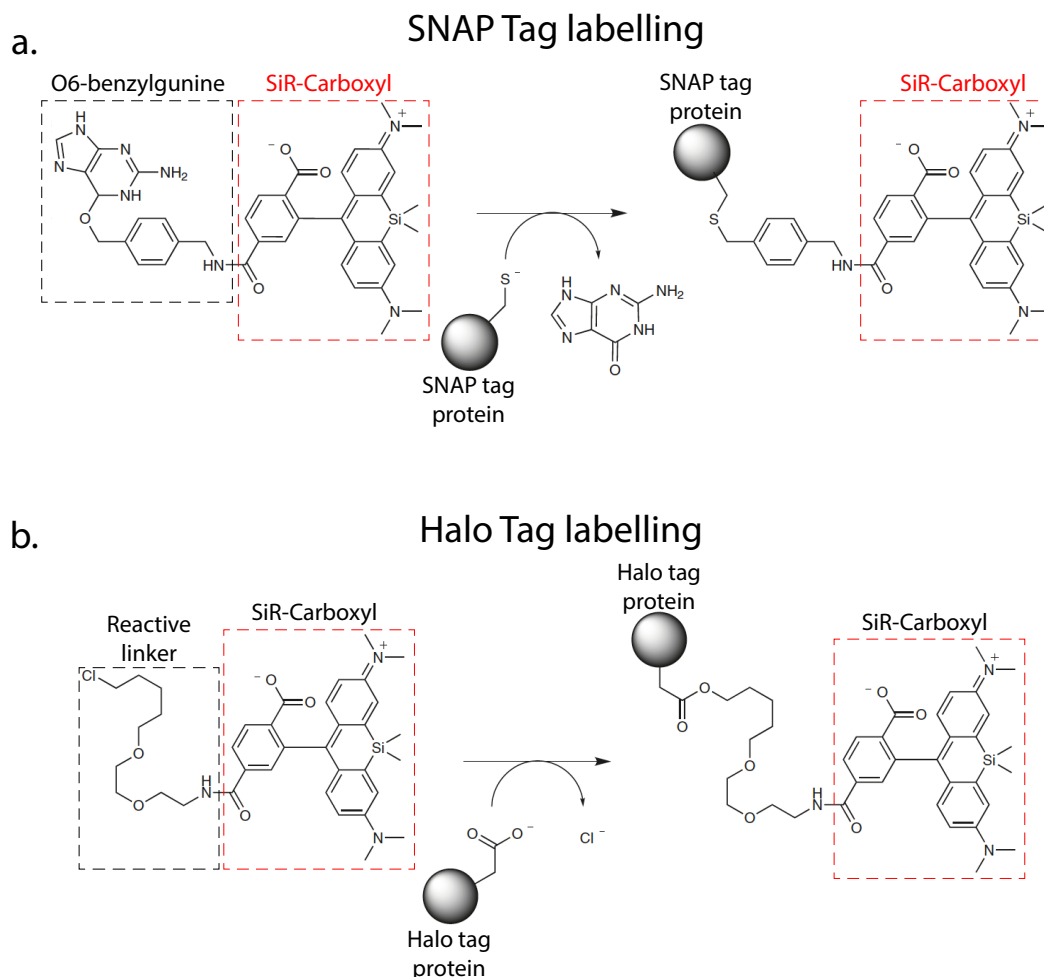


Figure 3.5: Self-labelling enzymes SNAP and Halo tag. (a) Reaction schematic for SNAP tag labelling with BG conjugated to SiR-carboxyl. (b) Reaction schematic for Halo tag labelling with CA-O₂ linker conjugated to SiR-carboxyl. This figure has been adapted from (Dean and Palmer, 2014) with permission.

Labeling of the protein of interest is done by creating a fusion protein of the enzyme tags at the N- or C-terminus of the protein of interest. The addition of the enzyme tag may disrupt protein function and localization; therefore, appropriate controls are required. The labeling stoichiometry between enzyme tag and ligand is described to be 1:1. However, studies show that both, attaching chemical moieties (fluorophores) and steric hinderances due to position of the enzyme tag have an effect on affinity of labels (Erdmann et al., 2019). For quantitative measurements, it is important to account for the fraction of enzyme tags that actually get labeled with a fluorophore.

Fluorescent proteins (FP) Photoactivatable (PA) and photoswitchable fluorescent proteins (PSFP) are utilized in SMLM as they have the ability to switch from dark to fluorescent state, or from one excitation and emission wavelength to another (Betzig et al., 2006; Hess et al., 2006). For some of these proteins photoactivation can be reversible or irreversible. This change in photophysical property can be through chemical modification, backbone cleavage or cis-trans isomerization of the PAFP chromophore (Lukyanov et al., 2005). Reversibly photoswitchable fluorescent proteins such as, Dronpa, enables the PAFP to be localized multiple times which results in smoother images due to increased sampling (Durisic et al., 2012). However, the photon yield is very low compared to reversibly photoswitchable organic dyes such as AF647. The low number of collected photons per switching cycle leads to lower localization precision. Irreversible PAFPs predominantly switch only once and emit a high number of photons. Therefore, they are ideal candidates for quantitative measurements to study protein complex stoichiometry.

Among all the labeling strategies for quantitative SMLM, the use of fluorescent proteins is most appealing due to the ease of implementation and ability to achieve 1:1 labeling stoichiometry. However, it is of importance to assess the effect of tagging on target protein function and localization. Some PAFPs have been found to oligomerize leading target protein to mislocalize and form aggregates (Wang et al., 2014). In addition it is crucial to factor in photoactivation efficiency and maturation times of PAFPs in the experimental design (Balleza et al., 2018; Durisic et al., 2012).

Antibodies and nanobodies Immunofluorescence (IF) uses antibodies to detect proteins of interest. It does not require target manipulation and is readily available for purchase against many targets. Direct IF is performed with a primary antibody that has been conjugated to a fluorophore. Indirect IF introduces a secondary antibody with an affinity to a primary antibody. In the latter, the secondary antibody is conjugated to a fluorophore. Antibodies are large molecules, approximately 150 kDa, they consist of two heavy chains (50 kDa each) and two light chains (25 kDa each) (Charles A Janeway et al., 2001). Thus, it possesses a large linkage error (> 15 nm) due to its dimensions. The binding of primary to secondary antibody does not follow a strict 1:1 stoichiometry and it is prone to clustering artifacts (Baumgart et al., 2016). Depending on the fluorophore conjugation strategies, an antibody can be conjugated to multiple dye molecules. These factors hamper direct quantitative readouts, but with carefully planned experimental controls, it is possible to extract accurate quantitative information (Ehmann et al., 2014).

Nanobodies have the same working principle as antibodies. However, they are significantly smaller, approximately 13 kDa. They can be easily raised against specific targets (Fridy et al., 2014) and stoichiometrically labelled with fluorophores (Pleiner et al., 2015). Nanobodies overcome many of the limitations of antibodies, thus making it useful for quantitative measurements. Nevertheless, the efficiency of

nanobodies binding to their target must still be taken in to account when performing quantitative imaging (Thevathasan et al., 2019).

As discussed thus far, there are different permutations and combinations of fluorophores and labeling strategies that can be applied for quantitative imaging, however, assessment of their performance is heavily reliant on conditions under which the samples are imaged.

3.1.3 Imaging conditions

Using SMLM it is possible to acquire data with substantially higher resolution compared to conventional methods. However, this requires long acquisition times, making quantitative live cell SMLM particularly challenging. Given the continuous exposure to high laser intensities and long acquisition time periods, cells experience phototoxicity. Therefore, in many quantitative SMLM measurements, the cells are fixed or the imaging buffer is supplemented with additives to maximize the output of each fluorophore and minimize phototoxicity. Within the domain of imaging conditions, parameters such as buffer composition, laser intensities and exposure times can be modulated. In the following section I will focus primarily on how buffer composition and acquisition conditions (laser intensity and exposure times) have an effect on data quality.

3.1.3.1 Buffer Conditions

The ability of organic fluorophores to transition between a dark and bright state is fundamental for SMLM. Photoswitching of the fluorophore is modulated by using additives in the imaging buffer. Depending on the chemical nature of fluorophores, different variants of T_1 (Fig. 3.1) are produced. For fluorophores derived from rhodamine, residual oxygen or oxidizing agents are required for favorable photoswitching behavior (Linde et al., 2011). This is in contrast to cyanine derivatives, which require an oxygen-free environment as its T_1 has a very high reactivity with oxygen (Heilemann et al., 2005). Therefore, obtaining optimal performance from a fluorophore requires careful optimization of the buffer composition. Molecular oxygen efficiently quenches fluorophores at T_1 to return fluorophores to S_0 , but this results in the formation of reactive and toxic singlet oxygen species. To prevent the formation of reactive oxygen species, an oxygen scavenging system is added to the imaging buffer.

Oxygen scavenger systems can either be enzymatic or chemical. For enzymatic reactions, glucose and a mixture of glucose oxidase (GLOX) and catalase (CAT) enzymes are added. GLOX catalyzes the reaction of glucose with oxygen to produce hydrogen peroxide and glucuronic acid. Catalase then breaks down hydrogen peroxide to H_2O and O_2 . Unfortunately, the production of glucuronic acid decreases

the pH of imaging buffers to levels that are not suitable for optimal fluorophore performance. Pyranose oxidase (POX) is thus used as an alternative to GLOX (Swoboda et al., 2012). POX catalyzes the reaction of glucose with oxygen to produce hydrogen peroxide and a ketone with no drastic effects on the pH of the buffer. Chemicals such as sulfites can be added to the imaging buffer to sequester oxygen away from the imaging buffer (Hartwich et al., 2018; Morello et al., 1964).

The removal of molecular oxygen results in a large fraction of fluorophores in T_1 which increases the probability of losing the fluorophore to photobleaching (Song et al., 1996). Besides oxidation of T_1 to return the fluorophore to S_0 , reducing agents such as beta-mercaptoethanol (BME), mercaptoethylamine (MEA), dithiothreitol (DTT), glutathione (GSH), Trolox and ascorbic acid (AA) are added to the imaging buffer (Heilemann et al., 2009; Turkowyd et al., 2016). The reduction of T_1 creates dark state radical anions that absorb wavelengths between 350–550 nm to facilitate the return of fluorophores to its fluorescent state (Linde et al., 2011). This enables controlled switching of fluorophores to its bright state by 405 nm illumination.

Additives such as cyclooctatetraene (COT) have been shown to increase photon yield for AF647 by directly bringing fluorophores at T_1 back to their ground state (Olivier et al., 2013; Widengren et al., 2007). The use of heavy water, D_2O , has been reported to increase photon yield for both organic and photoactivatable proteins (Ong et al., 2015). To empirically determine the increase or decrease in performance of the dye in different solutions, knowing the absolute number of fluorophores is needed for normalization purposes.

3.1.3.2 Acquisition conditions

Photoswitching kinetics of fluorophores are accelerated by increasing the power of the excitation laser (Bates et al., 2005; Heilemann et al., 2008). The bright state of the fluorophore would thus be shorter, allowing for shorter camera exposure times. This allows for acquisitions to be completed faster, increasing the throughput (Huang et al., 2013). However, higher excitation laser intensities increase the probability of photobleaching in a nonlinear trend, resulting in lower localization density (Lin et al., 2015). In general, as a rule of thumb, the exposure time set to 1.5 times the lifetime of a fluorophore's bright state. This would ensure that the localizations in subsequent frames are grouped as a single localization and not be counted multiple times resulting in overcounting. Finally, the photophysical properties of dyes are dependent on its individual chemistry and environment, therefore the optimal laser intensity and exposure time has to be determined using an imaging standard.

All the parameters discussed till now, highlight the need for an imaging standard that is versatile and capable of delivering the specific readouts as required. I will now proceed to discuss about properties a reference standard should possess.

3.2 Reference standard for SMLM

An imaging standard that objectively optimizes all the parameters, needs to fulfill the following requirements: It needs to

- Be robust and user friendly.
- Exhibit fluorophores/labels at distances that are relevant for 2D and 3D SMLM to help benchmark resolution capabilities of the system.
- Contain a defined stoichiometry to disentangle effects of labelling efficiency, fluorophore photophysics and number of epitopes.
- Be compatible with commonly used labelling approaches within the context of a cell.

Current standards for benchmarking have their strengths as well as weaknesses and are usually used complimentary to each other. They consist of artificial and cellular samples. Artificial samples used successfully are, quantum dots (QD), beads and DNA origami. QDs and beads are routinely used because of a high signal to noise ratio, photostability and ease of use for microscope and analysis software calibration. DNA origamis are particularly useful for placing fluorophores at precise 3D positions (Deschamps et al., 2014). They are versatile in enabling conjugation of protein probes and organic dyes with fixed distances and number of epitopes (Zanacchi et al., 2017). However, DNA origamis are difficult to assemble, require the use of purified proteins and measurements are done outside the context of a cell.

Within the context of a cell, microtubules, clathrin-coated pits, actin and mitochondria are commonly used as standards (Dempsey et al., 2011; Heilemann et al., 2008; Huang et al., 2008b; Lin et al., 2015; Linde and Sauer, 2014). Besides microtubules, these cellular standards are intrinsically variable. Microtubules are especially used as they form a regular structure and are abundant and easy to image. Many studies quantify various aspects of data quality based on sectional profiles drawn along or across sections of microtubules. The abundance of epitopes present on microtubules results in acceptable images even with very low labelling efficiencies. Therefore, microtubules have a low sensitivity when assessing labelling efficiency.

In the context of molecular counting for determining the stoichiometry of protein complexes, calibration of the microscope and measurements need to be done. This requires knowledge on the number of fluorophores or photoactivatable proteins present on the imaging standard. Knowing the absolute number of fluorophores enables characterization of the number of photoswitching events per fluorophore for correction and normalization purposes (Baldering et al., 2019; Fricke et al., 2015; Hummer et al., 2016). This approach requires accurate image segmentation and

and biochemically. By fitting structures of individual subunits obtained from X-ray crystallography into high resolution electron tomographic reconstructions of the NPC, the overall NPC structure has been solved with a pseudo-atomic resolution (Fig. 3.6c). The NPC has a diameter of approximately 110 nm and a total height of approximately 70 nm (Kosinski et al., 2016; Appen et al., 2015).

The NPC consists of approximately 30 nuclear pore proteins called nucleoporins (Nups). These Nups are present in multiples of 8 and are organized into stable subcomplexes positioned within the NPC (Beck and Hurt, 2017; Knockenhauer and Schwartz, 2016). Nups can be divided into two groups, namely scaffold and FG-Nups. FG-Nups are rich in phenylalanine (F) and glycine (G) amino acid residues, hence the name FG-Nups. They are mostly intrinsically disordered and have been reported to participate in nucleocytoplasmic transport (Li and Kohler, 2014). Due to the complex structural nature of FG-Nups, they have proved difficult to characterize. They are situated in the channel where they separate in a liquid phase to create a mesh-like network. The presence of a mesh-like network could be a reason why small proteins (< 30 kDa) are able to freely diffuse in and out of the nucleus (Ribbeck and Görlich, 2001).

Scaffolding Nups can be characterized into two subcomplexes comprising a majority of the NPC scaffold, namely, Y-complex and inner ring complex. The core members of the Y-complex are Nup96, Nup160, Nup133, Nup85, Nup107, SEC13 homologue 1 (Seh1) and Sec13. The core members of the inner ring complex are Nup205, Nup188, Nup155, Nup93, Nup35, Ndc1 and Nup98. The Y-complex is present on both the cytoplasmic and nuclear ring of the NPC. Tomographic maps of the NPC presented 32 Y-shaped features, consistent with dimensions that fit X-ray crystal structure of the Y-complex (Appen et al., 2015). This validated previous studies that used targeted proteomics and fluorophore counting, to propose that the Y-complex was present as 32 copies within a single NPC (Ori et al., 2013).

3.3.2 The Y-complex and Nup96

There are 16 copies of the Y-complex arranged in a head-to-tail orientation anti-clockwise on the cytoplasmic ring and clockwise on the nuclear ring. The Y-complex exists as dimers forming a concentric circle (Fig. 3.6b). As a result of interactions and a slight displacement in the position of dimers, there is an offset in the registration of the cytoplasmic and nuclear ring. An individual Y-complex can be further structurally described to possess a long arm, short arm, stem body and stem tip which comprise of different Nups. Nup96 is situated at the stem body of the Y-complex (Fig. 3.7b-d). Due to its position, all 32 copies of Nup96 are almost in register. The precise geometry, dimensions and stoichiometry of protein components make the NPC an ideal structure for resolution benchmarking and molecular counting. It is used as a target for validation of new imaging reference

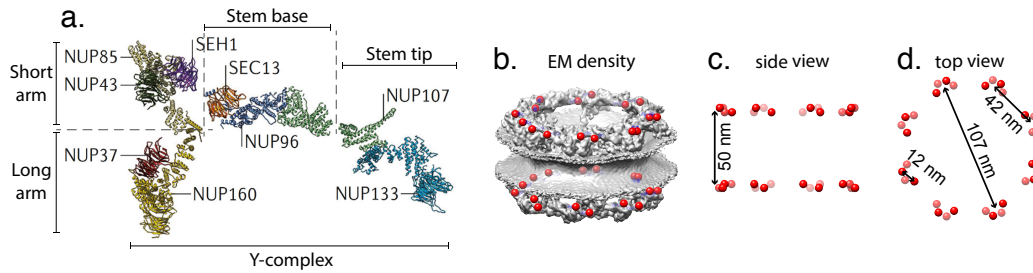


Figure 3.7: Y-complex substructure and position within the NPC (a) Organization of the respective Nups which make up the Y-complex. Nup96 is situated at the stem base of the Y-complex. (b) EM density (Appen et al., 2015) of the NPC with the c-terminal of Nup96 indicated in red. (c) Cross section schematic of the NPC with measured distance between the cytoplasmic and nuclear ring. (d) top view schematic of the NPC with distances between different copies of Nup96 indicated. This figure has been adapted from (a) (Beck and Hurt, 2017) with permission and (b) from (Thevathasan et al., 2019) on which I am co-first author.

standards and protein counting approaches (Cella Znacchi et al., 2019; Finan et al., 2015; Znacchi et al., 2017). Clear visualization of the NPC's eight-fold radial symmetry using fluorescence is dependent on which Nup is targeted and on the resolution of the microscope that is used (Fig. 3.7d).

4 | Results

4.1 Generation and validation of cell line

Four homozygous CRISPR knock-in cell lines were generated in collaboration with the Ellenberg's group. The cell line used was human bone osteosarcoma epithelial cells, U2OS. It is easy to culture and routinely used for microscopy as it is very flat and its nucleus is close to the coverslip. We tagged Nup96 endogenously with either mEGFP (GFP)(fluorescent protein), SNAP_f (SNAP)(self-labelling enzyme), Halo (self-labelling enzyme) or mMaple (photoconvertible protein). The Ellenberg group had an established CRISPR cell line generation pipeline used routinely to generate endogenously tagged cell lines. Ulf Matti and I cloned the donor plasmids and gRNA plasmids required for the generation of the cell lines respectively, which were then passed to members of the Ellenberg group for generation of the cell lines. To describe the pipeline briefly, U2OS wild-type (WT) cells were transfected with a donor plasmid containing the template for homologous recombination with the tag of interest and a plasmid containing two expression cassettes for a human codon-optimized Cas9D10A nickase and gRNA sequences. After transfection, positive clone selection was done using single cell sorting via fluorescence-activated cell sorting (FACS). Correct integration was validated using junction PCR. Sanger sequencing was performed to detect mutations within the insertion sites. To confirm homozygosity and exclude off-target integration of the tag, Southern blotting with two probes against Nup96 and the tag was performed, respectively. Finally, a Western blot was performed to characterize protein expression of the tagged protein.

Fig. 4.1 shows both Southern and Western blots done for validation of homozygosity of generated cell lines. Southern blots were performed with two probes against, Nup96 C-term and the respective tag introduced to the cell line (Fig. 4.1a-d). Clones were determined as homozygous when a single product (band) was detected for both probes. U2Os WT was loaded as a control sample. Based on Southern blot results, homozygous clones were then processed for Western blotting with an antibody against Nup98-96 precursor protein targeting residues 900-950 (Fig. 4.1e). Proteolytic cleavage of a 186 kDa precursor protein results in Nup98 (residues 1 - 880) and Nup96 (residues 881-1818). Compared to Nup96 from U2OS

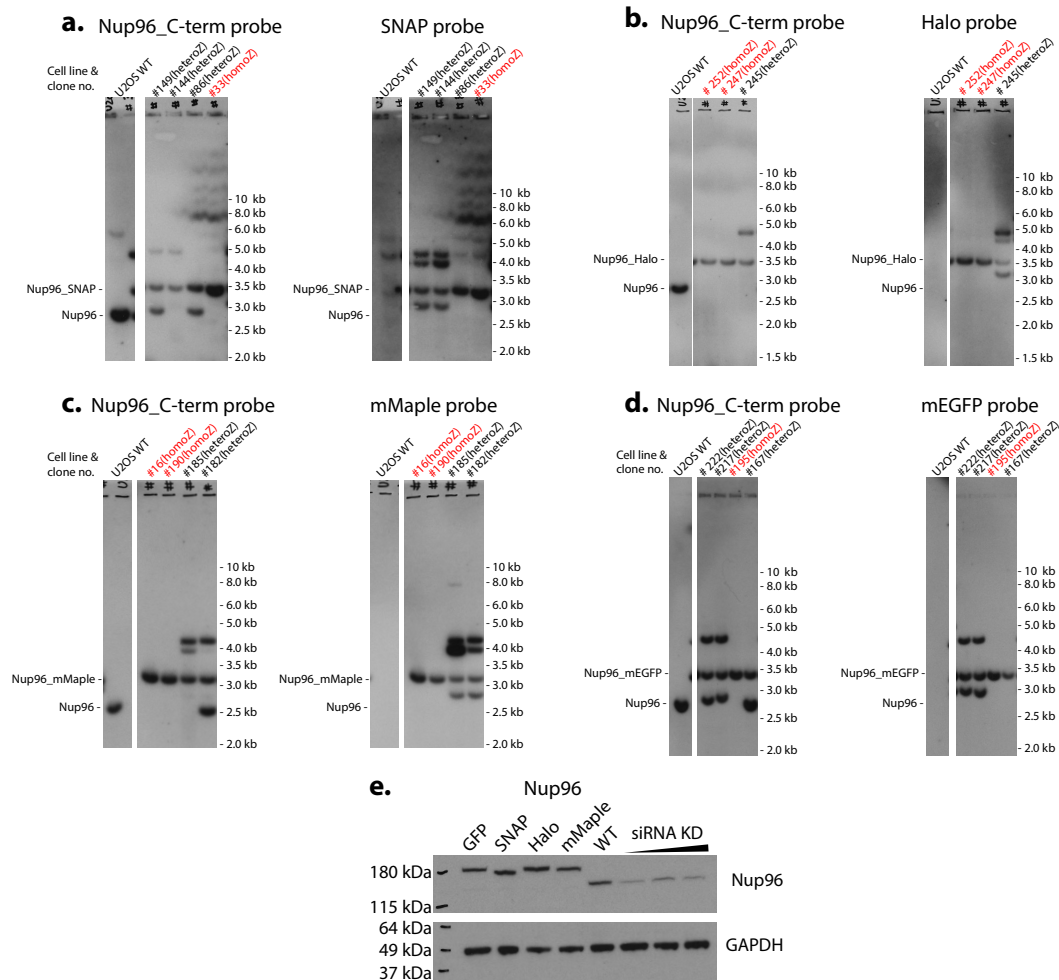


Figure 4.1: Validation of cell line homozygosity with Southern and western Blotting. (a-d) Southern blots of (a) Nup96-SNAP, (b)Nup96-Halo, (c)Nup96-mMaple, (d)Nup96-mEGFP. Blots to the left were from a probe against the C-terminus of Nup96. Blots to the right were from a probe against the respective tags. (e) Western blot of homozygous cell lines probed with an anti-Nup98 antibody. siRNA concentrations used: 0.6 μ g, 1.2 μ g and 1.8 μ g. Southern blots were performed by Bianca Nijmeijer, Moritz Kueblbeck and Sandra Correia from the Ellenberg group. Western blots were performed by me. This figure has been taken from (Thevathasan et al., 2019 on which I am a co-first author. It is being distributed under CC-BY-ND 4.0 international license.

WT, we observed protein band shifts according to the molecular weight of mEGFP (27 kDa), SNAP (19.4 kDa), Halo (33 kDa) and mMaple (27.2 kDa). U2OS WT cells that were treated with siRNA against Nup98 mRNA, showed reduced protein content thus validating the specificity of the antibody. Since a single protein band was observed, we were confident that these clones were homozygous.

4.2 The NPC as a 2D & 3D resolution standard

4.2.1 Resolving capabilities of imaging modalities

The NPC complex dimensions are well within the diffraction limit. It has a diameter of about 110 nm and the distance between the cytoplasmic and nuclear ring is approximately 50 nm. We used the cell lines to showcase the resolving capacity of commonly used microscope modalities. Under widefield, confocal and airy-scan, the NPCs are resolved as individual puncta (Fig. 4.2a-c). The ring structure of the NPC was resolved when the cell lines were imaged under superresolution modalities such as stimulated emission depletion (STED) and SMLM (Fig. 4.2d-g). Under STED microscopy, complete ring structures of the NPC were resolved (Fig. 4.2d). SMLM on Nup96-mMaple revealed individual corners of the NPC (Fig. 4.2e). We obtained the highest resolution using Nup96-SNAP labelled with organic dyes in single colour (Fig. 4.2f,g). The eight corners were still visible under dual colour imaging where the second label was introduced against the core of the NPC (Fig. 4.2h,i).

4.2.2 Quantifying 'Linkage Error'

The flatness of U2OS nucleus enabled the imaging of hundreds of NPCs at any given time. This allowed for automatic segmentation and statistical analysis on the geometry of NPCs (Fig. 4.3a). By fitting a circle onto each NPC we were able to measure a radius of 53.7 ± 2.1 nm (mean \pm SD) (N = 7 cells / 2536 NPCs) for Nup96-SNAP (Fig. 4.3b,c). Using our cell line, we could quantify the 'linkage error' introduced by the use of different labeling strategies (Fig. 4.3d). We measured 54.5 ± 2.6 nm for Nup96-Halo labeled with CA-O4-Cy5 (N = 6 cells / 4959 NPCs), 55.4 ± 3.5 nm for Nup96-mMaple (N = 6 cells / 4276 NPCs), 55.0 ± 1.9 nm for Nup96-GFP detected with a GFP nanobody labeled with AF647 (N = 6 cells / 2913 NPCs) and 64.3 ± 2.6 nm for Nup96-GFP detected with a primary – secondary antibody labeled with AF647 (N = 6 cells / 3158 NPCs).

4.2.3 Correction of depth-dependent aberration

The distance between both the cytoplasmic and nuclear ring make it an ideal structure to calibrate the microscope's capability to determine quantitative distances. We first imaged the nucleus at its equatorial plane Fig. 4.4a in 2D. This allowed visualization the side profile of both NPC rings and quantification of distances between both rings (Fig. 4.4b). We measured an average distance of 49.3 ± 5.2 nm (N = 14 cells / 379 NPCs) (Fig. 4.4c). Measuring NPC in 3D using astigmatism (Fig. 4.4d,e) we were able to score an average distance of 42.1 ± 1.1 nm (N = 8 cells / 1021 NPCs) (Fig. 4.4f, magenta plot), which was smaller than the value measure

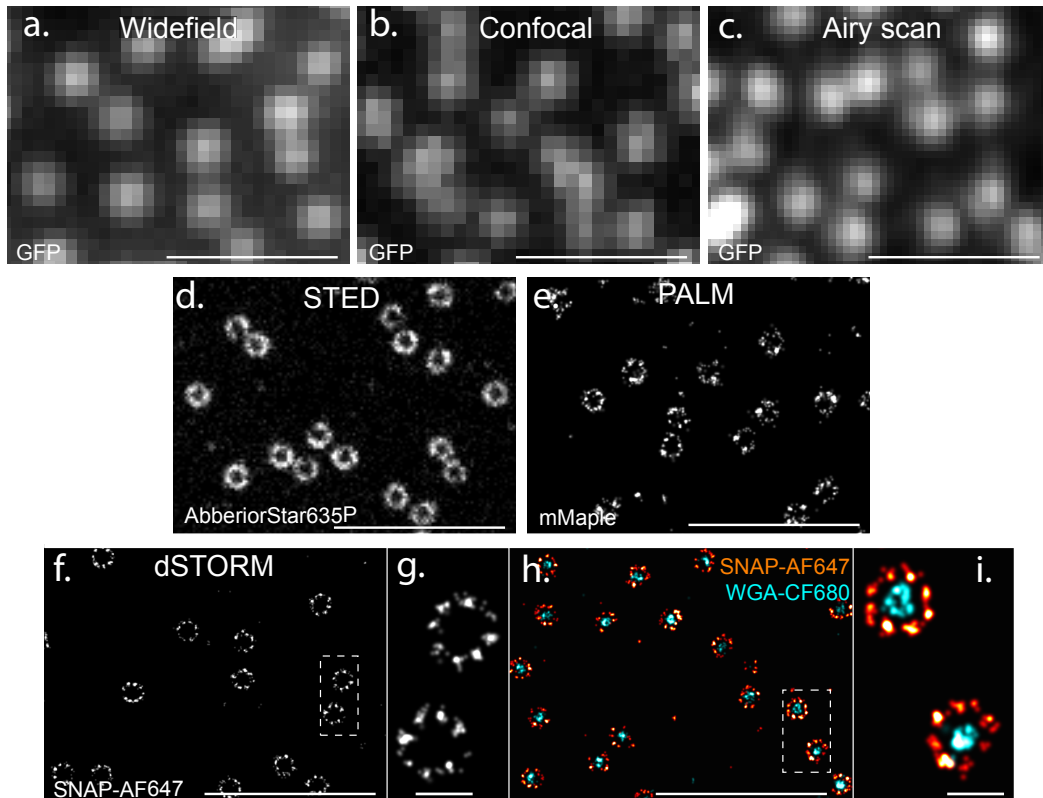


Figure 4.2: Gallery of Nup96 cell lines acquired across different imaging modalities. (a) Widefield, (b) confocal, (c) airy scan images of Nup96-GFP. (d) Unprocessed STED image of Nup96-GFP stained with an anti-GFP nanobody coupled to AbberiorStar635P. (e) SMLM image of Nup96-mMaple. (f) SMLM image of Nup96-SNAP labeled with BG-AF647. (g) Zoom in of the area marked by the white dotted lines in (f). (h) Dual colour SMLM image of Nup96-SNAP labeled with BG-AF647 (red) and WGA-CF680 (cyan). (i) Zoom in of the area demarcated within the white dotted lines in (h). Scale bars 1 μm (a-f, h) and 100 nm (g, i). All the images presented in this figure were acquired by Maurice Kahnwald. This figure has been adapted from (Thevathasan et al., 2019) on which I am a co-first author. It is being distributed under CC-BY-ND 4.0 international license.

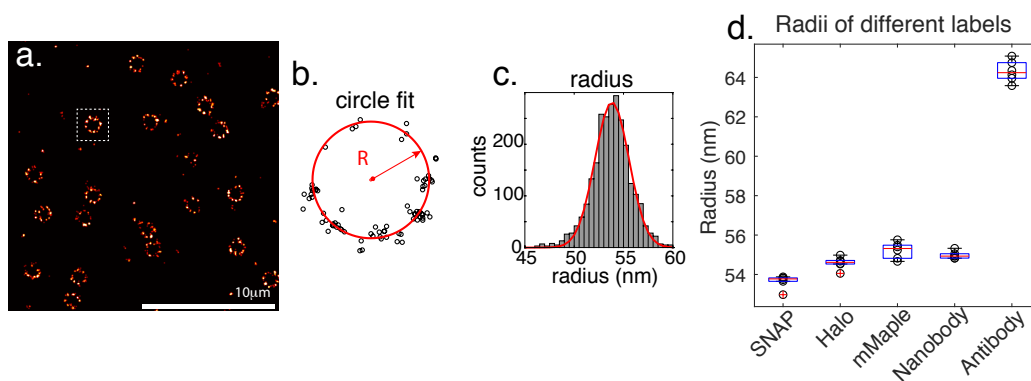


Figure 4.3: Quantifying 'Linkage Error'- NPCs as a 2D resolution standard. (a) Automatic detection and segmentation of individual NPCs. (b) Scoring the radius of NPCs by fitting it to a circle. (c) Histogram of fitted radii of Nup96-SNAP labeled with BG-AF647. (d) Box plot of fitted radii measured for each labeling strategy. Each data point corresponds to one cell. Data jointly produced by Maurice Kahnwald and me. This figure has been adapted from (Thevathasan et al., 2019) on which I am a co-first author. It is being distributed under CC-BY-ND 4.0 international license.

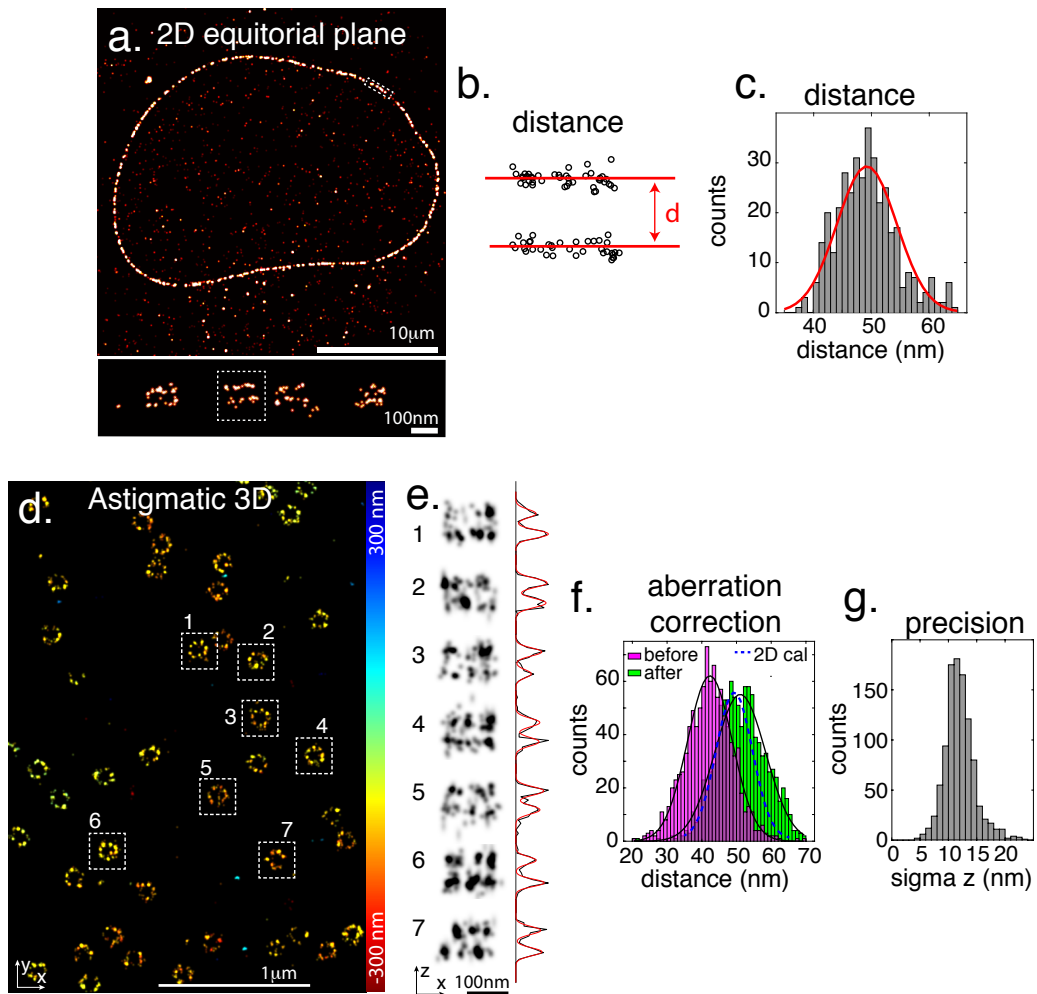


Figure 4.4: Correcting depth-dependent aberrations - NPCs as a 3D resolution standard. (a) Top panel, equatorial SMLM image of Nup96-SNAP labeled with BG-AF647. Bottom panel, zoom in of the area marked by the white dotted lines in the top panel showing cytoplasmic and nuclear ring of individual NPCs. (b) Scoring the distance between the cytoplasmic and nuclear ring. (c) Histogram of fitted distances between the cytoplasmic and nuclear ring. (d) 3D SMLM image of the nucleus closest to the coverslip. The localizations are color-coded according to their z-position. (e) x-z reconstructions of NPCs and its corresponding z-profiles boxed out in (d). (f) Histograms of measured z-profiles before (magenta) and after (green) correcting for depth-induced calibration errors. (g) Histogram of standard deviation calculated from a double Gaussian fit of z-profiles, indicating the limits of experimental localization precision. Data jointly produced by Yiming Li, Jonas Ries and me. This figure has been adapted from (Thevathasan et al., 2019) on which I am a co-first author. It is being distributed under CC-BY-ND 4.0 international license.

in 2D equatorial images. Using a method recently developed by our lab (Li et al., 2019), we were able to correct depth dependent aberration error and measure an average distance of 49.8 ± 1.9 nm (Fig. 4.4f, green plot). In addition we calculated a refractive index mismatch factor (RIMF) of 0.79. The upper-bound experimental localization precision in z was 13.3 ± 1.0 nm ($N = 8$ cells / 1021 NPCs) (Fig. 4.4g).

4.3 Labeling efficiency standard

Fluorescence microscopy requires labeling of the target of interest with a fluorophore. The different strategies of labelling are highlighted in the introduction. However, all these strategies have varying efficiencies. Protein and chromophore maturation have to be accounted for in the use of fluorescent proteins. In the case of organic dyes, fluorophore blinking and reactivations could report a higher labeling efficiency. Quantifying the efficiency of a labelling strategy is challenging when absolute numbers of the label is unknown. Our engineered Nup cell lines overcome this limitation as we have knowledge of the number of labels and corresponding labels that should be present within each NPC. Scoring the number of corners recorded per NPC gives us a measure of the effective labeling efficiency (ELE) of the label being used. We use the term ‘effective’ as it accounts for the population of target proteins that exhibit a fluorophore being detected and fitted with acceptable confidence. This in principle accounts for dye to ligand conjugation efficiency, bleached or invalid fluorophores.

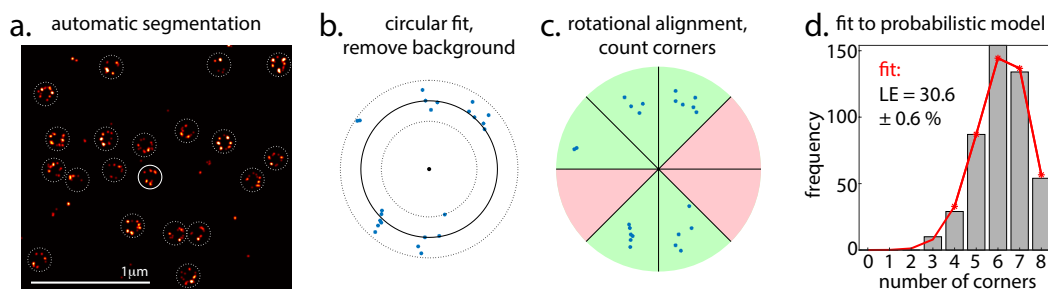


Figure 4.5: Workflow for calculating effective labeling efficiencies. (a) Automatic detection and segmentation of individual NPCs. (b) A circle is fit to the localizations. Localizations too close to the center and outside the circle are excluded as background. (c) The localizations are then rotated to optimally fit a rotationally eight-fold symmetric template. The number of slices containing at least one corner is counted. (d) A histogram of all the number of corners scored by NPCs are then fitted with a probabilistic model to determine the effective labelling efficiency. Jonas Ries designed and implemented this analysis pipeline. This figure has been adapted from (Thevathasan et al., 2019) on which I am a co-first author. It is being distributed under CC-BY-ND 4.0 international license.

4.3.1 Analysis pipeline

The NPCs are first automatically segmented (Fig. 4.5a). A circular fit is imposed. Localizations outside the circle were considered background localizations and discarded (Fig. 4.5b). The localizations are then rotated to fit a template consisting of a circle divided into 8 equal parts/slices (Fig. 4.5c). The number of slices containing localizations is then scored. ELE was determined by scoring hundreds of NPCs and performing statistical analysis with a probabilistic model (Fig. 4.5d). From the

analysis pipeline we scored: ELE, photons per localization, number localizations per NPC and per Nup96 protein.

4.3.2 Quantifying effective labeling efficiencies

All of the values reported in this section are represented in Fig. 4.6 and Table 4.1.

4.3.2.1 Self-labeling enzymes

Using the analysis pipeline, we looked at the labeling efficiency of Nup96-SNAP with BG-AF647 and measured an ELE of 58%. ELE of Nup96-Halo with CA-O2-AF647 was 36%. ELE was found to vary between 21-40% when we used different ligands or dyes with Nup96-Halo. We observed ELE of 29% when the polyethylene glycol (PEG) composition of the ligand was increased from two (CA-O2-AF647) to three (CA-O4-AF647). Photophysics of AF647 was not affected by the composition of ligand. ELE increased from 29% (CA-O4-AF647) to 40% (CA-O4-Cy5) between different variants of cyanine dyes. We observed lesser photons but higher number of localizations per NPC and protein with Cy5 and the inverse for AF647. Photoactivatable JF549 (PA-JF549) gave the lowest amount across ELE, photon count and number of localizations per NPC and protein.

4.3.2.2 Nanobodies and antibodies

We studied the ELE of nanobodies and antibodies targeted against GFP in our Nup96-GFP cell line. We observed the highest ELE, 75%, with commercial FluoTag®-X4 nanobodies (NB-X4-CF680). The commercial nanobody consists of a mixture of two nanobodies against 2 different GFP epitopes. Each nanobody is labelled with 2 fluorophores respectively. We obtained a similar ELE, 74%, with nanobodies labeled with a different dye, AF647. When we used commercial nanobodies labeled with a single fluorophore, FluoTag®-Q, we measured an ELE of 61 and 62% for AF647 and CF680, respectively. Indirect immunofluorescence using a primary-secondary antibody labelled with AF647 produced an ELE of 65%. Using our cell line, we were able to monitor the shelf-life of nanobodies made in-house. We observed a decrease in ELE from 45% to 25% over the duration of 2 years.

4.3.2.3 Photoactivatable protein, mMaple

Simulations to test the robustness of our analysis (Thevathasan et al., 2019) showed that we could quantify ELE even when individual corners are not clear. Therefore, we ran our ELE analysis on data acquired from our Nup96mMaple cell line. We

measured an ELE of 58%, even though all copies of Nup96 were tagged with mMaple.

4.3.2.4 Imaging buffer composition

Fluorophore photophysics is heavily dependent on the imaging buffer composition. Therefore, considerable effort is invested into optimizing buffer composition and conditions to attain maximum fluorophore performance. Fluorophore triplet quenching by oxygen promotes the production of radical oxygen species that induce phototoxicity and damage to existing fluorophores. Therefore enzymatic oxygen scavenging systems such as glucose oxidase / catalase (GLOX) mixture and chemicals such as sulfites are added to scavenge oxygen. We observed that addition of sulfite to the imaging buffer had adverse effects on AF647 photophysics compared to the use of GLOX. We recorded lower ELE (40%), photon count (7006) and number of localizations per NPC (19) and per protein (1.5).

Reducing agents like thiols are added to the imaging buffer to reduce fluorophores in the excited triplet state, T_1 , to a dark state for reactivation. Commonly used reducing agents are BME and MEA. We observed that AF647 performs better in the presence of BME compared to MEA. In our measurements, we did not observe a significant difference of performance of AF647 in D_2O . However, we did observe an increased photon yield from mMaple in D_2O compared to H_2O . In addition we detected no significant effect of paraformaldehyde fixation on mMaple photophysics.

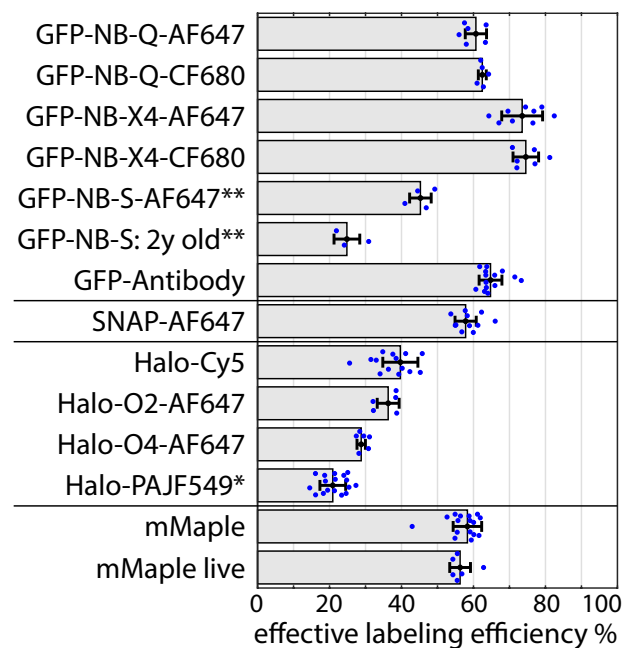


Figure 4.6: Effective labeling efficiencies of labeling strategies. Measured effective labeling efficiencies for the different cell lines with its respective ligands and different dyes. Bars represent the mean and error bars the standard deviation. Individual data points (blue) are from individual cells. Data jointly produced by Maurice Kahnwald and me. This figure has been adapted from (Thevathasan et al., 2019) on which I am a co-first author. It is being distributed under CC-BY-ND 4.0 international license.

Table 4.1: Various imaging conditions and analysis

Sample	Buffers	ELE [%]	Photons per localization	Localizations per NPC	Localizations per protein	N/cells/NPCs analyzed
U2OS-Nup96-SNAP-BG-AF647	GLOX/MEA	58 ± 3	10168 ± 982	73 ± 20	3.9 ± 0.9	4/11/72
U2OS-Nup96-SNAP-BG-AF647	GLOX/MEA in D ₂ O	56 ± 3	10079 ± 423	64 ± 8	3.6 ± 0.4	2/5/79
U2OS-Nup96-SNAP-BG-AF647	GLOX/BME	64 ± 4	12904 ± 689	110 ± 9	5.4 ± 0.5	3/8/24
U2OS-Nup96-SNAP-BG-AF647	Sulfite/MEA	40 ± 2	7006 ± 513	19 ± 2	1.5 ± 0.1	2/5/08
U2OS-Nup96-mMaple fixed	50 mM Tris in D ₂ O	58 ± 4	1783 ± 118	52 ± 6	2.8 ± 0.2	6 / 16 / 8146
U2OS-Nup96-mMaple fixed	50 mM Tris in H ₂ O	55 ± 4	1169 ± 36	44 ± 3	2.5 ± 0.2	2/7/26
U2OS-Nup96-mMaple live	50 mM Tris in D ₂ O	56 ± 3	1621 ± 159	52 ± 2	2.9 ± 0.1	3 / 6 / 1343
U2OS-Nup96-Halo-Cy5	GLOX/MEA	40 ± 5	11229 ± 639	60 ± 12	4.7 ± 0.6	5 / 14 / 5967
U2OS-Nup96-Halo-O2-AF647	GLOX/MEA	36 ± 3	15631 ± 592	40 ± 8	3.4 ± 0.4	2 / 5 / 1393
U2OS-Nup96-Halo-O4-AF647	GLOX/MEA	29 ± 1	14466 ± 518	40 ± 3	4.3 ± 0.2	2/6/95
U2OS-Nup96-Halo-PA-JF549	50 mM Tris in D ₂ O	21 ± 4	9420 ± 1050	9 ± 2	1.3 ± 0.1	3 / 17 / 4066
U2OS-Nup96-mEGFP-NB-Q-AF647	GLOX/MEA	61 ± 3	7027 ± 542	57 ± 9	2.9 ± 0.3	2/6/13
U2OS-Nup96-mEGFP-NB-Q-CF680	GLOX/MEA	62 ± 1	6129 ± 170	100 ± 17	5.0 ± 0.8	2 / 5 / 1805
U2OS-Nup96-mEGFP-NB-X4-AF647	GLOX/MEA	74 ± 6	6166 ± 575	92 ± 15	3.9 ± 0.4	2/9/03
U2OS-Nup96-mEGFP-NB-X4-CF680	GLOX/MEA	75 ± 4	6524 ± 236	134 ± 19	5.7 ± 0.8	2/6/11
U2OS-Nup96-mEGFP-S-NB-AF647	GLOX/MEA	45 ± 3	8770 ± 1522*	64 ± 21	4.5 ± 1.5	2 / 4 / 8768
U2OS-Nup96-mEGFP-S-NB-AF647 2y	GLOX/MEA	25 ± 4	6122 ± 1039	50 ± 11	6.2 ± 0.6	2 / 3 / 1000
U2OS-Nup96-mEGFP-Antibody-AF647	GLOX/MEA**	65 ± 3	4147 ± 156	141 ± 28	6.8 ± 1.2	3 / 14 / 7380

Note: Values are represented as mean ± SD. N represents the number of biological independent replicates. *Excitation laser intensity different compared to other experiments. ** 100 mM MEA instead of the usual 35 mM MEA used to reduce the fraction of fluorophores on the on-state at any given time. Data jointly produced by Maurice Kahnwald and me. This table has been taken from (Thevathasan et al., 2019) on which I am a co-first author. It is being distributed under CC-BY-ND 4.0 international license..

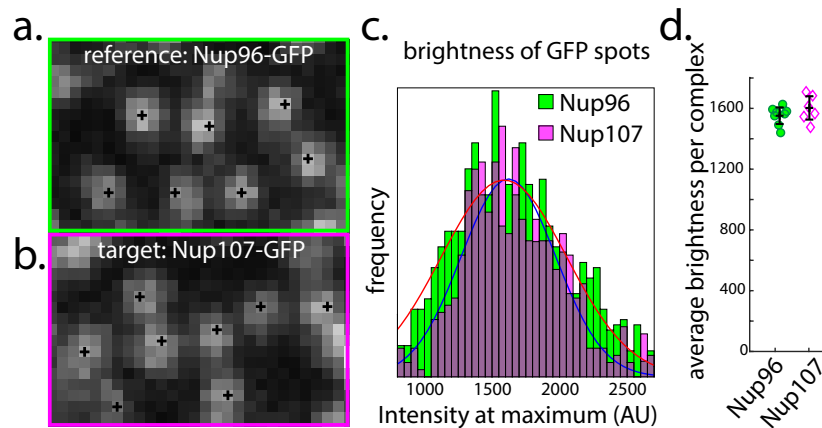


Figure 4.7: Determining protein copy numbers using diffraction-limited imaging. (a) Confocal image of Nup96-GFP serving as our reference standard. (b) Confocal image of Nup107-GFP which was the target protein number to be determined. Both (a) and (b) were acquired under identical microscope settings. (c) Histogram plot of intensity values extracted from individual NPC spots on the confocal image. A Gaussian fit is performed to determine mean intensity values. (d) Mean intensity value for both reference and target cells. Data jointly produced by Maurice Kahnwald and me. This figure has been adapted from (Thevathasan et al., 2019) on which I am a co-first author. It is being distributed under CC-BY-ND 4.0 international license.

4.4 Counting protein copy numbers

One of the main strengths of fluorescence microscopy is molecular specificity. In the context of studying composition of protein complexes, fluorescence microscopy is able to provide quantitative insights. However, converting grey values on images to absolute protein copy numbers is not straight forward. It requires the use of a calibrated microscope. Here, we demonstrate the use of U2OS Nup96-GFP cell to calibrate and determine the protein copy number of Nup107-GFP another NUP within the NPC of a HEK cell line. Nup107 is a member of the Y-complex, therefore exist in 32 copies within each NPC. Under diffraction-limited confocal imaging individual NPC appear as bright puncta (Fig. 4.7a,b). Isolated puncta were segmented and their brightness was calculated. This brightness value was a product of fluorescence from 32 GFP-labeled proteins. We calculated a mean intensity of 1552 ± 55 ADU ($N = 8$ cells / 10104) for puncta from U2OS Nup96-GFP and a mean intensity of 1603 ± 77 ADU ($N = 6$ cells / 7178) for puncta from HEK Nup107-GFP acquired under similar acquisition settings (Fig. 4.7c). We found similar data distribution and small variation in average brightness values obtained in both cases (Fig. 4.7d).

For counting using SMLM we used Nup96-mMaple cell line as a counting reference standard (Fig. 4.8a). As a target for validation we generated a stable HEK293T cell line overexpressing Nup107-mMaple with siRNA KD of endogenous Nup107 (Fig. 4.8b). We obtained a similar distribution and mean number of

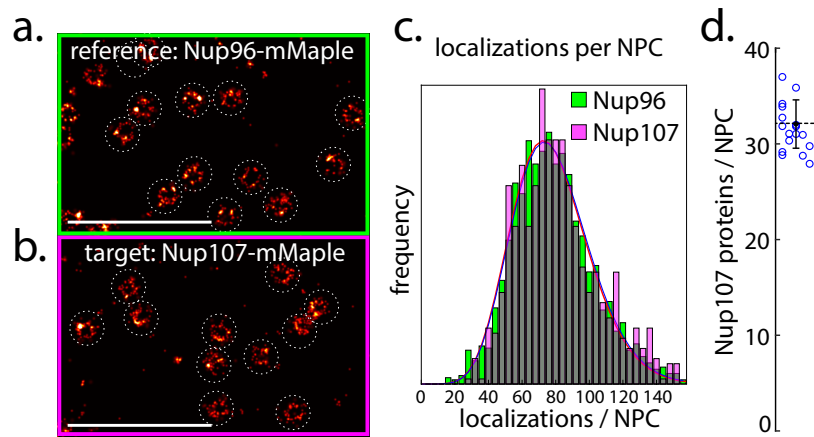


Figure 4.8: Determining protein copy numbers using SMLM imaging. (a) Reconstructed SMLM image obtained from our reference cell line, U2OS Nup96-mMaple. (b) Reconstructed SMLM image obtained from our target cell line, HEK293T Nup107-mMaple. (c) Histogram plot of number of localization from NPCs in both reference and target cell line. (d) The number of Nup107 per NPC calculated from the number of localizations. Each data point is an individual cell. Data jointly produced by Maurice Kahnwald and me. This figure has been adapted from (Thevathasan et al., 2019) on which I am a co-first author. It is being distributed under CC-BY-ND 4.0 international license.

localizations per NPC for both cell lines recorded under identical acquisition parameters (Fig. 4.8c). From the mean number of localizations from both the reference and target cell line, we calculated a copy number of 32.1 ± 2.5 ($N = 17$ cells / 1928 NPCs) Nup107 protein copies per NPC (Fig. 4.8d).

5 | Discussion

To reiterate from the introduction, an ideal reference standard for quantitative microscopy should:

- Be robust and user friendly.
- Exhibit fluorophores/labels at distances that are relevant for 2D and 3D SMLM to help benchmark resolution capabilities of the system.
- Contain a defined stoichiometry to disentangle effects of labelling efficiency, fluorophore photophysics and number of epitopes.
- Be compatible with commonly used labelling approaches, within the context of a cell.

Here, we have demonstrated with assays, that NPCs are suited to function as versatile reference standards for both quantitative diffraction-limited and superresolution fluorescence microscopy.

Using structural techniques, the NPC has been characterized to have a stereotypic architecture and well-defined stoichiometry of scaffolding NUPs (Beck and Hurt, 2017). Genetic tagging of a NUP, in this case, NUP96 allows positioning of fluorophores/labels at relevant distances to determine the 2D and 3D resolution capability of microscopes. Nup96 was chosen as its organization of 16 copies present on the cytoplasmic ring are in register with the 16 copies present on the nuclear ring, making clear visualization of the eightfold radial symmetry possible (Szymborska et al., 2013). The fixed copy number of Nup96, 32 copies, also meant that within each NPC there would maximally be 32 fluorophores or labels. This is especially important for assessing protein stoichiometry.

5.1 Cell line validation

Cell lines were validated to be homozygous using junction PCR, Sanger sequencing, Southern (Fig. 4.1a-d) and Western blotting (Fig. 4.1e). Confirmation of homozygosity of the generated cell lines was essential to prevent confounding variables and artifacts in our final analysis.

Nup96 is a result of proteolytic cleavage of the Nup98-96 precursor protein. Nup96 has a molecular weight of 105 kDa and Nup98 is 91.6 kDa. We detected single Nup96 protein bands in our western blot. The detected Nup96 band migrated at a higher MW, between 115–180 kDa. This could be due to post-translational modifications such as glycosylation, which increases the molecular weight of the protein. Glycosylation of Nups has been reported to facilitate nucleocytoplasmic transport (Li and Kohler, 2014). To ensure the specificity of the antibody used to detect Nup96, we performed an siRNA KD against Nup96. We observed a decrease in amount of Nup96 protein detected in our siRNA treated cell lysate (Fig. 4.1e). We also probed our membrane with an antibody against Nup98 and observed that the bands detected by Nup96 antibody and Nup98 antibody were different (data not shown). Nup98 antibody detected a protein band that ran at a lower molecular weight, however it was still higher than 91.6 kDa. The shifts towards higher molecular weights of Nup96 in our CRISPR cell lines were consistent with the size of the tags added (Fig. 4.1e). With validation at the genomic, transcriptional and translational level, we were confident that the generated cell lines were homozygous for the respective tags.

5.2 Ease of use & reproducible

U2OS cells are immortalized cell lines routinely cultured in laboratories. They can be easily grown on glass coverslips and they have a characteristic flat morphology. Their general morphology results in their nucleus being flat and positioned very close to the coverslip. Confinement of NPCs to the nuclear membrane enables hundreds of NPCs to be imaged in a single focused plane for statistical analysis. Existing reference standards are usually expressed in the cytoplasm (Finan et al., 2015). This makes faithful segmentation and isolation signal from only the plane of focus challenging, thereby, increasing segmentation bias and intensity contribution from out of focus emitters. Imaging the appropriate Nup cell line using different imaging modalities, we showed that the ring structure could only be visualized with superresolution techniques (STED and SMLM) and the radial eightfold symmetry with SMLM alone. The ability to perform dual colour SMLM on NPCs enables the cell lines to be used to optimize parameters for optimal dual colour imaging simultaneously within the same reference sample.

5.3 2D & 3D calibration

We observed some degree of variation in dimensions of NPCs (Fig. 4.3c, Fig. 4.4c), as reported by structural studies (Beck et al., 2007). The amount of variation was still found to be smaller than that which has been reported for 3D DNA origamis (Deschamps et al., 2014). We observed a correlation between the 'linkage error' and

the size of label used, emphasizing the need to account for the effect labels have on measurements regarding target size and proximity (colocalization or arrangement within a protein complex). In the lateral dimension, SMLM provides a high spatial resolution. However, in the axial dimension the spatial resolution effectively depreciates by a factor of 2-3, due to depth dependent aberrations resulting in systematic localization errors. These aberrations are due to the refractive index mismatch between the immersion oil on the objective and the coverslip versus the aqueous imaging buffer and is depth dependent. It results in an image that is compressed in z and it can be corrected using a refractive index mismatch factor (RIMF) (Diaspro et al., 2002). Using a method recently developed by our lab, we were able to correct depth dependent aberration errors (Li et al., 2019). Using 2D ring distance measurement from equatorial plane of the nucleus and corrected ring distances measured in 3D astigmatism, we were able to calculate a RIMF of 0.79, consistent with previous publications (Huang et al., 2008b).

5.4 Quantifying effective labeling efficiencies

5.4.1 Labels

We show that the type of fluorophore, number of fluorophores and type of linkers used have strong effects on measured ELE. For all labeling strategies we did not achieve 100% ELE and this could be due to issues at the level of the labels or fluorophore or a combination of both. At the level of labels, it could be due to non-functional labels, loss of epitope due to fixation and lack of accessibility by the ligand. We measured the highest ELE, 75%, when we used a mixture of two nanobodies with a total of four fluorophores (NB-Fluo®Tag-X4) for labeling. In the initial off-switching step at the start of an acquisition, high laser intensities are used. This not only pushes fluorophores to the dark state but it also increases the probability that a fluorophore is bleached (Lin et al., 2015). Therefore, with more fluorophores per label, the probability of losing all the fluorophores is lower. The label in this case has a higher probability of being visualized. This is exemplified by a reduced ELE, 62%, by a single nanobody labelled with one fluorophore (NB-FluoTag®-Q).

5.4.2 Fluorophores

At the level of fluorophores, we observed varying ELE with different ligand linker lengths for the Halo ligands and different fluorophores (AF647 vs Cy5 vs PA-JF549) (Table. 4.1), emphasizing that different linker lengths has an effect on of the ligand's ability to bind to Halo. Photophysical properties of dyes are also influenced by labeling strategies used. Looking at the photon statistics of AF647 across different

labeling strategies we note the almost similar numbers of photons (≈ 10000) emitted by BG-AF647 and CA-O₂-AF647 and significantly lower photons (≈ 7000) emitted by NB-Q-AF647. The variable performance of dyes with respect to labeling strategy and ligands was also observed in a recent study done by Erdmann and colleagues. They reported that far red rhodamines were brighter by 9 folds with Halo labeling than compared to SNAP labeling, indicating that regardless of the chemical background, the immediate environment around the dye has an impact on its photophysics (Erdmann et al., 2019; Takakura et al., 2017). Using our Nup cell line we could quantitatively assess this to find the optimal labeling strategy and buffer conditions for each dye. It is noteworthy to mention that the calculated ELE based on the cell lines may not translate a 100% as ELE of other targets. At best, it serves as an indicator of efficiency of the optimization steps being performed are beneficial or not. This is a shortcoming experienced by all reference standards due to differences in immediate nanoenvironments and epitope accessibility of different cellular structures.

5.4.3 Buffer conditions

Buffer compositions and conditions play an important role in determining fluorophore photophysical properties. Amongst all the fluorophores, AF647, exhibits characteristics favorable for SMLM imaging. It emits a high number photons and switches between bright and dark states efficiently. We used our Nup96-SNAP cell line labeled with BG-AF647 and recorded effects of varied buffer composition on AF647 performance. The use of heavy water, D₂O has been reported to increase the photostability and quantum yield of rhodamine (Sinha et al., 2002), oxazines (Lee et al., 2013) and cyanine dyes (Klehs et al., 2014). We did not observe a significant difference in photon yield by AF647 in the presence of D₂O. This is contrary to what Klehs et al. (2014) has reported for cyanine dyes, albeit, they report only an increase of 200 photons in the presence of D₂O. They also recorded on average 2100 photons from AF647, which was much less than what we have measured (> 10000). This large difference could be due to different acquisition settings (filter settings, laser powers and exposure time) and different fitting algorithms.

Chemical additives such as the thiols BME and MEA are reducing agents necessary for SMLM with AF647. They reduce AF647 in the excited triplet state to a dark state. Quick reduction of AF647 to the dark state results in a lower probability of photobleaching. This then enables reactivation with UV laser for subsequent localization. With BME, we observed a 6% higher ELE, higher number of photons emitted, higher number of localization per NPC and individual Nup96 protein compared to MEA. This indicates that in the presence of BME, AF647 is efficiently pushed to the dark state and not photobleached quickly. This is consistent with what others have reported (Dempsey et al., 2011). This information is useful especially

if the target being imaged is of low copy number. Using the optimal reducing agent could mean the difference between localizing the molecule and losing it to photobleaching. Alternatively, one could probe the target with a labelling strategy that decorates the structure of interest with a higher number of fluorophores.

5.4.4 Oxygen scavenging system

Oxygen is usually actively removed in many single molecule fluorescence studies as it results in the formation of toxic oxygen species which are phototoxic to the sample and fluorophores present (Aitken et al., 2008; Harada et al., 1990; Nahidiazar et al., 2016). Here, we looked at the difference between an enzymatic (GLOXC) and a chemical (sodium sulfite) based oxygen scavenging system (Hartwich et al., 2018). We observed a significant reduction in photons emitted by AF647 in the presence of sodium sulfite. It is noteworthy that AF647 exhibited much less localizations per NPC and Nup96 protein, indicating reduced photoswitching, contrary to what was reported by Hartwich and colleagues. The reduced photon count and number of photoswitching cycles could also be due to different concentrations of MEA or different excitation laser intensities used by the authors, which was not reported in the paper. Nevertheless, sodium sulfite has been described to be a much more efficient oxygen scavenger compared to GLOXC and it ensures that imaging buffer pH is kept constant (Gardner, 1968; Yagi and Inoue, 1962).

5.5 Counting protein copy numbers

Many cellular functions are carried out by protein-protein interactions such as receptor clustering or recruitment of proteins in a stoichiometric manner. From a structural and cell biological perspective, it is of great interest to determine the absolute number of proteins involved in effecting the cellular process. There are different approaches to determining absolute copy number. One such method would be to use bleaching steps to determine protein numbers. Each bleaching step corresponds to an individual protein (Ulbrich and Isacoff, 2007). This approach however is limited to low copy numbers (< 7) as higher protein copy numbers result in fluctuating fluorescence signal and different rates of photobleaching making the identification of discrete photobleaching steps difficult even with the aid of mathematical models (Chen et al., 2014b).

Another method to determine a protein's copy number is based on the total fluorescence intensity that is measured for a known number of protein molecules (Coffman and Wu, 2012; Hack et al., 2000). This approach requires careful calibration of the microscope with imaging standards of known number of proteins. As discussed above, most labeling strategies do not achieve a 1:1 labeling stoichiometry. Therefore, genetic encoded FPs are recommended as it minimizes errors from lack of

labeling. In addition all endogenous proteins should be tagged. With CRISPR-Cas9 technology, this is now possible and it ensures that expression levels of the proteins are maintained at endogenous levels. In theory, labeling with a fusion protein should be 1:1 stoichiometry with the target protein, hence 100%. However, one has to factor in incomplete protein folding which would result in the inability of the chromophore to mature, quenching due to close proximity of FPs and loss of chromophore due to photobleaching during the initial off-switching. Quantifying this loss and correcting for it is especially important for determining absolute protein copy numbers. We showed that our Nup96-GFP cell line was able to control for the various unknowns and quantify the number of Nup107-GFP in a different cell line (Fig. 4.7).

SMLM provides the possibility of accurately determining protein copy numbers of small dense protein complexes that cannot be resolved with diffraction-limited microscopy. However, the number of localizations recorded consists of a convolution of the number of fluorophore and its reactivations. One way to circumvent this problem would be to use a reference counting standard. Counting standards such as, DNA origamis, self-assembling oligomers with fixed stoichiometry, receptors and even dimers or trimers of fluorescent protein have been used (Baldering et al., 2019; Finan et al., 2015; Lee et al., 2012). However, often times calibration based on such approaches are heavily dependent on stringent segmentation cutoffs and algorithmic parameters. This is not the case in our Nup96-mMaple cell line. Since all the NPCs are embedded within the nuclear membrane, they are restricted to a single focal plane making segmentation and analysis straightforward. Using the number of localizations recorded per NPC in our Nup96-mMaple cell line as a reference, we could calculate 32 protein copies of Nup107 present in our stable HEK293T cell line (Fig. 4.8). We also verified that fixation with PFA did not affect the photophysical properties of mMaple (Table. 4.1).

6 | Future outlook

In this project we generated four homozygous cell lines with Nup96 tagged with GFP, SNAP, Halo and mMaple as reference standards for quality control in fluorescence and superresolution microscopy. We have showcased the performance capacity of NPCs to function as robust and reproducible standards for microscope calibration, fluorophore characterization, imaging buffer optimization and determining protein copy numbers. These cell lines were generated with the intent of distribution to the broader community. Our hope is that other labs would test out different dye combinations, assess sample preparation methods, report on new dye performance or effects of a new buffer component based on data collected using our cell lines. We also anticipate the generation of more homozygous cell lines tagged with new labels or fluorescent proteins by the broader community. The reception of our Nup96 cell lines has been very positive and in fact, first publication utilizing our cell lines are in press and another is currently under review (Schlichthaerle et al., 2019).

7 | Materials & Methods

7.1 Generation of CRISPR cell lines

7.1.1 Genome editing plasmids

Genome editing was carried out using CRISPR-Cas9D10A nickase in accordance with the protocol stated in Koch et al., 2018. Donor plasmid encoding for Nup96-mEGFP was constructed from synthetic oligonucleotides and/or PCR products. The synthetic Nup96-mEGFP gene was flanked by left (1.1 kb) and right (0.8 kb) homology arms for the C-terminus of Nup96. To enable easy tag manipulation a linker sequence (5' ACTAGTCGACGGTACCGCGGGCCCCGGGATCCACCGGCCGGTCGCCACC 3') with multiple cloning sites was included into the left homology arm. The synthetic gene fragment was subsequently inserted into pMA-RQ (AmpR) vector back bone. Donor plasmids encoding for mMaple (McEvoy et al., 2012), SNAP_f tag (Sun et al., 2011) (NEB) and Halo tag (Los et al., 2008) (Promega), were assembled using EagI-HF and NheI-HF restriction enzymes (NEB) to exchange out mEGFP. The gRNA sequences used are sense: (5' GTTGGGAGCCTGTGAGCCCC 3') and antisense: (5' CAGTTCTCGCAGATAGGACT 3').

7.1.2 Southern blotting of Nup96

Southern blotting was done as described in Koch et al., 2018. We used Wizard Genomic DNA purification kit (promega) to obtain genomic DNA, that was subsequently digested with SspI-HF and MfeI-HF restriction enzymes (NEB). The probe sequences used are as follows:

Nup96 C-term:

5'-TCCAGTTTCTCTCTGCCACATCCACCTGTTTAAATTATCTACATGGCTTGT
GATTTTTCAGGATTTATTACTGTTTTGTGTTTTCTTATTTATTTTCTATCAGTT
TCATGAGAGCAAATAACCTGTCTTGCTCTTGATCCTCCTGCCCCCTGCACA

CAGCTTTTTTGGTGTTTTAGAAAAGGCTATAAACTTGGAGTCAGGGGACCT-3';

mEGFP:

5'-CACATGAAGCAGCACGACTTCTTCAAGTCCGCCATGCCCCGAAGGCTAC
GTCCAGGAGCGCACCATCTTCTTCAAGGACGACGGCAACTACAAGACCC
GCGCCGAGGTGAAGTTCGAGGGCGACACCCTGGTGAACCGCATCGAGCT
GAAGGGCATCGACTTCAAGGAGGACGGCAACATCCTGGGGCACAAGCTG
GAGTACAACTACAACAGCCACAACGTCTATATCATGGCCGACAAGCAGA
AGAACGGCATCAAGGTGAACTTCAAGATCCGCCACAACATCGAGGACGG
CAGCGTGCAGCTCGCCGACCACTACCAGCAGAACACCC-3';

mMaple:

5'-AGCATGACCTACGAGGACGGCGGCATCTGCATCGCCACCAACGACATC
ACAATGGAGGAGGACAGCTTCATCAACAAGATCCACTTCAAGGGCACGA
ACTT-3';

SNAPtag:

5'AAAGACTGCGAAATGAAGCGCACCCACCCTGGATAGCCCTCTGGGCAAG
CTGGAAGTGTCTGGGTGCGAACAGGGCCTGCACCGTATCATCTTCCTGGG
CAAAGGAACATCT-3';

HaloTag:

5'TGCATTGCTCCAGACCTGATCGGTATGGGCAAATCCGACAAACCAGACC
TGGGTTATTTCTTCGACGACCACGTCCGCTTCATGGATGCCTTCATCGAAG
C-3'

7.1.3 siRNA silencing of Nup96

To examine the specificity of anti Nup98 antibody we seeded U2OS cells on to a 35 mm cell culture dish. 48 h following seeding, we transfected the cells using lipofectamine 200 (Life technologies) to insert MISSION[®] esiRNA Human nup98 (esirna1) (Sigma, EHU087381-20 μ g, Lot: BEV) was introduced using lipofectamine 2000 (life technologies). Subsequently 48h after transfection cell layer was mechanically scrapped and cell lysate collected for western blotting.

7.1.4 Western blotting of Nup96

The U2OS cell lysates collected above were resuspended in Pierce RIPA buffer (Cat. #89900; Lot no. NF170965; ThermoFisher Scientific) along with Complete

protease inhibitors (Roche) and phenylmethanesulfonylfluoride (PMSF) added. We then measured the cell lysate protein concentration using Pierce BCA protein assay kit (Cat. #23225; Lot no. QI223168; ThermoFisher Scientific). 50 μg of the cell lysate was loaded onto a 4-12% gradient gel and run at 165 V constant for 45-60 mins. The running buffer used was 1X MOPS-SDS buffer (NuPAGE) at room temperature (RT). Once completed the proteins were then transferred to a PVDF membrane at 15 V constant for 60 min in cold 1X transfer buffer with 10% (v/v) methanol (Bolt™) at RT. Following transfer, blocking of membranes were performed for 1 hr at RT. Blocking buffer used was 10% (w/v) milk in TBS-T pH 7.6. Membranes were then incubated in 1:2000 diluted primary antibody (pAb anti-Nup98, Cat. #NB1000-93325; LotA1; Novus) in 3% (w/v) BSA in TBS-T at 4°C overnight. Prior to addition of secondary antibody the membranes were washed with TBS-T for 5 min at room temperature. We used 1:10000 diluted secondary antibody in 5% (w/v) milk in TBS-T. Incubation was carried out at RT for 1 hour. Following subsequent washing of membranes with TBS-T, chemiluminescence reagents were added to visualize the protein bands under film exposure.

7.2 Cell culture maintenance

U2OS and stable HEK293T Nup107-mMaple used in the project were cultured in cell culture medium (DMEM [Gibco; #11880-02] containing 1x MEM NEAA [Cat #11140-035; Gibco], 1x GlutaMAX [Cat #35050-038; Gibco] and 10% [v/v] fetal bovine serum [Cat #10270-106; Gibco]) at 37°C and 5% CO₂. Cells were grown to 70-80% confluency and then passaged using Tryp-LE for dissociation. To induce expression of Nup107-mMaple in the stable HEK293T cells, cell culture media was supplemented with doxycycline (final conc. 1 $\mu\text{g}/\text{mL}$).

7.3 Sample preparation

All buffers used for sample preparation are listed in Table 7.1.

7.3.1 Coverslip preparation and cell seeding

High precision 24 mm round glass coverslips (No. 1.5H; Cat #117640; Marienfeld, Lauda-Königshofen, Germany) were acid (methanol:hydrochloride acid, 1:1) cleaned overnight under constant stirring. Afterwards, the coverslips were rinsed 3X with copious amounts of water till neutral pH. They were then left to dry in the cell culture hood under laminar flow. Finally the coverslips were irradiated with UV for 30 mins.

Table 7.1: Buffers used for sample preparation

Buffer	Composition	Reference
FB Fixation buffer	2.4% (w/v) formaldehyde in PBS	
PB Permeabilization buffer	0.4% (v/v) Triton X-100 in PBS	
QS Quenching buffer	100 mM NH ₄ Cl in PBS	
TRB Transport Buffer	20 mM HEPES pH7.5 110mM KAc 1 mM EGTA 250 mM Sucrose in H ₂ O	Pleiner et al., 2015 Göttfert et al., 2017
TBA Transport buffer with BSA	1% (w/v) BSA in TRB	Pleiner et al., 2015 Göttfert et al., 2017

For SMLM imaging, cells were seeded onto cleaned glass coverslips such that they would be 50-70% confluency on the day of fixation/imaging. For diffraction-limited microscopy, cells were seeded onto 35 mm dishes with 10 mm glass bottom insert (Cat #627860; Greiner Bio-One). For SMLM imaging of stable HEK293T cells, before seeding cells, the coverslips were treated with 10 $\mu\text{g}/\text{mL}$ fibronectin for 3 hours at 37 °C. After incubation the coverslips were washed and in ddH₂O and the cells were introduced to the treated coverslip.

7.3.2 SNAP-tag labeling

U2OS-Nup96-SNAP cells were first prefixed briefly for 30 secs in **FB**, followed by a 3 min incubation in **PB**. The cells were then incubated for 30 mins in **FB**. After incubation, **FB** was aspirated away and the remaining 2.4% (w/v) formaldehyde (FA) was quenched in **QS** for 5 mins before being washed twice for 5 mins in PBS. A blocking step for 30 mins with Image-iT FX signal enhancer (ThermoFisher Scientific) was performed before staining in SNAP dye duffer (1 μM BG-AF647 [New England Biolabs; #S9136S], 1 μM DTT in 0.5% [w/v] BSA in PBS) for 2 hrs at RT. After staining the cells were rinsed three times for 5 mins each with PBS.

7.3.3 Nanobody labeling of Nup96-mEGFP fusion proteins

U2OS-Nup96-mEGFP cells were stained as per protocol described in Pleiner *et al.* (2015). Cells underwent a prefixation step for 30 secs with **TRB** containing FA followed by two 5 mins wash steps in **TRB**. To selectively permeabilize the plasma membrane, the cells were incubated for 8 mins on ice in **TRB** containing 25 $\mu\text{g}/\text{mL}$ digitonin (Cat #D141; Sigma Aldrich). After incubation the cells were washed twice for 5 mins each in **TBA**. The cells underwent 2 rounds of staining. The cells were first incubated on ice in **TBA** containing 100 nM of anti-GFP nanobodies

(NanoTag Biotechnologies, FluoTag-Q [Cat #N0301] or FluoTag-X4 [Cat #N0304], either conjugated to AF647, CF680 or STAR 635P) for 30 min. After incubation, the cells were rinsed with two washing steps in **TBA** for 5 mins each. After rinsing the cells were incubated in **TBA** containing 3% (w/v) FA for 10 mins, after which they were rinsed two times for 5 mins. The nuclear membrane was permeabilized for 3 mins in **PB**. After permeabilization the cells were incubated once again on ice with anti-GFP nanobodies (50 nM in TBA, same nanobodies used as in previous round of staining) for 30 min. After the second staining, cells were rinsed with PBS twice for 15 mins each. For STED-imaging FluoTag-X4-STAR 635P stained samples were mounted on Mowiol (Calbiochem) upside down on a microscope slide. The edges of the coverslip were sealed with nail polish and allowed to set overnight at RT.

7.3.4 Indirect immunostaining of Nup96-mEGFP fusion proteins

U2OS-Nup96-mEGFP cells were first prefixed briefly for 30 secs in **FB**, followed by a 10 min incubation in 0.1% (v/v) Triton X-100 in PBS. The cells were then washed two times for 5 mins each in PBS. After which the cells were incubated in **FB** for 20 mins. After fixation, the fixative was quenched with a 5 min incubation in **QS**, followed by two washes in PBS for 5 mins each. The cells were then further permeabilized with 0.2% (v/v) Triton X-100 in PBS for 10 mins, then washed two times for 5 mins each. The cells were then blocked with 2% (w/v) BSA in PBS for 1 hr. After the blocking step, the coverslip was incubated in primary rabbit anti-GFP antibodies (Cat #598; MBL International) diluted 1:250 in PBS containing 2% (w/v) BSA overnight at 4 °C. After incubation the coverslip was rinsed two times for 5 mins each. The coverslip was then incubated with secondary anti-rabbit antibody conjugated with AF647 dye (custom made, diluted 1:300 in PBS containing 2% [w/v] BSA) for 1 h at RT.

7.3.5 Halo tag labeling in fixed cells

U2OS-Nup96-Halo cells were stained with a slightly adapted protocol used for nanobody labeling as mentioned earlier (7.3.3). Instead of using different concentrations during the two staining steps, the cells were incubated for 1 hr at RT with the same concentration of HaloTag dye buffer (5 μ M of Cy5-HaloTag ligand [Lavis Lab, HHMI Janelia Research campus] or HaloTag-ligand-O2-AF647/HaloTag-ligand-O4-AF647 [custom substrates from Peps4LS, Heidelberg] in TBA). All other steps were carried out as stated above.

7.3.6 Halo tag labeling in live cells

Coverslips with U2OS-Nup96-Halo cells grown to 50 - 70% confluency were incubated for 1 hr with pre-warmed cell culture media containing

PA-JF-549-Halo-Tag ligand (250-5000 nM concentrations were tested with results indicating no significant change in labeling efficiency, Lavis Lab, HHMI Janelia Research campus) at 37 °C and 5% CO₂. After incubation the cells were then rinsed three times with pre-warmed cell culture media and allowed to recover in pre-warmed cell culture media without dye for 1 hr. After 1 hr, the cells were rinsed in PBS three times. They were then prefixed for 30 secs in **FB**. After a brief prefixation, the cells were permeabilized for 3 mins followed by a 30 min incubation in **FB**. The fixative was quenched with a 5 min incubation in **QS**, followed by two washes in PBS for 5 mins each.

7.3.7 Fixation of Nup96-mMaple

U2OS-Nup96-mMaple cells were prefixed for 30 secs in **FB**. After that, the cells were permeabilized for 3 mins followed by a 30 min incubation in **FB**. The fixative was quenched with a 5 min incubation in **QS**, followed by two washes in PBS for 5 mins each.

7.4 Microscopes

7.4.1 SMLM microscope

A custom built microscope as described in Mund *et al.* (2018) was used for all SMLM data acquisition. Briefly, output from a commercial laser box containing Luxx 405, 488 and 638 and Cobolt 561 lasers (LightHub; Omicron-Laserage Laserprodukte, Dudenhofen, Germany) and an additional 640 nm booster laser (iBeam smart, Toptica, Gräfelfing, Germany) were collimated and focused onto a speckle reducer (Cat #LSR-3005-17S-VIS; Optotune, Dietikon, Switzerland). After the speckle reducer, the beam was coupled into a multi-mode fiber (Cat #M105L02S-A; Thorlabs, Newton, NJ, USA). An achromatic lens was used to magnify and focus the output of the fiber into the sample to homogeneously illuminate approximately 1000 μm^2 . To enable TIRF imaging, a single mode fiber (Omicron, LightHUB) could be plugged to the output of the laser box. To remove fluorescence generated by the fiber, the laser was guided through a laser clean up filter (390/482/563/640 HC Quad; AHF, Tübingen, Germany). The emission from the sample was collected with a high numerical aperture (NA) oil-immersion objective (160x/1.43-NA; Leica, Wetzlar, Germany) and filtered by a band pass with respect to the fluorophore being imaged. 525/50 [Cat #FF03-525/50-25, Semrock, Rochester, NY, USA] for mEGFP; 600/60 [Cat #NC458462, Chroma, Bellows Falls, VT, USA] for mMaple and PA-JF549 and 700/100 [Cat #ET700/100m, Chroma] for AF647, Cy5 and CF680. The Evolve512D EMCCD camera (Photometrics, Tucson, AZ, USA) was used to capture images. *z*-focus was focus stabilized using an IR-laser that was totally internally

Table 7.2: Acquisition parameters

Sample	No.of frames	Frametime (ms)	Laser intensity (kW/cm ²)
U2OS Nup96-mEGFP Nanobodies	~60-90k	15/20/30	~6
U2OS Nup96-mEGFP Antibodies	~70-120k	15	~9
U2OS Nup96-Halo O2-AF647	~50k	50	~6
U2OS Nup96-Halo O4-AF647	~20-30k	50	~6
U2OS Nup96-Halo O4-Cy5	~40-70k	40	~6
U2OS Nup96-Halo PA-JF548	~10k	50	~3.5
U2OS Nup96-SNAP AF647	~50-70k	30/40	~6
U2Os Nup96-mMaple	~10-50k	50	~3.5
HEK Nup107-mMaple	~20-50k	50	~3.5

reflected off the sample coverslip to a quadrant photodiode. The photodiode was connected to a closed-loop feedback with an objective piezo positioner (Physik Instrumente, Karlsruhe, Germany). The various components of the microscope were controlled by a field-programmable gate array (Mojo; Embedded Micro, Denver, CO, USA). A feedback algorithm was used to control the pulse length of the 405 nm (laser intensity 27.5 W/cm²) to ensure that a fixed number of localizations are sustained throughout the acquisition. Acquisition parameters have been summarized in Table 7.2. Depending on the cell line and experiment respective imaging buffers listed in Table 7.3 were used. Buffers were exchanged every 2 hours to prevent the acidification of buffer due to accumulation of glucuronic acid in GLOX oxygen scavenging system. Acquisitions were acquired until no further localizations were observed under continuous UV illumination.

7.4.2 Pixel size calibration

The microscope's effective pixel size was calibrated using a fluorescent beads sample. Fluorescent beads were placed on a glass coverslip and mounted on the microscope. Images of the fluorescent beads at multiple defined focal positions were taken using a calibrated sample stage (SmarAct, Oldenburg, Germany) operated in close loop. The pixel size was calculated by measuring the translation of many beads.

7.4.3 Confocal microscopy

U2OS-Nup96-mEGFP samples were fixed and prepared on 35 mm glass bottom dishes as described in the preparation protocol mentioned above. Imaging of the samples was carried out using an Olympus FV3000 laser scanning microscope with a 60x/1.40 NA oil immersion objective (Olympus; PLAPON 60XOSC2), in combination with a motorized stage. The operating software used was Fluoview software (Olympus). The pixel size was set as ~70 nm in x and y plane. Fluorescence emission passed through a 550/100 bandpass filter and 1.0 airy unit (202 μ m) wide pinhole prior to detection on the four GaAsP spectral detectors. A z -stack comprising

Table 7.3: Composition of imaging buffers used

Buffer	Composition	Sample	Reference
50 mM Tris in D ₂ O	50 mM Tris/HCl pH 8 in 95% (v/v) D ₂ O	U2OS Nup96-Halo PA-JF549 U2OS Nup96-mMaple HEK Nup107-mMaple	
50 mM Tris in H ₂ O	50 mM Tris/HCl pH 8 in H ₂ O	U2OS Nup96-mMaple	
GLOX/MEA	50 mM Tris/HCl pH 8 10 mM NaCl 10% (w/v) D-Glucose 500 µg/mL Glucose oxidase 40 µg/mL Glucose Catalase 35 mM MEA in H ₂ O	U2OS Nup96-mEGFP Nanobodies U2OS Nup96-mEGFP Antibodies* U2OS Nup96-Halo O2-AF647 U2OS Nup96-Halo O4-AF647 U2OS Nup96-Halo O4-Cy5 U2OS Nup96-SNAP AF647	Heilemann et al., 2005
GLOX/BME	50 mM Tris/HCl pH 8 10 mM NaCl 10% (w/v) D-Glucose 500 µg/mL Glucose oxidase 40 µg/mL Glucose Catalase 143 mM BME in H ₂ O	U2OS Nup96-SNAP AF647	Bates et al., 2005
GLOX/MEA in D ₂ O	50 mM Tris/HCl pH 8 10 mM NaCl 10% (w/v) D-Glucose 500 µg/mL Glucose oxidase 40 µg/mL Glucose Catalase 143 mM BME in 90% (v/v) D ₂ O	U2OS Nup96-SNAP AF647	
Sulfite/MEA	50 mM Tris/HCl pH 8 50 mM Na ₂ SO ₃ /NaOH pH 8 35 mM MEA in H ₂ O	U2OS Nup96-SNAP AF647	

Note: *GLOX/MEA with 100 mM MEA instead of 3 mM to decrease the fraction of fluorophores in their on-state to suitable density.

of 3–5 planes 250 nm apart from each other was obtained for each nucleus around the basal plane of the nucleus to gain maximum fluorescence intensity for all NPCs.

7.4.4 Airy-scan microscopy

Samples of U2OS-Nup96-GFP cells were fixed on 35 mm glass bottom dishes according to the previously mentioned preparation protocol. Airy image acquisition was performed using a Zeiss LSM 880 with an added Airy FAST detector module (Zeiss); combined with a 63x/1.4NA oil immersion objective (Zeiss; Plan-Apochromat 63x/1.4 Oil DIC M27) and operated via the ZEN software (Zeiss; black edition). Pixel size was fixed at ~40 nm in both x and y planes. The samples were first focused at the basal plane of the nucleus and 488 nm laser was then used to excite mEGFP. Resulting emission was collected using a 495–550 nm bandpass filter, 570 nm longpass filter and a 1.25 airy unit (60 μm) pinhole onto the 32 GaAsP detectors. The z -stack acquired for each nucleus consisted of 3–5 slices 200 nm apart from each other around the basal plane. ZENs airy-scan processing with default deconvolution parameters was used for post-processing.

7.4.5 STED microscopy

Samples for nanobody staining of U2OS-Nup96-GFP were prepared in accordance with the protocol. The prepared samples were subsequently imaged using an Abberior STED/RESOLFT microscope (Abberior Instruments; Expert Line) operated by the Inspector software. The microscope contains an IX83 stage (Olympus) combined with a UPlsn-S Apochromat 100x/NA 1.40 oil objective (Olympus). The pixel size was fixed at 15 nm in both x and y planes. To obtain super-resolved images, donut shaped depletion was performed using a 775 nm laser together with a 640 nm pulsed laser, concurrently exciting STAR 635P tagged Nup96-mEGFP. Within the nucleus a single plane of the lower side was imaged, and resulting emission was collected via a 685/70 nm bandpass filter. Depletion power of 150 mW was used in each sample. High depletion powers may in theory cause an additional increase in resolution, though however in this particular instant, our samples were rather dim, and therefore experienced a strong bleaching effect and high noise.

7.4.6 Ratiometric dual-color SMLM

In ratiometric dual-color imaging of AF647 and CF680 was performed by splitting the emitted fluorescence with a 665LP beamsplitter (Cat#ET6651p, Chroma), that is filtered using a 685/70 (Cat#ET685/70m, Chroma) bandpass filter (transmitted light) or a 676/37 (Cat#FF01-676/37-25, Semrock) bandpass filter (reflected light), and subsequently imaged in parallel on different regions of the EMCCD camera. The

color of each individual blink was determined by calculating the ratio of intensities in the two channels.

7.4.7 Astigmatic 3D SMLM

A cylindrical lens ($f = 1000$ mm; Cat #LJ1516L1-A, Thorlabs) was used to induce astigmatism for 3D SMLM data acquisition. An experimental point spread function model was generated from z -stacks with defined displacement of 15–20 regions of fluorescent beads (Li et al., 2018c). The z -positions of individual localizations were then determined based on the generated model. z -stack of beads embedded in agarose were used to determine systematic fitting errors induced by depth dependent aberrations as previously described in (Li et al., 2019).

7.5 Data analysis

All data analysis listed in this project, were performed using custom designed software written within MATLAB. The software can be readily accessed at (github.com/jries/SMAP). Instructions for installation are indicated in the README.md. The Help menu contains step-by-step guidelines on software usage along with all information on its use in data analysis.

7.5.1 Fitting

A symmetric Gaussian PSF model (fitting free parameters were: x , y , PSF size, photon yield per localization and background per pixel) using maximum likelihood estimation (MLE) was used to fit 2D data. An experimentally derived PSF model (fitting free parameters were: x , y , z , photons yield per localization and background per pixel) using an MLE was used to fit 3D data.

7.5.2 Post-processing

Drift correction was done using a custom algorithm that used redundant cross-correlation. Long lived localizations captured over multiple frames were combined into a single localization by applying a weighted average of x , y and z positions and taking the total sum of photons per localization and background. Rendered localizations were filtered for based on: localization precision (0–10 nm for dSTORM; 0–25 nm for PALM). This was done to exclude dim events. In the case of 2D data, localizations were filtered for PSF size (0–150 nm) to remove out-of-focus localizations. Poorly fitted localizations were excluded based on their log-likelihood (LL). If the measured LL was lesser than the mean (LL)-3*STD(LL), was discarded. Localizations were then rendered as 2D elliptical Gaussian with a width (factor 0.4)

proportional to their localization precision. All reported mean photon yield per localizations were calculated based on filtered localizations.

7.5.3 Segmentation

NPCs were automatically segmented. Super resolved images were convoluted with a kernel comprising of a ring with dimensions representing the radius of a Gaussian convoluted NPC. The segmentation was cleaned up by applying a two step filtering process. 1) A circle fit was imposed and structures <40 nm and >70 nm radi were rejected. 2) A circle with fixed radius was then imposed on the remaining localizations. The center coordinates were determined. Structures where $>25\%$ of the localizations were within 40 nm of the center or $>40\%$ of localizations were >70 nm away were rejected. A comparison between automatic segmentation and manual segmentation showed data to be well within a difference of 1.2% in measured ELE and has $<5\%$ error in mean number of localizations per NPC.

7.5.4 Geometric analysis

Geometric analyses of segmented NPCs were performed on the coordinates of the localization.

7.5.5 Analysis of profiles

To generate line profiles in the x - y plane, a linear region of interest (ROI) was first drawn. Only the localizations that were within a rectangular ROI with a fixed width along the linear ROI were selected. The coordinates of the localizations were then projected to the x -axis along the linear ROI. The localizations were then represented as a histogram. A single or a double Gaussian function was then fit onto the histograms. For line profiles along the z -axis, a histogram of z -coordinates of the localizations within the linear ROI were represented as a histogram. A single or a double Gaussian function was then fit onto the histograms. It is important that line profiles are generated from sufficient localizations represented as a histogram and not as Gaussian kernels. With a Gaussian kernel rendering, single localizations can result in profiles that can be 'resolved' if their distance apart is larger than the arbitrary kernel size.

7.5.6 Radius of NPC

A circular model was imposed on the segmented NPC's localization coordinates (free parameters: x , y , and radius of circle)

7.5.7 Distance between cytoplasmic and nucleoplasmic rings in 2D data

2D ring distances were calculated from images acquired from the mid-plane of a nucleus. NPCs were manually segmented. Profiles perpendicular to the nuclear envelope with a fixed width of 200 nm were drawn. Localizations within this linear ROI were rotated and histograms of the localizations were generated. A double Gaussian function was then fit onto the histograms to determine the distance between the rings.

7.5.8 Distance between cytoplasmic and nucleoplasmic rings in 3D data

Segmented NPCs were fit with a 3D template consisting of two parallel rings with a fixed radius (radius was experimentally determined earlier) and variable x, y, z , rotational angle and distance between the ring. For validation, the localizations were rotated according to their rotational such that all the NPCs were aligned, allowing for their z -profile to be fitted with a double Gaussian function.

7.6 Determination of effective labeling efficiencies

This entire analysis pipeline was written by Jonas Ries and can be found in Thevathasan et al., 2019. To score the number of visible corners present in each NPC, the following procedure was done: 1) the segmented localizations of the NPC were fitted with a circle with fixed radius (as experimentally determined earlier). The localization coordinates were converted to polar coordinates ϕ_i, r_i . 2) Localizations too close to the center of the ring ($r_i < 30$ nm) or too far away ($r_i > 70$ nm) were deemed as background. 3) The rotation of the structure was determined by minimizing:

$$\phi_{rot} = \arg \min_{\phi_{rot}} (\phi_{rot} - \phi_i \bmod \pi/4) \quad (7.1)$$

4) the number of segments containing one localization from histogram of ϕ_i was created with a bin width of $\pi/4$ and a start bin of $\phi_{rot} - \pi/8$ were counted. 5) A histogram of the number of corners of all scored NPCs was created. A probabilistic model (described below) was fitted to the histogram with effective labelling efficiency as a free fitting parameter. 6) Bootstrapping with 20 re-sampled data sets was used to calculate statistical error.

7.6.1 Probabilistic model for effective labeling efficiency

"The binomial probability density function

$$B(k|n, p) = \binom{n}{k} p^k (1-p)^{n-k} \quad (7.2)$$

describes the probability of observing k successes in n independent trials, where the probability of success in any given trial is p . Thus, the probability of a corner of the NPC (consisting of 4 labels) to be dark is $p_{dark} = B(0|4, p_{dark})$ and the probability to see a corner with at least one label is $p_{bright} = 1 - p_{dark}$. The probability for N out of 8 corners being bright and visible is:

$$p(N|p_{label}) = B(N|8, p_{bright}) = B(N|8, 1 - B(0|4, p_{label})) \quad (7.3)$$

" (Thevathasan et al., 2019).

7.6.2 Determination of number of localizations per fluorophore

The number of localizations (blinking events) N_b detected per fluorophore can be calculated based on the ELE, the number of localizations per NPC N_i , and the number of Nup96 molecules per NPC $N_{Nup96} = 32$:

$$N_b = \frac{N_i}{N_{Nup96} ELE} \quad (7.4)$$

7.7 Counting protein copy numbers

7.7.1 Counting in diffraction-limited microscopy using Nup96-mEGFP as a reference

A simple analysis was performed to compare brightness of reference and target structures from confocal images. 1) The image offset was subtracted and photobleaching was corrected. 2) The maximum intensity projection of 3 frames from the focal plane of NPC was convoluted with a Gaussian ($\sigma = 0.5$ pixels). The image was upsampled with a factor of two by cubic spline interpolation. 4) The local maxima were determined and a threshold was imposed based on the histogram of intensity values from the maxima. 5) A histogram of maxima intensities above the threshold were fitted with a Gaussian function to extract the mean intensity values $\langle I_t \rangle$ and $\langle I_r \rangle$ for target and reference cell lines respectively. 6) With N_r , being the copy number of reference proteins, the copy number of the target protein, N_t , can

be calculated using:

$$N_t = \frac{N_r \langle I_t \rangle}{\langle I_r \rangle} \quad (7.5)$$

7.7.2 Counting in mammalian cells using Nup96-mMaple as a reference

NPCs were segmented automatically as described earlier. Only nuclear pores in focus were used for analysis (mean PSF value < 145 nm). Merged localizations (L_r, L_t) in a circular ROI of diameter of 220 nm. Using the mean number of localizations per NPC $\langle I_t \rangle$ and $\langle I_r \rangle$ the copy number of the target complex can be calculated using 7.5

Part II

Visualizing the self-assembly of alpha-synuclein polymorphs

8 | Aims

Amyloid fibrils exhibit structural polymorphism even under similar solution conditions. These fibril polymorphs have been shown to be present in different neurodegenerative phenotypes. Current methods to investigate the self-assembly of fibril polymorphs are limited in sensitivity (fluorescent spectroscopy) and ability to measure kinetic parameters (EM and Cryo-EM).

To this end, my aim is to

1. Use SMLM to visualize individual amyloid fibrils
2. Differentiate these fibrils with respect to its underlying ultra-structure
3. Measure the self-assembly process of these fibrils with respect to its ultra-structural features

In this project I will use alpha-synuclein as a model protein which exhibits fibril polymorphism in Parkinson's disease.

9 | Introduction

Amyloid fibrils are filamentous aggregates of protein with a cross-beta-sheet structure (Fändrich, 2007; Nilsson, 2004). Many of these amyloids are pathogenic and are hallmarks of disease, especially in neurodegeneration (Koo et al., 1999; Sipe and Cohen, 2000). However, recent studies have shown the presence of physiologically functional amyloids (Pham et al., 2014; Maji et al., 2009) as well as potential uses in the areas of material sciences (Scheibel et al., 2003) and bionanotechnology (Bolisetty and Mezzenga, 2016). Therefore, having a detailed understanding of amyloid structure and its corresponding aggregation characteristics could potentially yield novel therapeutic options and technology.

The presence of amyloid fibrils in neurodegenerative disorders such as Alzheimer's disease (AD), frontotemporal dementia (FTD) and Parkinson's disease (PD) increased research into the role played by amyloid fibrils in the diseased context. In this project we will base our study on amyloids fibrils formed by alpha-synuclein, a protein implicated in neurodegeneration collectively called synucleinopathies.

9.1 Alpha-synuclein in Parkinson's disease

Accumulation of alpha-synuclein was first described in PD, a slow progressive neurodegenerative disorder of the central nervous system (Spillantini et al., 1997). Alpha-synuclein accumulation has also been reported in dementia with lewy bodies (DLB), multi system atrophy (MSA) and lysosomal-storage disorders such as Gaucher's disease (Wong and Krainc, 2017). PD diagnosis is only definitive when a pathological brain autopsy reveals:

1. the presence of proteinaceous inclusions called Lewy bodies (LB) or Lewy neurites (LN) and,
2. the selective degeneration and loss of dopaminergic neurons in the substantia nigra pars compacta (SNpc) using immunohistochemistry techniques.

Clinical symptoms such as resting tremors, muscular rigidity and bradykinesia manifest due to specific loss of dopaminergic neurons in the SNpc. These neurons secrete dopamine, which is a neurotransmitter at the synapse

facilitating synaptic transmission. The supplementation of dopamine precursor, L-3,4-dihydroxyphenylalanine (L-DOPA) helps to alleviate PD symptoms, however with prolonged use, L-DOPA loses its efficacy. In an attempt for early diagnosis, clinical biomarkers and positron emission tomography (PET) imaging tracers are currently under active research and development (He et al., 2018). An early diagnosis could dramatically improve the quality of life for patients.

To develop therapeutic solutions, extensive research is being done to understand the etiology of PD. Studies into the composition of LB and LN have revealed them to constitute a mixture of proteins, lipids and different organelles (Shahmoradian et al., 2019; Spillantini et al., 1997). Immunohistochemistry against alpha-synuclein on brain tissue sections identified the presence of alpha-synuclein in LB and LN (Spillantini et al., 1997). Alpha-synuclein is a small presynaptic protein which was first identified as a precursor protein for the non-beta amyloid component (NAC) in amyloid plaques in brain tissue from patients suffering from AD (Uéda et al., 1993). PD is predominantly idiopathic with aging as the highest risk factor. However, there is a 2% incidence of familial PD. Familial PD is a result of a single-base mutations within alpha-synuclein with a high penetrance rate within family members. There is an early onset of clinical symptoms in familial PD (Polymeropoulos et al., 1997). Duplications and triplications of the gene locus encoding for alpha-synuclein result in autosomal dominant forms of familial PD (Chartier-Harlin et al., 2004; Singleton et al., 2003). These findings suggest that a single gene defect in alpha-synuclein could result in a disease phenotype.

9.2 Alpha-synuclein's native structure

There are three isoforms of synuclein, alpha, beta and gamma (Clayton and George, 1999). Alpha-synuclein is encoded by the SNCA gene and is expressed highly in the brain and red blood cells (Iwai et al., 1995; Scherzer et al., 2008). It has a molecular weight of 14.4 kDa and has three distinct regions in its primary sequence, namely the amino-terminal (N-term), amphipathic domain (residues 1-60), the non-amyloid-beta-component (NAC) domain (residues 61-95) and the carboxy-terminal (C-term) acidic domain (residues 96-140) (Fig. 9.1a). Biophysical characterization of alpha-synuclein using circular dichroism (CD) and nuclear magnetic resonance (NMR) has revealed it to be a structurally disordered protein (Bertoncini et al., 2005; Fauvet et al., 2012; Weinreb et al., 1996). The N-terminal region contains 11 amino acid residue repeats predicted to facilitate formation of an amphipathic alpha-helix. This was indeed the case, the N-terminus and NAC (residues 1-95) were found to adopt an alpha-helical structure and bound to the surface of lipid membrane and SDS micelles ((Fig. 9.1b) (Fusco et al., 2014; Ulmer et al., 2005). The NAC domain is required for fibril formation as large deletions from this domain abrogate fibril formation. The C-terminal region remained disordered

and flexible. Due to its disordered structure under non-denaturing conditions, alpha-synuclein migrates as a protein with the apparent molecular weight of 57-60 kDa, and under denaturing conditions it migrates as 14 kDa.

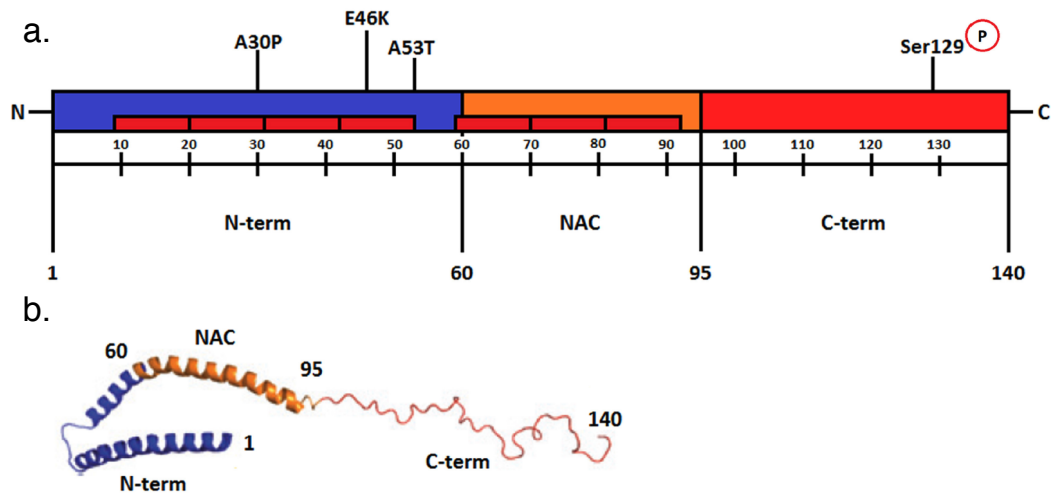


Figure 9.1: An illustration of the regions and structure of alpha-synuclein. (a) Alpha-synuclein has three distinct regions in its primary sequence, 1) The amino-terminal (N-term) amphipathic domain (residues 1-60), 2) The non-amyloid-beta-component (NAC) domain (residues 61-95) and 3) The carboxy-terminal (C-term) acidic domain (residues 96-140). Single base mutations leading to Familial PD and post-translational modifications site are indicated. (b) Schematic representation of micelle-bound alpha-synuclein. Figure taken from (Gallegos et al., 2015) distributed under Creative Commons Attribution License (CC-BY-4.0)

9.3 Alpha-synuclein mutations and post-translational modifications

Gene mutations resulting in familial PD are enriched in the N-terminal region. Single-base mutations A30P, E46K and A53T were the first few to have been discovered and characterized (Fig. 9.1a Krüger et al., 1998; Polymeropoulos et al., 1997; Zarranz et al., 2004). Mutations H50Q, G51D and A53E have been found relatively recently and are still being studied (Lesage et al., 2013; Pasanen et al., 2014; Proukakis et al., 2013). Although all these mutations have been identified in patients, they result in different symptoms and disease onsets. Patients with the A53T mutation tend to exhibit an early disease on-set, compared to patients with the H50Q (Fujioka et al., 2014). This heterogeneity is also reflected in *in vitro* characterization studies of these mutants presenting conflicting results. For the A53T mutation, independent studies have demonstrated accelerated fibril formation *in vitro* (Conway et al., 1998; Conway et al., 2000; Flagmeier et al., 2016). However, for A30P mutation there is less consensus on its effects on fibril elongation (Lemkau et al., 2012; Narhi et al., 1999). This could very well be due to different protein purification

strategies and solution conditions, that heavily impact fibril formation kinetics (Hoyer et al., 2002; Buell et al., 2014). It could also be due the lack of physiological reconstitution in experimental conditions, which is extremely challenging to achieve.

In normal physiology and in disease states alpha-synuclein is found to be post-translationally modified. Within the cell, acetylation of the N-terminus has been reported to facilitate the formation of the alpha-helical secondary structure which prevents oligomerization (Bartels et al., 2014; Bu et al., 2017; Iyer et al., 2016). In the disease context, many studies have characterized the phosphorylation status of alpha-synuclein. Alpha-synuclein's C-terminus consists of many charged residues which are post-translationally modified (Zhang et al., 2019). Of them, serine residue 129 (S129) is found to be predominantly phosphorylated within LB (Anderson et al., 2006). This observation has been recapitulated in both cellular and organotypic models of PD (Elfarrash et al., 2019; Sugeno et al., 2008; Smith et al., 2005). Mechanistic understanding of the effects of phosphorylated S129 is still unknown. However, kinases involved in phosphorylation have been identified and it has been shown that phosphorylation is not absolutely needed for aggregation and spreading (Elfarrash et al., 2019; Okochi et al., 2000; Pronin et al., 2000).

9.4 Alpha-synuclein's physiological role

Due to its disordered nature, it has been difficult to study the physiological role of alpha-synuclein. It was first identified to be present at synapses and nuclear membrane, hence the name, "synuclein" (Maroteaux and Scheller, 1991). Within cells it has a predominantly presynaptic and peri-nuclear subcellular localization. It is implicated in modulation of mRNA transcript levels (Sugeno et al., 2016; Surguchev and Surguchov, 2017), ATP levels (Ludtmann et al., 2018; Ludtmann et al., 2016) and synaptic vesicle recycling (Nemani et al., 2010; Xu et al., 2016). More recently, alpha-synuclein's direct interactions with VAMP2 and synapsins (proteins present on synaptic vesicles) have been shown to promote synaptic vesicle clustering, restricting mobility and inhibiting movement of vesicles to the presynaptic active zone, attenuating exocytosis (Atias et al., 2019; Sun et al., 2019). The binding of calcium to the C-terminus of alpha-synuclein has been shown to increase association with synaptic vesicles (Lautenschläger et al., 2018). These independent studies hint strongly towards alpha-synuclein's physiological role in modulating membrane vesicle trafficking within the context of the synapse.

9.5 Alpha-synuclein in disease

In sporadic and familial PD there is an increased accumulation of alpha-synuclein. This may be due to increased expression (multiplication of gene locus), propensity

to aggregate (single base pair mutation, A53T) or a defective protein degradation and clearance machinery (chaperone-mediated autophagy [CMA]). Correlation of early disease onset and severity with the multiplication of gene locus indicate that an increase in concentrations of wild-type alpha-synuclein is sufficient for a disease phenotype. Impaired synaptic vesicle recycling resulting in aberrant dopamine release and uptake has been reported in transgenic mice overexpressing alpha-synuclein (Janezic et al., 2013; Lundblad et al., 2012; Masliah et al., 2000). Protein degradation pathways are activated in the cell to overcome defects in various membrane vesicle trafficking due to increased concentrations of alpha-synuclein. Wild-type alpha-synuclein is selectively transported to the lysosomes for degradation via CMA. However, the mutants A30P and A53T were found to inhibit its own degradation by acting as lysosome uptake blockers (Cuervo et al., 2004). Suppression of autophagy in mouse models have led to neurodegenerative disease phenotypes (Hara et al., 2006; Komatsu et al., 2006). The upregulation of autophagy using the mTOR inhibitor rapamycin is currently being explored as a potential therapeutic avenue (Malagelada et al., 2010). Therefore, within the cell, the formation of LB and LN can be viewed as an attempt by the cell to sequester alpha-synuclein away preventing its disruption in normal cell physiology (Lashuel et al., 2013).

9.6 Conformations of alpha-synuclein during aggregation

The formation of LB is suggested to comprise of alpha-synuclein transitioning between different conformations. Since alpha-synuclein is a disordered protein its conformational flexibility enables it to exist as monomers, oligomers and fibrils within cells. Biochemical isolation and characterization of oligomers from LB present in brain samples identified the presence of low- and high-molecular weight oligomers (Tsigelny et al., 2008). These oligomers are SDS resistant and rich in beta-sheet content. In vitro aggregation assays corroborate the formation and presence of oligomers in the process of fibril formation (Winner et al., 2011). There are several oligomeric species, evident from the different morphologies (spherical, chain-like and annular) to different fibril formation propensities (Breydo and Uversky, 2015). Some oligomeric species convert to form fibrils while others do not. The mechanisms involved in the transitions of these oligomers are still poorly understood.

Immunolabeling together with electron microscopy studies revealed that insoluble fibrils within LB and LN in human brain tissue contained alpha-synuclein (Arima et al., 2000). This discovery led to the hypothesis that the presence and formation of fibrils resulted in neuronal cell death. Subsequently, many studies reported findings for (Hansen et al., 2011; Peelaerts et al., 2015; Pieri et al., 2012) and against fibril toxicity (Karpinar et al., 2009; Winner et al., 2011).

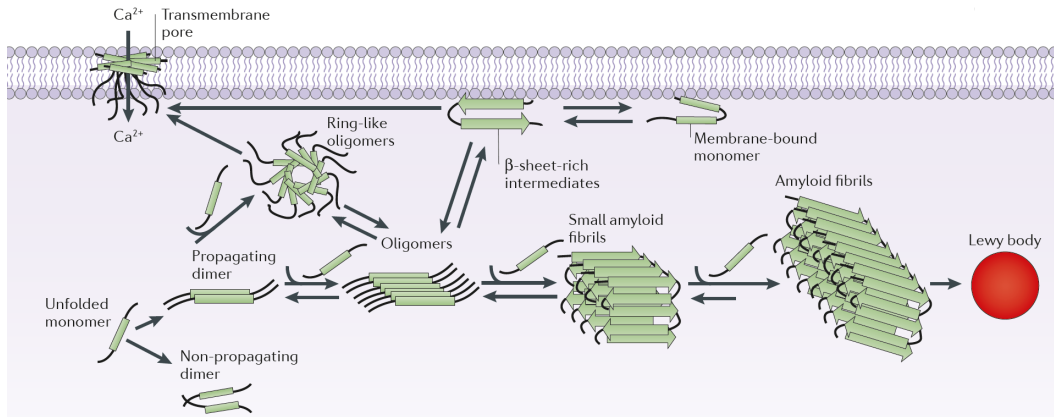


Figure 9.2: Alpha-synuclein oligomer formation. Alpha-synuclein aggregation occurs within the cytoplasm or at the cell membrane. Due to an increased concentration or mutation, increased interaction of unfolded monomers could lead to association and formation of dimers. Dimers could then form ring-like oligomers or oligomers that subsequently form fibrils. Ring-like oligomers are able to interact with cell membranes to affect cell permeability causing an influx of calcium resulting in cellular death. Interaction of fibrils with cellular organelles would lead to the formation of Lewy bodies. Figure adapted from (Lashuel et al., 2013) with permission.

Thus, the field still lacks a common consensus regarding the fibril hypothesis. Another hypothesis that is currently in momentum is that toxicity is mediated by oligomeric species of alpha-synuclein (Winner et al., 2011). This hypothesis is supported by a study showing that the alpha-synuclein mutant A30P forms an energetically trapped population of oligomers which are unable to form fibrils (Conway et al., 2000). Annular/ring-like oligomers are reported to form pores leading to influx of calcium ions into the cell resulting in cell death (Fig.9.2) (Danzer et al., 2007). Additionally, oligomers are reported to result in mitochondrial toxicity (Di Maio et al., 2016). The conflicting results reported in current studies, and the varying hypotheses proposed, further highlight the need for detailed understanding of alpha-synuclein fibril structure and its respective aggregation characteristics. Understanding mechanistically how oligomers transition to fibrils (sequestering potentially toxic oligomers) or preventing toxic amyloid fibril amplification has tremendous therapeutic potential.

9.7 Alpha-synuclein fibrils

Many proteins implicated in neurodegenerative diseases are found in the fibrillar form. Structural characterization of fibrils has offered insight into the organization and formation of these fibrils. Based on X-ray fibre diffraction patterns, amyloid fibrils are described to have a cross-beta sheet structure (Sunde et al., 1997; Sunde and Blake, 1997). The diffraction pattern had a strong reflection at 4.7 Å on the vertical meridional axis and a more diffuse reflection at 8 - 11 Å on the horizontal equatorial

axis (Fig. 9.3a). It translated to individual beta-sheet strands perpendicular to fibril axis to have a 4.7 Å spacing and the two beta-sheets which ran parallel to the fibril axis to have a 8-11 Å spacing (Fig. 9.3b). This formed the core of a protofilament (Fig. 9.3a,c,d). The association of a number of protofilaments form an amyloid fibril (Fig. 9.3e).

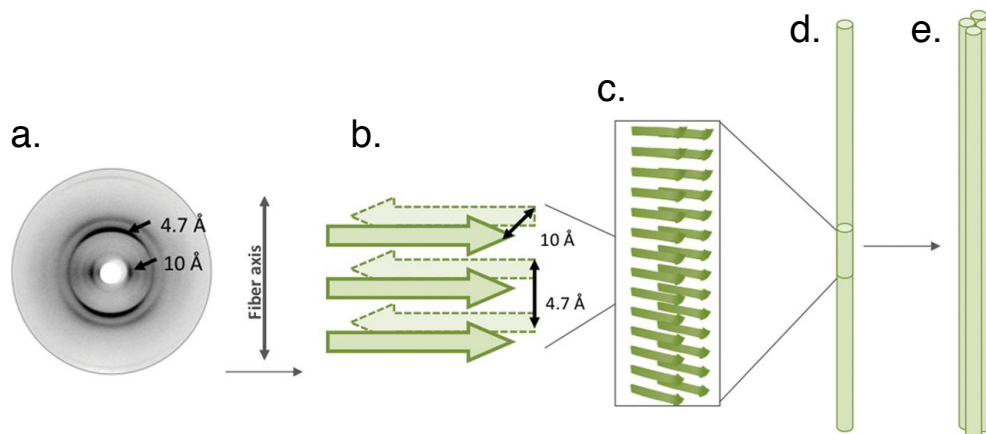
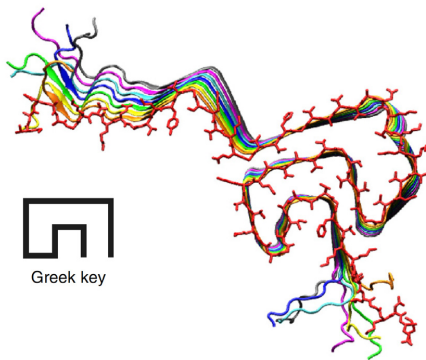


Figure 9.3: Amyloid fibril core structure and organization. Schematic of an amyloid fibril core structure and organization. (a) Cross-beta diffraction pattern obtained from amyloid fibrils. (b) Schematic translating the cross-beta diffraction pattern which form the core, (c) of a protofilament, (d). (e) The protofilaments associate to form an amyloid fibril. Figure taken from (Serpell, 2014) with permission.

Alpha-synuclein amyloid fibril molecular structure was first solved using solid-state NMR (ssNMR) (Tuttle et al., 2016). With the introduction of direct electron detectors and improved single-particle data acquisition and processing pipelines, the structure of the fibrils were also solved with cryogenic electron microscopy (cryo-EM) (Guerrero-Ferreira et al., 2018). The core structure solved from both techniques consisted of two protofibrils adopting a Greek key topology consisting of eight in register parallel beta-strands (Fig. 9.4a). The protofibril interaction interface consists of predominantly the Pre-NAC domain, which also consequently is where most of the mutations linked to familial PD are found (Fig. 9.4b). Under an electron microscope, negatively stained amyloid fibrils are described as long, unbranched filaments. However, these filaments are documented to exhibit morphological features such as straights, ribbons, tubes and laterally associated sheets (Goldsbury et al., 2000). Figure 9.5 exemplifies the type of fibril polymorphism observed in WT alpha-synuclein fibrils prepared by me. This polymorphism is a key feature of amyloid fibrils as it occurs even in fibrils of the same polypeptide composition within a defined solution condition.

There are four classes of polymorphisms that have been described: segmental, packing, side-chain and assembly polymorphism (Greenwald and Riek, 2010; Riek, 2017). Side-chain polymorphism is a result of differences in amino-acid side-chain conformation while maintaining its hydrogen bond network. Packing

a. Structure solved using ssNMR



b. Structure solved using Cryo-EM

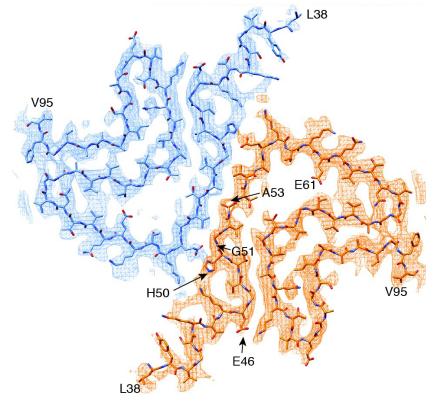


Figure 9.4: Molecular structure of alpha-synuclein fibrils. (a) Structure of a single protofilament solved using ssNMR, with the fibril core exhibiting a Greek key morphology. (b) Structure of a fibril composed of two protofilament solved using cryo-EM. Each protofilament adopts a similar fold as in (a). Figure (a) has been adapted from (Tuttle et al., 2016) with permission. Figure (b) has been adapted from (Guerrero-Ferreira et al., 2018) which is distributed under Creative Commons Attribution 4.0 International (CC BY 4.0).

polymorphism is due to differences in beta-sheet packing of the polypeptide. Segmental polymorphism is due to different amino acid sequences within the polypeptide participate in forming the beta-sheet structures (Colletier et al., 2011). Side-chain, packing and segmental polymorphism together determine the conformation of the protofibrils, the most fundamental unit of cross-beta identity. Out of this arises the formation of different protofibril interfaces. Due to repeat induced cooperativity, otherwise weak and non-specific binding between protofibril interfaces is translated to strong interaction. Assembly polymorphism arises due to different interactions between protofilaments with similar local atomic structural arrangements (Fitzpatrick et al., 2013; Paravastu et al., 2008).

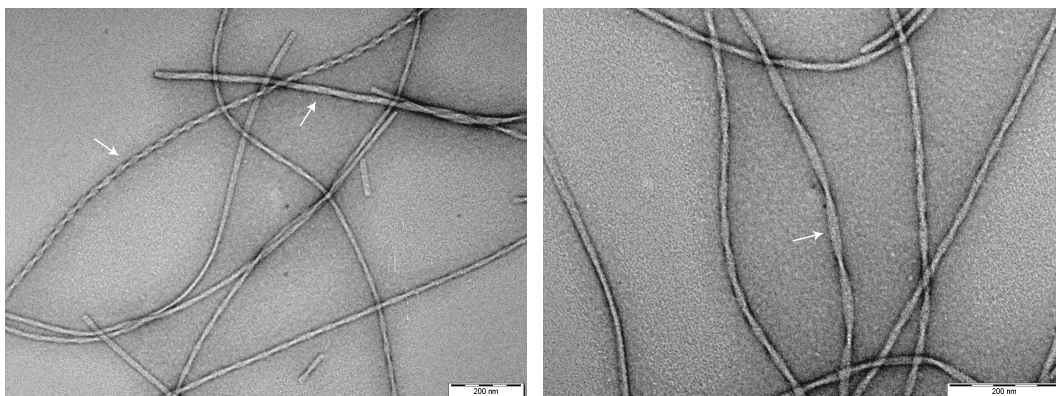


Figure 9.5: Transmission electron microscopy (TEM) image of alpha-synuclein fibril polymorphism. TEM image of alpha-synuclein fibril polymorphism. Alpha-synuclein fibrils formed in the same aggregation solution. White arrows point to fibrils with differing morphology. Scale bar, 200 nm.

Recently, in addition to the existing alpha-synuclein fibril structure (Guerrero-Ferreira et al., 2018), three distinct alpha-synuclein fibril polymorphs have been identified by cryo-EM (Guerrero-Ferreira et al., 2019; Li et al., 2018a). The first two polymorphs were named 'rod' and 'twister' alpha-synuclein polymorph. The 'rod' polymorph's protofibril conformation was similar to that which was proposed by earlier studies (Fig. 9.6 polymorph 1a). It consisted of two protofibrils, having a width of 99 Å and a pitch of 920 Å. The 'twister' polymorph protofibril conformation was different (Fig. 9.6 polymorph 1b). Although, it shared a similar beta-arch core kernel to the 'rod' polymorph, the steric zipper interface between the two polymorphs were mainly around the NAC domain of alpha-synuclein and it had a width of 96 Å and a pitch of 460 Å. Guerrero-Ferreira et al., (2019) introduced two other polymorphs (Fig. 9.6 polymorph 2a,2b). Both fibril polymorphs consisted of two protofibrils. However, they interacted not via the conventional steric zipper interface but with the formation of intermolecular salt bridges. In one polymorph, it was between amino acid residues K45 and E57 of the opposing protofibril. In the other polymorph, there was only one salt bridge at E46 connecting the two protofibrils. Both polymorphs exhibit assembly polymorphism (Fig. 9.6).

9.8 Measuring the self-assembly of fibrils

Amyloid fibrils elongate by recruiting monomers in a self-templating manner. The recruited monomer adopts the respective conformation of the protofibril. This ensures the persistence of each unique polymorph. This is especially important in the context of alpha-synuclein in PD and other amyloid proteins implicated in neurodegenerative disorders being described to exhibit prion-like spreading in disease. In PD, Braak et al., (2003) proposed a staging model of Lewy pathology with sequential development in anatomically connected regions of the brain. This has been supported by observation of LB in fetal graft neurons in human PD patients and graft animal models (Kordower et al., 2008; Li et al., 2008; Desplats et al., 2009). Many modes of transmission of oligomers and seeding fibrils between tissues and cells have been studied. In light of the self-templating property of amyloid fibril polymorphs, efforts are underway to characterize the disease phenotype observed according to an individual polymorph (Gribaudo et al., 2019). It is hypothesized that the large variation in phenotypes observed in synucleopathies could be the effect of different fibril polymorphs. Peelaerts et al., (2015), injected fibrils of defined morphology into rat brain and showed differences in *in vivo* amplification, spreading and histopathological phenotype with respect to fibril morphology. Different conformations of alpha-synuclein are found to be enriched in neurons with LB in human PD compared to oligodendrocytes in human MSA brain samples (Peng et al., 2018; Yamasaki et al., 2019). Evidence from these studies suggest that amyloid fibril polymorphism plays an intrinsic role in the disease phenotype.

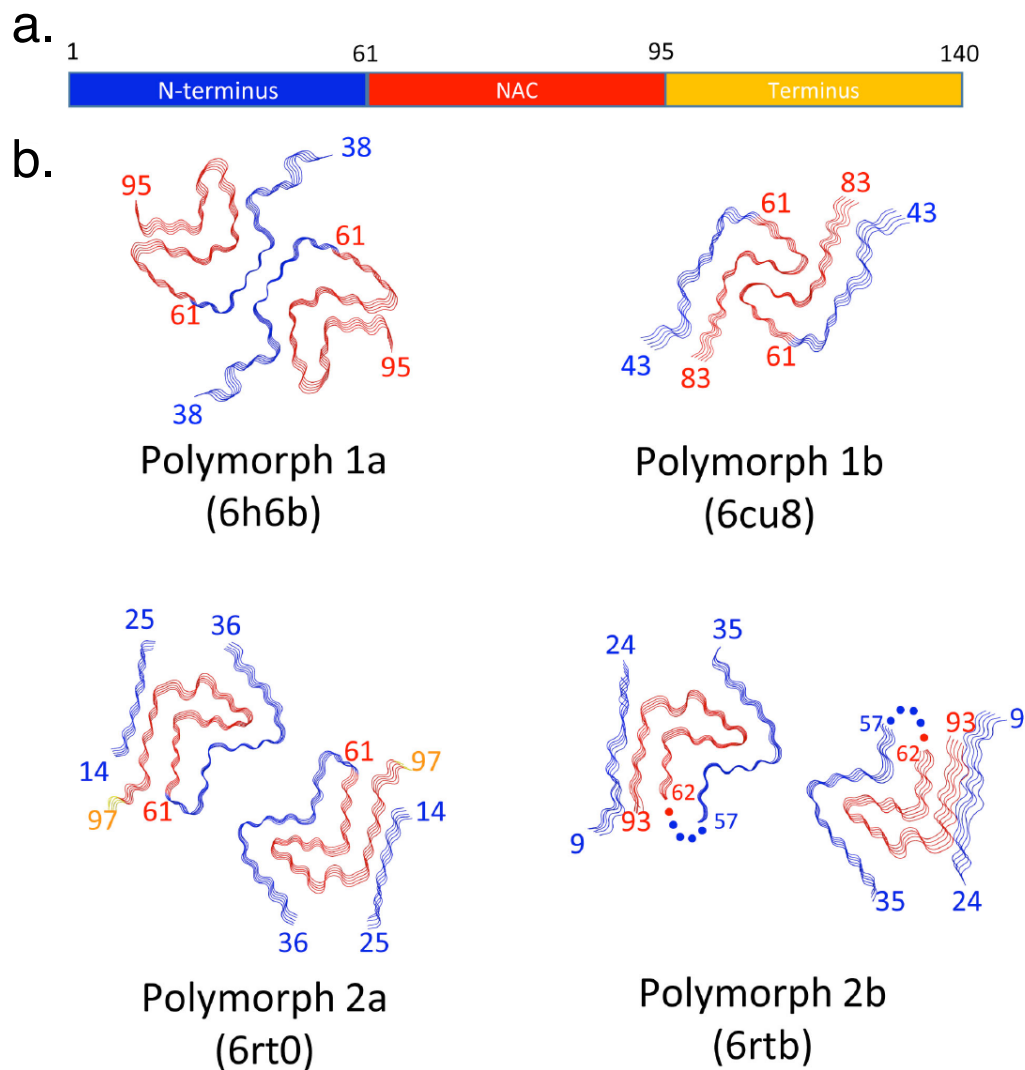


Figure 9.6: Molecular structures of alpha-synuclein polymorphs. (a) Alpha-synuclein regions color coded. (b) All four alpha-synuclein polymorph molecular structures with their corresponding Protein Data Bank (PDB) ID in brackets below the structure. Here the steric zipper interface interaction between protofilaments for polymorph 1A (Guerrero-Ferreira et al., 2018) and 1B (Li et al., 2018a) is clearly visualized. For polymorphs 2a and 2b completely different protofilament arrangements are observed that are held together by two ionic salt bridges for polymorph 2a and only one ionic salt bridge for polymorph 2b. Figure taken from (Guerrero-Ferreira et al., 2019) which is distributed by Creative Commons Attribution-NonCommercial-NoDerivatives 4.0 International (CC BY-NC-ND 4.0).

In vitro aggregation of purified alpha-synuclein (or other amyloid forming proteins for that matter) help to understand and characterize its self-assembly from monomers to fibrils in defined solution conditions. Techniques such as dynamic light scattering (DLS), fluorescence spectroscopy, electron and fluorescence microscopy are used to study the process of alpha-synuclein aggregation. DLS allows the determination of hydrodynamic radii of macromolecules in solution within a time course allowing kinetic measurements. An advantage of DLS is that it is label-free,

requiring no modifications to the proteins. However, DLS loses its sensitivity to detect oligomeric species with the presence of higher molecular weight molecules in the solution (Plotegher et al., 2014). Approaches in electron microscopy allow identification of oligomeric species and classification of fibril polymorphs. At present only endpoint measurements of the aggregation process is studied due to limitations in sample preparation procedures (drying during the staining process or fixation) and imaging under vacuum. In this respect, fluorescence spectroscopy or microscopy techniques have an advantage of direct labeling of proteins (molecular specificity) and its ability to record aggregation kinetics in real-time.

Fluorescent proteins (FP) have been used to tag and follow aggregation of alpha-synuclein in live cells (Ham et al., 2010), with the caveat that FPs are much larger than alpha-synuclein monomers (GFP is 28 kDa, while alpha-synuclein is 14 kDa). The increase in molecular weight of the fusion protein could introduce artifacts in protein expression, folding, localization and physiological function. Another strategy would be to use site-specific labeling of proteins via cysteine residues within a protein's amino sequence (Cremades et al., 2012; Pinotsi et al., 2014). However, dye charge and ratio of labeled to unlabeled monomers have strong effects on fibril morphology and aggregation (Mučibabić et al., 2016). A recent correlative STED/AFM study showed that fibrils formed from a mixture of labeled and unlabeled monomers, resulted in two distinct populations of fibrils. One population of fibrils composed of both labeled and unlabeled fibrils and a second population with fibrils composed of unlabeled monomers (Cosentino et al., 2019). This not only highlights the effects of labeling but also a general limitation in fluorescence microscopy that the underlying context is missed. Only targets that have a fluorophore would be seen in fluorescence microscopy.

One way to minimize the artifacts from attaching a fluorophore would be to use extrinsic fluorogenic amyloid binding dyes such as Congo-red (CR), Thioflavin-T (ThT) and luminescent conjugated oligothiophenes (LCO). Extrinsic dyes undergo conformational changes when bound to alpha-synuclein (or any amyloid structure), resulting in stoke shifts in their fluorescence emission spectrum and increased quantum yield. Most extrinsic dyes interact and bind to side chains present at the face of cross-beta-sheet rich structures resulting in increased fluorescence emission (fluorogenic) (Fig. 9.7) (Krebs et al., 2005; Schütz et al., 2018). Recently, LCO have been used to study the aggregation of alpha-synuclein. LCO have also been shown to detect oligomeric species or aggregate species of alpha-synuclein at a much earlier time-point compared to ThT (Klingstedt et al., 2011). Although the use of extrinsic dyes does not require protein manipulation, they still physically interact with alpha-synuclein. CR has a high affinity for alpha-synuclein and seems to have an inhibitory effect on aggregation (Frid et al., 2007). The majority of aggregation assays use the increase of ThT fluorescence intensity as a quantitative read out for aggregation. However, a study has shown that the brightness of fluorescence is also

dependent on the conformation of alpha-synuclein (Sidhu et al., 2016). Self-assembly of amyloid fibrils is followed label-free based on emission of intrinsic fluorescence when excited with 405 nm excitation and detection between 450-500 nm. It is hypothesized that emission results from the electronic levels that become available due to hydrogen bond network that is formed by the cross beta-sheet structure of amyloid during self-assembly (Chan et al., 2013).

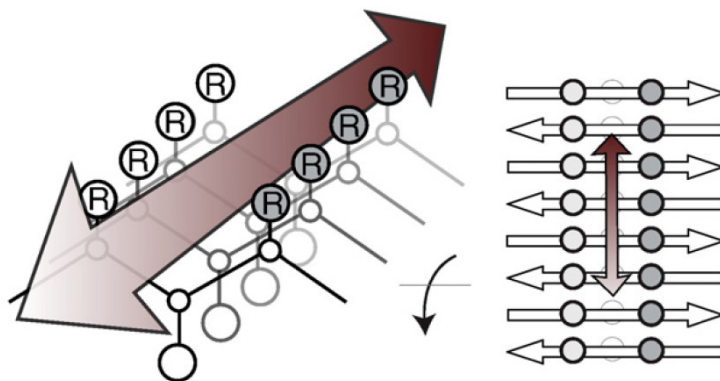


Figure 9.7: A structural illustration of cross beta-sheets in fibrils and amyloid binding dye interaction with fibrils. Amyloid binding dyes are proposed to bind along side chains on the surface of beta-sheets which form a "channel" (brown arrow) along the long axis of beta-sheets. Figure adapted from (Biancalana and Koide, 2010) with permission.

The self-assembly process of amyloid fibrils in general consists of soluble protein monomers transitioning into insoluble highly ordered fibrils. The change in stability of monomers in solution can be effected by the introduction of an air-water interface, presence of lipid membranes and changes in solution conditions such as temperature and pH (Buell et al., 2014; Galvagnion et al., 2015; Campioni et al., 2014). They are all capable of inducing changes in monomer conformation to favour fibrillization. Alpha-synuclein's model of fibril formation consist of natively unfolded conformations > intermediates/misfolded conformations > nucleation/oligomers > fibril (Fig. 9.8a Uversky et al., 2001). Oligomers and fibrils are protein conformations that are beta-sheet rich. Using ThT to follow the self-assembly process results in a characteristic sigmoidal shape, a lag phase, exponential growth phase and finally a plateau phase. In the lag phase, the protein solution predominantly contains unfolded and misfolded monomers, the fluorescence emitted by ThT is low as there is very little beta-sheet containing species. As time proceeds, nucleation occurs and oligomers are formed, and the fluorescence emitted increases exponentially. The oligomers then transition to become fibrils. The energy barrier that is required for a monomer to template onto a fibril is much lower compared to nucleation, therefore, the monomers are sequestered away into fibrils in the final plateau phase (Fig. 9.8b) (Brown et al., 2018). By fitting the sigmoidal curve, parameters such as, duration of lag phase, rate constant of the exponential growth phase and the maximum intensity at the plateau phase (Nielsen et al., 2001)

can be measured. Depending on the perturbations done, these parameters provide means of quantification for mechanistic study of the self-assembly process.

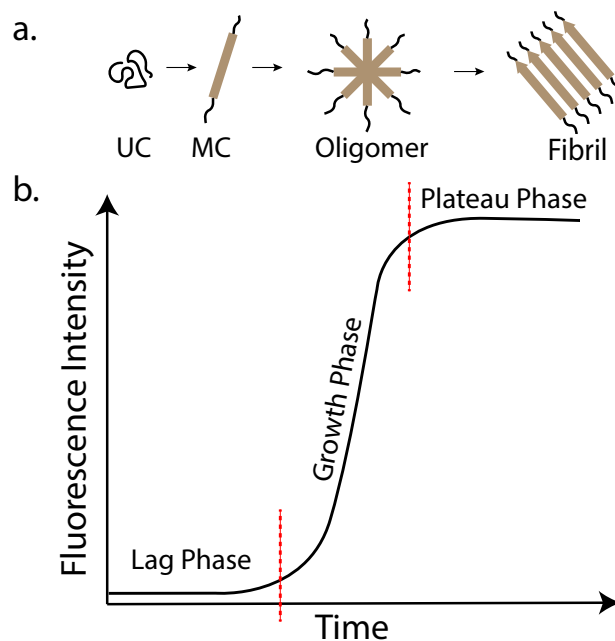


Figure 9.8: Self-assembly process of amyloid fibrils. (a) A schematic showing the transition of a native monomer in unfolded conformation (UC), transitioning to an intermediate misfolded conformation (MC), then to an oligomer which is a nucleation step and finally to a fibril. (b) Characteristic sigmoidal curve that is observed in a fluorescence aggregation assay. The increase in fluorescence is due to the increasing beta-sheet content of the assay. There are three distinct phases, the lag phase (monomers and intermediates), exponential phase (oligomers and fibrils) and finally a plateau phase (predominantly fibrils).

Extensive studies have been performed with different permutations and combination of reaction conditions to show effects on the self-assembly kinetics of fibrils. Reaction conditions such as increase in monomer concentration, ionic strength, pH, temperature, physical agitation and additives such as crowding agents and lipids all have an effect on the self-assembly process (Knowles et al., 2007; Narkiewicz et al., 2014; Buell et al., 2013). From these *in vitro* aggregation assays it was deduced that, in the case of alpha-synuclein, fibrils elongate by addition of monomers and not oligomers (Buell et al., 2014). Changing solution conditions not only changes the rate of self-assembly but it is also able to bias the formation of a particular fibril morphology (Bousset et al., 2013; Hoyer et al., 2002). These aggregation assays reveal the general process of self-assembly and endpoint structure. However, they lack the sensitivity to inform on specific amyloid polymorphs. As mentioned earlier, these bulk aggregation assays contain a mixed population of fibril polymorphs. This is also the reason for much of the heterogeneity in the current studies. One solution is to experimentally follow the self-assembly process of a single fibril.

9.9 Studying self-assembly of single fibrils

Using total internal reflection fluorescence (TIRF) microscopy and ThT, the elongation of individual fibrils was first visualized by Ban et al., 2003 using amyloid fibrils formed from beta2-microglobulin was documented. This assay was then adapted for different amyloid proteins, aBeta (1-40) (Ban and Goto, 2006), glucagon (Andersen et al., 2009), amylin (Patil et al., 2011) and alpha-synuclein (Wördehoff et al., 2015). Using covalently linked fluorophores, elongation of fibrils from yeast prion protein, Sup35 (Inoue et al., 2001), alpha-synuclein *in vitro* and *in vivo* (Pinotsi et al., 2014; Pinotsi et al., 2016) and aBeta (1-42) (Young et al., 2017) were reported. Although all these studies looked at fibril elongations of fibrils formed from different proteins, they described common fibril elongation characteristics such as, unidirectional, polarized bidirectional elongation and intermittent stop and growth phases. This suggests that amyloid fibrils share a common elongation mechanism. The protofilaments are stacked on top of each other at the fibril interface and this dense packing causes asymmetry between both fibril ends (Guerrero-Ferreira et al., 2019). As a result different templating interfaces are exposed to solution monomers to template against for fibril incorporation. Therefore, the addition of monomer at one end is more efficient than the other resulting in polarized growth (Guerrero-Ferreira et al., 2018).

9.10 Characterization of self-assembly kinetics

The intermittent stop and growth phases have been proposed to be due to two distinct kinetic processes. The first process is a 'dock', where the solution monomer binding to the fibril template interface is reversible, and a second phase, 'lock' where the binding of the monomer is irreversible and it gets incorporated into a part of the fibril. A fibril's growth end is only able to incorporate an additional monomer when the last monomer is 'locked' in place (Esler et al., 2000). Fibril elongation rates change according to temperature (Arrhenius behavior) and according to monomer concentrations (Young et al., 2017). It was also observed that a large portion of fibrils failed to elongate under experimental conditions and amongst the fibrils that elongated, there were large heterogeneity in final length and elongation rates (Pinotsi et al., 2014; Young et al., 2017). Even though these studies successfully monitored the elongation of single fibrils, they failed in ability to discriminate different fibril polymorphs which could potentially explain the large variations observed.

9.11 Superresolution imaging of amyloid fibrils

SMLM has been used to study amyloid fibril elongation (Pinotsi et al., 2014; Young et al., 2017). However, it was not possible to report on structure and dynamic information of a respective fibril. Using the dSTORM approach required the use of specific dyes (AF647 and AF568). These dyes had to be covalently linked to alpha-synuclein via cysteine labeling. Since alpha-synuclein lacked cysteines in its primary sequence, it was necessary to introduce a cysteine moiety for labeling by site-directed mutagenesis. As discussed above, any modification done to a monomer (mutations and dye charge) would result in a deviation or introduce a bias in conformational form. In addition, dSTORM imaging requires a specific imaging buffer composition that is not compatible for monitoring fibril elongation in real time. Therefore, a different SMLM strategy has to be adopted.

Point accumulation for imaging in nanoscale topography (PAINT) is an imaging strategy that is compatible with SMLM. Here, the object being imaged is continuously targeted by fluorescent probes. Its utility was demonstrated by imaging large unilamellar vesicles (LUV) with Nile red (Sharonov and Hochstrasser, 2006). Nile red is a dye that is fluorogenic upon binding to hydrophobic environments like LUV. Fluorogenic dyes emit fluorescence only when their aromatic rings are planarized due to interaction with its environment. In solution the molecule's aromatic rings are freely rotating around their connecting bonds and are therefore, non-fluorescent. This results in very low fluorescence background signal. Using nanomolar concentrations of dye, each individual dye binding event is spatially separated. This allows a single dye binding event to be treated as an individual PSF. By fitting this PSF with a 2D Gaussian function, the precise localization of the dye molecule can be calculated. After a period of acquisition, all the localizations can be rendered in one image to represent the underlying object. Using this approach, it is possible to reach a very high localization precision. The limiting factor is the number of photons emitted per fluorescent probe binding event.

All of the above mentioned amyloid binding dyes are fluorogenic and are therefore compatible with the PAINT imaging approach. Visualization of single amyloid fibrils using binding activated localization microscopy (BALM) was pioneered in the lab of Jonas Ries (Fig. 9.9) (Ries et al., 2013). BALM was first used to visualize the organization of the bacterial chromosome with fluorogenic DNA binding dyes (Schoen et al., 2011). At the time of the study, it was apt to call the method BALM, however, since the working principle was the same and in the interest of not adding an additional acronym to the field, we will refer to it as PAINT. Ries et al., (2013), performed PAINT with an anionic LCO, penter-formyl thiophene acetic acid (pFTAA), on alpha-synuclein fibrils demonstrating its ability to visualize single amyloid fibrils with localization precision < 20 nm (Ries et al., 2013). There

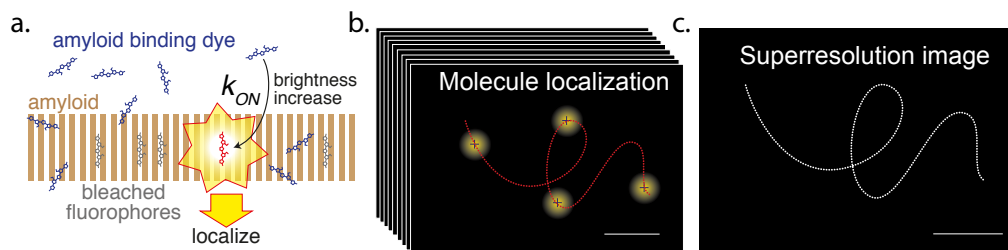


Figure 9.9: PAINTing alpha-synuclein fibrils.(a) A schematic showing the working principle of PAINtTing alpha-synuclein fibrils. Fibrils are incubated in the presence of amyloid binding dyes. In solution, the dyes are not fluorescent. Upon binding to the cross-beta-sheet structure of the fibril, the dyes aromatic rings are planarized to result in energy absorption and emission of fluorescence. The molecule is then localized from its fluorogenic event and bleached away. (b) This process is repeated iteratively over multiple images. To ensure that each binding event is spatially separated, nanomolar concentrations of the dyes are used. (c) After acquiring multiple frames, all recorded localizations can then be rendered in one image to reconstruct the underlying structure of the fibrils. Reprinted (adapted) with permission from (Ries et al., 2013). Copyright (2013) American Chemical Society.

are a few advantages with this imaging approach. Firstly, the protein monomers are not modified since the dyes interact only with the cross-beta sheet structure directly. Secondly, because there would be more dye molecules present in solution than binding sites present on the fibril, therefore very high labeling can be achieved. Another unique opportunity which is presented, is the ability to study the dye's optical signature upon binding.

9.12 Inferring fibril features from optical signatures

9.12.1 Spectral properties of dyes

Most exogenous dyes exhibit broad emission spectra. The emission spectrum of a dye is influenced by its chemical environment (pH, solvent polarity, ionic strength and others). Based on this principle, Bongiovanni et al., (2016), performed multi-dimensional SMLM imaging using PAINT. From each dye binding event, they calculated its position and measured the emission spectrum of each localization. They called this method spectrally-resolved PAINT (sPAINT). By placing a blazed transmission diffraction grating on the emission beam path, two major diffraction orders were created. Both orders, the zeroth and the first order were captured on different portions of the camera chip. The zeroth order was used to calculate the position ($x-y$) and the first order was used to collect the spectral information of the corresponding localization (Fig. 9.10a,b). Using synthetic vesicles of known composition and hydrophobicity, they calibrated the spectral properties of Nile red in different hydrophobic environments (Fig. 9.10c). Using these calibrated values,

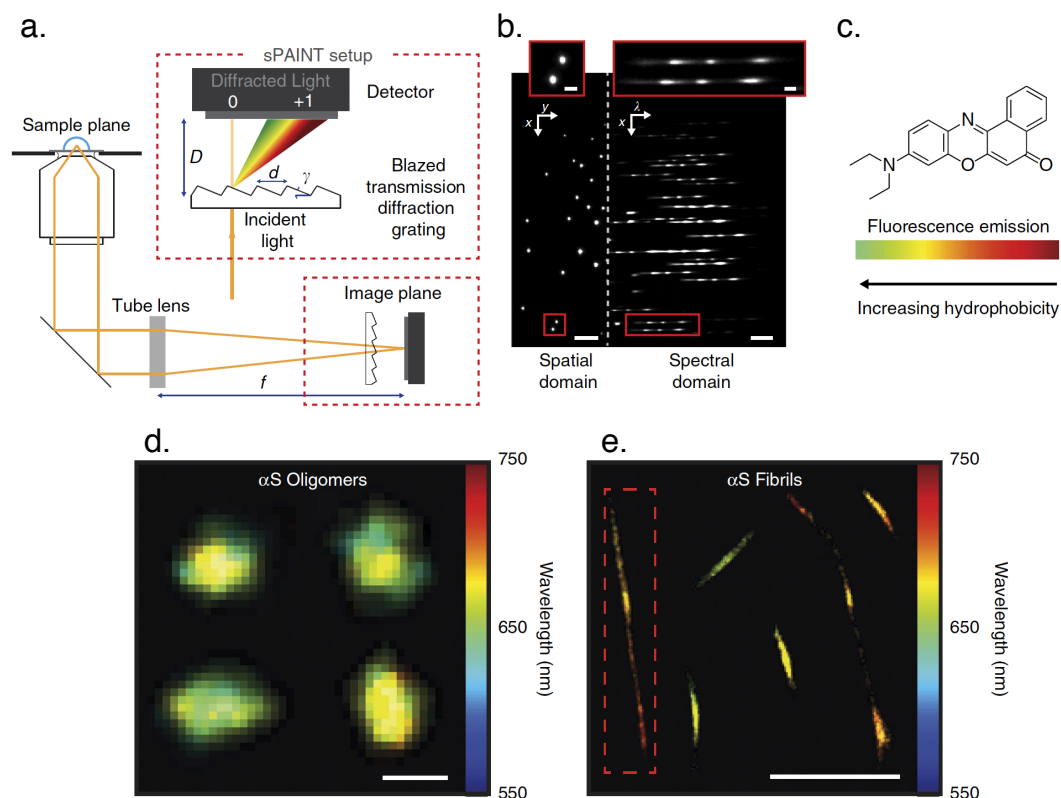


Figure 9.10: Spectrally-resolved PAINt. Mapping surface hydrophobicity with spectrally-resolved PAINt (sPAINT). (a) Schematic of optical setup. Single molecule events collected by a high NA objective are passed through a blazed transmission diffraction grating. This creates two major diffraction orders which are captured on different areas of the camera chip. (b) Representative raw sPAINT data of 100 nm TetraSpeck beads, labeled with four distinct fluorophores. Signal from each distinct fluorophore is spectrally separated in the spectral channel. Scale bars are 5 μm ($x-y$) and 100 nm ($x-\lambda$). (c) Chemical structure of Nile red and its emission wavelength range in different hydrophobic environments. (d,e) sPAINT image of alpha-synuclein oligomers (d) and (e). Scale bar in (d) is 100 nm and scale bar in (e) is 1 μm . This figure has been adapted from (Bongiovanni et al., 2016). It is distributed under Creative Commons Attribution 4.0 International (CC BY 4.0).

they then empirically showed that oligomers and fibrils of alpha-synuclein had different surface hydrophobicity signatures. Mature fibrils were less hydrophobic compared to oligomers (Fig. 9.10d,e). From the data presented in their paper it also seemed that within fibrils, there were heterogeneities in the hydrophobic signatures (Fig. 9.10e). However, they did not explore this further in the context of fibril polymorph differentiation. Nile red is not characterized as an amyloid binding dye, therefore it would be interesting to investigate if established amyloid binding dyes (ThT and pFTAA) exhibit any spectral properties that could help distinguish different polymorphs. In fact, LCOs consist of a swiveling pentameric oligothiophene backbone that has been shown to exhibit differing emission spectra based on the conformational freedom of this backbone (Klingstedt et al., 2011; Sjöqvist et al., 2014; Yuan et al., 2015). This property was used to differentiate amyloid-beta fibrils from neurofibrillary tangles in human AD brain sections.

9.12.2 Polarization dipole of dyes

Polarized light is an electromagnetic wave with an electric field that oscillates perpendicularly to its direction of propagation. In unpolarized light, the orientation of its electric field changes over time while being perpendicular to its direction of propagation. Lasers used for excitation of fluorophores in fluorescence microscopy are polarized (Murphy and Davidson, 2012). Polarized light can be decomposed into a combination of two polarization states, namely, p (parallel) and s (perpendicular) with respect to the plane of incidence.

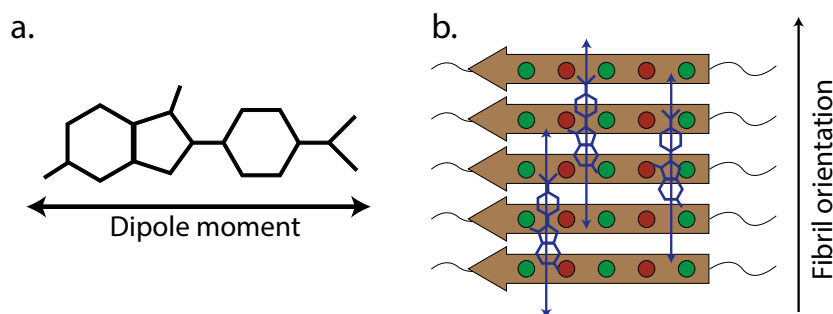


Figure 9.11: Dipole moment of dyes and its orientation bound to amyloid fibrils. (a) Chemical structure of ThT with an arrow below indicating the general orientation of the dipole moment. (b) Illustration of dipole orientations of dye molecules bound to an amyloid fibril. The dipole moments of dye molecules orient parallel to the fibrils' orientation.

All fluorophores possess a transition dipole moment. This dipole moment is orientated along the long axis of the dye molecule (Fig. 9.11a). The absorption efficiency of the dye molecule is dependent on its dipole orientation with respect to the excitation laser's electric field. The fluorophore would only be able to absorb energy when its dipole moment is parallel to the excitation laser's electric field (Duboisset et al., 2013). The corresponding emission of the fluorophore is polarized according to its dipole moment. In most biological samples, fluorophores in solution are freely rotating. The rotational speed of these molecules are at timescales smaller than image acquisition rates. Therefore, they visit all possible orientations to absorb energy to emit fluorescence even under linearly polarized excitation lasers. However, should the fluorophore be restricted in rotational motion, as is the case here, its dipole moment directly reports the dye's orientation. The polarization of its emission can be used a readout for this.

This polarization can be recorded using a polarizer or polarization beam splitter. A polarizer allows transmission of one particular polarization orientation (p or s) (Fig. 9.12a). The polarizer is then rotated at fixed angles and fluorescence intensity is recorded. Plotting the fluorescence intensity against the angular displacement of the polarizer would result in a sinusoidal curve (Fig. 9.12b). The degree of dipole moment rotational restriction can be measured from the modulation extent of the sinusoidal curve. The peak intensity reflects the angle of the dipole moment with

respect to the plane of incidence (Varela et al., 2018). A polarization beam splitter splits the dye's polarization into two orthogonal analyzer directions which are then recorded in two different channels (Fig. 9.12c). The measured intensities' difference in both channels normalized against the total intensity from both channels gives a polarization factor that describes the orientation of the dye molecule with respect to the plane of incidence (Fig. 9.12d) (Cruz et al., 2016).

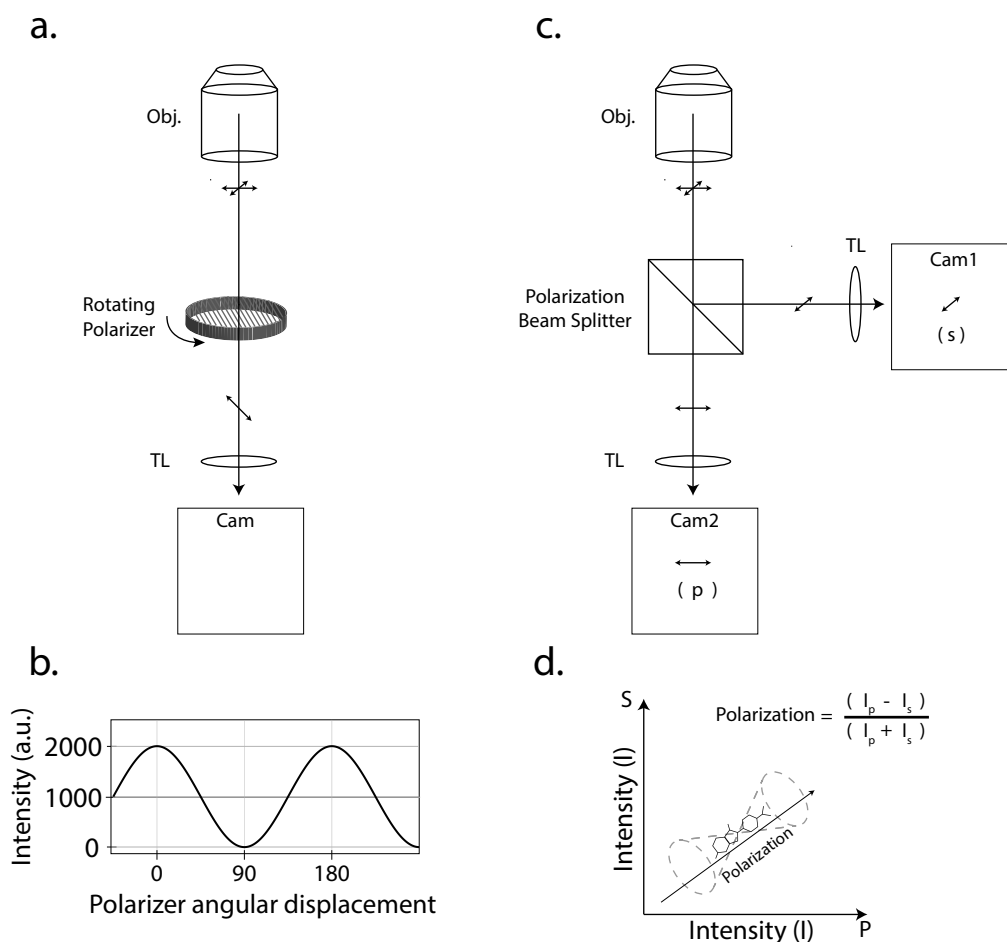


Figure 9.12: Polarizer and polarization beam splitter optical setups and its respective readout. (a) Optical setup with a rotating polarizer. (b) Imaging a fluorophore with a fixed dipole moment, would result in a sinusoidal intensity trace with respect to the rotational displacement of the polarizer. (c) Optical setup with a polarization beam splitter. (d) Fluorescence intensity based on the orientation of each single molecule's polarization is captured on two different channels. By taking the difference in intensity in both channels and normalizing it to the total intensity recorded in both channels, the polarization of each event can be calculated.

The use of a polarizer is suited for ensemble measurements (diffraction-limited microscopy) as the fluorescence signal is stable, allowing for multiple acquisitions of the same field of view. However, under single-molecule studies where the lifetime of each event is short, acquiring multiple images with different angles of rotation may not be possible. Therefore, in single-molecule studies, polarization beam splitters are used in place. It enables instantaneous polarization characterization by splitting

the intensity of each single molecule event according its two orthogonal components in x and y . However, in this configuration contribution from the z component is invisible.

Polarization studies done with amyloid binding dyes bound to amyloids show that the polarization dipole moments of the dye molecules are orientated along the length of the fibrils (Fig. 9.11b) (Lee et al., 2018; Krebs et al., 2005). This is in accordance to crystal structure characterization of dyes bound to amyloid fragments (Biancalana et al., 2009). Oligomers are beta-sheet rich structures with very little structural order and they exhibit low polarization modulation. The transition of oligomer to fibrillar structures is reflected in the gradual increase of polarization modulation being recorded (Lee et al., 2018). At the single-molecule level, Shaban, H. et al, (2017) showed that by analyzing the polarization orientation of individual dye molecules it was possible to decipher the fibril ultra-structure corresponding to protofilament twist within an amyloid fibril. They did not proceed to characterize or differentiate different fibril polymorphs.

Progress in the field of neurodegenerative disorders, especially in PD, has been slow despite the amount of resources that is invested into understanding the disease etiology. This is in part due to the lack of a representative disease model that is able to recapitulate symptoms and phenotypes. A large part of the problem, however, is the highly complex nature of the proteins implicated in these diseases. They are highly polymorphic and elusive to characterize. Thanks to advancements in the field of cryo-EM, we are now able to identify and characterize these polymorphs. The next step would be to understand the role these structural features play in the self-assembly process of these fibrils. In the optical microscopy field, specifically in SMLM, there has been steady incremental steps towards filling this gap in knowledge. This project is aimed at addressing and closing this gap in knowledge.

10 | Results

10.1 Protein purification and characterization

Since this project was part of a Sinergia consortium with three other groups based in Switzerland, I received reagents and knowledge transfer on protein expression and purification of alpha-synuclein. We were provided with DNA constructs encoding for human alpha-synuclein wild-type (WT) and mutants (A30P, E46K and A53T) in pRK172 expression vector from our collaborator Prof. Dr. Roland Riek. All protein expression and purification was done at the protein expression and purification core (PEPCORE) facility at EMBL.

The purification strategy was adapted from Huang (2005)(Huang et al., 2005). The adapted workflow comprised of periplasmic extraction, ion-exchange chromatography (IEX) and hydrophobic interaction chromatography (HIC). Using the shared protocol I was able to express and purify my own alpha-synuclein protein. However, I was getting a low yield of protein (4 mg) and observed significant batch to batch variations in my protein aggregation assays. This led to multiple rounds of troubleshooting and optimization. In the end, I found that alpha-synuclein did not bind to the HIC columns and eluted out as pure alpha-synuclein in the flow through (FT). In addition I added a final size exclusion chromatography (SEC) step to remove trace amounts of salt and complete exchange into my working buffer (20 mM MES pH 6).

The protocol received from the consortium used HiPrep phenyl FF 16/10 columns for HIC. The column has a phenyl hydrophobic ligand coupled to 6% crosslinked agarose matrix. Our PEPCORE had a RESOURCE PHE column, which had a phenyl hydrophobic ligand coupled to monodispersed rigid polystyrene/divinylbenzene matrix. Since the ligands were the same I used the RESOURCE PHE column for HIC. After analysing the fractions in the gel, I noticed that the amount of protein that bound to the column was little compared to the amount in the FT (Fig. 10.1a).

The FT still had a significant amount of contaminant proteins present (Lane 2 & 3 in Fig. 10.1a). To recover the protein from the FT, I ran the FT from the RESOURCE

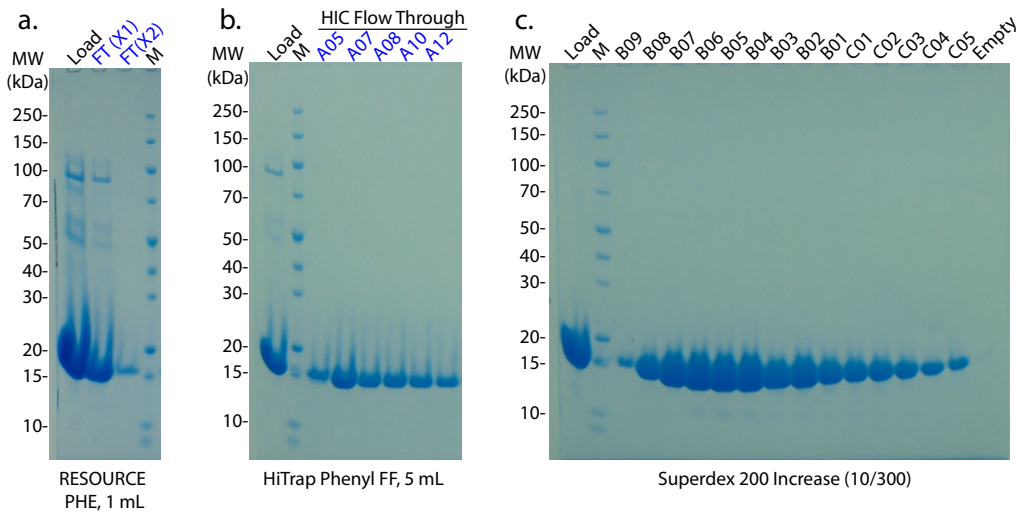


Figure 10.1: Protein fractions from HIC and SEC analyzed on SDS-PAGE gels
 (a) HIC fractions obtained from RESOURCE PHE, 1 mL column. Alpha-synuclein does not bind to the column but elutes out in the flow through (FT). The FT is a mixture of alpha-synuclein and contaminants. (b) HIC fractions obtained from HiTrap Phenyl FF, 5 mL column. Alpha-synuclein still elutes out in the FT, however, it is free of contaminants. (c) FT from the (b) is concentrated and run through a Superdex 200 (10/300) column. The load and the fractions are pure alpha-synuclein.

PHE column onto a HiTrap phenyl Fast Flow (high sub) column which has a phenyl hydrophobic ligand coupled to 6% crosslinked agarose matrix.

Once again, I observed alpha-synuclein mostly in the FT (Fig. 10.1b). However, the contaminant proteins bound to the column and eluted later in the elution gradient. The FT was then dialysed and concentrated for SEC (Fig. 10.1c). Lane 1 in Fig. 10.1c, which is the concentrated FT, shows a single protein band. The SEC fractions of B09 to B01 were pooled, concentrated to 450–500 μ M and aliquoted into thin walled PCR for storage in -80 °C. Recovering the protein from the FT enabled us to get a significantly higher yield (40 mg) and reproducibility between batches of protein purification.

10.2 Super resolution imaging of alpha-synuclein fibrils

10.2.1 Visualization of alpha-synuclein fibrils

There are a couple of strategies for super resolution imaging of alpha-synuclein fibrils. They could be visualized using immunofluorescence with either primary or secondary antibodies conjugated to organic dyes (Pinotsi et al., 2016). Studies have also been done with direct covalent linking of organic dyes to introduced cysteines within alpha-synuclein monomers (Pinotsi et al., 2014) or tagging with a fluorescent protein (Ham et al., 2010). However, to achieve minimum linkage error and have minimal effects on fibril morphology and self-assembly, fibrils are best probed with exogenous dyes that bind to the fibril structure. There are many amyloid binding dyes that bind directly onto the fibril's beta sheet structure.

Luminescent conjugated polymers (LCP) are a class of amyloid binding dyes which are fluorogenic upon binding to amyloid fibrils (Sigurdson et al., 2007; Nilsson et al., 2007). Previous work in our lab utilized the PAINT imaging strategy with pentameric formyl thiophene acetic acid (pFTAA), a LCP, to achieve a localization precision of ~20 nm (Ries et al., 2013). I then set out to look for other dyes that could bind to amyloids and are compatible with PAINT imaging strategy. I found four dyes spanning the whole spectrum which were able to fulfill both criteria, namely, Thioflavin-T (ThT), pFTAA, Nile red and Nile blue. Using a confocal microscope with a spectrum detector, I collected the fluorescence emission spectra of these dyes bound to alpha-synuclein fibrils (Fig. 10.2). I adapted our microscope filter configuration for PAINT measurement for each dye based on its fluorescent emission spectra.

Fig. 10.3 contains representative images, photon statistics and line profiles along the fibrils PAINTed with the respective dyes. From the measurements, I recorded the highest mean photon count for Nile blue (2418), pFTAA (1527), Nile red (881) and ThT (575). A Gaussian fit was performed to describe line profiles along the fibrils. The calculated mean sigma value of the curves were similar and reported a mean of 16.25 nm. This indicated that the localization precision of our single molecule events was the factor limiting the reachable resolution.

These measurements were performed on fibrils adsorbed onto a plasma cleaned coverslip, therefore the contribution of nonspecific localizations were minimal. As one of the aims of this project was to use the dyes in an fibril self-assembly assay, I qualitatively assessed the performance of the dyes in staining fibrils at the end point of an self-assembly assay and noted that Nile red and Nile blue were not able to specifically stain fibrils (data not shown). The images consisted of mainly nonspecific background. ThT and pFTAA were both able to specifically stain fibrils. However, ThT is excited using 405 nm (Fig. 10.3) wavelength, which was not compatible with

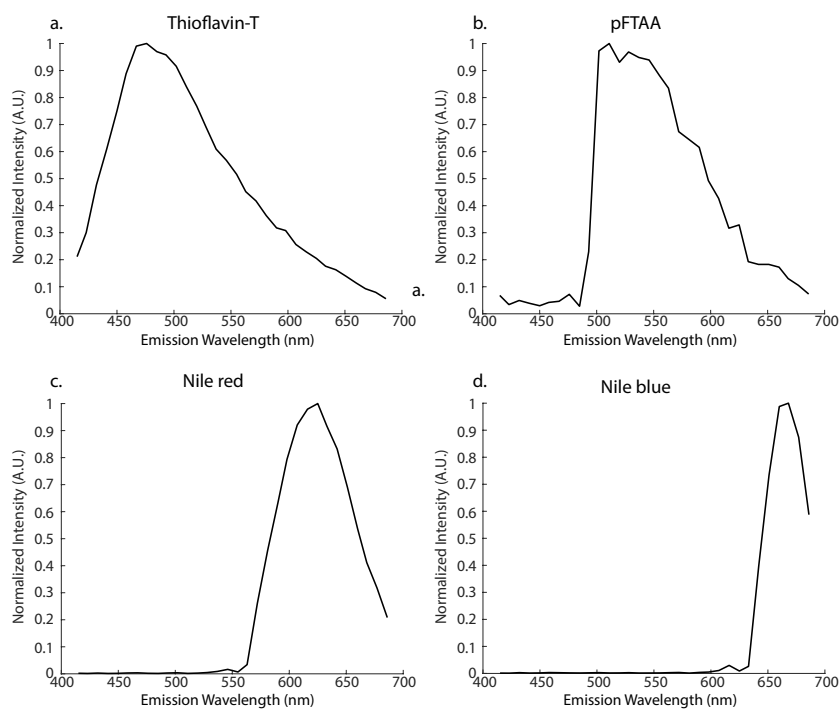


Figure 10.2: Fluorescence emission spectrum of dyes bound to alpha-synuclein (a) Emission spectrum of Thioflavin-T (ThT) bound to alpha-synuclein fibrils (Excitation wavelength: 405 nm). (b) Emission spectrum of pFTAA bound to alpha-synuclein fibrils (Excitation wavelength: 488 nm). (c) Emission spectrum of Nile red bound to alpha-synuclein fibrils (Excitation wavelength: 561 nm). (d) Emission spectrum of Nile blue bound to alpha-synuclein fibrils (Excitation wavelength: 640 nm).

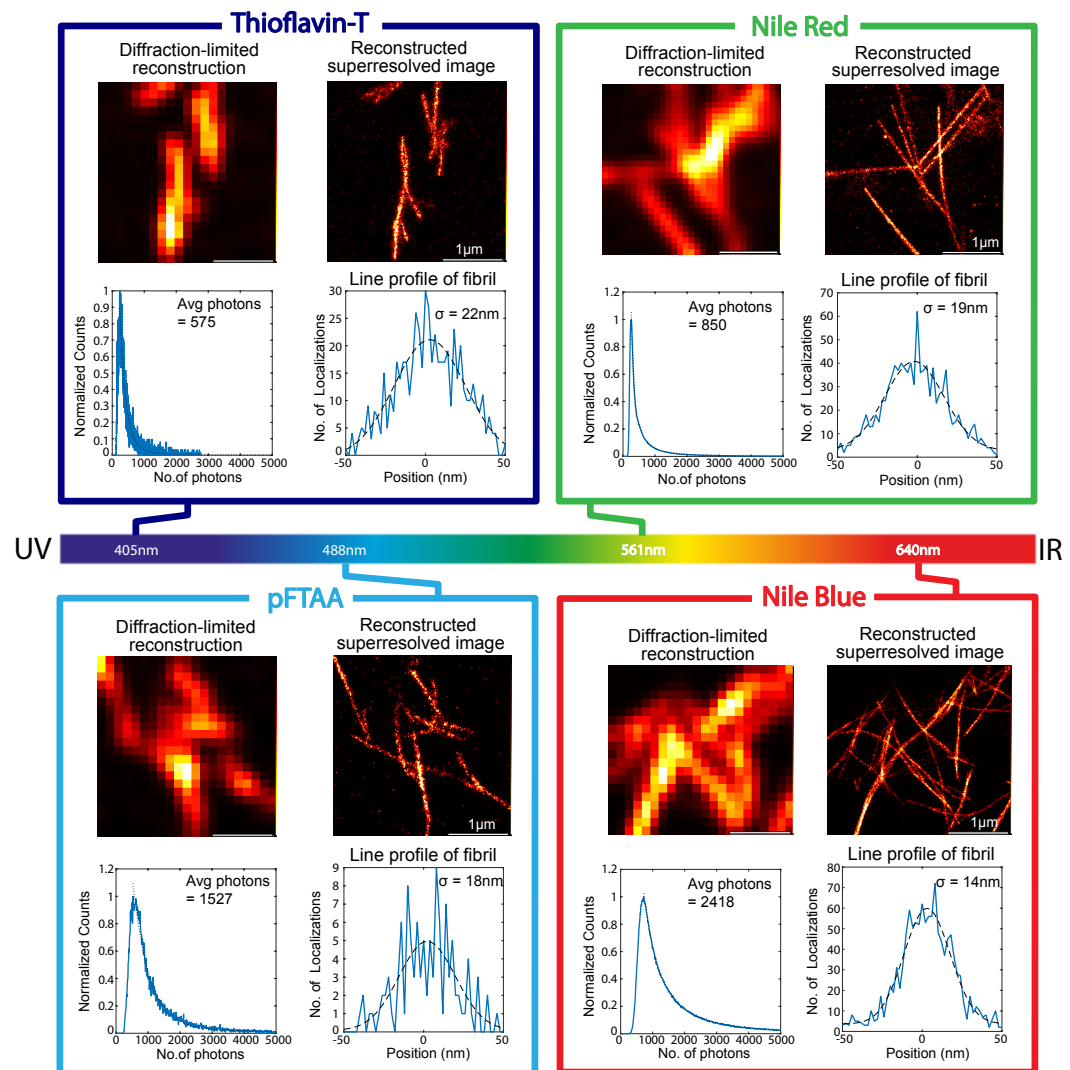


Figure 10.3: Compatibility and performance of various dyes with PAIN T imaging Four different dyes that span the visible spectrum capable of visualizing individual alpha-synuclein fibrils

Table 10.1: Summary of the different filter settings and its respective S/N ratio recorded

Dichroic Mirror	Filter Setup	Photons	Locp	BG	SNR
488LP	525f-500LP	2206	22.4	439	5.0
488LP	582f-500LP	2018	19.7	192	10.5
488LP	617f-500LP	1934	19.5	184	10.5
532-640BP	585f-500LP	2478	20.4	306	8.0
532-640BP	617f-500LP	1958	21.1	204	9.6
532-640BP	500LP	3851	21.5	1182	3.2

488LP, 488 longpass filter; 532-640BP, 532-640 bandpass filter; 525f, 525/50 bandpass filter; 582f, 582/75 bandpass filter; 617f, 617/73 bandpass filter; 500LP, 500 longpass filter; Locp, localization precision; BG, background; SNR, signal to noise ratio.

our microscope configuration and was found to inhibit self-assembly of fibrils by means of free radical formation that damaged fibrils. Due to these reasons, I used pFTAA for all the following experiments.

10.2.2 Finding the optimal conditions for PAINTing with pFTAA

10.2.2.1 Optical filter configuration

To get the best signal to noise ratio (SNR), I tested combinations of different optical filter configurations (Table 10.1). I first performed measurements with the 488 long pass (488LP) and 532-640 band pass (532-640BP) dichroic mirrors. I found that 488LP gave a better signal to noise ratio due to lower background. A 500LP filter had to be added to prevent residual 488 nm excitation from reaching the camera chip. Based on the emission spectra (Fig. 10.2b), the highest signal was recorded between 500–550 nm. Using a 525/50 filter is optimal within this region. When a 525/50 filter was used, I recorded a high photon count, however the background recorded was also high which resulted in a low SNR and a low localization precision. I found that we got the highest SNR when either the 585/50 or 617/73 filters were used. I used the 585/50 filter for all subsequent experiments as it enabled signal collection from 560 to 610 nm, where the signal in the spectrum was higher and had a narrower transmission compared to the transmission of the 617/73 filter.

10.2.2.2 Buffers

I assessed the performance of pFTAA in phosphate buffer saline (PBS) pH 6, 2-(N-morpholino)ethanesulfonic acid (MES) pH 6 and Tris-buffered saline (TBS) pH 6. I did not observe significant differences in SNR ratio and localization precision (Table 10.2). No significant difference was also observed when the pH was varied in the same buffer (TBS). Since no significant advantage was observed in different

Table 10.2: Summary of pFTAA performance in different buffer conditions

Buffer Condition	Photons	Locp	BG	S/N
11.8 mM PBS pH 6	1806	20.8	134	13.4
20 mM MES pH 6	1484	20.8	132	11.2
20 mM TBS pH 6	1525	21.8	141	10.8
20 mM TBS pH 7.4	1324	21.5	131	10.1
20 mM TBS pH 8	1331	21.2	125	10.6

Locp, localization precision; BG, background; S/N, signal to noise ratio.

buffers, all my following experiments were done in 20 mM MES pH 6 as it was the working buffer for my fibril self-assembly assay.

10.2.2.3 pFTAA spectral properties

One exciting property of pFTAA (LCO) described by Klingstedt et. al (2011) is that its emission spectrum depends on the backbone conformation of amyloids. This could potentially enable us to distinguish alpha-synuclein polymorphs based on emission spectra. To test this, we first characterized the emission spectra of different amyloids, amyloid-beta (1–42), alpha-synuclein and neurofibrillary tangles (Tau). Amyloids were generated using respective purified proteins in contrast to Klingstedt et al., 2011. Emission spectra of the respective amyloids bound to ThT (Fig. 10.4a), pFTAA (Fig. 10.4b) and Nile red (Fig. 10.4c) showed no significant difference in the emission profiles between the different amyloids.

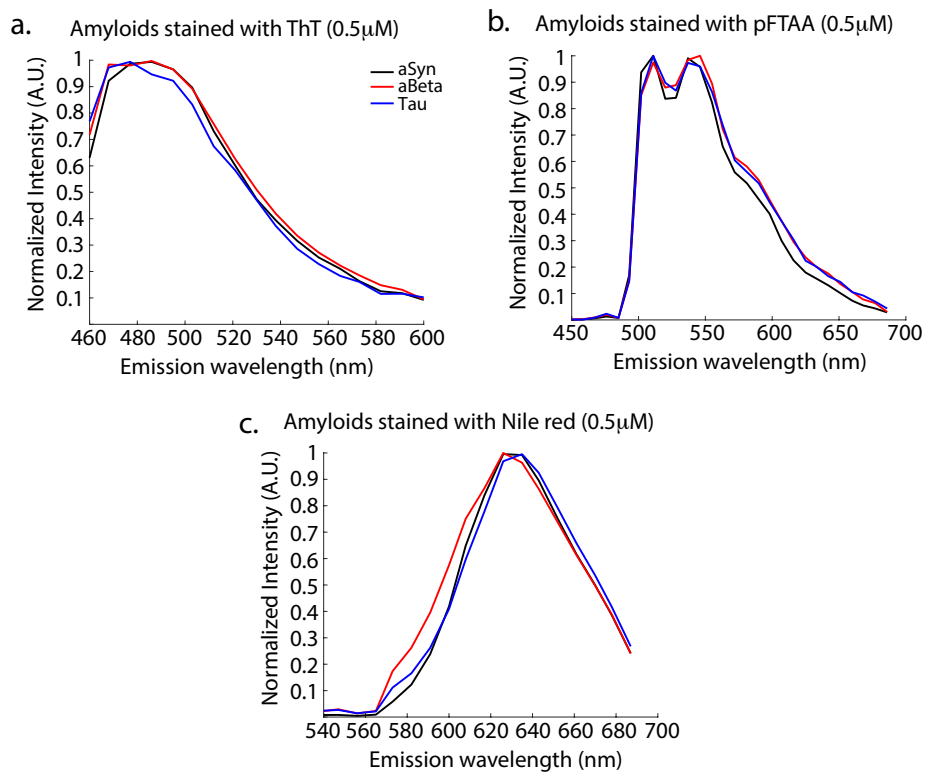


Figure 10.4: Different amyloids stained with dyes. Bulk emission spectra of (a) ThT, (b) pFTAA, (c) Nile red staining of alpha-synuclein (black), amyloid-beta (red) and neurofibrillary tangles – Tau (blue). The lack of difference in emission spectra prevents the differentiation of amyloids.

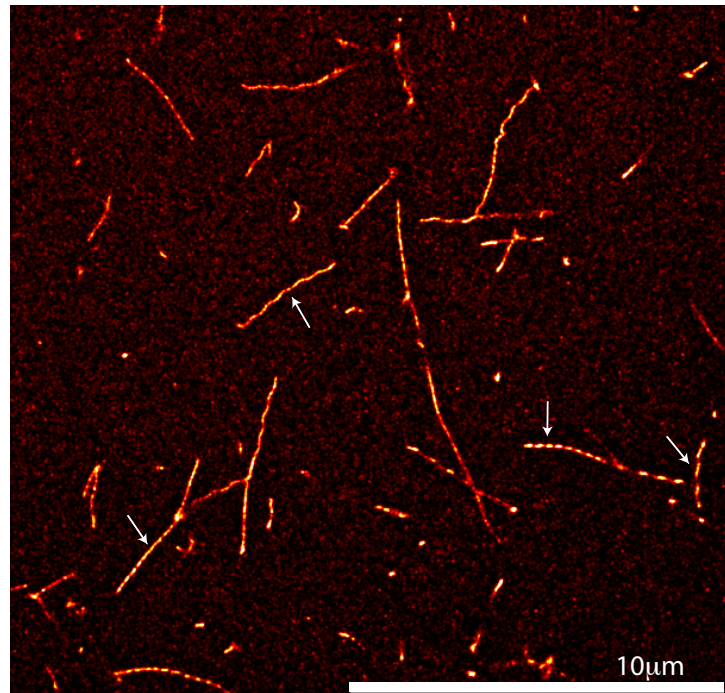


Figure 10.5: Reconstructed image showing fibrils with different morphology. The white arrows pointed to fibrils with wavy and straight morphology. There are also fibrils with periodic punctate localization decorations.

10.3 Differentiating different alpha-synuclein polymorphs

Having characterized and optimized conditions for PAINTing alpha-synuclein using pFTAA, I then assessed pFTAA's capacity of differentiating different alpha-synuclein fibril polymorphs. The reconstructed superresolved image shown in Fig. 10.5 showed fibrils with different localization decoration patterns (pointed to by white arrows). To quantitatively differentiate polymorphs, I assessed the optical signature of each localization, namely, emission spectrum, polarization and localization distribution on individual fibrils.

10.3.1 Localizations emission spectrum

Different protofilament arrangement within amyloid fibril polymorphs result in different interfaces which are accessible to amyloid binding dyes. The fluorescence emission spectra of each pFTAA dye molecule is reliant on the number of thiophene aromatic rings that have been planarized upon binding to the fibril (Yuan et al., 2015). Bulk measurements (Fig. 10.4b) reflect the average fluorescence emission spectra of all dye molecules that are bound. This masks the ability of assessing the specific contribution of each dye molecule's fluorescence emission spectrum with respect to its binding environment. In this aspect, PAINT is well suited as it collects fluorescent signal from each single dye binding event.

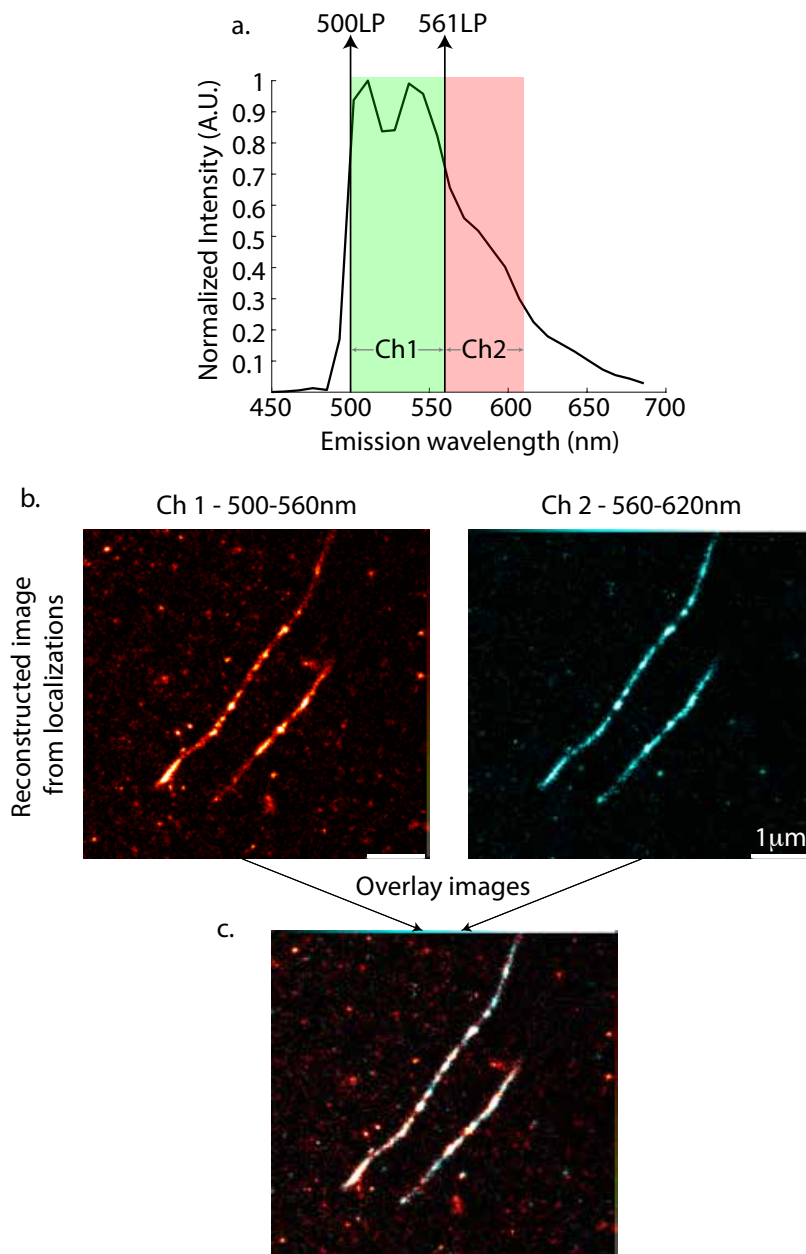


Figure 10.6: Reconstructions of localizations from two channels recording from different segments of pFTAA emission spectrum. (a) A 500 long pass (LP) ensures that only emissions above 500 nm are transmitted. A 561LP dichroic mirror splits the emission such that 500 - 560 nm is collected in channel 1 and 560 - 620 nm are collected in channel 2. (b) Reconstruction of localization collected in the respective channels. (c) A merge of images collected from both channels. Localizations from both channels are randomly distributed along the fibril.

To measure the differences in fluorescence emission spectra of individual dye molecules in the same ROI, we adapted our microscope to assign specific emission spectrum windows onto 2 respective channels. Based on the fluorescence emission spectrum in Fig. 10.6a, we recorded localizations within 500 nm to 620 nm. By placing a 560 nm long pass dichroic mirror in the optical path, we were able to reflect signal recorded from 500–560 nm onto one channel (Fig. 10.6b) and the transmitted

signal from 560–620 nm onto a second channel (Fig. 10.6b).

We were able visualize the fibril in both channels individually. When the reconstructions were overlaid (Fig. 10.6d), we observed random decoration of localizations over the fibril length from both channels. We did not observe spatial preference for signal collected from individual channels.

10.3.2 Localizations distribution and polarization

Shaban, H. et al., (2017) demonstrated the ability to describe the ultra-structure of insulin amyloid fibrils by analysing the polarization of individual fluorophores. Amyloid binding dyes bind to the fibril's beta sheet structure with their dipole moment oriented along the length of the fibril (Krebs et al., 2005). To measure the polarization of each localization I adapted the microscope setup with the addition of a polarization beam splitter along the emission beam path (Fig. 10.7a). The emission signal was then separated into two orthogonal polarization directions which were then recorded in two different channels or cameras. The polarization, P , of each localization is calculated by the ratio of measured intensity difference between each channel and the sum of intensities from both channels. Reconstruction of localizations recorded in each channel yielded images of the same field of view that were significantly different. I observed that fibrils reconstructed in each channel had a preferred orientation. Fibrils orientated longitudinally to the surface were predominantly in one channel (Fig. 10.7b) and fibrils orientated laterally to the surface were in the other channel (Fig. 10.7c). Fibrils oriented diagonally with respect to the surface were observed in both channels. This indicated a very strong dipole registration along the length of the fibril as localizations with opposing polarizations are dim and are therefore not detected. When the two channels were overlaid, we observed that within a single fibril there were periodic segments that had different polarization values (Fig. 10.7d).

Next, I then assessed if the distribution of localizations over the length of the fibril could be a potential descriptor of fibril ultra-structure. Localizations were binned into 10 nm bins and the median of each bin was calculated. I observed that the calculated median of the bins deviated away from the central axis of the fibril in a sinusoidal pattern (Fig. 10.8a). I will call this line profile, 'deviation line profile' from here on. To identify the presence of a predominant periodicity, an autocorrelation analysis was performed on the sinusoidal line profile. The periodicity of the line profile was determined by measuring the displacement of the first peak after the 0 peak (Fig. 10.8b).

Performing the same analysis on the localization's calculated polarization values, I observed a sinusoidal line profile with respect to the fibril's central axis (Fig. 10.8c). An autocorrelation analysis was performed on the line profile obtained from the polarization values (Fig. 10.8d). For fibril polymorph 1 in

Fig. 10.8, I measured a periodicity of 232 nm for the deviation line profile and a periodicity of 250 nm for the polarization line profile. I also identified a fibril polymorph that had significantly different measures of periodicity for deviation (585 nm) and polarization (591 nm) compared to polymorph 1 (Fig. 10.8e-h). Both these fibrils are visibly and quantitatively different even though they were exposed to similar solution conditions (monomer concentration, salt and pH). I then analysed deviation and polarization periodicities of 254 fibrils recorded from three independent experiments. I observed periodicity distributions from 100–700 nm for both deviation and polarization with <2% of fibrils without clear periodicity (Fig. 10.9a-b). To check for any correlation between each fibrils deviation and polarization, I plotted a scatter plot of both parameters against each other (Fig. 10.9 c). There seem to be a cluster around 270–300nm, but no clear correlation (correlation coefficient: 0.24) was observed between the two parameters.

For all subsequent analysis, I used the periodicity obtained from the deviation and polarization of fibrils as a descriptors of fibrils.

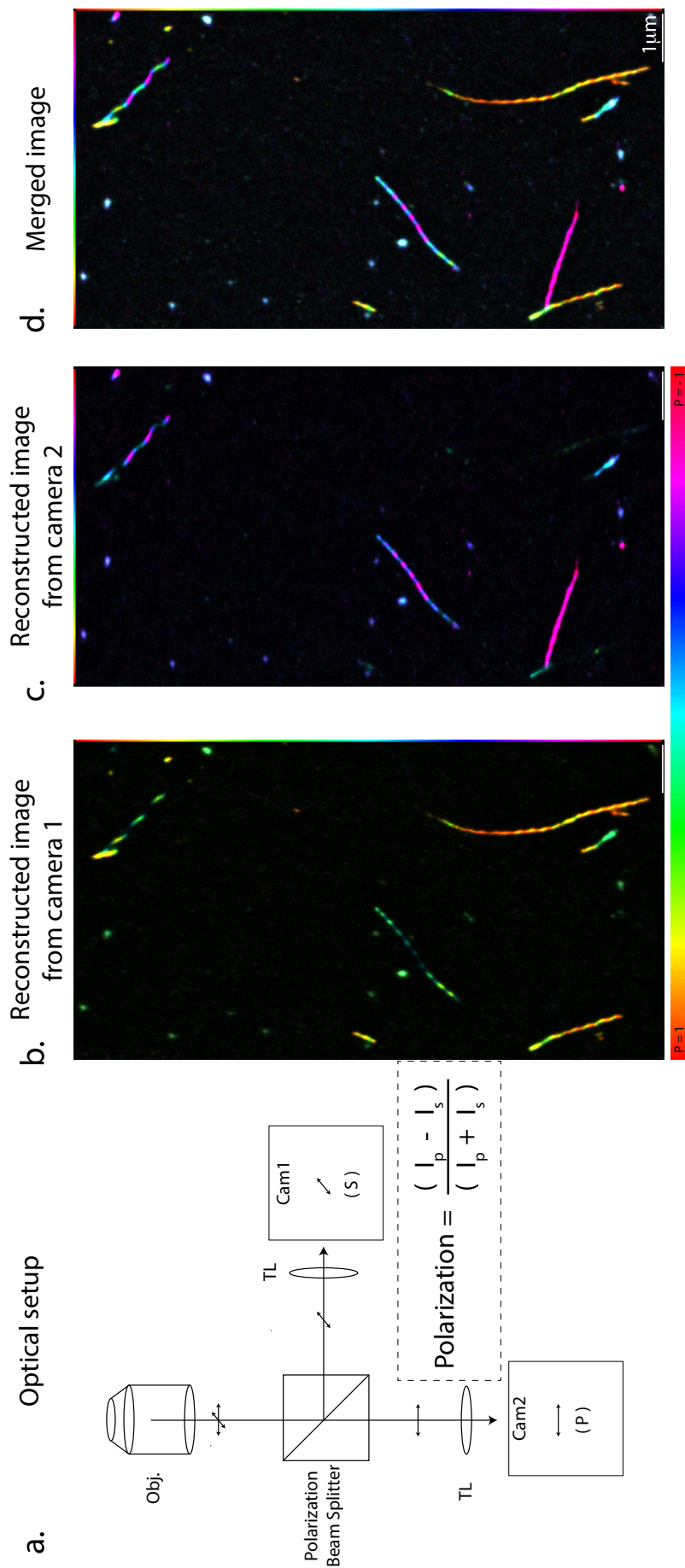


Figure 10.7: Fibrils exhibit periodic segments with different polarization readouts. (a) A simple illustration of the optical path with a polarization beam splitter put in place. Dotted line box (insert) containing the equation for calculating the polarization of localizations based on intensity difference in the two channels over the total intensity collected. (b) and (c) are reconstructions localizations recorded in individual channels. In (b), we see that the fibrils are oriented longitudinally and in (c), fibrils are oriented laterally. Fibrils which are orientated diagonally are captured in both channels. (d) Merged of (b) and (c). We observed that segments on fibrils contain polarization values which are of a different polarization value indicating different orientations of dye binding sites.

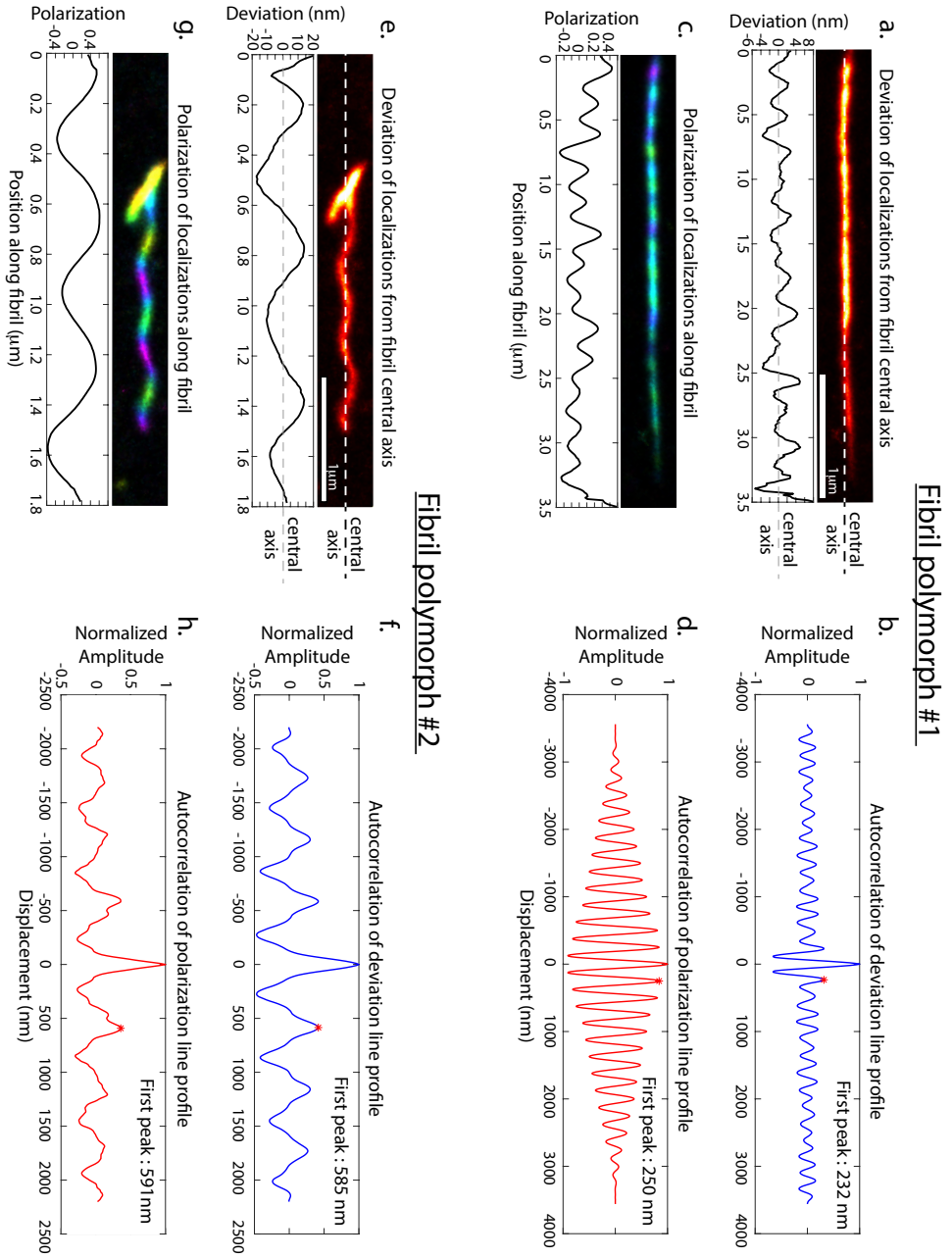


Figure 10.8: Characterization of fibril morphology based on periodicity of deviation and polarization (a) Fibril polymorph 1, top panel, SMILM reconstruction of a straightened fibril. Bottom panel, line profile indicating the deviation of localizations with respect to the central axis. (b) An autocorrelation analysis of the line profile from (a). The displacement of the first peak after the 0 peak was scored as the measure of periodicity. In this case 232 nm. (c) Top panel, the same fibril presented in (a) but with the localizations color coded according to their polarization value. Bottom panel, line profile of the measured polarization value along the length of the curve. (d) An autocorrelation analysis of the line profile from (c), indicating a periodicity value of 250 nm. (e-h) Fibril polymorph 2, the layout of figures are the same as fibril polymorph 1. Fibril polymorph 2 is qualitatively and quantitatively different from fibril polymorph 1. The analysis pipeline was designed by both Yu-Le Wu, a PhD student in our lab and myself.

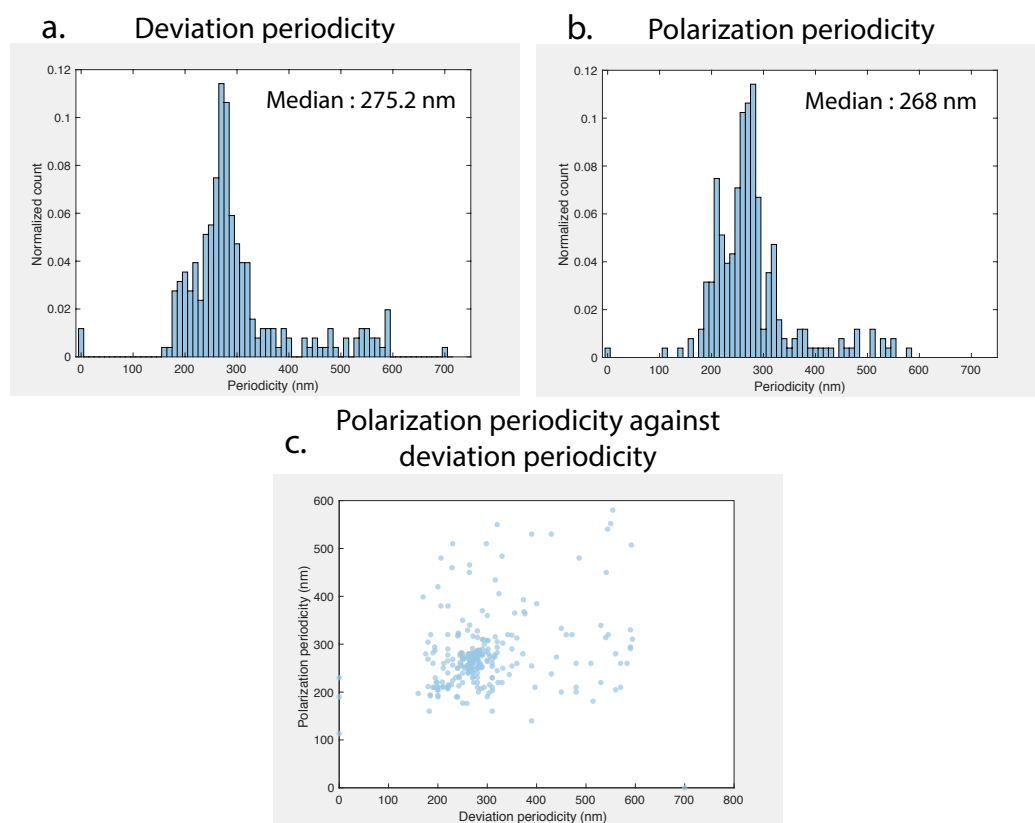


Figure 10.9: Distribution of fibrils deviation and polarization periodicities. Fibrils elongated in 200 μM monomer with 18.5 mM MgCl_2 . (a) Histogram distribution of measured deviation periodicities. (b) Histogram distribution of measured polarization periodicities. (c) Scatter plot of polarization periodicity against deviation periodicity. $N = 254$ fibrils from 3 independent experiments.

10.4 Visualizing the self-assembly of alpha-synuclein fibrils

The self-assembly of fibrils from a monomer solution to fibrils takes a long period of time (hours to days). The self-assembly process is usually accelerated by modulating self-assembly conditions such as: monomer concentration, ionic strength of buffer, pH, increased temperature, agitation and the addition of seeds (Buell et al., 2014). Seeds are small fragments of preformed fibrils obtained by sonicating longer fibrils. By supplementing seeds to the self-assembly assay, the process of self-assembly bypasses the initial lag phase and proceeds onto the exponential phase of templating and elongation of seed fragments. To measure the self-assembly process of fibrils I adapted the self-assembly assay described in Wördehoff et al., (2015).

Seeds adsorbed on a coverslip were incubated in the presence of monomers and pFTAA (Fig. 10.10). To perform PAINT measurements, nano-molar concentrations of pFTAA were used to obtain spatially separated single molecule dye binding events. As the monomers template and extend the fibril, new binding sites on the cross-beta-sheet structure of the fibril are formed for dye molecules to bind. It is then be possible to reconstruct the self-assembly process by looking at the time when the localizations appear along the fibril.

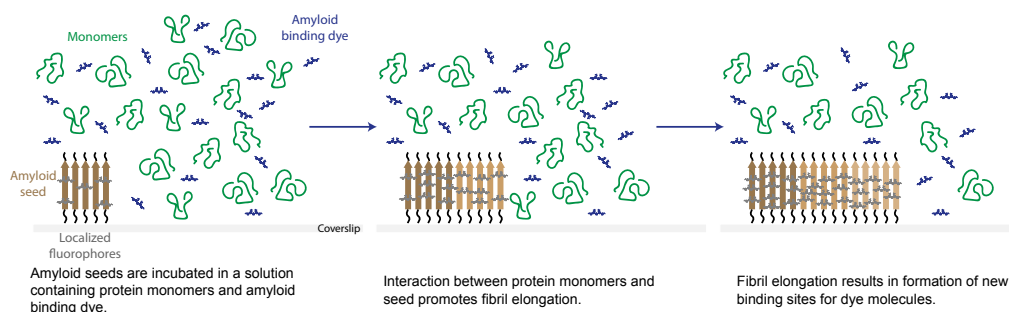


Figure 10.10: Cartoon of the self-assembly assay. Amyloid seeds adsorbed to the coverslip are incubated with a solution containing monomers and dye molecules. Decoration of the seed fraction by dye molecules are recorded. As the assay progresses, monomers in solution are templated onto the seed fragment to elongate the fibril. Elongation of the fibril results in the creation of new binding sites for dye molecules to bind. Reconstruction of the localizations according to the time they were recorded enable visualization of fibril elongation.

Under PAINT imaging conditions, constant illumination with 488 nm excitation resulted in phototoxicity. I observed elongation only in regions outside of the illuminated region (Fig. 10.11a-b). The observed phototoxicity was alleviated by the use of lower excitation intensities, addition of pyranose oxidase catalase (POXC) + glucose (an oxygen scavenger system) and ascorbic acid (a reducing agent) (Fig. 10.11c - f). The final composition of the protein monomer solution that was added to the seeds consists of:

- 200 μM of alpha-synuclein monomers in 20 mM MES pH 6
- 15 μg POXC
- 2% (w/v) glucose
- 18.5 mM MgCl_2
- 7.5 mM Ascorbic acid
- 2 nM pFTAA

With the optimized protein monomer solution and acquisition parameters, I was able to measure the self-assembly of fibrils across the whole field of view (Fig. 10.12). This enabled 12 hours of recording with approximately 100 fibrils per field of view for statistical analysis.

Figure 10.13a depicts reconstructions of a fibril at defined timepoints of the self-assembly assay. The localizations are color-coded according to the time when they were recorded during the self-assembly assay. Localizations are represented using the 'jet' lookup table, that means early localizations are color-coded as blue and later localizations are color-coded as red. It is clear that the fibril elongates as the assay progresses. A kymograph was generated to analyse the dynamics of fibril elongation. All the localizations along the length of the fibril were plotted according to when it appeared during the self-assembly assay (Fig. 10.13b). From the kymograph I observe that fibril elongation is not continuous. It elongates in an intermittent manner with periods of no growth. To quantify these elongation characteristics, the boundary of the fibril growing end is segmented (Fig. 10.14 light green line). A running window average is applied to smooth the boundary (Fig. 10.14 white line). Periods of no growth is demarcated as stop steps (Fig. 10.14a). The growth rate of the fibrils are calculated from the gradient of the kymograph boundary (Fig. 10.14a).

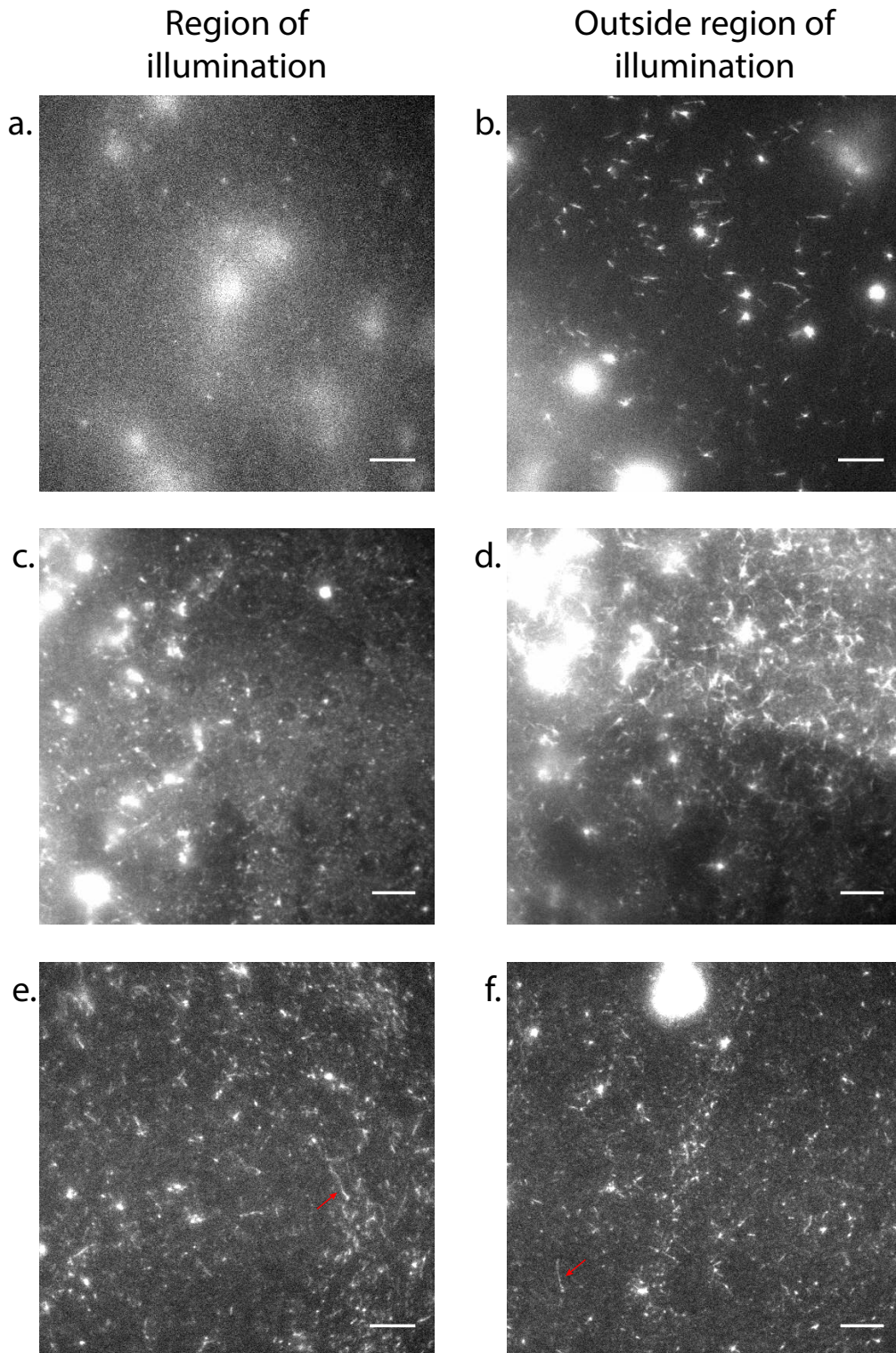


Figure 10.11: Alleviating phototoxicity with oxygen scavenger system and ascorbic acid. (a) Illumination under PAINTE imaging conditions with pFTAA (2 nM) resulted in no fibril elongation within the illuminated region. (b) Fibril elongation was not affected outside of the illuminated region. (c) The addition of an oxygen scavenger system (POXC + glucose) helped alleviate the phototoxicity. (d) Outside the illuminated region fibril elongation was longer. (e & d) Fibril elongation was found to be the same in both illuminated and non-illuminated regions when ascorbic acid was added together with the POXC oxygen scavenger system. Scale bars are 10 μm .

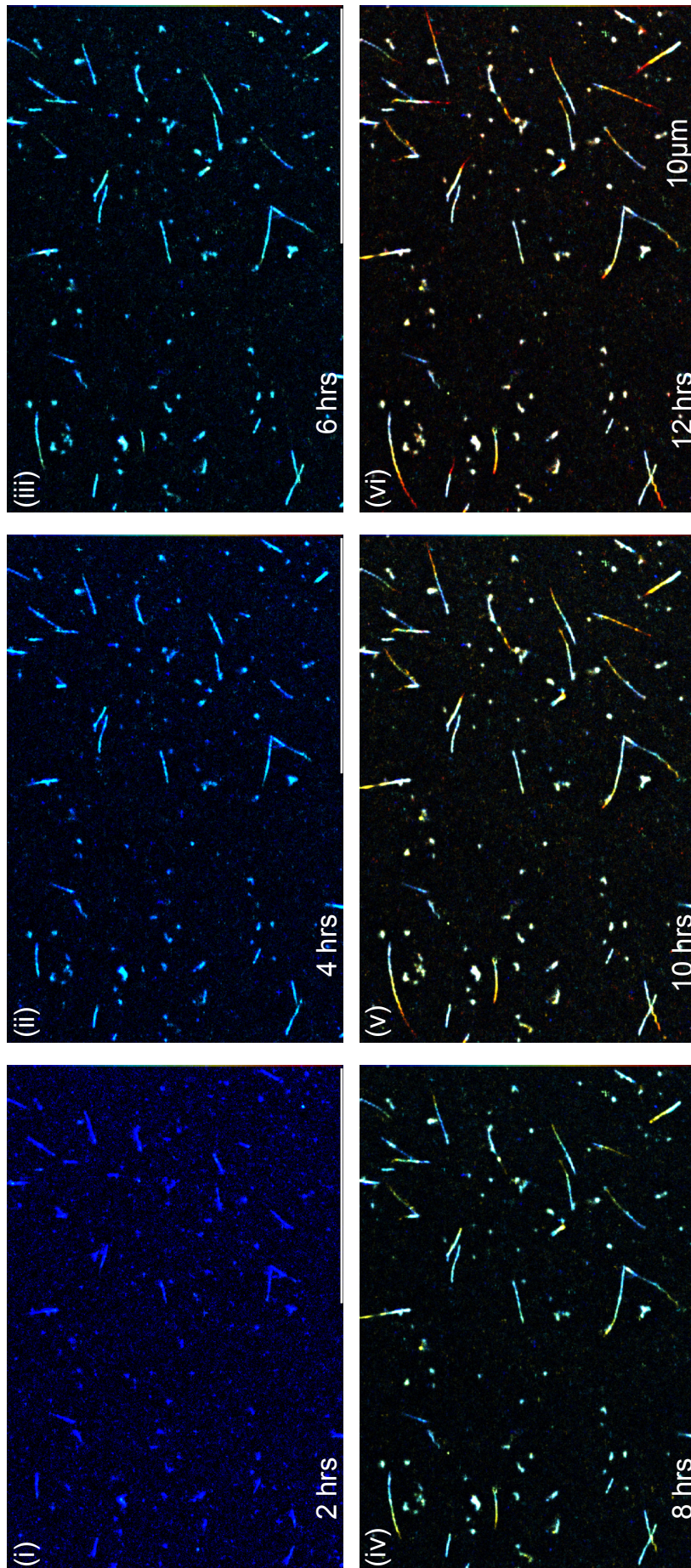


Figure 10.12: Reconstruction of the field of view at specific timepoints of the self-assembly assay. An image montage of localizations that accumulated until the indicated time point (2 hour intervals). The localizations are color coded using the jet lookup table. Early localizations are colored blue and localizations appearing later are colored red. From each field of view a minimum of 60 fibrils could be segmented and analyzed increasing statistically power.

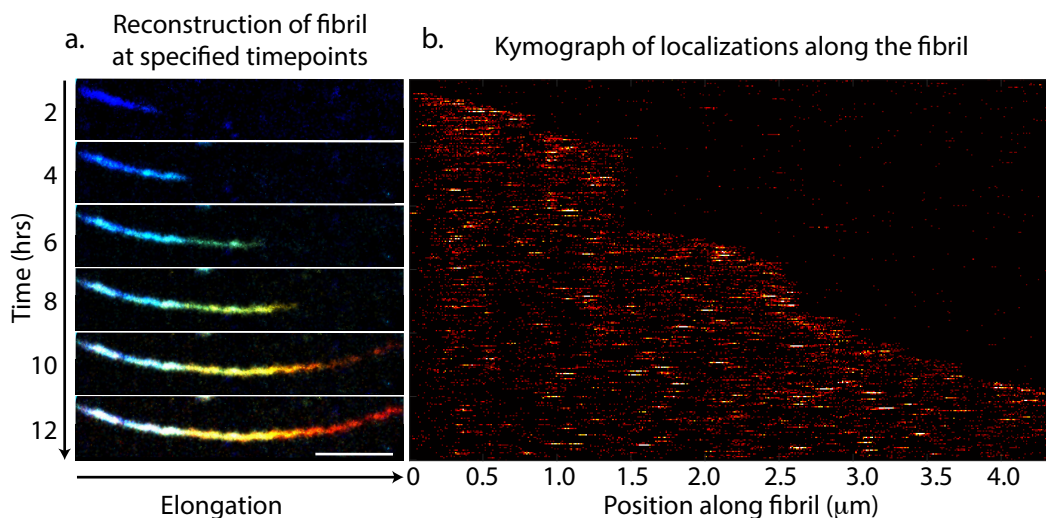


Figure 10.13: Kymographs help visualize fibril elongation characteristics. (a) Reconstruction of a segmented fibril at set timepoints of the self-assembly assay. The localizations are color-coded using the 'jet' lookup table. Early localizations are colored blue and later localizations were colored red. (b) A kymograph can be generated by plotting all the localizations on the fibril according to the time at which they were recorded. Fibrils are observed to exhibit an intermittent growth characteristic with stop and growth phases. Scale bar is 1 μm .

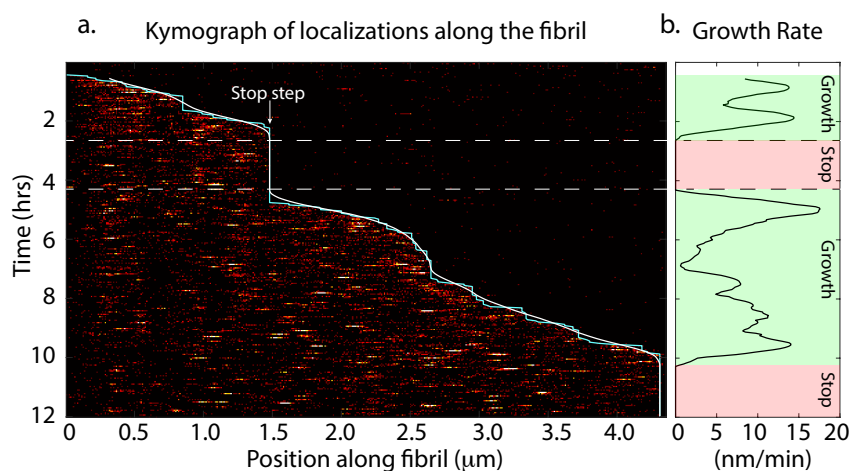


Figure 10.14: Analysis of the kymograph. (a) A rough boundary is first drawn to find the growing end of the fibril (light green). A smooth factor is applied on the rough boundary to result in a new smoothed boundary (white). Periods of no growth were demarcated as stop steps. (b) The growth rate of the fibril was obtained from the gradient of the fibril boundary. The analysis pipeline was designed by both Yu-Le Wu, a PhD student in our lab and myself.

10.5 Measuring the self-assembly under different conditions

With the ability to characterize self-assembly characteristics of fibrils with respect to their morphology, I then investigated the effects of changing solution conditions on fibril morphology and self-assembly. The parameters I scored were:

- Total length of fibrils (panel a. in Fig. 10.15, 10.16, 10.17)
- Total average growth rate (panel b. in Fig. 10.15, 10.16, 10.17)
- Periodicity of deviations (panel c. in Fig. 10.15, 10.16, 10.17)
- Periodicity of polarization (panel d. in Fig. 10.15, 10.16, 10.17)
- Number of growth steps per fibril (panel e. in Fig. 10.15, 10.16, 10.17)
- Growth rate per step (panel f. in Fig. 10.15, 10.16, 10.17)
- Length of growth steps (panel g. in Fig. 10.15, 10.16, 10.17)
- Duration of stop steps (panel h. in Fig. 10.15, 10.16, 10.17)

I measured these parameters over two conditions:

- In the presence or absence of salt (18.5 mM MgCl₂ and 1 mM EDTA) (Fig. 10.15)
- Increased monomer concentration (200 μ M and 400 μ M) (Fig. 10.16)

We observed that fibrils elongated in the absence of salt were 25% longer than fibrils grown in the presence of salt (Fig. 10.15a). This increase was reflected in a higher overall growth rate (4.1 nm/min compared to 2.1 nm/min) (all reported measures are median values) and growth step rate (4.9 nm/min compared to 2.8 nm/min) recorded for fibrils elongated in the absence of salt. Interestingly, both conditions had similar number of growth steps. However, the two conditions differed in the length of each growth step and duration of stop steps. In the absence of salt, fibrils had 29.7% shorter stop times and 17.0% longer growth steps. Fibrils grown in the absence of salt also presented with shorter period length for both deviation and polarization.

I then performed the self-assembly assay with a higher amount of monomers to see if the fibrils could achieve faster growth rates as compared to fibrils grown in the absence of salt. When the concentration of monomers was doubled (200 μ M to 400 μ M) (Fig. 10.16), we observed an overall increase of 9.7% in the final total length of fibrils in the presence of higher concentration of monomers. This increase in length was a result of a higher growth rate per step (3.2 nm/min). There was very little difference in average growth rate, number of growth steps, length of growth steps or durations of stop steps between the two conditions. Interestingly, fibrils

grown in 400 μM of monomers presented slightly longer period length for deviation and shorter period length for polarization.

I next compared growth characteristics of fibrils grown in the absence of salt and fibrils grown with a monomer concentration of 400 μM (Fig. 10.17). I observed that fibrils grown in the absence of salt were 15.6% longer. Fibrils grown in 400 μM monomer conditions had slower average growth rates, growth rate per step, length of growth step and they had a longer duration of stops even though there were more monomers present. The deviation and polarization period length presented by fibrils grown in 400 μM was larger for both deviation and polarization when compared to fibrils grown in the absence of salt. This hinted that fibrils grown in the presence and absence of salt were fundamentally different. I decided to investigate if there were any relationships between the different fibril descriptor parameters I scored.

From the deviation periodicity histograms, the distribution of fibrils grown in the absence of salt seemed to be more left shifted (dark orange) compared to fibrils grown in the presence of salt (blue). Therefore, I plotted a scatter plot of the autocorrelation amplitude of the deviation line curves against the measured deviation periodicity (Fig. 10.18a). I observed a similar spread of data points for both conditions, however, there seems to be a trend towards fibrils grown in the presence of salt having higher autocorrelation amplitude values (indicating stronger deviation) compared to fibrils grown in the absence of salt. A similar trend was observed for a scatter plot between amplitude and polarization.

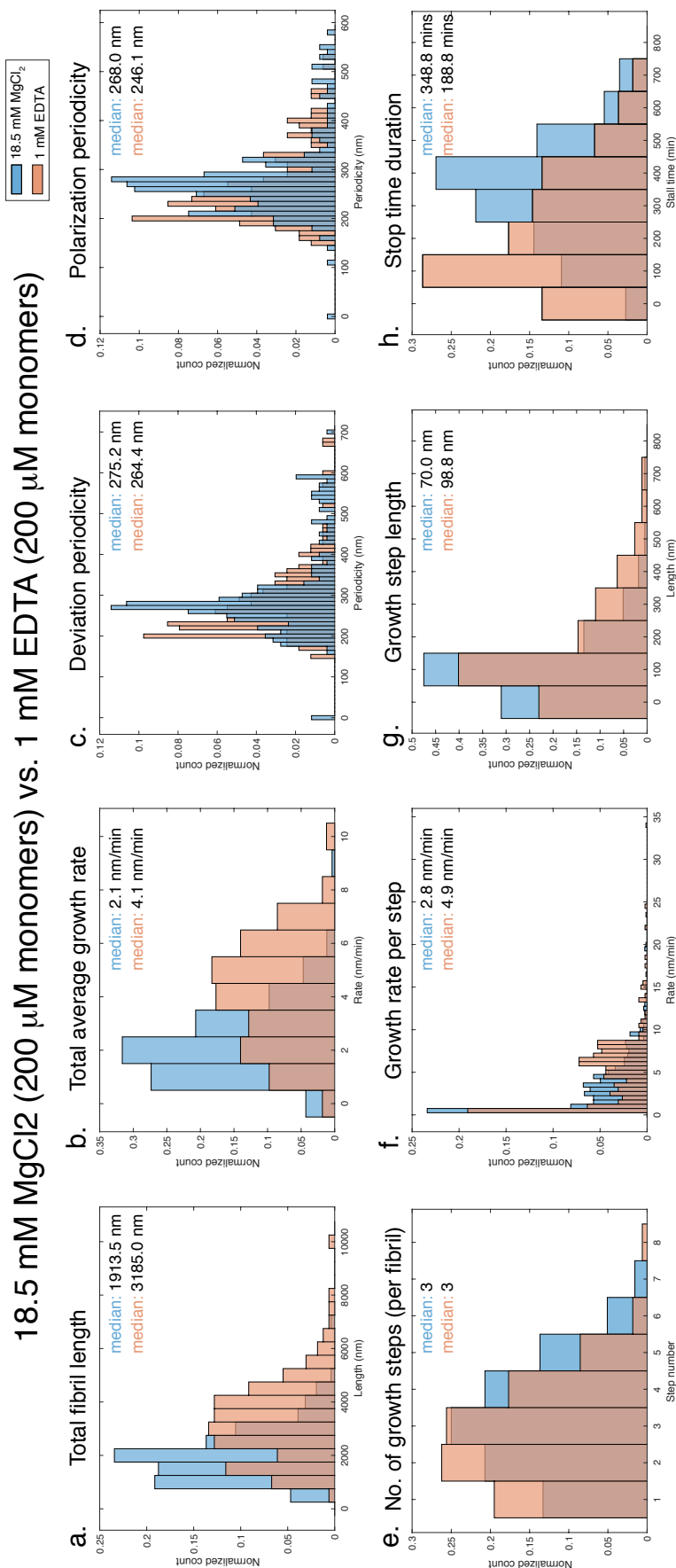


Figure 10.15: Growth characteristics of fibrils in the presence and absence of salt taken from both, kymograph and fibril characterization. Histogram plots of parameters scored from both conditions. (a) Total fibril lengths measured at the end of the assay (b) The average growth rate over the entire duration of the assay. (c) Deviation periodicity of fibrils. (d) Polarization periodicity of fibrils. (e) Number of growth steps per fibril. (f) Growth rate per growth step of fibrils. (g) Length of growth steps. (h) Duration of stop steps. (N = 18.5 mM MgCl₂: 827 steps / 254 fibrils and 1 mM EDTA: 493 steps / 164 fibrils)

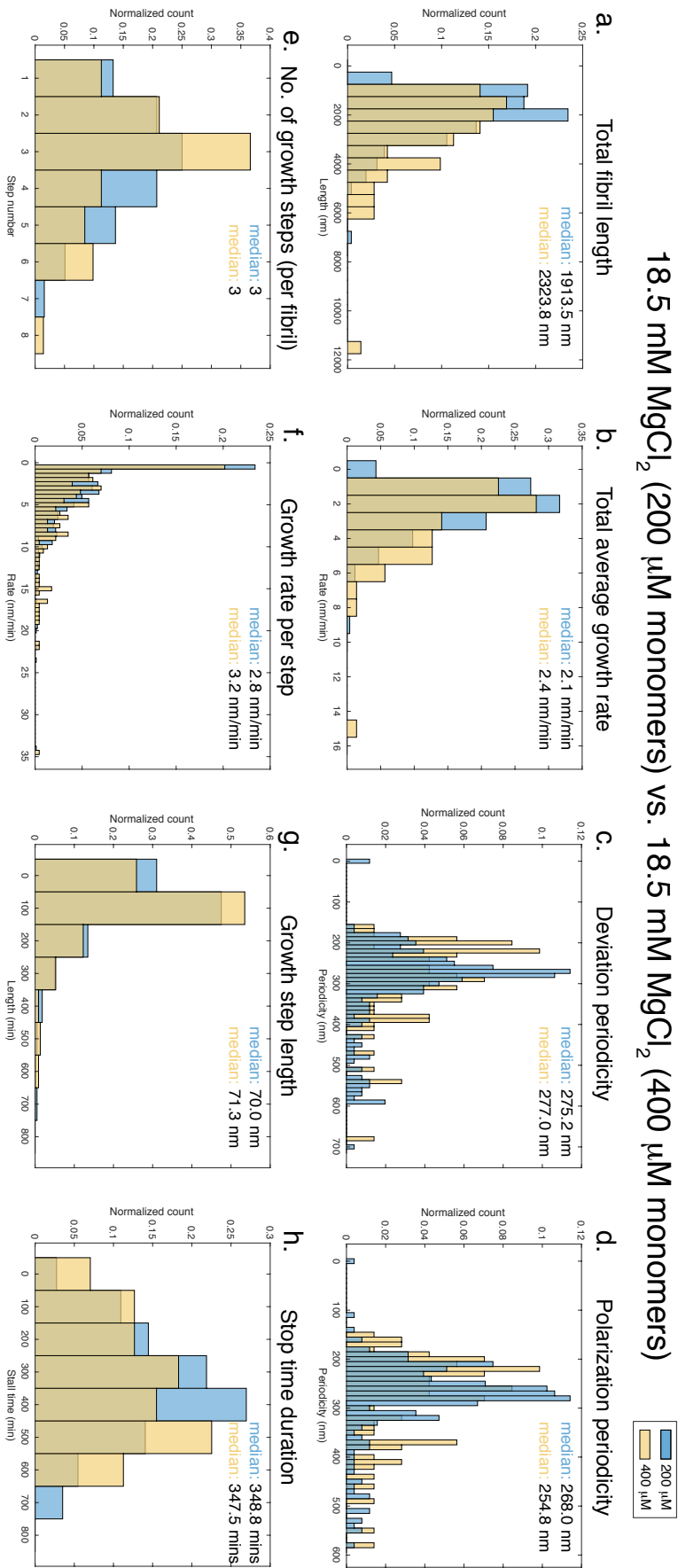
18.5 mM MgCl₂ (200 μ M monomers) vs. 18.5 mM MgCl₂ (400 μ M monomers)

Figure 10.16: Growth characteristics of fibrils in different monomer concentrations, kymograph and fibril characterization. Histogram plots of parameters scored from both conditions. (a) Total fibril lengths measured at the end of the assay (b) The average growth rate over the entire duration of the assay. (c) Deviation periodicity of fibrils. (d) Polarization periodicity of fibrils. (e) Number of growth steps per fibril. (f) Growth rate per growth step of fibrils. (g) Length of growth steps. (h) Duration of stop steps. (N = 200 μ M: 827 steps/254 fibrils and 400 μ M: 236 steps/71 fibrils)

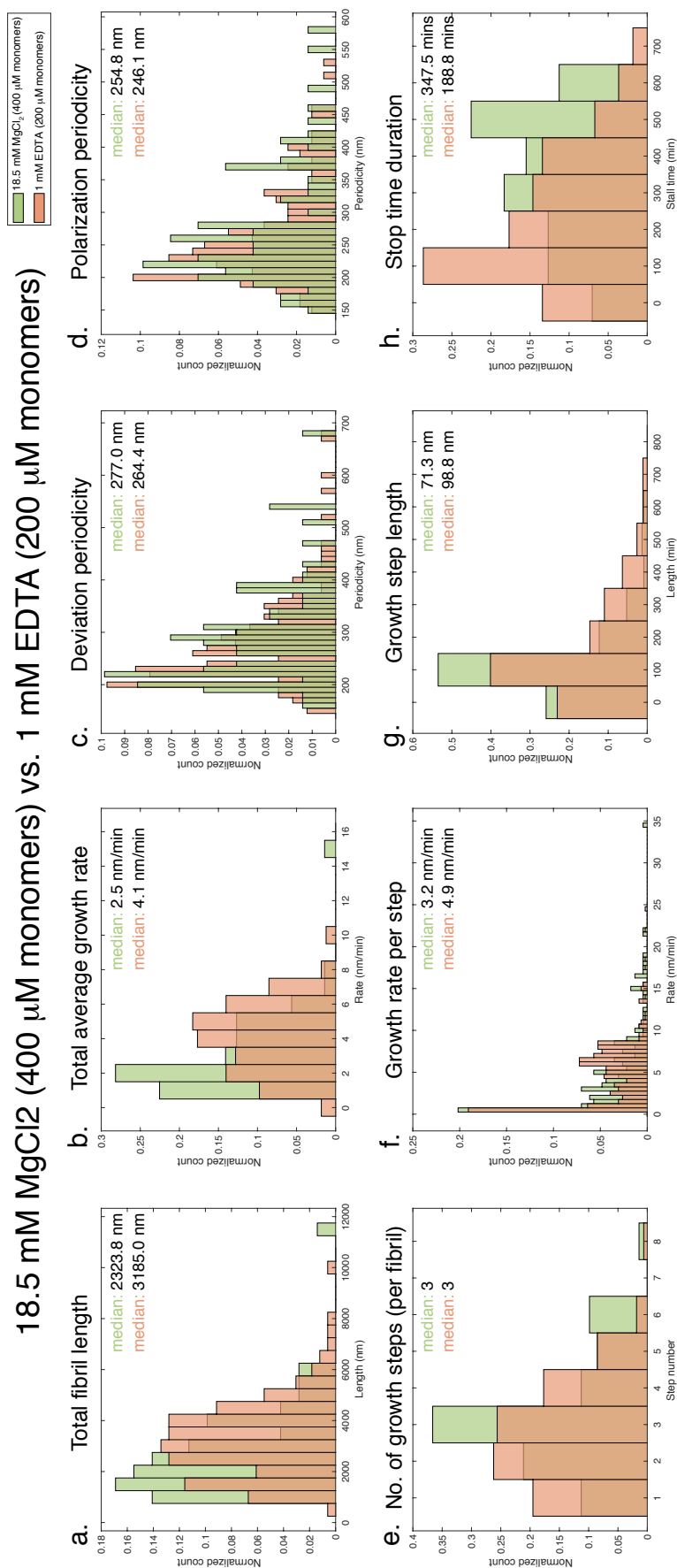


Figure 10.17: Growth characteristics of fibrils in 400 μ M monomer compared to no salt conditions, kymograph and fibril characterization. Histogram plots of parameters scored from both conditions. (a) Total fibril lengths measured at the end of the assay (b) The average growth rate over the entire duration of the assay. (c) Deviation periodicity of fibrils. (d) Polarization periodicity of fibrils. (e) Number of growth steps per fibril. (f) Growth rate per growth step of fibrils. (g) Length of growth steps. (h) Duration of stop steps. (N = 400 μ M: 236 steps/71 fibrils and 1 mM EDTA: 493 steps/164 fibrils)

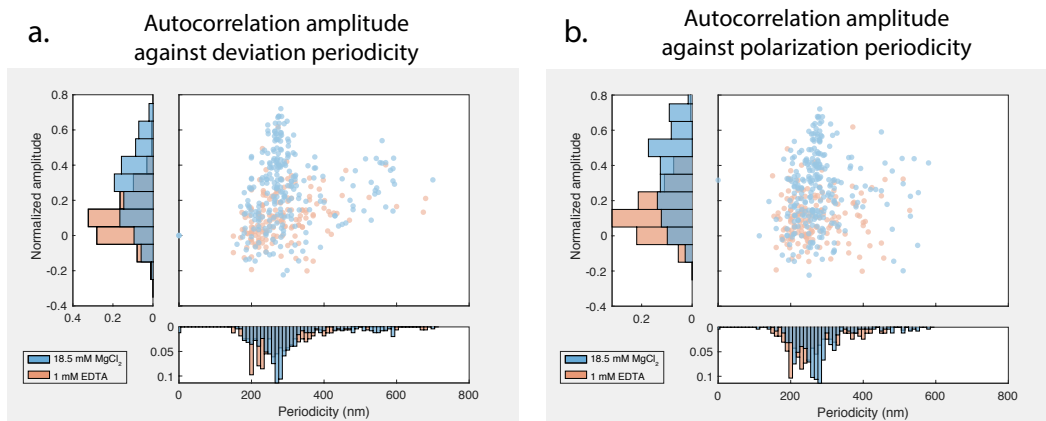


Figure 10.18: Scatter plot of autocorrelation amplitude of deviation and polarization against its respective periodicity. (a) Amplitude of first peak in the correlogram for deviation against its periodicity. (b) Amplitude of first peak in the correlogram for polarization against its periodicity. The amplitude of fibrils grown in the presence of salt are higher compared to in the absence of salt indicating a stronger periodicity persistency throughout the length of the fibril. (N = 18.5 mM MgCl₂: 254 fibrils and 1 mM EDTA: 164 fibrils)

10.6 Measuring the self-assembly with a solution change midway

To investigate if the different growth characteristics were due to different seed polymorphs or solution conditions, I adapted the self-assembly assay to incorporate a change of protein solution at the midpoint of the self-assembly assay. This would allow me to measure individual fibril growth kinetics of the same fibril in both solution conditions. As depicted in Fig. 10.19, self-assembly of the fibrils were first recorded with 200 μM monomers with 18.5 mM MgCl_2 for 10 hrs. After which, the protein solution was removed from the imaging chamber and rinsed three times with 20 mM MES pH 6. After rinsing, fresh 200 μM monomers with 1 mM EDTA was added and the second round of acquisition was started for 10 hours.

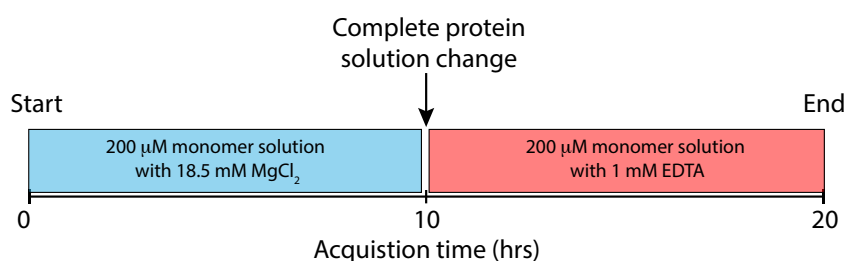


Figure 10.19: Schematic of experimental workflow for change of buffer experiments. The self-assembly assay was set up as before. For the first 10 hours seeds were exposed to monomer solution containing 18.5 mM MgCl_2 . Once the acquisition was completed, the buffer was changed carefully to ensure that the field of view was moved as little as possible. The chamber was rinsed three times with 20 mM MES pH 6. After that, fresh monomer solution containing 1 mM EDTA was added to the chamber and localizations were recorded for another 10 hours.

I then analysed the data by splitting the dataset into two parts, first part: in the presence of salt and the second part: in the absence of salt (Fig. 10.20). The median total fibril length recorded was 2103 nm. Most of the growth was recorded during the first part of the acquisition with an average growth rate of 2.31 nm/min in the first part and almost no growth (0.35 nm/min) in the second part of the acquisition. The lack of growth during the second part of the acquisition is consistent with a lower number of steps, lower growth step rate, shorter length of growth step and longer stop durations scored. Due to the lack of growth it was not possible to score the periodicity of deviation and polarization from the second part of the acquisition.

Fibril elongation assay with a change in solution conditions

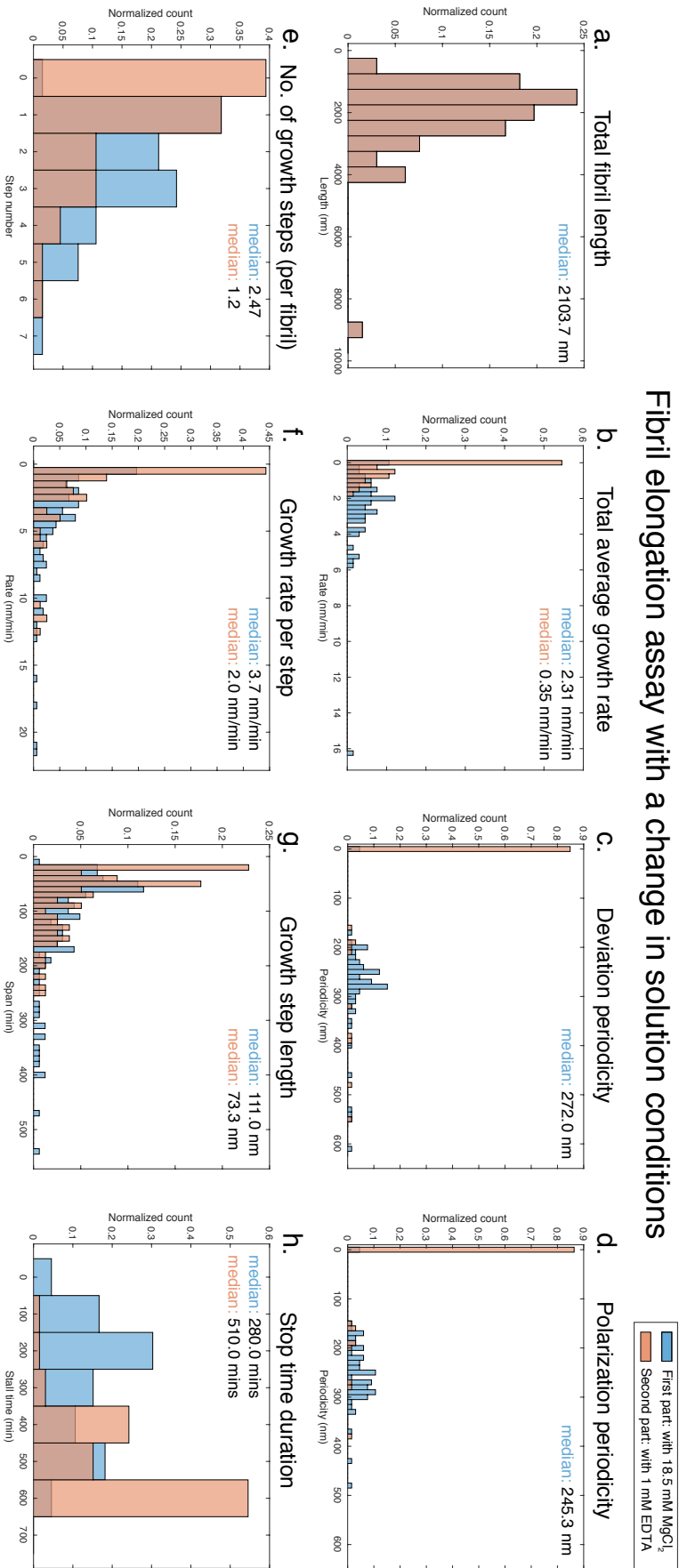


Figure 10.20: Growth characteristics of fibrils when the solution condition is changed. Kymograph and fibril characterization. Histogram plots of parameters scored from both conditions. (a) Total fibril lengths measured at the end of the assay (b) The average growth rate over the entire duration of the assay. (c) Deviation periodicity of fibrils. (d) Polarization periodicity of fibrils. (e) Number of growth steps per fibril. (f) Growth rate per growth step of fibrils. (g) Length of growth step. (h) Duration of stop steps. (N = First part(18.5 mM MgCl₂): 147 steps/65 fibrils and second part(1 mM EDTA): 93 steps/65 fibrils)

10.7 Correlative SMLM/EM of amyloid fibril self-assembly assay

The fibrils I have measured presented periodicities of approximately 260–270 nm for both deviation and polarization. To gain insight of the fibril's ground truth morphology, I performed EM on fibrils that were grown on glass coverslips under the standard self-assembly assay conditions. At the endpoint of the assay, the fibrils were resin embedded (Fig. 10.21a,b). The first 150 nm of the resin was sectioned and imaged under TEM.

Figure 10.21c shows electron micrographs of fibrils grown in the presence of salt. Fibrils of different morphology (straight and wavy fibrils) were clearly visible. Figure 10.21d shows electron micrographs of fibrils grown in the absence of salt. In the absence of salt, fibril morphologies appeared more homogeneous and they did not present with large wavy phenotype. Qualitative inspection of multiple fibril electron micrographs showed that the fibrils that elongated in the presence or absence of salt were morphologically different.

I then extended the self-assembly assay to perform correlative SMLM/EM. The self-assembly assay was performed on 50 μm gridded coverslips. After PAINT imaging the fibrils were resin embedded and sectioned for TEM imaging. Under TEM we were able to find back the fibrils that were imaged using SMLM (Fig. 10.22a). With the ability to perform correlative SMLM/EM on the self-assembly assay, I am now able to report on the self-assembly characteristics (Fig. 10.22b), ultra-structure of fibril based on polarization (Fig. 10.22c), and to provide the structural ground truth of the fibrils with EM. This is preliminary data and therefore extensive analysis has not been done. However, a quick analysis on one of the fibrils qualitatively shows the morphology of a fibril with a measured periodicity of 265 nm.

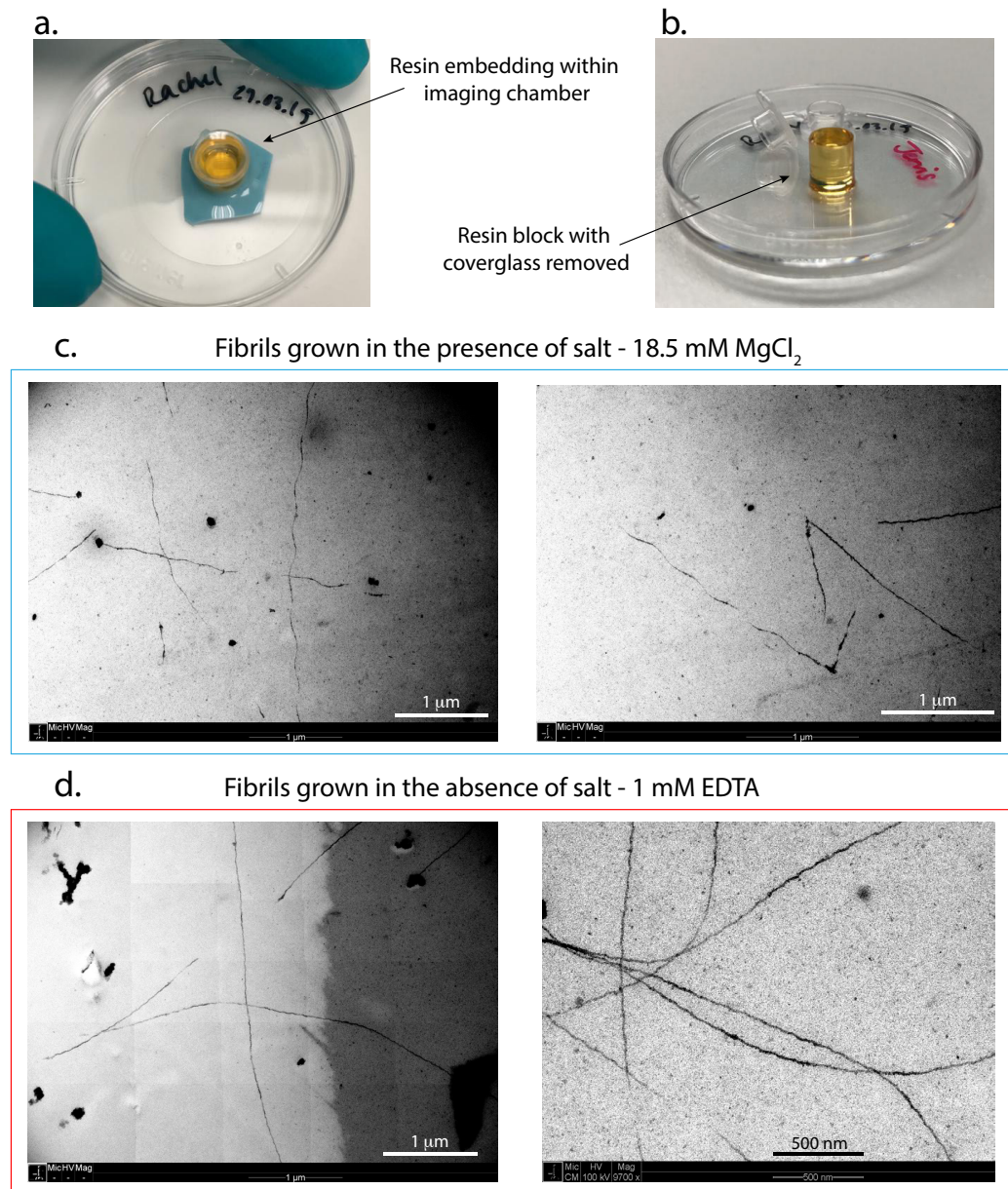


Figure 10.21: Resin embedding and TEM imaging of fibrils grown in the presence and absence of salt. (a) Resin embedding within the imaging chamber. (b) Resin block removed from imaging chamber and coverglass. (c) Electron micrographs of fibrils grown in the presence of 18.5 mM MgCl_2 . The fibrils exhibit a wavy morphology. (d) Electron micrographs of fibrils grown in the presence of 1 mM EDTA (absence of salt). The fibrils exhibit a wavy morphology. The resin embedding, sectioning was performed and TEM data was collected together with Rachel Mellwig from the EMCF at EMBL.

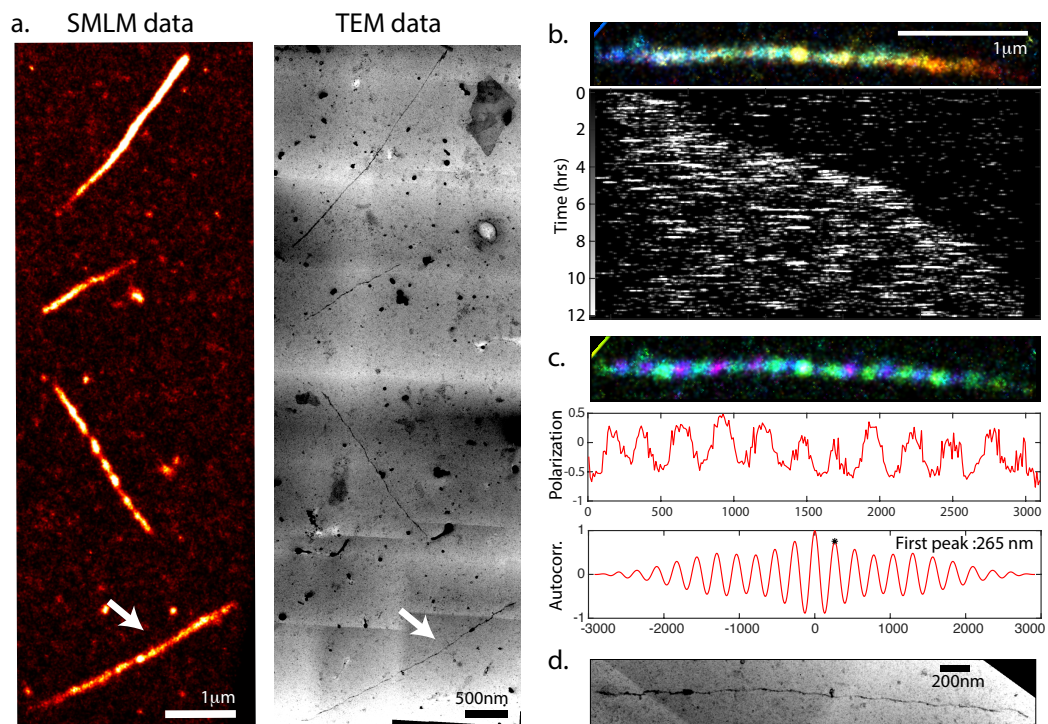


Figure 10.22: Correlative SMLM/EM of fibril self-assembly assay. (a) Reconstructed field of view of fibrils imaged under SMLM (left panel) and the same field of view in TEM (right panel). White arrow points to the fibril depicted in (b), (c) and (d). (b) Top panel, localization on the fibril color-coded temporally. Bottom panel, fibril's respective kymograph showing fibril growth characteristics. (c) Top panel, localization on the fibril color-coded according to polarization. Middle panel, polarization line profile of the fibril. Bottom panel, correlogram of the polarization line. First indicated by a black asterisks, 265 nm. (d) A zoomed in electron micrograph of the fibril. The resin embedding, sectioning was performed and TEM data was collected together with Rachel Mellwig from the EMCF at EMBL.

11 | Discussion

In the second part of my thesis, I extended the domain of SMLM in structural imaging by establishing a fibril self-assembly assay that enables structural characterization and reporting of assembly dynamics. The sensitivity of this assay allows for direct observation of effects of perturbations at the level of individual fibrils. Finally, I showed that this assay is adaptable for correlative study using single-molecule localization and electron microscopy.

11.1 Visualizing and differentiating individual fibril polymorphs

My first aim in this project was to visualize single alpha-synuclein fibrils with the purpose of differentiating them according to their ultra-structure. To this end, I used the PAINT imaging method with pFTAA to visualize individual amyloid fibrils (Ries et al., 2013). pFTAA staining was amyloid specific and produced a high number of photons per binding event. This allowed for dense fibril labeling with a high localization precision (20 nm) (Fig. 10.3). Reconstructions of fibrils after PAINT imaging (Fig. 10.5), showed fibrils with different localization decoration patterns. To characterize these fibrils, I assessed the optical signature of each localization, namely, emission spectrum, polarization, localization density and decoration on individual fibrils.

11.1.1 Differentiating fibrils

Emission spectrum. pFTAA has been described to exhibit changes in emission spectrum when bound to different amyloids (Klingstedt et al., 2011; Klingstedt et al., 2013b; Klingstedt et al., 2013a; Nilsson et al., 2012). The exact binding mechanism of pFTAA has not been characterized. Molecular simulations indicate that planarization of its conjugate oligothiophene backbone results in a red shifted emission spectrum when bound in a conformationally restricting pocket (Sjöqvist et al., 2014). The degree of change in the emission spectrum is dependent on the number of oligothiophene rings that have been planarized (Yuan et al., 2015). This

presented itself as an opportunity to distinguish different fibril polymorphs based on differences in emission spectra. I tested pFTAA's capability to distinguish fibrils based on bulk staining and single molecule binding events to report on differences in nano-environment along the fibril.

In my hands, I did not observe changes in the bulk emission spectrum profile of pFTAA bound to different amyloids (Fig. 10.4). Spectral separation of single molecule binding events also did not provide additional insights on differences within the fibril structure (Fig. 10.6). To ensure that my experimental methods were correct I contacted the corresponding author of Klingstedt et al. (2011), Professor Peter R. Nilsson. He replied,

"The emission differences that we see for p-FTAA is from A-beta and tau aggregates are in human AD tissue samples. We have also tried staining of recombinant A-beta and tau fibrils with p-FTAA and, similar as your observations, we do not see any spectral differences between these recombinant species. Thus, we can only observe spectral differences in human AD sections."

Thus it seems that the spectral shifts that were reported were due to specific amyloid interactions with molecules (lipids or other proteins) within the tissue sections and not observable with purified protein *in vitro*.

Polarization. Another measure of the dye's nano-environment would be the polarization of each binding event. It would provide information on the orientation of the dye's dipole moment which can be translated as a readout for the direction of the binding site. This characteristic was used by Shaban et al., (2017) to visualize the ultra-structure of insulin fibrils using ThT. Analyzing the polarization of pFTAA localizations, I found that similar to ThT, pFTAA binds to the fibril with its dipole moment oriented along the long axis of the fibril (Fig. 10.7). ThT binds to the channels formed by the side chains of the amino acid residues that form the cross-beta-sheet structure (Fig. 9.7) (Biancalana and Koide, 2010).

More interestingly, I found that defined segments along the length of the fibril had different polarization values in a repetitive manner. This meant that the orientation of the binding sites were different and indicated the presence of structural differences along the fibril. This alternating difference in orientation of binding sites could be due to the helical twist present along the core beta-sheet backbone or be a result of overall twisted morphology of the fibrils (Fig. 10.8 e,g) (Guerrero-Ferreira et al., 2018; Li et al., 2018a). An autocorrelation analysis was performed on the polarization line profiles to measure the periodicity (Fig. 10.8 c,d). Analyzing 254 fibrils, I observed a distribution of periodicities (from 100—600 nm) with a median of 268 nm (Fig. 10.9 b).

Localization distribution. The distribution of localizations along the length of the fibril also followed a sinusoidal pattern similar to the polarization line profiles (Fig. 10.8 a,b). The deviation line profile from 254 fibrils had a distribution of periodicities (100–700 nm) with a median of 275 nm (Fig. 10.9 a). There is a slight difference in the periodicity observed for polarization compared to deviation. However, it is not clear if this difference is due to an underlying structural feature or errors introduced from measurements. I also did not observe any relationship between polarization periodicity and deviation periodicity, except for that the data points showed some clustering (Fig. 10.9c). Therefore, the fibrils present in my assay exhibit a periodicity of ~270 nm.

Structural characterization of WT alpha-synuclein from cryo-EM measurements has reported a helical twist of approximately 92 nm (Li et al., 2018a) and 120 nm (Li et al., 2018b). One particular alpha-synuclein fibril polymorphs has been shown to present periodicity of 42 nm (Li et al., 2018a). These measurements are very far from the periodicity measurements I have recorded in my assay and I hardly measure fibrils with periodicities below 150 nm. However, in a AFM study that looked at the morphology of WT alpha-synuclein fibrils documented fibrils that possessed periodicities of up to 310 nm (Sidhu et al., 2017). Therefore, the periodicities I observe could be a polymorph conformation that is kinetically favored in the current buffer condition. Due to alpha-synuclein's disordered nature, solution conditions are important in determining the final fibril morphology (Bousset et al., 2013; Hoyer et al., 2002; Makky et al., 2016). Another factor to be considered is surface effects on fibril morphology. The fibrils measured have been grown on a glass coverslip and the periodicities could arise due to interaction with the glass surface. This can be addressed by adapting my current growth assay to have the fibrils grown on a lipid bilayer with different lipid compositions.

Structural information was required to understand if the periodicity of 270 nm was due to the helical twist of the core beta-sheet backbone or due to an overall twisted/wavy morphology of the fibril. Therefore, I resin embedded the fibrils grown in my self-assembly assay and performed TEM imaging on resin sections with the fibrils. From the preliminary data I have obtained (Fig. 10.21, 10.22), it looks like the periodicity stemmed from an overall twisted/wavy morphology of the fibrils. It was also very clear that there was a large distribution in the degree of twist/wavy morphology exhibited by the fibrils. This explains the large distribution of periodicities of deviation and polarization that was measured (Fig. 10.9). Unfortunately, the quality of data did not allow for visualization of helical twist of the core beta-sheet backbone. Strikingly, fibrils that were grown in solution without any salt looked more homogeneous in distribution of morphology (Fig. 10.21).

11.2 Visualizing the self-assembly of alpha-synuclein fibril

My third aim of the project was to visualize the self-assembly process. I adapted the elongation assay from Wördehoff et al., (2015). A substantial amount of time and effort was spent troubleshooting and optimizing to find conditions that allowed for SMLM recording of fibril elongation.

11.2.1 Identifying ideal conditions for fibril elongation

Photo-inhibition. Under PAINT imaging conditions of constant laser illumination, I observed photo-inhibition effects within the field that was illuminated (Fig. 10.11 a,b). One source of photo-inhibition is from the presence of molecular oxygen in the imaging buffer. The rationale being that reactive oxygen species (ROS) attack on the amyloid backbone disrupts fibril elongation. Dye molecules that have been excited from their ground state to their excited state are able to enter a triplet-excited state by inter system crossing. Dye molecules in the triplet-excited state are readily oxidized by oxygen to return to the ground state, however, this creates ROS which induces photo-inhibition effects (Linde et al., 2011). Another source of ROS would be the from the 488 nm excitation. Molecular oxygen has been described to have absorption maxima at 477, 577, 630, 760, 919, 1063 and 1264 nm (Gudkov et al., 2012). The lower limit absorption maximum of 477 nm is very close to our 488 nm laser excitation. Therefore, in many single molecule imaging studies oxygen scavenger systems are utilized to sequester oxygen (Aitken et al., 2008; Harada et al., 1990; Swoboda et al., 2012). With the addition of an oxygen scavenger system, I observed an improvement, however, the fibrils in the illuminated region were shorter compared to regions outside the illuminated region (Fig. 10.11 b,c). Ozawa et al., (2009) have described the destruction of amyloid fibrils with laser beam irradiation. They showed that with 455 nm excitation wavelength, beta2-microglobulin amyloid fibrils could be destroyed by free radicals produced from the bleaching of ThT and this is exacerbated with dissolved oxygen. To retard the photobleaching of pFTAA, I added ascorbic acid, a reducing agent to the protein solution (Widengren et al., 2007). With the addition of ascorbic acid, fibril elongation within the illuminated ROI was similar to the rest of the coverslip (Fig. 10.11 c,d).

Protein solution purity. Using a protocol that was provided by our collaborators, I observed batch to batch variations in my fibril elongation assays. The protocol was adapted from Huang et al., (2005) where the authors originally used periplasmic extraction and ion-exchange chromatography (IEX) to obtain purified alpha-synuclein (80 mg). The protocol obtained from our collaborators included an additional hydrophobic interaction chromatography (HIC) step after IEX. This was required as the fractions containing alpha-synuclein after IEX also contained

contaminant proteins (Fig. 10.1 a,b, lane 1). However, I observed that alpha-synuclein did not bind to the HIC column but was mostly present in the flow through (FT). The alpha-synuclein fractions that were obtained from gradient elution had the presence of a contaminant protein and it was very little in amount (4 mg). By changing the HIC column from RESOURCE PHE, 1 mL to a HiTrap Phenyl FF, 5 mL, alpha-synuclein fractions in the FT were found to be pure and of considerable amount (40 mg) (Fig. 10.1). Both columns have the same phenyl hydrophobic ligand. A possible explanation could be that the contaminant proteins bind to 6% crosslinked agarose matrix (HiTrap Phenyl FF) better than the polystyrene/divinylbenzene matrix (RESOURCE PHE). Alternatively, it could also be that the 5 mL column presented more surface area contaminant proteins to interact and to bind. To distinguish these hypotheses, further investigation is required.

11.2.2 Fibril elongation consists of intermittent stop and growth phases

Fibril elongation characteristics. After much optimization, I found conditions compatible with visualizing single fibril elongation. Figure 10.12 is a time lapsed reconstruction of a cropped field of view capturing the elongation of multiple fibrils. This enables data analysis from hundreds of fibrils. Previous studies have described fibril elongation to be unidirectional and bidirectional from seed fragments (Pinotsi et al., 2014; Young et al., 2017). In my assay, fibrils predominantly grew from one end, although in some cases, bidirectional growth was observed. Unfortunately, since there is the probability that seeds could be present in clumps, I am not able to report on proportions of fibrils that report unidirectional or bidirectional growth. I also do not observe fibril branching, a growth characteristic that has been described for other amyloid proteins during fibril elongation (Andersen et al., 2009). Based on the EM images obtained from resin embedded fibrils grown in my assay, I am confident that the elongations recorded are from individual fibrils and not from bundled or laterally associated fibrils. It was also evident that some fibril elongation proceeds from clumps of seeds. The surface of the fibril in the EM images was often decorated with blobs that stained with the heavy metal stain. These blobs could be fibril surface catalyzed oligomers (Gaspar et al., 2017) or non-specific dirt from the heavy metal staining.

To analyze the growth characteristics of each fibril, kymographs were generated by plotting all the localization along the fibril according to the time at which they were recorded (Fig. 10.13). From the kymograph, I observed that fibrils exhibited intermittent stop and growth phases (Fig. 10.14). This growth characteristic has been reported for alpha-synuclein (Hoyer et al., 2004; Wördehoff et al., 2015) and other amyloidogenic proteins such as A-beta (Ban and Goto, 2006; Kellermayer et al., 2008; Young et al., 2017), glucagon (Feringhoff-Borg et al., 2010) and beta2-microglobulin (Ban et al., 2003). These stop and growth phases have been proposed to arise from

two distinct kinetic processes, 'dock' and 'lock'. When a monomer of kinetically favored conformation approaches the growing end of the fibril, it is able to 'dock' and 'lock' onto the fibril end to allow for the addition of the next monomer thus elongating the fibril (growth phase). However, when a monomer of the wrong conformation is bound to the growing end of the fibril, it first needs to reconfigure to the conformation of the fibril end and 'lock' in place before the next monomer can be incorporated. Hence, fibril elongation is disrupted until the monomer is locked in place (stop phase). These stop and growth phases have also been described to be caused by surface interaction, especially in the case of mica surface (Kellermayer et al., 2008). Although present, these surface interaction are weaker on quartz surfaces (Ban and Goto, 2006). It would be interesting to investigate if these observed stop and growth phases were to coincide with structural features such as deviation or polarization periodicities.

11.3 Fibril elongation characteristics in different solution conditions

From the kymograph, I scored the growth rates of the fibrils from the gradient of the boundary demarcating the growing end. In addition to growth rates, information on the number of growth and stop steps and their corresponding rates, length and duration were extracted. I first compared fibril elongation characteristics in different buffer conditions, namely, in the presence of salt (18.5 mM MgCl₂) and in the absence of salt (1 mM EDTA) (Fig. 10.15). We observed very different elongation characteristics. Overall, fibrils that were grown in the absence of salt were much longer compared to fibrils grown in the presence of salt. The average growth rate was close to double for fibrils grown in the absence of salt (4.1 nm/min) compared to fibrils grown in the presence of salt (2.1 nm/min) (Fig. 10.15 b). Previous studies on alpha-synuclein elongation, report growth rates ranging from 1–8.5 nm/min (Table 11.1). It is difficult to make a meaningful comparison with these studies as they were all performed in different solution conditions (Buell et al., 2014; Pinotsi et al., 2014), have differences in protein purification resulting in different conformations being enriched or a small sample size (Wördehoff et al., 2015). Nevertheless, the rates reported in this study are within the range of growth rates that have been reported by others (Table 11.1). From my analysis of growth rates, fibrils grown in the absence of salt exhibit shorter stop durations, longer growth steps and faster growth rates per step compared to fibrils grown in the presence of salt (Fig. 10.15 f,g,h). Interestingly, a study by Buell et al., (2013) using methods that probe protein aggregation using bulk solution and surface methods showed that increasing salt concentration resulting in an increase in fibril elongation. In their study, bovine insulin and PI3K-SH3 amyloids were used, and so the overall charge and the effect of salt on these amyloids would be different. In another study done by the same

Table 11.1: Summary of reported WT alpha-synuclein fibril growth rates

Study	Buffer	Monomer concentration	Type of assay	Growth rate
Buell et al., 2014	PBS pH 7.4 at 37 °C	20 μ M	Ensemble	1.0 nm/min
Pinotsi et al., 2014	20 mM PB pH 6.5	80 μ M	Single fibril (53)	1.0 nm/min
Wördehoff et al., 2015	20 mM MES pH 6, 10 mM MgCl ₂	160 μ M	Single fibril (25)	8.5 nm/min
This work	20 mM MES pH 5.5, 18.5 mM MgCl ₂	200 μ M	Single fibril (254)	2.1 nm/min
This work	20 mM MES pH 5.5, 1 mM EDTA	200 μ M	Single fibril (164)	4.1 nm/min

All experiments carried out at room temperature unless explicitly stated. Numbers within brackets indicate the number of fibrils analyzed.

group of authors, but on alpha-synuclein, showed that addition of salt showed faster aggregation rates using ThT fluorescence as a readout. However, they showed that the increase came from the formation of higher order aggregation structures into the solution that stained for ThT as well (Buell et al., 2014). Therefore the increased fibril elongation rates which I observed could be due to solution conditions being unfavorable for higher order structures, thereby allowing more monomers to be available for fibril elongation.

To investigate if the fibrils grown in the presence of salt could reach growth rates observed in no salt conditions, I doubled the concentration of monomers from 200 μ M to 400 μ M while keeping salt concentrations constant (Fig. 10.16). I did not observe a significant increase in growth rate with increased monomer concentration. In fact the average growth was similar, the fibrils in 400 μ M had a faster growth rate per growth step (3.2 nm/min) (Fig. 10.16 b) but they were still slower than the growth step rates of fibrils grown in the absence of salt (4.9 nm/min; Fig. 10.17 b). This indicates that the growth rates of fibrils grown in the presence of salt were in the upper limits of fibril growth rates due to saturated monomer concentration, highlighting that the fibrils grown in the presence of salt were different from the fibrils grown in the absence of salt. To identify if there were difference in the structural descriptors I looked at the autocorrelation amplitude with respect to the deviation and polarization periodicities of the fibrils grown in both conditions (Fig. 10.18). The scatter plots for both deviation and polarization periodicities against autocorrelation amplitude showed similar distributions. There was a trend towards fibrils grown in the presence of salt possessing a higher autocorrelation amplitude compared to fibrils grown in the absence. Indicating that the periodicities observed in fibrils grown in the presence of salt were more persistent throughout the length of the fibril. This was confirmed in the EM images of resin embedded fibrils grown in the two different conditions. Fibrils grown in the absence of salt were significantly less wavy and fibril morphologies were more homogeneous.

11.4 Fibril elongation is dependent on solution conditions

The difference in fibril growth characteristics in the two solution conditions could arise due to the presence of distinct populations of seed fragments which elongate only in favorable solution conditions or it could be a result of different monomer conformations due to different buffer conditions. This could be addressed by observing how individual fibril growth characteristics change when solution conditions are changed midway of a self-assembly assay. To the best of my knowledge, existing fibril elongation assays and studies have not been able to study fibril elongation characteristics in such a manner. I adapted my self-assembly assay to incorporate a wash and a complete change of protein solution. I performed a pilot experiment where for the first 10 hours fibril elongation was recorded in the presence of monomer solution containing salt, after which the solution was changed and fibril elongation of the same fibrils were acquired for an additional 10 hours (Fig. 10.19). From this experiment, I was able to score fibril elongations from 65 fibrils (Fig. 10.20). For the first 10 hours, the average fibril growth rate (2.3 nm/min) was similar to what I had been observed previously. The fibrils recorded shorter stop durations (280 mins) and faster growth step rates (3.7 nm/min) compared to what had been observed before, thus they had longer total fibril lengths (2.1 μm). These differences could be due to a smaller sample size. However, more interestingly, the same fibrils did not elongate in the second half of the acquisition when the solution condition was changed. The average growth rate decreased to 0.35 nm/min, most of the fibrils simply stopped growing completely, as evident in the number of growth steps and stop durations recorded (Fig. 10.20 e,h).

The stop in growth could be explained by the fibrils being damaged by the change of the buffer, although this is highly unlikely, as there were still some fibril elongation recorded in the field of view. Nevertheless, the control experiment with a change solution step with both parts of the experiment having the same solution condition has to be done. However, if this preliminary data holds true, it hints towards the existence of two or more distinct populations of seed polymorphs that would only elongate if solution conditions are favorable. If there were two different seed populations, I should have seen new fibrils appearing and elongating in the second part of my elongation assay, when the buffer was changed. However, this was not predominantly observed (I observed one fibril). This could be due to the seeds being damaged by dye binding and then subsequently bleaching and destroying the backbone in the first 10 hours of acquisition when it was not able to elongate. This can be easily tested by performing the assay under the diffraction-limited TIRF with images taken every 10 minutes, instead of constant illumination to minimize photobleaching.

11.5 Correlative SMLM/EM for validation of structural features observed in SMLM

A major milestone in this project is the ability to now perform the self-assembly assay in a correlative manner with SMLM and TEM (Fig. 10.22). Although I am able to measure fibril descriptors such as deviation and polarization from my SMLM data, it is still not clear at which threshold to determine the declaration of one fibril as a distinct polymorph over another. In this regard, being able to relate measured structural descriptors to structural ground truth obtained from EM as a reference would be helpful in determining a meaningful threshold for my SMLM data. In addition, the measured periodicities in SMLM can be used to validate if resin embedding has effects on morphology of fibrils.

12 | Future outlook

I have achieved the three aims that were set out for this project. I have established a robust assay that allows for structural characterization and profiling of fibril growth dynamics. I have shown that within a defined solution condition, fibrils present a large variation of structural morphologies. The next step would be to perform additional correlative SMLM/EM assays to correlate the periodicities I measure with structural features observed in the electron micrographs. Curating a database of fibrils would then enable me to definitively determine thresholds to distinguish one polymorph to another.

The preliminary finding that fibril elongation was strictly dependent on solution conditions is very interesting and to my knowledge has not been reported before. However, the appropriate control experiment has to be done and different combinations and orders of solution conditions have to be tested. The large variation and inconsistencies in the amyloid field could be explained by the presence of distinct populations of fibril polymorphs that only respond to specific solution conditions. This stresses the need to analyze effects of perturbations at the level of individual fibrils polymorphs.

Finally, it would be beneficial to translate this imaging method, specifically the structural characterization of fibrils using SMLM, into a biological cell. To enable correlation of fibril morphology with subcellular localization and study effects on cellular physiology effected by distinct polymorphs.

13 | Material & Methods

13.1 Alpha-synuclein expression and purification

Alpha-synuclein expression was done together with the Protein expression and purification core (PEPCORE) facility at EMBL.

13.1.1 Alpha-Synuclein expression

Human wild-type (WT) alpha-synuclein was expressed in Escherichia coli BL21 DE3 cells using pRK172 plasmid. The plasmid was a kind gift from Prof. Roland Riek, ETH Zürich. Transformation of the plasmid into bacteria was done via the heat shock method. In brief, 50 μ L BL21(DE3) competent cells were thawed on ice for 30 mins. After which 1 μ L of DNA was added to the cells and mixed gently. The cells and DNA mixture was incubated on ice for 10 mins. A heat shock was then applied to the mixture by placing the tube in 42 °C for 45 secs and then immediately on ice for 2 mins. To facilitate recovery, 800 μ L of lysogeny broth (LB) medium is added to the tube and incubated at 37 °C in a thermomixer with constant agitation of 750 rpm for 30 mins. After incubation the transformed cells are plated onto LB agar plates supplemented with ampicillin. Depending on experimental scheduling the agar plates were either incubated at 37 °C overnight or at room temperature (RT) for 48 hrs.

For a one liter expression culture, a 100 ml LB with 100 μ L of 100 mg/mL carbenicillin was inoculated with 2 - 3 bacterial colonies and incubated at 37 °C under constant agitation of 180 - 200 rpm for 12-14 hrs overnight (use a 500 mL conical flask to ensure optimal aeration).

55 mL of the starter culture was then added to 1 L of LB with 1 mL of 100 mg/mL carbenicillin. An initial OD₆₀₀ measurement was noted. The 5 L flask was incubated in a 37 °C under constant agitation of 180 - 200 rpm. The OD₆₀₀ was measured periodically. Once the OD₆₀₀ reached between 0.6 - 0.8, 1 mL of 1 M Isopropyl beta-D-1-thiogalactopyranoside (IPTG) was added to induce protein production. The culture was incubated for another 4 hrs at 37°C.

Table 13.1: Buffers used for protein purification

Buffer	Composition
Osmotic shock buffer	30 mM Tris pH 7.4 40% sucrose 2 mM EDTA
MgCl ₂ buffer	3.3 mM MgCl ₂
Ion exchange chromatography (IEX) equilibration buffer	20 mM Tris pH 8.0
IEX elution buffer	20 mM Tris pH 8.0 1 M NaCl
2X sample buffer	50 mM Tris-HCl pH 7.5 1 mM EDTA 2% SDS 100 mM DTT 25% Glycerol 0.2 mg/ml Bromphenolblue
Hydrophobic interaction chromatography (HIC) elution buffer	50 mM Bis-Tris pH 7.0 1 M (NH ₄) ₂ SO ₄
HIC elution buffer	50 mM Bis-Tris pH 7.0
Size-exclusion chromatography (SEC) running buffer	20 mM MES pH 6.0

13.1.2 Periplasmic extraction

After 4 hrs of induction, the cells were centrifuged at 5000 rpm for 20 mins at RT. The supernatant was discarded. The bacterial cell pellet was resuspended by gentle pipetting in 100 mL of osmotic shock buffer and incubated at RT for 1 min. After incubation, the cell suspension was centrifuged at 10900 rpm (14000 g) for 20 mins at 4 °C. The supernatant was discarded. The bacterial cell pellet was resuspended by gentle pipetting in 90 mL of ice cold water saturated with 3.33 mM MgCl₂. The cell suspension was then centrifuged at 10900 rpm (14000 g) for 20 mins in 4 °C. The supernatant contained alpha-synuclein and was then filtered through a 0.45 μm filter and stored at 4 °C.

13.1.3 Ion-exchange chromatography (IEX)

Ion-exchange was performed on a 5 mL HiTrap Q column. Columns were stored in 20 % ethanol. The column was prepared by running 5 column volumes of water, IEX elution buffer (Table.13.1), IEX equilibration buffer (Table.13.1) with respect to order subsequently at flow rates of 1-4 mL/min. The sample was then loaded onto the column at a flow rate of 1 mL/min. Proteins that did not bind to the column were collected in the flow through (FT). Once the absorbance reading at 280 nm (A280) stabilized, an elution gradient of 0-100 % over 120 mins with a flow rate of

1 mL/min was started. From the onset of the elution gradient, 1 mL elution fractions were collected.

To determine the fractions that contained alpha-synuclein, fractions based on the A280 elution profile, were run on a 4 - 12 % Bis-Tris gel in MES buffer. 20 μ L of each fraction was mixed with 20 μ L of 2 X sample loading buffer (Table.13.1). The mixed protein sample was then boiled at 95 °C for 5 mins. After boiling the samples were briefly centrifuged and loaded into their respective wells in the gel. The gel was run at 240 V for 41 mins. Once the protein loading dye reached the bottom of the gel, the plastic encasing was opened and the gel was transferred to a container for ease of Coomassie staining.

To stain the gels with Coomassie, SDS had to be removed from the gel. This was done by placing the gel in water and microwaving it for 30 secs followed by a 5 mins incubation time. This was repeated 3 times. After the washing step, Coomassie was added to the gel and microwaved for 15 secs. The gel was then incubated in Coomassie until protein bands became visible. After visualization, fractions that contained alpha-synuclein were pooled and dialyzed into hydrophobic interaction chromatography (HIC) equilibration buffer using 3.5 kDa membrane overnight at 4 °C with gentle stirring.

13.1.4 Hydrophobic-interaction chromatography (HIC)

From this step, we were able to purify two populations of alpha-synuclein. The first population does not bind to the column and flows through during the loading and washing step and is very clean/pure. The second population gets eluted by the gradient and has a lower purity. HIC was performed on 5 mL HiTrap Phenyl FF columns. Columns were stored in 20 % ethanol. The column was prepared by running 5 column volumes of water, HIC elution buffer (Table.13.1), HIC equilibration buffer (Table.13.1) with respect to order subsequently at flow rates of 1 - 4 mL/min. The sample was then loaded onto the column at a flow rate of 0.5 mL/min. Proteins that did not bind to the column were collected in the FT. Pure alpha-synuclein is found in the FT, to prevent the protein from precipitating or forming oligomers, the FT was immediately dialyzed into size-exclusion chromatography (SEC) running buffer (Table.13.1) using a 3.5 kDa membrane overnight at 4 °C with gentle stirring.

Once the absorbance reading at 280 nm (A280) stabilized, an elution gradient of 0-100 % over 40 mins with a flow rate of 1 mL/min was started. From the onset of the elution gradient, 1 mL elution fractions were collected. Fractions containing alpha-synuclein were identified using SDS-PAGE gel and Coomassie staining as described earlier in the text. The fractions containing pure alpha-synuclein were dialyzed into SEC running buffer using a 3.5 kDa membrane overnight at 4 °C with gentle stirring.

13.1.5 Size-exclusion chromatography

Superdex 200 increase (10 / 300) column was used for SEC. Column was equilibrated the day before by running 2 column volumes of water followed by SEC running buffer at flow rates of 0.4 mL/min. Protein were finally stored in SEC running buffer (20 mM MES pH 6). Dialyzed protein solution were concentrated using 10 kDA Amicon[®] Ultra centrifugal filter to approximately 1 mL and injected on to the SEC column. Samples were run at a flow rate of 0.5 mL/min. Fractions of 0.5 mL were collected. Samples of fractions were analyzed using SDA-PAGE and Coomassie staining. Fractions that were pure and did not show protein degradation were pooled together.

Final protein concentration was determined using NanoDrop. Proteins were concentrated to ~5 - 6mg/mL (~400 μ M). Aliquots of ~30 μ L were then stored in thin walled PCR tube in -80 °C.

13.2 Alpha-synuclein fibril formation

100 μ M of monomer solution was incubated in a 2 ml round bottom Eppendorf tube. The Eppendorf tube cap was wrapped with paraffin tape. The tube was then placed in a benchtop thermomixer with a heated lid. It was incubated at 37 °C under constant agitation of 800 rpm.

The formation and presence of fibrils were validated with negative staining on electron microscopy. EM grids were glow discharged using PELCO easiglow glow discharge device at the electron microscopy core facility. After glow discharge, 5 μ L of fibril solution was added to each grid and allowed to sit for 1 min. The grid was then blotted on a Whatman 50 filter paper to remove the fibril solution. The grid then underwent two wash steps with water, each time the grid was placed on a water droplet 30 secs and then blotted on Whatman 50 filter paper. The grid was then placed on a drop of 2 % uranyl acetate for 10 secs and then blotted on Whatman 50 filter paper. As a final staining step, the grid was placed on a drop of 2 % uranyl acetate for 1 min and then blotted on Whatman 50 filter paper. The remaining liquid on the grid was allowed to air dry. Once the grid was dried, it was imaged on FEI Morgagni transmission electron microscope (100 kV) at the electron microscopy facility (EMCF).

Once the presence of fibrils was confirmed, part of the fibril solution was kept at 4 °C and the remainder was aliquoted as 1 μ L of fibril solution aliquots into thin-walled PCR tubes and stored at -80 °C.

13.3 Alpha-synuclein seed generation

Seed fragments were generated by sonicating fibrils formed in solution. Sonication fragments fibrils into ~200 nm seed fragments. 1 μ L of fibril solution aliquots in thin-walled PCR tubes were diluted 100 X (addition of 99 μ L of 20 mM MES pH 6) resulting in a final fibril concentration of 1 μ M. The tube was then sonicated for 35 secs in a waterbath sonicator at 4 °C. To ensure that all the fibril solution collected to the bottom of the tube, it was spun down briefly on a table-top PCR tube centrifuge. Sonicated seeds were stored at 4 °C.

13.4 Fibril formation of beta-amyloid (1-42)

The beta-amyloid (1-42) aggregation kit was purchased from rPeptide. Fibril formation was performed as directed by the instruction provided with the kit. Lyophilized protein was resuspended in 500 μ L of 5 mM Tris to bring the protein concentration to 1 mg/mL. The protein solution was transferred to an Eppendorf tube and incubated at 37 °C for 3 hrs. The presence of fibrils were confirmed by staining with ThT and visualization using light microscopy.

13.5 Fibril formation of Tau

Purified protein monomers of truncated Tau (R1-R4) with P301L mutation were given to me by Cedric Leu, a PhD student in the laboratory of Prof. Henning Stahlberg. Fibril formation was performed according to the protocol provided by Cedric. Tau monomers were stored in 50 mM MES pH 6.25, 100 mM NaCl, 2 mM DTT at a concentration of 0.15 mg/mL. To induce the formation of fibrils, monomer solution was thawed and diluted 1:2 in 0.2 mg/mL heparin in 50 mM MES pH 6.25. The monomer solution was then incubated at 37 °C overnight. The presence of fibrils were confirmed by staining with ThT.

13.6 Sample preparation for spectral imaging

8 well labtek chambers were first plasma cleaned. 100 μ L of 0.14 mg/mL alpha-synuclein fibrils, 100 μ L of 1 mg/mL beta-amyloid (1-42) fibrils, 100 μ L of 0.15 mg/mL Tau fibrils were introduced to individual wells. Respective dyes were diluted to a final concentration of 0.5 μ M in 100 μ L of TBS pH 7.4 in each well. Fibrils were incubated in dye solution for 1 hr. After incubation, the wells were rinsed with 500 μ L of TBS pH 7.4 twice. The wells were then filled with 300 μ L of TBS pH 7.4 and setup for imaging on the Zeiss LSM 780.

13.7 Spectral imaging on the Zeiss LSM 780

The fluorescence emission spectra (400nm-700nm) respect to each of dye was recorded using the Lambda scan functionality of a Zeiss LSM780 microscope following the manufacturer's guideline. A 63x/1.4NA oil immersion objective (Zeiss; Plan-Apochromat 63x/1.4 Oil DIC M27) was used. ThT was excited with 405 nm wavelength. pFTAA was excited with 488 nm wavelength. Nile red was excited with 561 nm wavelength. Nile blue was excited with 640 nm wavelength.

13.8 Imaging fibrils on glass coverslip

Coverslips were first acid cleaned and stored in a cell culture hood (Thevathasan et al., 2019). Before use, the coverslips were plasma cleaned using a plasma cleaner for 5 mins under power setting of 5. Fibrils in solution were diluted 10-fold and added to the plasma cleaned coverslip and allowed to sit for 5 mins. After incubation the coverslip was rinsed twice with 1 mL of 20 mM MES pH 6 (or the respective buffer). The coverslip was then mounted onto the microscope stage. 300 μ L of 20 mM MES pH 6 (or respective buffer) was then added to the coverslip on the microscope stage. For bulk staining of fibrils on the coverslip respective dyes were added to get a final working concentration of 1 μ M. For PAINT imaging of fibrils, the final working concentration of dyes was in the 1 - 3 nM regime.

13.9 Construction of chambers for seeded aggregation assays

0.2 mL individual PCR tubes were cut 6.5 mm from the top, to generate chambers. This was done by Henry Werner from the Mechanical workshop at EMBL. These chambers were then attached to plasma cleaned coverslips using UV glue or two-component silicon glue.

13.10 Fibril elongation assay

13.10.1 Imaging chamber construction

Acid cleaned coverslips were used. Just before imaging chamber construction, the coverslips were plasma cleaned for 5 mins. After that, the cut top-half of PCR tube was glued to the coverslip. For correlative superresolution & electron microscopy, 50 μ m gridded coverslip [Cat #10817, Ibidi, Gräfelfing, Germany) was used. Special care was paid to ensure that the chamber was positioned in the center of the coverslip.

To prevent accidental shifting in the position of the chamber, the chamber was first glue with 2 small drops of UV glue applied with a pipette tip. The drops were then cured under a UV lamp irradiation for 5 mins. Once the drops were cured, more UV glue was applied around the tube to seal and hold down the chamber. To allow all the glue to set, the setup was cured under UV lamp irradiation for another 5 mins. For correlative superresolution & electron microscopy, instead of UV glue, two component silicon glue was used.

13.10.2 Seed adsorption to the coverslip

Prior to seed adsorption, the glass surface was passivated with 0.2 M MgCl₂. 50 μ L of 0.2 M MgCl₂ was added to the glass surface within the chamber and allowed to sit for 5 mins. After 5 mins the volume of 0.2 M MgCl₂ was pipetted out (care was taken to ensure that the glass surface did not dry out). 12 μ L of 1 μ M seeds were diluted into 88 μ L of 20 mM MES pH 6. From this dilution, 50 μ L of seed solution was added to the imaging chamber. The seed solution was allowed to remain in the chamber for 2.5 mins. After that, 46 μ L of seed solution was pipetted out (4.0 μ L was left in the chamber to ensure that the chamber surface did not dry out). The chamber was rinsed three times with 50 μ L of 20 mM MES pH 6. After rinsing, 50 μ L of 1.5 % (w/v) BSA in PBS pH 7.4 was added to the chamber and incubated for 1 hr at RT on an orbital shaker. After blocking for 1 hr, the chamber was rinsed three times with 50 μ L of 20 mM MES pH 6.

13.10.3 Protein monomer solution for fibril elongation assay

The total volume of protein solution for all fibril elongation experiments was set at 70 μ L. Concentrated protein monomer (> 400 μ M) were stored in volumes that were needed for single experiments. This was done to avoid multiple freeze thaw cycles. Once the monomers thawed, the tube was briefly spun down on a table top PCR tube centrifuge. 7.0 μ L of 20% (w/v) glucose, 1.5 μ L of 20 x pyranose oxidase / catalase (POXC) enzyme mixture, 1.3 μ L of 1 M MgCl₂, 1.3 μ L of 400 μ M ascorbic acid (freshly prepared), 1.0 μ L of 150 nM pFTAA in 20 mM MES pH 6 was added to the protein monomer solution. 20 mM MES pH 6 was added to bring the final volume up to 70 μ L. To remove all salt from the solution 0.1 mM of EDTA was added instead of MgCl₂. The protein monomer solution was mixed by pipetting. After mixing the protein solution was added to the chamber. The chamber was then carefully capped with a PCR tube cap. The imaging chamber was then set up on the microscope stage for imaging.

13.11 Fibril elongation assay with change in solution conditions

Changing solution conditions from 18.5 mM MgCl₂ to no salt (1 mM EDTA). Fibril elongation assay was set up as per description above. After acquisition of 240,000 frames with 150 ms exposure time (total 10 hrs), the protein monomer solution was changed while still mounted on the microscope stage. A reference image was captured to determine the field of view. The chamber cap was carefully removed using flat tip forceps. Special care was paid to ensure that the chamber or microscope stage was not moved. This is to ensure that the same field of view was maintained. The protein monomer solution in the chamber was then pipetted out with a gel loading tip. 70 μ L of 20 mM MES pH 6 was added to the chamber for rinsing purposes. The rinsing buffer was pipetted out and 70 μ L of protein monomer solution containing 1 mM EDTA was added to the chamber. The chamber cap was then carefully placed back on the chamber using flat tip forceps. The field of view was then compared to the reference image captured before the change of buffer. If there had been no change, the focus was adjusted and the acquisition of 240,000 frames with 150 ms exposure time (total 10 hrs) was started.

13.12 Correlative electron microscopy

All electron microscopy work was performed with Rachel Mellwig at the EMBL electron microscopy core facility (EMCF).

13.12.1 Resin embedding

Resin embedding was performed after fibrils were elongated in the imaging assay as described earlier.

Two different protocols were used. The first one was using the Pelco BioWave microwave and in the second one the samples were processed on the bench.

For the non-correlative experiments, the filaments were processed with the Pelco BioWave Microwave (Ted Pella, USA). Filaments were fixed with 2.5% glutaraldehyde in 20 mM MES buffer, pH 6.0 followed by 1% osmium tetroxide in water, then 1% uranyl acetate in water and processed in the microwave according to Schieber et al., 2010. The samples were then dehydrated through a series of EtOH steps: 50%, 70%, 90% and twice with 100% for 40 seconds each in the microwave. They were then infiltrated with a 50% EPON (Serva) and EtOH mix in the microwave for 3 minutes and then twice with 100% on the bench and placed in the oven at 60°C overnight. Note: Microwave settings were the same as Schieber et al., 2010 for the dehydration and infiltration steps, just different times and percentages were used.

Coverslips were removed the next day by dipping them into liquid nitrogen and hot water.

For the correlative experiments, the filaments were fixed with 2.5% (v/v) glutaraldehyde in 20 mM MES buffer, pH 6.0 for 5 minutes. They were then rinsed twice with MES buffer and then stained with 1% (w/v) osmium tetroxide in water for 5 minutes. The samples were rinsed twice with water and further stained with 1% (w/v) uranyl acetate in water and then rinsed again twice with water. They were then taken through a series of dehydration steps with EtOH (50%, 70%, 90%; all [v/v]), 5 min. each step. The samples were further dehydrated 2 times with 100% EtOH. They were then infiltrated with a 50% EPON (Serva) and EtOH mix and twice with 100% EPON. Samples were placed in the oven at 60 °C overnight and coverslips were removed the next day by dipping them into liquid nitrogen and hot water.

13.12.2 Resin sectioning and Imaging

Thin sections (70 nm and 150 nm) were cut with an ultra 35° diamond knife (Diatome, Switzerland) and placed onto formvar-coated (Serva, Germany) copper palladium slot grids (PLANO, Germany). Grids were imaged in a JEOL, JEM 2100 Plus electron microscope (JEOL, Japan) at 120kV.

13.13 SMLM Microscope setup

All SMLM data were acquired on a custom-built microscope designed and built by Jonas Ries and Joran Deschamps. Briefly, output from an iChrome MLE laser box (Toptica, Gräfelfing, Germany) was collimated by a 75 mm lens [AC254-075-A, Thorlabs], followed by an achromatic quarter-wave plate [Cat #AQWPIOM-580]. To remove fluorescence generated by the fiber, the laser was guided through a laser clean up filter (400-410/482/563/631-640 HC Quad; AHF, Tübingen, Germany) before being focused by a 150 mm lens [AC508-150-A, Thorlabs] onto the back-focal plane of the objective housed in a custom microscope body. The emission from the sample was collected with a high numerical aperture (NA) oil-immersion objective (APON 100xHOTIRF; Olympus, Japan) and passed through 488 longpass dichroic [Cat #F48-486, AHF Analysentechnik, Germany], preventing laser light to enter the detection path. The sample was then imaged on an intermediate image plane by the tube lens [U-TLU, Olympus]. The fluorescence was subsequently filtered by a 500 longpass filter [FELH0500, Thorlabs] and by a bandpass filter corresponding to the fluorophore being imaged: 525/50 [Cat #FF03-525/50-25, chroma] for ThT; 582/75 [FF01-582/75-25, Semrock] for pFTAA; 617/73 [Cat #F39-617, Semrock] for Nile red and 700/100 [Cat #ET700/100m, Chroma] for Nile blue. A pair of relay lenses (AC254-200-A and AC254-250-A, Thorlabs) in 4f configuration finally forms

the image of the sample onto the camera (iXon Ultra 897 Andor, Oxford Instruments, Belfast, Northern Ireland). A beam splitter can be inserted, giving rise to two channels, each imaged on one half of the camera. For polarization measurements, a polarization beam splitter [PBS251, Thorlabs] was placed in the detection beam path. For two-channel emission spectrum measurements a 561 longpass dichroic [F48-640, AHF] was inserted. Focus stabilization was performed using a near infra-red laser [iBeamSmart 750, Toptica] totally internally reflected off the sample coverslip and detected by a quadrant photodiode [SD197-23-21-041, Laser components, Olching, Germany]. The photodiode was connected to a closed-loop electronics feedback with the objective piezo positioner (P-726, Physik Instrumente, Karlsruhe, Germany). To filter out the IR focus lock laser from the image, a 750 shortpass filter [FES0750, Thorlabs] was placed just before the camera. The various components of the microscope were controlled by a field-programmable gate array (Mojo; Alchitry, Denver, CO, USA) and Micro-manager (OpenImaging, San Francisco, USA).

13.14 Data acquisition

A drop of Zeiss 518f immersion oil was applied to the objective. The imaging chamber was then gently lowered over the oil droplet, special care was taken to ensure that no air bubbles were introduced. The back focal plane (BFP) was checked to ensure the absence of an air bubble. If there was an air bubble, the sample was remounted with a new drop of immersion oil. The microscope was controlled via a micromanager software written and implemented by Joran Deshamps. The camera was set to 200 gain and speed to 10 Hz. Exposure time was set at 150 ms. 488 nm excitation was set at 20% power of 100 mW laser. Using 488 nm excitation the imaging plane was identified by ensuring that single molecule events recorded were in focus. Once the focus plane was determined. The focus lock system was activated. To ensure that imaging was performed under total internal reflection conditions (TIRF), the excitation laser spot was positioned at the edge of the BFP. After a final inspection to ensure that the imaging plane was in focus, the acquisition was started. Acquisition parameters were 300,000 frames, 150 ms exposure time with no interval which amounted to 12.5 hours of total acquisition. All fibril elongation assays were recorded under these acquisition settings unless otherwise stated. Localizations were fitted concurrent to acquisition.

13.15 Data analysis

All Single molecule localization and subsequent analyses were performed in the custom-written software single molecule analysis platform (SMAP). SMAP is written in Matlab by Jonas Ries and it is available at: <https://github.com/jries/SMAP>

13.15.1 Fitting localizations

Raw tiff files were loaded into SMAP under localize > input image. Localizations were fitted using the fit_fastsimple workflow. To fit localizations simultaneously during acquisition, the 'Online analysis' box was checked. To identify localizations to fit, under SMAP > localize > peak finder, the region to be fitted was determined and the dynamic factor was set to 1. First, the image background was calculated and subtracted. The resulting image was then used for peak detection. A region of interest was cut out around the detected peaks from the original raw images which were then fitted using a GPU-based maximum-likelihood estimator fitter. The localizations' unique ID, position coordinates, number of photons, background, theoretical localization precision, PSF size and life time were recorded. Once the fitting was completed, the fitted data was automatically saved.

13.15.2 Filtering and rendering localizations

Once the localizations were fitted, all the localizations were rendered with a symmetric Gaussian distribution with a standard deviation equal to the localization precision. Localizations with a localization precision of > 30 nm and PSF of < 80 and > 160 nm were filtered out.

13.15.3 Intensity calculation (2 channel – polarization)

A transformation file was first calculated to match pixels for intensity calculation. This was done by navigating to SMAP > plugins > process > assign2C > 2C intensity from images 2 cam. Within the pop up window, roi2int_fitG was checked; roi size was set to 7; fix PSF size (in terms of number of pixels – measured PSF/128); fit on BG was unchecked. The directory that contained the raw tiff and transformation files was loaded. Both target and reference boxes were checked. This is to ensure that we extract intensities from both channels. Intensities for each pixel in the corresponding channel were saved as individual field variables labeled fit_nr (reference) and fit_nt (target).

13.15.4 Polarization calculation

Polarization for each localization was calculated using the math parser built within SMAP. It can be found under SMAP > Process > Modify > MathParser. Polarization for each localization was calculated by:

$$\text{polarization} = \frac{(\text{fit_nr} - \text{fit_nt})}{(\text{fit_nr} + \text{fit_nt})} \quad (13.1)$$

13.15.5 Registering 2 channels

The function for this can be found under SMAP > Process > Register > Apply Transformation tab. The calculated transformation file was loaded. Set channel box was checked to ensure that the reference channel was 1 and the target channel was 2.

13.15.6 Drift correction

Drift correction of images was performed after transformation. This was done using the drift correction function found in SMAP > Process > Drift. Drift correction was performed by dividing the entire acquisition into 10 segments which were then temporally cross correlated to determine and correct the drift.

13.15.7 Fibril segmentation

Fibril segmentation and analysis plugins were written by Yu-Le Wu, a PhD student in our lab. Fibrils were segmented in ROI manager within SMAP > ROIs. The FOV for sites was set to 5000 nm and for cell it was set to 75000 nm. This was to ensure that the entire imaged ROI would fall into a single cell to prevent fibrils from being separated into different cells. A cell was made using SMAP > Plugin > ROIManager > segment > makeCellGrid. Fibrils were first automatically detected and segmented using SMAP > Plugin > ROIManager > segment > fibrilFinder. Intensity cutoff was set to 0.028. All localizations in the field of view were rendered as a 2D histogram. A median filtering step was applied to remove sparse background. Next, a Top-hat filtering was applied to the histogram to remove uneven background. An intensity-based threshold was then applied to the filtered histogram to create masks of fibrils. The masks were then used to define the region of fibrils. Fibrils that have been detected in neighbouring "cells" were then re-segmented manually.

13.15.8 Straightening fibrils

Fibrils were usually curved. Therefore a simple line profile was not sufficient to describe the fibril for analysis purposes. To straighten the fibrils, a cubic spline fit was performed on the fibrils. All the localizations were projected onto the fitted spline (central axis of the fibrils). As a result, the x -coordinate of a localization was its projected position on the central axis. The y -coordinate was the distance between the localization and the central axis.

13.15.9 Descriptive analysis of fibrils

Two features, the deviation of localizations from the axis and the polarization of the localizations were quantified. The straightened fibrils were first divided into bins with widths of 10 nm. A curve was plotted through the median of each bin. To identify if there was a periodicity along the curve, an autocorrelation analysis was applied. Periodicity values were determined by scoring the first peak in the correlogram.

13.15.10 Analysis of kymographs

Kymographs were generated by plotting the time when each localizations appeared against its corresponding position along the length of the straightened fibril. Localizations in the kymograph had a bin width of 10 nm for the length of the fibril and 1000 frames (2.5 mins) for time. To detect the boundary of the growing end, a crude boundary to demarcate a foreground (localization within the fibril) and a background (localizations outside the fibrils) was identified. To identify the boundary, a cumulative histogram accumulated from the last frame bin and the last position bin was first derived from the kymograph. Next, the last bin with a value between 95 and 104 at each time bin was picked to form the raw boundary. A greedy algorithm was then applied to refine the raw boundary with a constraint that only allows stop and monotonic increase of positions overtime. For each time bin, the algorithm moves the boundary to further non-zero position bins to minimize the objective function value *val*:

$$val = \sqrt{w_1(d_f - 1)^2 + d_b^2} - w_2d_b \quad (13.2)$$

Where d_f and d_b are the foreground and background densities respectively given a boundary and w_1 and w_2 are weighting factors. The objective function was designed for maximizing the foreground density towards one and minimising its background counterpart towards zero, allowed a background offset weighted by the factor w_2 . w_1 was set to a constant of 0.07 and w_2 to 0.1. The refined boundary was then acquired with the sequential optimisation starting from the last time bin to the first. Next, the refined boundary was smoothed by a Gaussian filtering with a window size of 20 bins and a sigma of 7 bins. The dynamics of a fibril were then measured based on the smoothed boundary. Specifically, the derivative of the smoothed boundary, a function of time, was calculated as the fibril's speed profile. A threshold of 0.2 nm/min was applied to the profile to determine steps and stalls. Stall time, step speed, step time and average speed of a fibril were then calculated based on the profile.

L^AT_EX

I composed this thesis with Overleaf, and used a custom document structure based on the 'Masters/Doctoral Thesis' L^AT_EXtemplate (www.latextemplates.com, authors Steve Gunn, Sunil Patel, vel@latextemplates.com), modified by Markus Mund, which is available under CC BY-NC-SA 3.0 (<http://creativecommons.org/licenses/by-nc-sa/3.0/>).

Bibliography

- Abbe, E. (1873). "Beiträge zur Theorie des Mikroskops und der mikroskopischen Wahrnehmung". In: *Archiv für Mikroskopische Anatomie* 9.1, pp. 413–468. DOI: 10.1007/BF02956173.
- Aitken, Colin Echeverría, R. Andrew Marshall, and Joseph D. Puglisi (2008). "An Oxygen Scavenging System for Improvement of Dye Stability in Single-Molecule Fluorescence Experiments". In: *Biophysical Journal* 94.5, pp. 1826–1835. DOI: 10.1529/biophysj.107.117689.
- Andersen, Christian Beyschau, Hisashi Yagi, Mauro Manno, Vincenzo Martorana, Tadato Ban, Gunna Christiansen, Daniel Erik Otzen, Yuji Goto, and Christian Rischel (2009). "Branching in Amyloid Fibril Growth". In: *Biophysical Journal* 96.4, pp. 1529–1536. DOI: 10.1016/j.bpj.2008.11.024.
- Anderson, John P. et al. (2006). "Phosphorylation of Ser-129 Is the Dominant Pathological Modification of alpha-Synuclein in Familial and Sporadic Lewy Body Disease". In: *Journal of Biological Chemistry* 281.40, pp. 29739–29752. DOI: 10.1074/jbc.M600933200.
- Appen, Alexander von et al. (2015). "In situ structural analysis of the human nuclear pore complex". In: *Nature* 526.7571, pp. 140–143. DOI: 10.1038/nature15381.
- Aquino, Daniel, Andreas Schönle, Claudia Geisler, Claas v Middendorff, Christian A. Wurm, Yosuke Okamura, Thorsten Lang, Stefan W. Hell, and Alexander Egner (2011). "Two-color nanoscopy of three-dimensional volumes by 4Pi detection of stochastically switched fluorophores". In: *Nature Methods* 8.4, pp. 353–359. DOI: 10.1038/nmeth.1583.
- Arima, K., T. Mizutani, M. A. Alim, H. Tonozuka-Uehara, Y. Izumiyama, S. Hirai, and K. Uéda (2000). "NACP/alpha-synuclein and tau constitute two distinctive subsets of filaments in the same neuronal inclusions in brains from a family of parkinsonism and dementia with Lewy bodies: double-immunolabeling fluorescence and electron microscopic studies". In: *Acta Neuropathologica* 100.2, pp. 115–121.
- Atias, Merav, Yaara Tevet, Jichao Sun, Alexandra Stavsky, Shani Tal, Joy Kahn, Subhojit Roy, and Daniel Gitler (2019). "Synapsins regulate alpha-synuclein functions". In: *Proceedings of the National Academy of Sciences* 116.23, pp. 11116–11118. DOI: 10.1073/pnas.1903054116.
- Baldering, Tim N., Marina S. Dietz, Karl Gatterdam, Christos Karathanasis, Ralph Wieneke, Robert Tampé, and Mike Heilemann (2019). "Synthetic and genetic dimers as quantification ruler for single-molecule counting with PALM". In: *Molecular Biology of the Cell* 30.12. Ed. by Diane Lidke, pp. 1369–1376. DOI: 10.1091/mbc.E18-10-0661.
- Balleza, Enrique, J. Mark Kim, and Philippe Cluzel (2018). "Systematic characterization of maturation time of fluorescent proteins in living cells". In: *Nature Methods* 15.1, pp. 47–51. DOI: 10.1038/nmeth.4509.
- Ban, Tadato and Yuji Goto (2006). "Direct Observation of Amyloid Growth Monitored by Total Internal Reflection Fluorescence Microscopy". In: *Methods in Enzymology*. Vol. 413. Amyloid, Prions, and Other Protein Aggregates, Part C. Academic Press, pp. 91–102. DOI: 10.1016/S0076-6879(06)13005-0.
- Ban, Tadato, Daizo Hamada, Kazuhiro Hasegawa, Hironobu Naiki, and Yuji Goto (2003). "Direct Observation of Amyloid Fibril Growth Monitored by Thioflavin T Fluorescence".

- In: *Journal of Biological Chemistry* 278.19, pp. 16462–16465. DOI: 10.1074/jbc.C300049200.
- Bartels, Tim, Nora C. Kim, Eric S. Luth, and Dennis J. Selkoe (2014). “N-Alpha-Acetylation of alpha-Synuclein Increases Its Helical Folding Propensity, GM1 Binding Specificity and Resistance to Aggregation”. In: *PLoS ONE* 9.7. Éd. by Annalisa Pastore, e103727. DOI: 10.1371/journal.pone.0103727.
- Bates, Mark, Timothy R. Blosser, and Xiaowei Zhuang (2005). “Short-Range Spectroscopic Ruler Based on a Single-Molecule Optical Switch”. In: *Physical Review Letters* 94.10, p. 108101. DOI: 10.1103/PhysRevLett.94.108101.
- Baumgart, Florian, Andreas M. Arnold, Konrad Leskovar, Kaj Staszek, Martin Fölser, Julian Weghuber, Hannes Stockinger, and Gerhard J. Schütz (2016). “Varying label density allows artifact-free analysis of membrane-protein nanoclusters”. In: *Nature Methods* 13.8, pp. 661–664. DOI: 10.1038/nmeth.3897.
- Beck, Martin and Ed Hurt (2017). “The nuclear pore complex: understanding its function through structural insight”. In: *Nature Reviews Molecular Cell Biology* 18.2, pp. 73–89. DOI: 10.1038/nrm.2016.147.
- Beck, Martin, Vladan Lučić, Friedrich Förster, Wolfgang Baumeister, and Ohad Medalia (2007). “Snapshots of nuclear pore complexes in action captured by cryo-electron tomography”. In: *Nature* 449.7162, pp. 611–615. DOI: 10.1038/nature06170.
- Bertoncini, Carlos W., Young-Sang Jung, Claudio O. Fernandez, Wolfgang Hoyer, Christian Griesinger, Thomas M. Jovin, and Markus Zweckstetter (2005). “Release of long-range tertiary interactions potentiates aggregation of natively unstructured alpha-synuclein”. In: *Proceedings of the National Academy of Sciences of the United States of America* 102.5, p. 1430. DOI: 10.1073/pnas.0407146102.
- Betzig, Eric, George H. Patterson, Rachid Sougrat, O. Wolf Lindwasser, Scott Olenych, Juan S. Bonifacino, Michael W. Davidson, Jennifer Lippincott-Schwartz, and Harald F. Hess (2006). “Imaging intracellular fluorescent proteins at nanometer resolution”. In: *Science (New York, N.Y.)* 313.5793, pp. 1642–1645. DOI: 10.1126/science.1127344.
- Biancalana, Matthew and Shohei Koide (2010). “Molecular mechanism of Thioflavin-T binding to amyloid fibrils”. In: *Biochimica Et Biophysica Acta* 1804.7, pp. 1405–1412. DOI: 10.1016/j.bbapap.2010.04.001.
- Biancalana, Matthew, Koki Makabe, Akiko Koide, and Shohei Koide (2009). “Molecular mechanism of thioflavin-T binding to the surface of beta-rich peptide self-assemblies”. In: *Journal of Molecular Biology* 385.4, pp. 1052–1063. DOI: 10.1016/j.jmb.2008.11.006.
- Bolisetty, Sreenath and Raffaele Mezzenga (2016). “Amyloid–carbon hybrid membranes for universal water purification”. In: *Nature Nanotechnology* 11.4, pp. 365–371. DOI: 10.1038/nnano.2015.310.
- Bongiovanni, Marie N. et al. (2016). “Multi-dimensional super-resolution imaging enables surface hydrophobicity mapping”. In: *Nature Communications* 7, p. 13544. DOI: 10.1038/ncomms13544.
- Bousset, Luc et al. (2013). “Structural and functional characterization of two alpha-synuclein strains”. In: *Nature Communications* 4, p. 2575. DOI: 10.1038/ncomms3575.
- Braak, Heiko, Kelly Del Tredici, Udo Rüb, Rob A. I. de Vos, Ernst N. H. Jansen Steur, and Eva Braak (2003). “Staging of brain pathology related to sporadic Parkinson’s disease”. In: *Neurobiology of Aging* 24.2, pp. 197–211.
- Breydo, Leonid and Vladimir N. Uversky (2015). “Structural, morphological, and functional diversity of amyloid oligomers”. In: *FEBS Letters. Dynamics, flexibility, and intrinsic disorder in protein assemblies* 589.19, pp. 2640–2648. DOI: 10.1016/j.febslet.2015.07.013.
- Brown, James W. P., Georg Meisl, Tuomas P. J. Knowles, Alexander K. Buell, Christopher M. Dobson, and Céline Galvagnion (2018). “Kinetic barriers to alpha-synuclein protofilament formation and conversion into mature fibrils”. In: *Chemical Communications* 54.56, pp. 7854–7857. DOI: 10.1039/C8CC03002B.

- Bu, Bing et al. (2017). "N-Terminal Acetylation Preserves alpha-Synuclein from Oligomerization by Blocking Intermolecular Hydrogen Bonds". In: *ACS Chemical Neuroscience* 8.10, pp. 2145–2151. DOI: 10.1021/acscchemneuro.7b00250.
- Buell, Alexander K., Peter Hung, Xavier Salvatella, Mark E. Welland, Christopher M. Dobson, and Tuomas P.J. Knowles (2013). "Electrostatic Effects in Filamentous Protein Aggregation". In: *Biophysical Journal* 104.5, pp. 1116–1126. DOI: 10.1016/j.bpj.2013.01.031.
- Buell, Alexander K., Céline Galvagnion, Ricardo Gaspar, Emma Sparr, Michele Vendruscolo, Tuomas P. J. Knowles, Sara Linse, and Christopher M. Dobson (2014). "Solution conditions determine the relative importance of nucleation and growth processes in alpha-synuclein aggregation". In: *Proceedings of the National Academy of Sciences* 111.21, pp. 7671–7676. DOI: 10.1073/pnas.1315346111.
- Bykov, Yury S., Mirko Cortese, John A. G. Briggs, and Ralf Bartenschlager (2016). "Correlative light and electron microscopy methods for the study of virus–cell interactions". In: *FEBS Letters* 590.13, pp. 1877–1895. DOI: 10.1002/1873-3468.12153.
- Campioni, Silvia, Guillaume Carret, Sophia Jordens, Lucrèce Nicoud, Raffaele Mezzenga, and Roland Riek (2014). "The Presence of an Air–Water Interface Affects Formation and Elongation of alpha-Synuclein Fibrils". In: *Journal of the American Chemical Society* 136.7, pp. 2866–2875. DOI: 10.1021/ja412105t.
- Cella Zanacchi, Francesca, Carlo Manzo, Raffaella Magrassi, Nathan D. Derr, and Melike Lakadamyali (2019). "Quantifying Protein Copy Number in Super Resolution Using an Imaging-Invariant Calibration". In: *Biophysical Journal* 116.11, pp. 2195–2203. DOI: 10.1016/j.bpj.2019.04.026.
- Chan, Fiona T. S., Gabriele S. Kaminski Schierle, Janet R. Kumita, Carlos W. Bertoncini, Christopher M. Dobson, and Clemens F. Kaminski (2013). "Protein amyloids develop an intrinsic fluorescence signature during aggregation". In: *The Analyst* 138.7, pp. 2156–2162. DOI: 10.1039/c3an36798c.
- Charles A Janeway, Jr, Paul Travers, Mark Walport, and Mark J. Shlomchik (2001). "The structure of a typical antibody molecule". In: *Immunobiology: The Immune System in Health and Disease. 5th edition*.
- Chartier-Harlin, Marie-Christine et al. (2004). "alpha-synuclein locus duplication as a cause of familial Parkinson's disease". In: *The Lancet* 364.9440, pp. 1167–1169. DOI: 10.1016/S0140-6736(04)17103-1.
- Chen, Bi-Chang et al. (2014a). "Lattice light-sheet microscopy: imaging molecules to embryos at high spatiotemporal resolution". In: *Science (New York, N.Y.)* 346.6208, p. 1257998. DOI: 10.1126/science.1257998.
- Chen, Yalei, Nathan C. Deffenbaugh, Charles T. Anderson, and William O. Hancock (2014b). "Molecular counting by photobleaching in protein complexes with many subunits: best practices and application to the cellulose synthesis complex". In: *Molecular biology of the cell*. DOI: 10.1091/mbc.E14-06-1146.
- Chozinski, Tyler J., Lauren A. Gagnon, and Joshua C. Vaughan (2014). "Twinkle, twinkle little star: Photoswitchable fluorophores for super-resolution imaging". In: *FEBS Letters* 588.19, pp. 3603–3612. DOI: 10.1016/j.febslet.2014.06.043.
- Clayton, David F. and Julia M. George (1999). "Synucleins in synaptic plasticity and neurodegenerative disorders". In: *Journal of Neuroscience Research* 58.1, pp. 120–129. DOI: 10.1002/(SICI)1097-4547(19991001)58:1<120::AID-JNR12>3.0.CO;2-E.
- Coffman, Valerie C. and Jian-Qiu Wu (2012). "Counting protein molecules using quantitative fluorescence microscopy". In: *Trends in Biochemical Sciences* 37.11, pp. 499–506. DOI: 10.1016/j.tibs.2012.08.002.
- Coles, Benjamin C., Stephen E. D. Webb, Noah Schwartz, Daniel J. Rolfe, Marisa Martin-Fernandez, and Valentina Lo Schiavo (2016). "Characterisation of the effects of optical aberrations in single molecule techniques". In: *Biomedical Optics Express* 7.5, pp. 1755–1767. DOI: 10.1364/BOE.7.001755.

- Colletier, Jacques-Philippe et al. (2011). "Molecular basis for amyloid-beta polymorphism". In: *Proceedings of the National Academy of Sciences of the United States of America* 108.41, pp. 16938–16943. DOI: 10.1073/pnas.1112600108.
- Conway, K. A., J. D. Harper, and P. T. Lansbury (1998). "Accelerated in vitro fibril formation by a mutant alpha-synuclein linked to early-onset Parkinson disease". In: *Nature Medicine* 4.11, pp. 1318–1320. DOI: 10.1038/3311.
- Conway, Kelly A., Seung-Jae Lee, Jean-Christophe Rochet, Tomas T. Ding, Robin E. Williamson, and Peter T. Lansbury (2000). "Acceleration of oligomerization, not fibrillization, is a shared property of both alpha-synuclein mutations linked to early-onset Parkinson's disease: Implications for pathogenesis and therapy". In: *Proceedings of the National Academy of Sciences* 97.2, pp. 571–576. DOI: 10.1073/pnas.97.2.571.
- Cosentino, Michela, Claudio Canale, Paolo Bianchini, and Alberto Diaspro (2019). "AFM-STED correlative nanoscopy reveals a dark side in fluorescence microscopy imaging". In: *Science Advances* 5.6, eaav8062. DOI: 10.1126/sciadv.aav8062.
- Cremades, Nunilo et al. (2012). "Direct Observation of the Interconversion of Normal and Toxic Forms of alpha-Synuclein". In: *Cell* 149.5, pp. 1048–1059. DOI: 10.1016/j.cell.2012.03.037.
- Cruz, Cesar Augusto Valades, Haitham Ahmed Shaban, Alla Kress, Nicolas Bertaux, Serge Monneret, Manos Mavrikakis, Julien Savatier, and Sophie Brasselet (2016). "Quantitative nanoscale imaging of orientational order in biological filaments by polarized superresolution microscopy". In: *Proceedings of the National Academy of Sciences* 113.7, E820–E828. DOI: 10.1073/pnas.1516811113.
- Cuervo, Ana Maria, Leonidas Stefanis, Ross Fredenburg, Peter T. Lansbury, and David Sulzer (2004). "Impaired Degradation of Mutant alpha-Synuclein by Chaperone-Mediated Autophagy". In: *Science* 305.5688, pp. 1292–1295. DOI: 10.1126/science.1101738.
- Dani, Adish, Bo Huang, Joseph Bergan, Catherine Dulac, and Xiaowei Zhuang (2010). "Super-resolution Imaging of Chemical Synapses in the Brain". In: *Neuron* 68.5, pp. 843–856. DOI: 10.1016/j.neuron.2010.11.021.
- Danzer, Karin M., Dorothea Haasen, Anne R. Karow, Simon Moussaud, Matthias Habeck, Armin Giese, Hans Kretzschmar, Bastian Hengerer, and Marcus Kostka (2007). "Different species of alpha-synuclein oligomers induce calcium influx and seeding". In: *The Journal of Neuroscience: The Official Journal of the Society for Neuroscience* 27.34, pp. 9220–9232. DOI: 10.1523/JNEUROSCI.2617-07.2007.
- Dean, Kevin M and Amy E Palmer (2014). "Advances in fluorescence labeling strategies for dynamic cellular imaging". In: *Nature Chemical Biology* 10.7, pp. 512–523. DOI: 10.1038/nchembio.1556.
- Dempsey, Graham T., Joshua C. Vaughan, Kok Hao Chen, Mark Bates, and Xiaowei Zhuang (2011). "Evaluation of fluorophores for optimal performance in localization-based super-resolution imaging". In: *Nature Methods* 8.12, pp. 1027–1036. DOI: 10.1038/nmeth.1768.
- Deschamps, Joran, Markus Mund, and Jonas Ries (2014). "3D superresolution microscopy by supercritical angle detection". In: *Optics Express* 22.23, pp. 29081–29091. DOI: 10.1364/OE.22.029081.
- Deschamps, Joran, Andreas Rowald, and Jonas Ries (2016). "Efficient homogeneous illumination and optical sectioning for quantitative single-molecule localization microscopy". In: *Optics Express* 24.24, pp. 28080–28090. DOI: 10.1364/OE.24.028080.
- Deschout, Hendrik, Francesca Cella Zanacchi, Michael Mlodzianoski, Alberto Diaspro, Joerg Bewersdorf, Samuel T. Hess, and Kevin Braeckmans (2014). "Precisely and accurately localizing single emitters in fluorescence microscopy". In: *Nature Methods* 11.3, pp. 253–266. DOI: 10.1038/nmeth.2843.
- Desplats, Paula, He-Jin Lee, Eun-Jin Bae, Christina Patrick, Edward Rockenstein, Leslie Crews, Brian Spencer, Eliezer Masliah, and Seung-Jae Lee (2009). "Inclusion formation and neuronal cell death through neuron-to-neuron transmission of alpha-synuclein".

- In: *Proceedings of the National Academy of Sciences* 106.31, p. 13010. DOI: 10.1073/pnas.0903691106.
- Di Maio, Roberto et al. (2016). "alpha-Synuclein binds to TOM20 and inhibits mitochondrial protein import in Parkinson's disease". In: *Science Translational Medicine* 8.342, 342ra78. DOI: 10.1126/scitranslmed.aaf3634.
- Diaspro, Alberto, Federico Federici, and Mauro Robello (2002). "Influence of refractive-index mismatch in high-resolution three-dimensional confocal microscopy". In: *Applied Optics* 41.4, pp. 685–690. DOI: 10.1364/AO.41.000685.
- Dobson, Christopher M. (2019). "Biophysical Techniques in Structural Biology". In: *Annual Review of Biochemistry* 88.1, pp. 25–33. DOI: 10.1146/annurev-biochem-013118-111947.
- Duboisset, Julien, Patrick Ferrand, Wei He, Xiao Wang, Hervé Rigneault, and Sophie Brasselet (2013). "Thioflavine-T and Congo Red Reveal the Polymorphism of Insulin Amyloid Fibrils When Probed by Polarization-Resolved Fluorescence Microscopy". In: *The Journal of Physical Chemistry B* 117.3, pp. 784–788. DOI: 10.1021/jp309528f.
- Durisic, Nela, Antoine G. Godin, Claudia M. Wever, Colin D. Heyes, Melike Lakadamyali, and Joseph A. Dent (2012). "Stoichiometry of the human glycine receptor revealed by direct subunit counting". In: *The Journal of Neuroscience: The Official Journal of the Society for Neuroscience* 32.37, pp. 12915–12920. DOI: 10.1523/JNEUROSCI.2050-12.2012.
- Ehmann, Nadine et al. (2014). "Quantitative super-resolution imaging of Bruchpilot distinguishes active zone states". In: *Nature Communications* 5, p. 4650. DOI: 10.1038/ncomms5650.
- Elfarrash, Sara et al. (2019). "Organotypic slice culture model demonstrates interneuronal spreading of alpha-synuclein aggregates". In: *bioRxiv*, p. 681064. DOI: 10.1101/681064.
- Erdmann, Roman S. et al. (2019). "Labeling Strategies Matter for Super-Resolution Microscopy: A Comparison between HaloTags and SNAP-tags". In: *Cell Chemical Biology* 26.4, 584–592.e6. DOI: 10.1016/j.chembiol.2019.01.003.
- Esler, William P., Evelyn R. Stimson, Joan M. Jennings, Harry V. Vinters, Joseph R. Ghilardi, Jonathan P. Lee, Patrick W. Mantyh, and John E. Maggio (2000). "Alzheimer's Disease Amyloid Propagation by a Template-Dependent Dock-Lock Mechanism". In: *Biochemistry* 39.21, pp. 6288–6295. DOI: 10.1021/bi992933h.
- Fauvet, Bruno et al. (2012). "alpha-Synuclein in central nervous system and from erythrocytes, mammalian cells, and Escherichia coli exists predominantly as disordered monomer". In: *The Journal of Biological Chemistry* 287.19, pp. 15345–15364. DOI: 10.1074/jbc.M111.318949.
- Ferkinghoff-Borg, Jesper, Jesper Fonslet, Christian Beyschau Andersen, Sandeep Krishna, Simone Pigolotti, Hisashi Yagi, Yuji Goto, Daniel Otzen, and Mogens H. Jensen (2010). "Stop-and-go kinetics in amyloid fibrillation". In: *Physical Review E* 82.1, p. 010901. DOI: 10.1103/PhysRevE.82.010901.
- Finan, Kieran, Anika Raulf, and Mike Heilemann (2015). "A Set of Homo-Oligomeric Standards Allows Accurate Protein Counting". In: *Angewandte Chemie International Edition* 54.41, pp. 12049–12052. DOI: 10.1002/anie.201505664.
- Fiolka, Reto, Lin Shao, E. Hesper Rego, Michael W. Davidson, and Mats G. L. Gustafsson (2012). "Time-lapse two-color 3D imaging of live cells with doubled resolution using structured illumination". In: *Proceedings of the National Academy of Sciences* 109.14, pp. 5311–5315. DOI: 10.1073/pnas.1119262109.
- Fitzpatrick, Anthony W. P. et al. (2013). "Atomic structure and hierarchical assembly of a cross-beta amyloid fibril". In: *Proceedings of the National Academy of Sciences* 110.14, pp. 5468–5473. DOI: 10.1073/pnas.1219476110.
- Flagmeier, Patrick, Georg Meisl, Michele Vendruscolo, Tuomas P. J. Knowles, Christopher M. Dobson, Alexander K. Buell, and Céline Galvagnion (2016). "Mutations associated with familial Parkinson's disease alter the initiation and amplification steps of

- alpha-synuclein aggregation". In: *Proceedings of the National Academy of Sciences* 113.37, pp. 10328–10333. DOI: 10.1073/pnas.1604645113.
- Fricke, Franziska, Joel Beaudouin, Roland Eils, and Mike Heilemann (2015). "One, two or three? Probing the stoichiometry of membrane proteins by single-molecule localization microscopy". In: *Scientific Reports* 5, p. 14072. DOI: 10.1038/srep14072.
- Frid, Petrea, Sergey V. Anisimov, and Natalija Popovic (2007). "Congo red and protein aggregation in neurodegenerative diseases". In: *Brain Research Reviews* 53.1, pp. 135–160. DOI: 10.1016/j.brainresrev.2006.08.001.
- Fridy, Peter C. et al. (2014). "A robust pipeline for rapid production of versatile nanobody repertoires". In: *Nature Methods* 11.12, pp. 1253–1260. DOI: 10.1038/nmeth.3170.
- Fujioka, Shinsuke, Kotaro Ogaki, Pawel M. Tacik, Ryan J. Uitti, Owen A. Ross, and Zbigniew K. Wszolek (2014). "Update on novel familial forms of Parkinson's disease and multiple system atrophy". In: *Parkinsonism & Related Disorders* 20 Suppl 1, S29–34. DOI: 10.1016/S1353-8020(13)70010-5.
- Fusco, Giuliana, Alfonso De Simone, Tata Gopinath, Vitaly Vostrikov, Michele Vendruscolo, Christopher M. Dobson, and Gianluigi Veglia (2014). "Direct observation of the three regions in alpha-synuclein that determine its membrane-bound behaviour". In: *Nature Communications* 5, p. 3827. DOI: 10.1038/ncomms4827.
- Fändrich, M. (2007). "On the structural definition of amyloid fibrils and other polypeptide aggregates". In: *Cellular and Molecular Life Sciences* 64.16, pp. 2066–2078. DOI: 10.1007/s00018-007-7110-2.
- Gallegos, Scarlet, Carla Pacheco, Christian Peters, Carlos M. Opazo, and Luis G. Aguayo (2015). "Features of alpha-synuclein that could explain the progression and irreversibility of Parkinson's disease". In: *Frontiers in Neuroscience* 9. DOI: 10.3389/fnins.2015.00059.
- Galvagnion, Céline, Alexander K. Buell, Georg Meisl, Thomas C. T. Michaels, Michele Vendruscolo, Tuomas P. J. Knowles, and Christopher M. Dobson (2015). "Lipid vesicles trigger alpha-synuclein aggregation by stimulating primary nucleation". In: *Nature Chemical Biology* 11.3, pp. 229–234. DOI: 10.1038/nchembio.1750.
- Gardner, G. A. (1968). *Effects of Pasteurization or Added Sulphite on the Microbiology of Stored Vacuum Packed Baconburgers*. Journal of Applied Bacteriology.
- Gaspar, Ricardo, Georg Meisl, Alexander K. Buell, Laurence Young, Clemens F. Kaminski, Tuomas P. J. Knowles, Emma Sparr, and Sara Linse (2017). "Secondary nucleation of monomers on fibril surface dominates alpha-synuclein aggregation and provides autocatalytic amyloid amplification". In: *Quarterly Reviews of Biophysics* 50. DOI: 10.1017/S0033583516000172.
- Goldsbury, C., K. Goldie, J. Pellaud, J. Seelig, P. Frey, S. A. Müller, J. Kistler, G. J. S. Cooper, and U. Aebi (2000). "Amyloid Fibril Formation from Full-Length and Fragments of Amylin". In: *Journal of Structural Biology* 130.2, pp. 352–362. DOI: 10.1006/jjsbi.2000.4268.
- Goodwin, Paul C. (2007). "Evaluating Optical Aberration Using Fluorescent Microspheres: Methods, Analysis, and Corrective Actions". In: *Methods in Cell Biology*. Vol. 81. Digital Microscopy, 3rd Edition. Academic Press, pp. 397–413. DOI: 10.1016/S0091-679X(06)81018-6.
- Greenwald, Jason and Roland Riek (2010). "Biology of Amyloid: Structure, Function, and Regulation". In: *Structure* 18.10, pp. 1244–1260. DOI: 10.1016/j.str.2010.08.009.
- Gribaudo, Simona, Philippe Tixador, Luc Bousset, Alexis Fenyi, Patricia Lino, Ronald Melki, Jean-Michel Peyrin, and Anselme L. Perrier (2019). "Propagation of alpha-Synuclein Strains within Human Reconstructed Neuronal Network". In: *Stem Cell Reports* 12.2, pp. 230–244. DOI: 10.1016/j.stemcr.2018.12.007.
- Grimm, Jonathan B., Andrew J. Sung, Wesley R. Legant, Phuson Hulamm, Sylwia M. Matlosz, Eric Betzig, and Luke D. Lavis (2013). "Carbofluoresceins and Carborhodamines as Scaffolds for High-Contrast Fluorogenic Probes". In: *ACS Chemical Biology* 8.6, pp. 1303–1310. DOI: 10.1021/cb4000822.

- Grimm, Jonathan B. et al. (2016). "Bright photoactivatable fluorophores for single-molecule imaging". In: *Nature Methods* 13.12, pp. 985–988. DOI: 10.1038/nmeth.4034.
- Grimm, Jonathan B. et al. (2017). "A general method to fine-tune fluorophores for live-cell and in vivo imaging". In: *Nature Methods* 14.10, pp. 987–994. DOI: 10.1038/nmeth.4403.
- Gudkov, S. V., O. E. Karp, S. A. Garmash, V. E. Ivanov, A. V. Chernikov, A. A. Manokhin, M. E. Astashev, L. S. Yaguzhinsky, and V. I. Bruskov (2012). "Generation of reactive oxygen species in water under exposure to visible or infrared irradiation at absorption bands of molecular oxygen". In: *Biophysics* 57.1, pp. 1–8. DOI: 10.1134/S0006350912010113.
- Guerrero-Ferreira, Ricardo, Nicholas MI Taylor, Daniel Mona, Philippe Ringler, Matthias E. Lauer, Roland Riek, Markus Britschgi, and Henning Stahlberg (2018). *Cryo-EM structure of alpha-synuclein fibrils*. eLife.
- Guerrero-Ferreira, Ricardo et al. (2019). "Two new polymorphic structures of alpha-synuclein solved by cryo-electron microscopy". In: *bioRxiv*, p. 654582. DOI: 10.1101/654582.
- Gustafsson, M. G. L. (2000). "Surpassing the lateral resolution limit by a factor of two using structured illumination microscopy". In: *Journal of Microscopy* 198.2, pp. 82–87. DOI: 10.1046/j.1365-2818.2000.00710.x.
- Göttfert, Fabian, Tino Pleiner, Jörn Heine, Volker Westphal, Dirk Görlich, Steffen J. Sahl, and Stefan W. Hell (2017). "Strong signal increase in STED fluorescence microscopy by imaging regions of subdiffraction extent". In: *Proceedings of the National Academy of Sciences* 114.9, pp. 2125–2130. DOI: 10.1073/pnas.1621495114.
- Hack, Nicola J, Brian Billups, Peter B Guthrie, John H Rogers, Elizabeth M Muir, Thomas N Parks, and Stanley B Kater (2000). "Green fluorescent protein as a quantitative tool". In: *Journal of Neuroscience Methods* 95.2, pp. 177–184. DOI: 10.1016/S0165-0270(99)00178-8.
- Haji, Bassam, Jan Wisniewski, Mohamed El Beheiry, Jiji Chen, Andrey Revyakin, Carl Wu, and Maxime Dahan (2014). "Whole-cell, multicolor superresolution imaging using volumetric multifocus microscopy". In: *Proceedings of the National Academy of Sciences of the United States of America* 111.49, pp. 17480–17485. DOI: 10.1073/pnas.1412396111.
- Ham, Tjakko J. van, Alessandro Esposito, Janet R. Kumita, Shang-Te D. Hsu, Gabriele S. Kaminski Schierle, Clemens F. Kaminski, Christopher M. Dobson, Ellen A. A. Nollen, and Carlos W. Bertoncini (2010). "Towards multiparametric fluorescent imaging of amyloid formation: studies of a YFP model of alpha-synuclein aggregation". In: *Journal of Molecular Biology* 395.3, pp. 627–642. DOI: 10.1016/j.jmb.2009.10.066.
- Hansen, Christian et al. (2011). "alpha-Synuclein propagates from mouse brain to grafted dopaminergic neurons and seeds aggregation in cultured human cells". In: *The Journal of Clinical Investigation* 121.2, pp. 715–725. DOI: 10.1172/JCI43366.
- Hara, Taichi et al. (2006). "Suppression of basal autophagy in neural cells causes neurodegenerative disease in mice". In: *Nature* 441.7095, pp. 885–889. DOI: 10.1038/nature04724.
- Harada, Yoshie, Katsuhiko Sakurada, Toshiaki Aoki, David D. Thomas, and Toshio Yanagida (1990). "Mechanochemical coupling in actomyosin energy transduction studied by in vitro movement assay". In: *Journal of Molecular Biology* 216.1, pp. 49–68. DOI: 10.1016/S0022-2836(05)80060-9.
- Hartwich, Tobias M. P., Kenny Kwok Hin Chung, Lena Schroeder, Joerg Bewersdorf, Christian Soeller, and David Baddeley (2018). "A stable, high refractive index, switching buffer for super-resolution imaging". In: *bioRxiv*, p. 465492. DOI: 10.1101/465492.
- He, Runcheng, Xinxiang Yan, Jifeng Guo, Qian Xu, Beisha Tang, and Qiying Sun (2018). "Recent Advances in Biomarkers for Parkinson's Disease". In: *Frontiers in Aging Neuroscience* 10. DOI: 10.3389/fnagi.2018.00305.
- Heilemann, Mike, Emmanuel Margeat, Robert Kasper, Markus Sauer, and Philip Tinnefeld (2005). "Carbocyanine Dyes as Efficient Reversible Single-Molecule Optical Switch". In: *Journal of the American Chemical Society* 127.11, pp. 3801–3806. DOI: 10.1021/ja044686x.

- Heilemann, Mike, Sebastian van de Linde, Mark Schüttpelz, Robert Kasper, Britta Seefeldt, Anindita Mukherjee, Philip Tinnefeld, and Markus Sauer (2008). "Subdiffraction-Resolution Fluorescence Imaging with Conventional Fluorescent Probes". In: *Angewandte Chemie International Edition* 47.33, pp. 6172–6176. DOI: 10.1002/anie.200802376.
- Heilemann, Mike, Sebastian van de Linde, Anindita Mukherjee, and Markus Sauer (2009). "Super-Resolution Imaging with Small Organic Fluorophores". In: *Angewandte Chemie International Edition* 48.37, pp. 6903–6908. DOI: 10.1002/anie.200902073.
- Hell, Stefan W. and Jan Wichmann (1994). "Breaking the diffraction resolution limit by stimulated emission: stimulated-emission-depletion fluorescence microscopy". In: *Optics Letters* 19.11, pp. 780–782. DOI: 10.1364/OL.19.000780.
- Hell, Stefan W, Marcus Dyba, and Stefan Jakobs (2004). "Concepts for nanoscale resolution in fluorescence microscopy". In: *Current Opinion in Neurobiology* 14.5, pp. 599–609. DOI: 10.1016/j.conb.2004.08.015.
- Hess, Samuel T, Thanu P. K. Girirajan, and Michael D. Mason (2006). "Ultra-high resolution imaging by fluorescence photoactivation localization microscopy". In: *Biophysical Journal* 91.11, pp. 4258–4272. DOI: 10.1529/biophysj.106.091116.
- Hoess, Philipp, Markus Mund, Manuel Reitberger, and Jonas Ries (2018). "Dual-Color and 3D Super-Resolution Microscopy of Multi-protein Assemblies". In: *Protein Complex Assembly: Methods and Protocols*. Ed. by Joseph A. Marsh. Methods in Molecular Biology. New York, NY: Springer New York, pp. 237–251. ISBN: 978-1-4939-7759-8. DOI: 10.1007/978-1-4939-7759-8_14.
- Hoyer, Wolfgang, Thomas Antony, Dmitry Cherny, Gudrun Heim, Thomas M. Jovin, and Vinod Subramaniam (2002). "Dependence of alpha-synuclein aggregate morphology on solution conditions". In: *Journal of Molecular Biology* 322.2, pp. 383–393. DOI: 10.1016/s0022-2836(02)00775-1.
- Hoyer, Wolfgang, Dmitry Cherny, Vinod Subramaniam, and Thomas M. Jovin (2004). "Rapid Self-assembly of alpha-Synuclein Observed by In Situ Atomic Force Microscopy". In: *Journal of Molecular Biology* 340.1, pp. 127–139. DOI: 10.1016/j.jmb.2004.04.051.
- Huang, Bo, Wenqin Wang, Mark Bates, and Xiaowei Zhuang (2008a). "Three-dimensional super-resolution imaging by stochastic optical reconstruction microscopy". In: *Science (New York, N.Y.)* 319.5864, pp. 810–813. DOI: 10.1126/science.1153529.
- Huang, Bo, Sara A. Jones, Boerries Brandenburg, and Xiaowei Zhuang (2008b). "Whole-cell 3D STORM reveals interactions between cellular structures with nanometer-scale resolution". In: *Nature Methods* 5.12, pp. 1047–1052. DOI: 10.1038/nmeth.1274.
- Huang, Bo, Mark Bates, and Xiaowei Zhuang (2009). "Super resolution fluorescence microscopy". In: *Annual review of biochemistry* 78, pp. 993–1016. DOI: 10.1146/annurev.biochem.77.061906.092014.
- Huang, Chunjuan, Guoping Ren, Hui Zhou, and Chih-chen Wang (2005). "A new method for purification of recombinant human alpha-synuclein in Escherichia coli". In: *Protein Expression and Purification* 42.1, pp. 173–177. DOI: 10.1016/j.pep.2005.02.014.
- Huang, Fang et al. (2013). "Video-rate nanoscopy using sCMOS camera-specific single-molecule localization algorithms". In: *Nature Methods* 10.7, pp. 653–658. DOI: 10.1038/nmeth.2488.
- Huang, Fang et al. (2016). "Ultra-High Resolution 3D Imaging of Whole Cells". In: *Cell* 166.4, pp. 1028–1040. DOI: 10.1016/j.cell.2016.06.016.
- Hummer, Gerhard, Franziska Fricke, and Mike Heilemann (2016). "Model-independent counting of molecules in single-molecule localization microscopy". In: *Molecular Biology of the Cell* 27.22, pp. 3637–3644. DOI: 10.1091/mbc.E16-07-0525.
- Inoue, Yuji, Aiko Kishimoto, Jun Hirao, Masasuke Yoshida, and Hideki Taguchi (2001). "Strong Growth Polarity of Yeast Prion Fiber Revealed by Single Fiber Imaging". In: *Journal of Biological Chemistry* 276.38, pp. 35227–35230. DOI: 10.1074/jbc.C100304200.
- Iwai, Akihiko, Eliezer Masliah, Makoto Yoshimoto, Nianfeng Ge, Lisa Flanagan, H. A. Rohan de Silva, Agnes Kittel, and Tsunao Saitoh (1995). "The precursor protein of

- non-Abeta component of Alzheimer's disease amyloid is a presynaptic protein of the central nervous system". In: *Neuron* 14.2, pp. 467–475. DOI: 10.1016/0896-6273(95)90302-X.
- Iyer, Aditya, Steven J. Roeters, Nathalie Schilderink, Bob Hommersom, Ron M. A. Heeren, Sander Woutersen, Mireille M. A. E. Claessens, and Vinod Subramaniam (2016). "The Impact of N-terminal Acetylation of Alpha Synuclein on Phospholipid Membrane Binding and Fibril Structure". In: *Journal of Biological Chemistry*, jbc.M116.726612. DOI: 10.1074/jbc.M116.726612.
- Jablonski, A. (1933). "Efficiency of Anti-Stokes Fluorescence in Dyes". In: *Nature* 131.3319, p. 839. DOI: 10.1038/131839b0.
- Janezic, Stephanie et al. (2013). "Deficits in dopaminergic transmission precede neuron loss and dysfunction in a new Parkinson model". In: *Proceedings of the National Academy of Sciences* 110.42, E4016. DOI: 10.1073/pnas.1309143110.
- Juette, Manuel F., Travis J. Gould, Mark D. Lessard, Michael J. Mlodzianoski, Bhupendra S. Nagpure, Brian T. Bennett, Samuel T. Hess, and Joerg Bewersdorf (2008). "Three-dimensional sub-100 nm resolution fluorescence microscopy of thick samples". In: *Nature Methods* 5.6, pp. 527–529. DOI: 10.1038/nmeth.1211.
- Kaksonen, Marko and Aurélien Roux (2018). "Mechanisms of clathrin-mediated endocytosis". In: *Nature Reviews Molecular Cell Biology* 19.5, pp. 313–326. DOI: 10.1038/nrm.2017.132.
- Karpinar, Damla Pinar et al. (2009). "Pre-fibrillar alpha-synuclein variants with impaired beta-structure increase neurotoxicity in Parkinson's disease models". In: *The EMBO journal* 28.20, pp. 3256–3268. DOI: 10.1038/emboj.2009.257.
- Kellermayer, Miklós S. Z., Árpád Karsai, Margit Benke, Katalin Soós, and Botond Penke (2008). "Stepwise dynamics of epitaxially growing single amyloid fibrils". In: *Proceedings of the National Academy of Sciences* 105.1, pp. 141–144. DOI: 10.1073/pnas.0704305105.
- Keppler, Antje, Susanne Gendreizig, Thomas Gronemeyer, Horst Pick, Horst Vogel, and Kai Johnsson (2003). "A general method for the covalent labeling of fusion proteins with small molecules in vivo". In: *Nature Biotechnology* 21.1, p. 86. DOI: 10.1038/nbt765.
- Khoshouei, Maryam, Mazdak Radjainia, Wolfgang Baumeister, and Radostin Danev (2017). "Cryo-EM structure of haemoglobin at 3.2 Å determined with the Volta phase plate". In: *Nature Communications* 8, p. 16099. DOI: 10.1038/ncomms16099.
- Klar, Thomas A., Stefan Jakobs, Marcus Dyba, Alexander Egner, and Stefan W. Hell (2000). "Fluorescence microscopy with diffraction resolution barrier broken by stimulated emission". In: *Proceedings of the National Academy of Sciences* 97.15, p. 8206. DOI: 10.1073/pnas.97.15.8206.
- Klehs, Kathrin, Christoph Spahn, Ulrike Endesfelder, Steven F. Lee, Alexandre Fürstenberg, and Mike Heilemann (2014). "Increasing the brightness of cyanine fluorophores for single-molecule and superresolution imaging". In: *Chemphyschem: A European Journal of Chemical Physics and Physical Chemistry* 15.4, pp. 637–641. DOI: 10.1002/cphc.201300874.
- Klingstedt, Therése, Andreas Åslund, Rozalyn A. Simon, Leif B. G. Johansson, Jeffrey J. Mason, Sofie Nyström, Per Hammarström, and K. Peter R. Nilsson (2011). "Synthesis of a library of oligothiophenes and their utilization as fluorescent ligands for spectral assignment of protein aggregates". In: *Organic & Biomolecular Chemistry* 9.24, pp. 8356–8370. DOI: 10.1039/C1OB05637A.
- Klingstedt, Therése et al. (2013a). "Luminescent conjugated oligothiophenes for sensitive fluorescent assignment of protein inclusion bodies". In: *Chembiochem: A European Journal of Chemical Biology* 14.5, pp. 607–616. DOI: 10.1002/cbic.201200731.
- Klingstedt, Therése, Hamid Shirani, K. O. Andreas Åslund, Nigel J. Cairns, Christina J. Sigurdson, Michel Goedert, and K. Peter R. Nilsson (2013b). "The structural basis for optimal performance of oligothiophene-based fluorescent amyloid ligands: conformational flexibility is essential for spectral assignment of a diversity of protein

- aggregates". In: *Chemistry (Weinheim an Der Bergstrasse, Germany)* 19.31, pp. 10179–10192. DOI: 10.1002/chem.201301463.
- Knockenbauer, Kevin E. and Thomas U. Schwartz (2016). "The Nuclear Pore Complex as a Flexible and Dynamic Gate". In: *Cell* 164.6, pp. 1162–1171. DOI: 10.1016/j.cell.2016.01.034.
- Knowles, Tuomas P. J., Wenmiao Shu, Glyn L. Devlin, Sarah Meehan, Stefan Auer, Christopher M. Dobson, and Mark E. Welland (2007). "Kinetics and thermodynamics of amyloid formation from direct measurements of fluctuations in fibril mass". In: *Proceedings of the National Academy of Sciences* 104.24, pp. 10016–10021. DOI: 10.1073/pnas.0610659104.
- Koch, Birgit, Bianca Nijmeijer, Moritz Kueblbeck, Yin Cai, Nike Walther, and Jan Ellenberg (2018). "Generation and validation of homozygous fluorescent knock-in cells using CRISPR-Cas9 genome editing". In: *Nature Protocols* 13.6, pp. 1465–1487. DOI: 10.1038/nprot.2018.042.
- Koide, Yuichiro, Yasuteru Urano, Kenjiro Hanaoka, Takuya Terai, and Tetsuo Nagano (2011). "Evolution of Group 14 Rhodamines as Platforms for Near-Infrared Fluorescence Probes Utilizing Photoinduced Electron Transfer". In: *ACS Chemical Biology* 6.6, pp. 600–608. DOI: 10.1021/cb1002416.
- Komatsu, Masaaki et al. (2006). "Loss of autophagy in the central nervous system causes neurodegeneration in mice". In: *Nature* 441.7095, pp. 880–884. DOI: 10.1038/nature04723.
- Koo, Edward H., Peter T. Lansbury, and Jeffery W. Kelly (1999). "Amyloid diseases: Abnormal protein aggregation in neurodegeneration". In: *Proceedings of the National Academy of Sciences* 96.18, pp. 9989–9990. DOI: 10.1073/pnas.96.18.9989.
- Kordower, Jeffrey H., Yaping Chu, Robert A. Hauser, Thomas B. Freeman, and C. Warren Olanow (2008). "Lewy body-like pathology in long-term embryonic nigral transplants in Parkinson's disease". In: *Nature Medicine* 14.5, pp. 504–506. DOI: 10.1038/nm1747.
- Kosinski, Jan et al. (2016). "Molecular architecture of the inner ring scaffold of the human nuclear pore complex". In: *Science* 352.6283, pp. 363–365. DOI: 10.1126/science.aaf0643.
- Krebs, M. R. H., E. H. C. Bromley, and A. M. Donald (2005). "The binding of thioflavin-T to amyloid fibrils: localisation and implications". In: *Journal of Structural Biology* 149.1, pp. 30–37. DOI: 10.1016/j.jsb.2004.08.002.
- Krüger, Rejko et al. (1998). "AlaSOPro mutation in the gene encoding alpha-synuclein in Parkinson's disease". In: *Nature Genetics* 18.2, p. 106. DOI: 10.1038/ng0298-106.
- Kukulski, Wanda, Martin Schorb, Sonja Welsch, Andrea Picco, Marko Kaksonen, and John A. G. Briggs (2011). "Correlated fluorescence and 3D electron microscopy with high sensitivity and spatial precision". In: *The Journal of Cell Biology* 192.1, pp. 111–119. DOI: 10.1083/jcb.201009037.
- Kukulski, Wanda, Martin Schorb, Marko Kaksonen, and John A. G. Briggs (2012). "Plasma Membrane Reshaping during Endocytosis Is Revealed by Time-Resolved Electron Tomography". In: *Cell* 150.3, pp. 508–520. DOI: 10.1016/j.cell.2012.05.046.
- Kühlbrandt, Werner (2014). "The Resolution Revolution". In: *Science* 343.6178, pp. 1443–1444. DOI: 10.1126/science.1251652.
- Lang, Kathrin and Jason W. Chin (2014). "Bioorthogonal Reactions for Labeling Proteins". In: *ACS Chemical Biology* 9.1, pp. 16–20. DOI: 10.1021/cb4009292.
- Lashuel, Hilal A., Cassia R. Overk, Abid Oueslati, and Eliezer Masliah (2013). "The many faces of alpha-synuclein: from structure and toxicity to therapeutic target". In: *Nature Reviews. Neuroscience* 14.1, pp. 38–48. DOI: 10.1038/nrn3406.
- Lautenschläger, Janin et al. (2018). "C-terminal calcium binding of alpha-synuclein modulates synaptic vesicle interaction". In: *Nature Communications* 9.1, p. 712. DOI: 10.1038/s41467-018-03111-4.
- Lavis, Luke D. and Ronald T. Raines (2008). "Bright Ideas for Chemical Biology". In: *ACS Chemical Biology* 3.3, pp. 142–155. DOI: 10.1021/cb700248m.

- Lee, Ji-Eun et al. (2018). "Mapping Surface Hydrophobicity of alpha-Synuclein Oligomers at the Nanoscale". In: *Nano Letters* 18.12, pp. 7494–7501. DOI: 10.1021/acs.nanolett.8b02916.
- Lee, Sang-Hyuk, Jae Yen Shin, Antony Lee, and Carlos Bustamante (2012). "Counting single photoactivatable fluorescent molecules by photoactivated localization microscopy (PALM)". In: *Proceedings of the National Academy of Sciences* 109.43, pp. 17436–17441. DOI: 10.1073/pnas.1215175109.
- Lee, Steven F., Quentin Vérolet, and Alexandre Fürstenberg (2013). "Improved Super-Resolution Microscopy with Oxazine Fluorophores in Heavy Water". In: *Angewandte Chemie International Edition* 52.34, pp. 8948–8951. DOI: 10.1002/anie.201302341.
- Legant, Wesley R, Lin Shao, Jonathan B Grimm, Timothy A Brown, Daniel E Milkie, Brian B Avants, Luke D Lavis, and Eric Betzig (2016). "High-density three-dimensional localization microscopy across large volumes". In: *Nature Methods* 13, p. 359.
- Lemkau, Luisel R., Gemma Comellas, Kathryn D. Kloepper, Wendy S. Woods, Julia M. George, and Chad M. Rienstra (2012). "Mutant Protein A30P alpha-Synuclein Adopts Wild-type Fibril Structure, Despite Slower Fibrillation Kinetics". In: *Journal of Biological Chemistry* 287.14, pp. 11526–11532. DOI: 10.1074/jbc.M111.306902.
- "Lenses and Geometrical Optics" (2012). In: Murphy, Douglas B. and Michael W. Davidson. *Fundamentals of Light Microscopy and Electronic Imaging*. John Wiley & Sons, Ltd, pp. 53–77. ISBN: 978-1-118-38290-5. DOI: 10.1002/9781118382905.ch4.
- Lesage, Suzanne et al. (2013). "G51D alpha-synuclein mutation causes a novel Parkinsonian–pyramidal syndrome". In: *Annals of Neurology* 73.4, pp. 459–471. DOI: 10.1002/ana.23894.
- Li, Bin and Jennifer J. Kohler (2014). "Glycosylation of the nuclear pore". In: *Traffic (Copenhagen, Denmark)* 15.4, pp. 347–361. DOI: 10.1111/tra.12150.
- Li, Binsen et al. (2018a). "Cryo-EM of full-length alpha-synuclein reveals fibril polymorphs with a common structural kernel". In: *Nature Communications* 9.1, p. 3609. DOI: 10.1038/s41467-018-05971-2.
- Li, Jia-Yi et al. (2008). "Lewy bodies in grafted neurons in subjects with Parkinson's disease suggest host-to-graft disease propagation". In: *Nature Medicine* 14.5, pp. 501–503. DOI: 10.1038/nm1746.
- Li, Yaowang et al. (2018b). "Amyloid fibril structure of alpha-synuclein determined by cryo-electron microscopy". In: *Cell Research* 28.9, pp. 897–903. DOI: 10.1038/s41422-018-0075-x.
- Li, Yiming et al. (2018c). "Real-time 3D single-molecule localization using experimental point spread functions". In: *Nature Methods* 15.5, pp. 367–369. DOI: 10.1038/nmeth.4661.
- Li, Yiming, Yu-Le Wu, Philipp Hoess, Markus Mund, and Jonas Ries (2019). "Depth-dependent PSF calibration and aberration correction for 3D single-molecule localization". In: *Biomedical Optics Express* 10.6, pp. 2708–2718. DOI: 10.1364/BOE.10.002708.
- Lin, Yu et al. (2015). "Quantifying and Optimizing Single-Molecule Switching Nanoscopy at High Speeds". In: *PLOS ONE* 10.5. Éd. by Vadim E. Degtyar, e0128135. DOI: 10.1371/journal.pone.0128135.
- Linde, Sebastian van de, Anna Löschberger, Teresa Klein, Meike Heidebreder, Steve Wolter, Mike Heilemann, and Markus Sauer (2011). "Direct stochastic optical reconstruction microscopy with standard fluorescent probes". In: *Nature Protocols* 6.7, pp. 991–1009. DOI: 10.1038/nprot.2011.336.
- Linde, Sebastian van de and Markus Sauer (2014). "How to switch a fluorophore: from undesired blinking to controlled photoswitching". In: *Chemical Society Reviews* 43.4, pp. 1076–1087. DOI: 10.1039/C3CS60195A.
- Liu, Yuxi, Duc T. Huynh, and Todd O. Yeates (2019). "A 3.8 Å resolution cryo-EM structure of a small protein bound to an imaging scaffold". In: *Nature Communications* 10.1, pp. 1–7. DOI: 10.1038/s41467-019-09836-0.

- Los, Georgyi V. et al. (2008). "HaloTag: A Novel Protein Labeling Technology for Cell Imaging and Protein Analysis". In: *ACS Chemical Biology* 3.6, pp. 373–382. DOI: 10.1021/cb800025k.
- Ludtmann, Marthe H. R., Plamena R. Angelova, Natalia N. Ninkina, Sonia Gandhi, Vladimir L. Buchman, and Andrey Y. Abramov (2016). "Monomeric Alpha-Synuclein Exerts a Physiological Role on Brain ATP Synthase". In: *The Journal of Neuroscience: The Official Journal of the Society for Neuroscience* 36.41, pp. 10510–10521. DOI: 10.1523/JNEUROSCI.1659-16.2016.
- Ludtmann, Marthe H. R. et al. (2018). "alpha-synuclein oligomers interact with ATP synthase and open the permeability transition pore in Parkinson's disease". In: *Nature Communications* 9.1, p. 2293. DOI: 10.1038/s41467-018-04422-2.
- Lukinavičius, Gražvydas et al. (2013). "A near-infrared fluorophore for live-cell super-resolution microscopy of cellular proteins". In: *Nature Chemistry* 5.2, pp. 132–139. DOI: 10.1038/nchem.1546.
- Lukyanov, Konstantin A., Dmitry M. Chudakov, Sergey Lukyanov, and Vladislav V. Verkhusha (2005). "Photoactivatable fluorescent proteins". In: *Nature Reviews Molecular Cell Biology* 6.11, p. 885. DOI: 10.1038/nrm1741.
- Lundblad, Martin, Mickael Decressac, Bengt Mattsson, and Anders Björklund (2012). "Impaired neurotransmission caused by overexpression of alpha-synuclein in nigral dopamine neurons". In: *Proceedings of the National Academy of Sciences* 109.9, p. 3213. DOI: 10.1073/pnas.1200575109.
- Maji, Samir K. et al. (2009). "Functional Amyloids as Natural Storage of Peptide Hormones in Pituitary Secretory Granules". In: *Science (New York, N.Y.)* 325.5938, pp. 328–332. DOI: 10.1126/science.1173155.
- Makky, Ali, Luc Bousset, Jérôme Polesel-Maris, and Ronald Melki (2016). "Nanomechanical properties of distinct fibrillar polymorphs of the protein alpha-synuclein". In: *Scientific Reports* 6, p. 37970. DOI: 10.1038/srep37970.
- Malagelada, Cristina, Zong Hao Jin, Vernice Jackson-Lewis, Serge Przedborski, and Lloyd A. Greene (2010). "Rapamycin protects against neuron death in in vitro and in vivo models of Parkinson's disease". In: *The Journal of Neuroscience: The Official Journal of the Society for Neuroscience* 30.3, pp. 1166–1175. DOI: 10.1523/JNEUROSCI.3944-09.2010.
- Marion, Dominique (2013). "An Introduction to Biological NMR Spectroscopy". In: *Molecular & Cellular Proteomics: MCP* 12.11, pp. 3006–3025. DOI: 10.1074/mcp.O113.030239.
- Maroteaux, L. and R. H. Scheller (1991). "The rat brain synucleins; family of proteins transiently associated with neuronal membrane". In: *Molecular Brain Research* 11.3, pp. 335–343. DOI: 10.1016/0169-328X(91)90043-W.
- Masliah, Eliezer, Edward Rockenstein, Isaac Veinbergs, Margaret Mallory, Makoto Hashimoto, Ayako Takeda, Yutaka Sagara, Abbyann Sisk, and Lennart Mucke (2000). "Dopaminergic Loss and Inclusion Body Formation in alpha-Synuclein Mice: Implications for Neurodegenerative Disorders". In: *Science* 287.5456, pp. 1265–1269. DOI: 10.1126/science.287.5456.1265.
- McEvoy, Ann L. et al. (2012). "mMaple: A Photoconvertible Fluorescent Protein for Use in Multiple Imaging Modalities". In: *PLoS ONE* 7.12. DOI: 10.1371/journal.pone.0051314.
- Morello, J. A., Margot R. Craw, H. P. Constantine, and R. E. Forster (1964). "Rate of reaction of dithionite ion with oxygen in aqueous solution". In: *Journal of Applied Physiology* 19.3, pp. 522–525. DOI: 10.1152/jappl.1964.19.3.522.
- Mund, Markus, Charlotte Kaplan, and Jonas Ries (2014). "Localization microscopy in yeast". In: *Methods in Cell Biology* 123, pp. 253–271. DOI: 10.1016/B978-0-12-420138-5.00014-8.
- Mund, Markus et al. (2018). "Systematic Nanoscale Analysis of Endocytosis Links Efficient Vesicle Formation to Patterned Actin Nucleation". In: *Cell* 174.4, 884–896.e17. DOI: 10.1016/j.cell.2018.06.032.

- Murphy, Douglas B. and Michael W. Davidson (2012). *Fundamentals of Light Microscopy and Electronic Imaging*. Google-Books-ID: f8qhtqRjxQMC. John Wiley & Sons. 904 pp. ISBN: 978-1-118-38293-6.
- Mučibabić, M., M.M. Apetri, G.W. Canters, and T.J. Aartsma (2016). "The effect of fluorescent labeling on alpha-synuclein fibril morphology". In: *Biochimica et Biophysica Acta (BBA) - Proteins and Proteomics* 1864.10, pp. 1419–1427. DOI: 10.1016/j.bbapap.2016.07.007.
- Nahidiazar, Leila, Alexandra V. Agronskaia, Jorrit Broertjes, Bram van den Broek, and Kees Jalink (2016). "Optimizing Imaging Conditions for Demanding Multi-Color Super Resolution Localization Microscopy". In: *PLOS ONE* 11.7, e0158884. DOI: 10.1371/journal.pone.0158884.
- Narhi, Linda et al. (1999). "Both Familial Parkinson's Disease Mutations Accelerate alpha-Synuclein Aggregation". In: *Journal of Biological Chemistry* 274.14, pp. 9843–9846. DOI: 10.1074/jbc.274.14.9843.
- Narkiewicz, Joanna, Gabriele Giachin, and Giuseppe Legname (2014). "In vitro aggregation assays for the characterization of alpha-synuclein prion-like properties". In: *Prion* 8.1, pp. 19–32. DOI: 10.4161/pri.28125.
- Nemani, Venu M., Wei Lu, Victoria Berge, Ken Nakamura, Bibiana Onoa, Michael K. Lee, Farrukh A. Chaudhry, Roger A. Nicoll, and Robert H. Edwards (2010). "Increased expression of alpha-synuclein reduces neurotransmitter release by inhibiting synaptic vesicle reclustering after endocytosis". In: *Neuron* 65.1, pp. 66–79. DOI: 10.1016/j.neuron.2009.12.023.
- Nielsen, Liza, Ritu Khurana, Alisa Coats, Sven Frokjaer, Jens Brange, Sandip Vyas, Vladimir N. Uversky, and Anthony L. Fink (2001). "Effect of Environmental Factors on the Kinetics of Insulin Fibril Formation: Elucidation of the Molecular Mechanism". In: *Biochemistry* 40.20, pp. 6036–6046. DOI: 10.1021/bi002555c.
- Nilsson, K. Peter R. et al. (2007). "Imaging distinct conformational states of amyloid-beta fibrils in Alzheimer's disease using novel luminescent probes". In: *ACS chemical biology* 2.8, pp. 553–560. DOI: 10.1021/cb700116u.
- Nilsson, K. Peter R., Mikael Lindgren, and Per Hammarström (2012). "A pentameric luminescent-conjugated oligothiophene for optical imaging of in vitro-formed amyloid fibrils and protein aggregates in tissue sections". In: *Methods in Molecular Biology (Clifton, N.J.)* 849, pp. 425–434. DOI: 10.1007/978-1-61779-551-0_29.
- Nilsson, Melanie R (2004). "Techniques to study amyloid fibril formation in vitro". In: *Methods. Investigating Protein Folding, Misfolding and Nonnative States: Experimental and Theoretical Methods* 34.1, pp. 151–160. DOI: 10.1016/j.ymeth.2004.03.012.
- Okochi, Masayasu, Jochen Walter, Akihiko Koyama, Shigeo Nakajo, Minami Baba, Takeshi Iwatsubo, Laurent Meijer, Philipp J. Kahle, and Christian Haass (2000). "Constitutive Phosphorylation of the Parkinson's Disease Associated alpha-Synuclein". In: *Journal of Biological Chemistry* 275.1, pp. 390–397. DOI: 10.1074/jbc.275.1.390.
- Olivier, Nicolas, Debora Keller, Pierre Gönczy, and Suliana Manley (2013). "Resolution Doubling in 3D-STORM Imaging through Improved Buffers". In: *PLOS ONE* 8.7, e69004. DOI: 10.1371/journal.pone.0069004.
- Ong, Wei Qiang, Y. Rose Citron, Joerg Schnitzbauer, Daichi Kamiyama, and Bo Huang (2015). "Heavy water: a simple solution to increasing the brightness of fluorescent proteins in super-resolution imaging". In: *Chemical Communications (Cambridge, England)* 51.70, pp. 13451–13453. DOI: 10.1039/c5cc04575d.
- Ori, Alessandro et al. (2013). "Cell type-specific nuclear pores: a case in point for context-dependent stoichiometry of molecular machines". In: *Molecular Systems Biology* 9.1. DOI: 10.1038/msb.2013.4.
- Ozawa, Daisaku, Hisashi Yagi, Tadato Ban, Atsushi Kameda, Toru Kawakami, Hironobu Naiki, and Yuji Goto (2009). "Destruction of Amyloid Fibrils of a beta2-Microglobulin Fragment by Laser Beam Irradiation". In: *Journal of Biological Chemistry* 284.2, pp. 1009–1017. DOI: 10.1074/jbc.M805118200.

- Paravastu, Anant K., Richard D. Leapman, Wai-Ming Yau, and Robert Tycko (2008). "Molecular structural basis for polymorphism in Alzheimer's beta-amyloid fibrils". In: *Proceedings of the National Academy of Sciences* 105.47, pp. 18349–18354. DOI: 10.1073/pnas.0806270105.
- Pasanen, Petra, Liisa Myllykangas, Maija Siitonen, Anna Raunio, Seppo Kaakkola, Jukka Lyytinen, Pentti J. Tienari, Minna Pöyhönen, and Anders Paetau (2014). "A novel alpha-synuclein mutation A53E associated with atypical multiple system atrophy and Parkinson's disease-type pathology". In: *Neurobiology of Aging* 35.9, 2180.e1–2180.e5. DOI: 10.1016/j.neurobiolaging.2014.03.024.
- Patil, Sharadrao M., Andrew Mehta, Suman Jha, and Andrei T. Alexandrescu (2011). "Heterogeneous Amylin Fibril Growth Mechanisms Imaged by Total Internal Reflection Fluorescence Microscopy". In: *Biochemistry* 50.14, pp. 2808–2819. DOI: 10.1021/bi101908m.
- Pavani, Sri Rama Prasanna, Michael A. Thompson, Julie S. Biteen, Samuel J. Lord, Na Liu, Robert J. Twieg, Rafael Piestun, and W. E. Moerner (2009). "Three-dimensional, single-molecule fluorescence imaging beyond the diffraction limit by using a double-helix point spread function". In: *Proceedings of the National Academy of Sciences* 106.9, pp. 2995–2999. DOI: 10.1073/pnas.0900245106.
- Peelaerts, W., L. Bousset, A. Van der Perren, A. Moskalyuk, R. Pulizzi, M. Giugliano, C. Van den Haute, R. Melki, and V. Baekelandt (2015). "alpha-Synuclein strains cause distinct synucleinopathies after local and systemic administration". In: *Nature* 522.7556, pp. 340–344. DOI: 10.1038/nature14547.
- Peng, Chao et al. (2018). "Cellular milieu imparts distinct pathological alpha-synuclein strains in alpha-synucleinopathies". In: *Nature* 557.7706, p. 558. DOI: 10.1038/s41586-018-0104-4.
- Pfeffer, Stefan and Julia Mahamid (2018). "Unravelling molecular complexity in structural cell biology". In: *Current Opinion in Structural Biology*. Cryo electron microscopy: the impact of the cryo-EM revolution in biology • Biophysical and computational methods - Part A 52, pp. 111–118. DOI: 10.1016/j.sbi.2018.08.009.
- Pham, Chi L. L., Ann H. Kwan, and Margaret Sunde (2014). "Functional amyloid: widespread in Nature, diverse in purpose". In: *Essays In Biochemistry* 56, pp. 207–219. DOI: 10.1042/bse0560207.
- Pieri, Laura, Karine Madiona, Luc Bousset, and Ronald Melki (2012). "Fibrillar alpha-synuclein and huntingtin exon 1 assemblies are toxic to the cells". In: *Biophysical Journal* 102.12, pp. 2894–2905. DOI: 10.1016/j.bpj.2012.04.050.
- Pinotsi, Dorothea, Alexander K. Buell, Celine Galvagnion, Christopher M. Dobson, Gabriele S. Kaminski Schierle, and Clemens F. Kaminski (2014). "Direct Observation of Heterogeneous Amyloid Fibril Growth Kinetics via Two-Color Super-Resolution Microscopy". In: *Nano Letters* 14.1, pp. 339–345. DOI: 10.1021/nl4041093.
- Pinotsi, Dorothea, Claire H. Michel, Alexander K. Buell, Romain F. Laine, Pierre Mahou, Christopher M. Dobson, Clemens F. Kaminski, and Gabriele S. Kaminski Schierle (2016). "Nanoscope insights into seeding mechanisms and toxicity of alpha-synuclein species in neurons". In: *Proceedings of the National Academy of Sciences of the United States of America* 113.14, pp. 3815–3819. DOI: 10.1073/pnas.1516546113.
- Pleiner, Tino et al. (2015). "Nanobodies: site-specific labeling for super-resolution imaging, rapid epitope-mapping and native protein complex isolation". In: *eLife* 4. Ed. by Karsten Weis, e11349. DOI: 10.7554/eLife.11349.
- Plotegher, Nicoletta, Elisa Greggio, Marco Bisaglia, and Luigi Bubacco (2014). "Biophysical groundwork as a hinge to unravel the biology of alpha-synuclein aggregation and toxicity". In: *Quarterly Reviews of Biophysics* 47.1, pp. 1–48. DOI: 10.1017/S0033583513000097.
- Polymeropoulos, M. H. et al. (1997). "Mutation in the alpha-synuclein gene identified in families with Parkinson's disease". In: *Science (New York, N.Y.)* 276.5321, pp. 2045–2047. DOI: 10.1126/science.276.5321.2045.
- Pronin, Alexey N., Andrew J. Morris, Andrei Surguchov, and Jeffrey L. Benovic (2000). "Synucleins Are a Novel Class of Substrates for G Protein-coupled Receptor Kinases".

- In: *Journal of Biological Chemistry* 275.34, pp. 26515–26522. DOI: 10.1074/jbc.M003542200.
- Proukakis, Christos, Christopher G. Dudzik, Timothy Brier, Donna S. MacKay, J. Mark Cooper, Glenn L. Millhauser, Henry Houlden, and Anthony H. Schapira (2013). "A novel alpha-synuclein missense mutation in Parkinson disease". In: *Neurology* 80.11, p. 1062. DOI: 10.1212/WNL.0b013e31828727ba.
- Ram, Sripad, Jerry Chao, Prashant Prabhat, E. Sally Ward, and Raimund J. Ober (2007). "A novel approach to determining the three-dimensional location of microscopic objects with applications to 3D particle tracking". In: *Three-Dimensional and Multidimensional Microscopy: Image Acquisition and Processing XIV*. Three-Dimensional and Multidimensional Microscopy: Image Acquisition and Processing XIV. Vol. 6443. International Society for Optics and Photonics, p. 64430D. DOI: 10.1117/12.698763.
- Ribbeck, Katharina and Dirk Görlich (2001). "Kinetic analysis of translocation through nuclear pore complexes". In: *The EMBO Journal* 20.6, pp. 1320–1330. DOI: 10.1093/emboj/20.6.1320.
- Riek, Roland (2017). "The Three-Dimensional Structures of Amyloids". In: *Cold Spring Harbor Perspectives in Biology* 9.2, a023572. DOI: 10.1101/cshperspect.a023572.
- Ries, Jonas et al. (2013). "Superresolution imaging of amyloid fibrils with binding-activated probes". In: *ACS chemical neuroscience* 4.7, pp. 1057–1061. DOI: 10.1021/cn400091m.
- Scheibel, Thomas, Raghuvver Parthasarathy, George Sawicki, Xiao-Min Lin, Heinrich Jaeger, and Susan L. Lindquist (2003). "Conducting nanowires built by controlled self-assembly of amyloid fibers and selective metal deposition". In: *Proceedings of the National Academy of Sciences* 100.8, pp. 4527–4532. DOI: 10.1073/pnas.0431081100.
- Scherzer, Clemens R. et al. (2008). "GATA transcription factors directly regulate the Parkinson's disease-linked gene alpha-synuclein". In: *Proceedings of the National Academy of Sciences* 105.31, pp. 10907–10912. DOI: 10.1073/pnas.0802437105.
- Schieber, Nicole L., Susan J. Nixon, Richard I. Webb, Viola M. J. Oorschot, and Robert G. Parton (2010). "Chapter 18 - Modern Approaches for Ultrastructural Analysis of the Zebrafish Embryo". In: *Methods in Cell Biology*. Ed. by Thomas Müller-Reichert. Vol. 96. Electron Microscopy of Model Systems. Academic Press, pp. 425–442. DOI: 10.1016/S0091-679X(10)96018-4.
- Schlichthaerle, Thomas et al. (2019). "Direct visualization of single nuclear pore complex proteins using genetically-encoded probes for DNA-PAINT". In: *bioRxiv*, p. 579961. DOI: 10.1101/579961.
- Schnorrenberg, Sebastian, Tim Grotjohann, Gerd Vorbrüggen, Alf Herzig, Stefan W Hell, and Stefan Jakobs (2016). "In vivo super-resolution RESOLFT microscopy of *Drosophila melanogaster*". In: *eLife* 5. Ed. by Taekjip Ha, e15567. DOI: 10.7554/eLife.15567.
- Schoen, Ingmar, Jonas Ries, Enrico Klotzsch, Helge Ewers, and Viola Vogel (2011). "Binding-Activated Localization Microscopy of DNA Structures". In: *Nano Letters* 11.9, pp. 4008–4011. DOI: 10.1021/nl2025954.
- Schütz, Anne K. et al. (2018). "Binding of Polythiophenes to Amyloids: Structural Mapping of the Pharmacophore". In: *ACS Chemical Neuroscience* 9.3, pp. 475–481. DOI: 10.1021/acchemneuro.7b00397.
- Shaban, Haitham A., Cesar A. Valades-Cruz, Julien Savatier, and Sophie Basselet (2017). "Polarized super-resolution structural imaging inside amyloid fibrils using Thioflavine T". In: *Scientific Reports* 7.1, p. 12482. DOI: 10.1038/s41598-017-12864-9.
- Shahmoradian, Sarah H. et al. (2019). "Lewy pathology in Parkinson's disease consists of crowded organelles and lipid membranes". In: *Nature Neuroscience* 22.7, p. 1099. DOI: 10.1038/s41593-019-0423-2.
- Sharonov, Alexey and Robin M. Hochstrasser (2006). "Wide-field subdiffraction imaging by accumulated binding of diffusing probes". In: *Proceedings of the National Academy of Sciences* 103.50, pp. 18911–18916. DOI: 10.1073/pnas.0609643104.
- Shechtman, Yoav, Lucien E. Weiss, Adam S. Backer, Steffen J. Sahl, and W. E. Moerner (2015). "Precise Three-Dimensional Scan-Free Multiple-Particle Tracking over Large Axial

- Ranges with Tetrapod Point Spread Functions". In: *Nano Letters* 15.6, pp. 4194–4199. DOI: 10.1021/acs.nanolett.5b01396.
- Shroff, Hari, Catherine G. Galbraith, James A. Galbraith, and Eric Betzig (2008). "Live-cell photoactivated localization microscopy of nanoscale adhesion dynamics". In: *Nature Methods* 5.5, pp. 417–423. DOI: 10.1038/nmeth.1202.
- Shtengel, Gleb et al. (2009). "Interferometric fluorescent super-resolution microscopy resolves 3D cellular ultrastructure". In: *Proceedings of the National Academy of Sciences* 106.9, pp. 3125–3130. DOI: 10.1073/pnas.0813131106.
- Sidhu, Arshdeep, Ine Segers-Nolten, and Vinod Subramaniam (2016). "Conformational Compatibility Is Essential for Heterologous Aggregation of alpha-Synuclein". In: *ACS chemical neuroscience* 7.6, pp. 719–727. DOI: 10.1021/acschemneuro.5b00322.
- Sidhu, Arshdeep, Ine Segers-Nolten, Vincent Raussens, Mireille M. A. E. Claessens, and Vinod Subramaniam (2017). "Distinct Mechanisms Determine alpha-Synuclein Fibril Morphology during Growth and Maturation". In: *ACS Chemical Neuroscience* 8.3, pp. 538–547. DOI: 10.1021/acschemneuro.6b00287.
- Sigurdson, Christina J et al. (2007). "Prion strain discrimination using luminescent conjugated polymers". In: *Nature Methods* 4.12, pp. 1023–1030. DOI: 10.1038/nmeth1131.
- Singleton, A. B. et al. (2003). "alpha-Synuclein Locus Triplication Causes Parkinson's Disease". In: *Science* 302.5646, pp. 841–841. DOI: 10.1126/science.1090278.
- Sinha, S., A.K. Ray, S. Kundu, S. Sasikumar, and K. Dasgupta (2002). "Heavy-water-based solutions of rhodamine dyes: photophysical properties and laser operation". In: *Applied Physics B* 75.1, pp. 85–90. DOI: 10.1007/s00340-002-0932-6.
- Sipe, Jean D. and Alan S. Cohen (2000). "Review: History of the Amyloid Fibril". In: *Journal of Structural Biology* 130.2, pp. 88–98. DOI: 10.1006/jsbi.2000.4221.
- Sjöqvist, Jonas, Jérôme Maria, Rozalyn A. Simon, Mathieu Linares, Patrick Norman, K. Peter R. Nilsson, and Mikael Lindgren (2014). "Toward a Molecular Understanding of the Detection of Amyloid Proteins with Flexible Conjugated Oligothiophenes". In: *The Journal of Physical Chemistry A* 118.42, pp. 9820–9827. DOI: 10.1021/jp506797j.
- Smith, Wanli W., Russell L. Margolis, Xiaojie Li, Juan C. Troncoso, Michael K. Lee, Valina L. Dawson, Ted M. Dawson, Takashi Iwatsubo, and Christopher A. Ross (2005). "Alpha-synuclein phosphorylation enhances eosinophilic cytoplasmic inclusion formation in SH-SY5Y cells". In: *The Journal of Neuroscience: The Official Journal of the Society for Neuroscience* 25.23, pp. 5544–5552. DOI: 10.1523/JNEUROSCI.0482-05.2005.
- Song, L., C. A. Varma, J. W. Verhoeven, and H. J. Tanke (1996). "Influence of the triplet excited state on the photobleaching kinetics of fluorescein in microscopy". In: *Biophysical Journal* 70.6, pp. 2959–2968. DOI: 10.1016/S0006-3495(96)79866-1.
- Spillantini, M. G., M. L. Schmidt, V. M. Lee, J. Q. Trojanowski, R. Jakes, and M. Goedert (1997). "Alpha-synuclein in Lewy bodies". In: *Nature* 388.6645, pp. 839–840. DOI: 10.1038/42166.
- Stepanek, Ludek and Gaia Pigino (2016). "Microtubule doublets are double-track railways for intraflagellar transport trains". In: *Science* 352.6286, pp. 721–724. DOI: 10.1126/science.aaf4594.
- Sugeno, Naoto, Atsushi Takeda, Takafumi Hasegawa, Michiko Kobayashi, Akio Kikuchi, Fumiaki Mori, Koichi Wakabayashi, and Yasuto Itoyama (2008). "Serine 129 Phosphorylation of alpha-Synuclein Induces Unfolded Protein Response-mediated Cell Death". In: *Journal of Biological Chemistry* 283.34, pp. 23179–23188. DOI: 10.1074/jbc.M802223200.
- Sugeno, Naoto, Sandra Jäckel, Aaron Voigt, Zinah Wassouf, Julia Schulze-Hentrich, and Philipp J. Kahle (2016). "alpha-Synuclein enhances histone H3 lysine-9 dimethylation and H3K9me2-dependent transcriptional responses". In: *Scientific Reports* 6. DOI: 10.1038/srep36328.
- Sun, Jichao, Lina Wang, Huan Bao, Sanjay Premi, Utpal Das, Edwin R. Chapman, and Subhojit Roy (2019). "Functional cooperation of alpha-synuclein and VAMP2 in

- synaptic vesicle recycling". In: *Proceedings of the National Academy of Sciences* 116.23, pp. 11113–11115. DOI: 10.1073/pnas.1903049116.
- Sun, Xiaoli et al. (2011). "Development of SNAP-tag fluorogenic probes for wash-free fluorescence imaging". In: *Chembiochem: A European Journal of Chemical Biology* 12.14, pp. 2217–2226. DOI: 10.1002/cbic.201100173.
- Sunde, M. and C. Blake (1997). "The structure of amyloid fibrils by electron microscopy and X-ray diffraction". In: *Advances in Protein Chemistry* 50, pp. 123–159.
- Sunde, Margaret, Louise C Serpell, Mark Bartlam, Paul E Fraser, Mark B Pepys, and Colin C. F Blake (1997). "Common core structure of amyloid fibrils by synchrotron X-ray diffraction" Edited by F. E. Cohen". In: *Journal of Molecular Biology* 273.3, pp. 729–739. DOI: 10.1006/jmbi.1997.1348.
- Surguchev, Alexei A. and Andrei Surguchov (2017). "Synucleins and Gene Expression: Ramblers in a Crowd or Cops Regulating Traffic?" In: *Frontiers in Molecular Neuroscience* 10. DOI: 10.3389/fnmol.2017.00224.
- Swoboda, Marko, Jörg Henig, Hsin-Mei Cheng, Dagmar Brugger, Dietmar Haltrich, Nicolas Plumeré, and Michael Schlierf (2012). "Enzymatic Oxygen Scavenging for Photostability without pH Drop in Single-Molecule Experiments". In: *ACS Nano* 6.7, pp. 6364–6369. DOI: 10.1021/nn301895c.
- Sydor, Andrew M., Kirk J. Czymmek, Elias M. Puchner, and Vito Mennella (2015). "Super-Resolution Microscopy: From Single Molecules to Supramolecular Assemblies". In: *Trends in Cell Biology* 25.12, pp. 730–748. DOI: 10.1016/j.tcb.2015.10.004.
- Szyborska, Anna, Alex de Marco, Nathalie Daigle, Volker C. Cordes, John A. G. Briggs, and Jan Ellenberg (2013). "Nuclear Pore Scaffold Structure Analyzed by Super-Resolution Microscopy and Particle Averaging". In: *Science* 341.6146, pp. 655–658. DOI: 10.1126/science.1240672.
- Takakura, Hideo et al. (2017). "Long time-lapse nanoscopy with spontaneously blinking membrane probes". In: *Nature Biotechnology* 35.8, pp. 773–780. DOI: 10.1038/nbt.3876.
- Thevathasan, Jervis Vermaal et al. (2019). "Nuclear pores as versatile reference standards for quantitative superresolution microscopy". In: *bioRxiv*, p. 582668. DOI: 10.1101/582668.
- Thompson, Russell E., Daniel R. Larson, and Watt W. Webb (2002). "Precise Nanometer Localization Analysis for Individual Fluorescent Probes". In: *Biophysical Journal* 82.5, pp. 2775–2783. DOI: 10.1016/S0006-3495(02)75618-X.
- Tsigelny, Igor F. et al. (2008). "Mechanisms of Hybrid Oligomer Formation in the Pathogenesis of Combined Alzheimer's and Parkinson's Diseases". In: *PLOS ONE* 3.9, e3135. DOI: 10.1371/journal.pone.0003135.
- Turkowyd, Bartosz, David Virant, and Ulrike Endesfelder (2016). "From single molecules to life: microscopy at the nanoscale". In: *Analytical and Bioanalytical Chemistry* 408.25, pp. 6885–6911. DOI: 10.1007/s00216-016-9781-8.
- Tuttle, Marcus D. et al. (2016). "Solid-state NMR structure of a pathogenic fibril of full-length human alpha-synuclein". In: *Nature Structural & Molecular Biology* 23.5, pp. 409–415. DOI: 10.1038/nsmb.3194.
- Ulbrich, Maximilian H. and Ehud Y. Isacoff (2007). "Subunit counting in membrane-bound proteins". In: *Nature Methods* 4.4, pp. 319–321. DOI: 10.1038/nmeth1024.
- Ulmer, Tobias S., Ad Bax, Nelson B. Cole, and Robert L. Nussbaum (2005). "Structure and dynamics of micelle-bound human alpha-synuclein". In: *The Journal of Biological Chemistry* 280.10, pp. 9595–9603. DOI: 10.1074/jbc.M411805200.
- Uversky, Vladimir N., Jie Li, and Anthony L. Fink (2001). "Evidence for a Partially Folded Intermediate in alpha-Synuclein Fibril Formation". In: *Journal of Biological Chemistry* 276.14, pp. 10737–10744. DOI: 10.1074/jbc.M010907200.
- Uéda, K. et al. (1993). "Molecular cloning of cDNA encoding an unrecognized component of amyloid in Alzheimer disease". In: *Proceedings of the National Academy of Sciences* 90.23, pp. 11282–11286. DOI: 10.1073/pnas.90.23.11282.

- Vangindertael, J., R. Camacho, W. Sempels, H. Mizuno, P. Dedecker, and K. P. F. Janssen (2018). "An introduction to optical super-resolution microscopy for the adventurous biologist". In: *Methods and Applications in Fluorescence* 6.2, p. 022003. DOI: 10.1088/2050-6120/aaae0c.
- Varela, Juan A., Margarida Rodrigues, Suman De, Patrick Flagmeier, Sonia Gandhi, Christopher M. Dobson, David Klenerman, and Steven F. Lee (2018). "Optical Structural Analysis of Individual alpha-Synuclein Oligomers". In: *Angewandte Chemie (International Ed. in English)* 57.18, pp. 4886–4890. DOI: 10.1002/anie.201710779.
- Wang, Siyuan, Jeffrey R. Moffitt, Graham T. Dempsey, X. Sunney Xie, and Xiaowei Zhuang (2014). "Characterization and development of photoactivatable fluorescent proteins for single-molecule-based superresolution imaging". In: *Proceedings of the National Academy of Sciences of the United States of America* 111.23, pp. 8452–8457. DOI: 10.1073/pnas.1406593111.
- Weinreb, P. H., W. Zhen, A. W. Poon, K. A. Conway, and P. T. Lansbury (1996). "NACP, a protein implicated in Alzheimer's disease and learning, is natively unfolded". In: *Biochemistry* 35.43, pp. 13709–13715. DOI: 10.1021/bi961799n.
- Widengren, Jerker, Andriy Chmyrov, Christian Eggeling, Per-Åke Löfdahl, and Claus A. M. Seidel (2007). "Strategies to Improve Photostabilities in Ultrasensitive Fluorescence Spectroscopy". In: *The Journal of Physical Chemistry A* 111.3, pp. 429–440. DOI: 10.1021/jp0646325.
- Winner, Beate et al. (2011). "In vivo demonstration that alpha-synuclein oligomers are toxic". In: *Proceedings of the National Academy of Sciences* 108.10, pp. 4194–4199. DOI: 10.1073/pnas.1100976108.
- Wong, Yvette C. and Dimitri Krainc (2017). "alpha-synuclein toxicity in neurodegeneration: mechanism and therapeutic strategies". In: *Nature Medicine* 23.2, pp. 1–13. DOI: 10.1038/nm.4269.
- Wördehoff, Michael M., Oliver Bannach, Hamed Shaykhalishahi, Andreas Kulawik, Stephanie Schiefer, Dieter Willbold, Wolfgang Hoyer, and Eva Birkmann (2015). "Single fibril growth kinetics of alpha-synuclein". In: *Journal of Molecular Biology* 427.6, pp. 1428–1435. DOI: 10.1016/j.jmb.2015.01.020.
- Xu, Jianhua et al. (2016). "alpha-Synuclein Mutation Inhibits Endocytosis at Mammalian Central Nerve Terminals". In: *Journal of Neuroscience* 36.16, pp. 4408–4414. DOI: 10.1523/JNEUROSCI.3627-15.2016.
- Xu, Ke, Guisheng Zhong, and Xiaowei Zhuang (2013). "Actin, spectrin, and associated proteins form a periodic cytoskeletal structure in axons". In: *Science (New York, N.Y.)* 339.6118, pp. 452–456. DOI: 10.1126/science.1232251.
- Yagi, S. and H. Inoue (1962). "The absorption of oxygen into sodium sulphite solution". In: *Chemical Engineering Science* 17.6, pp. 411–421. DOI: 10.1016/0009-2509(62)85010-6.
- Yamasaki, Tertia R., Brandon B. Holmes, Jennifer L. Furman, Dhruva D. Dhavale, Bryant W. Su, Eun-Suk Song, Nigel J. Cairns, Paul T. Kotzbauer, and Marc I. Diamond (2019). "Parkinson's disease and multiple system atrophy have distinct alpha-synuclein seed characteristics". In: *Journal of Biological Chemistry* 294.3, pp. 1045–1058. DOI: 10.1074/jbc.RA118.004471.
- Yang, T. Tony et al. (2018). "Super-resolution architecture of mammalian centriole distal appendages reveals distinct blade and matrix functional components". In: *Nature Communications* 9.1, p. 2023. DOI: 10.1038/s41467-018-04469-1.
- Young, Laurence J., Gabriele S. Kaminski Schierle, and Clemens F. Kaminski (2017). "Imaging Abeta(1–42) fibril elongation reveals strongly polarised growth and growth incompetent states". In: *Physical Chemistry Chemical Physics* 19.41, pp. 27987–27996. DOI: 10.1039/C7CP03412A.
- Yuan, Xiangai, Wanwan Zhang, Ling-Hai Xie, Jing Ma, Wei Huang, and Wenjian Liu (2015). "Role of Planar Conformations in Aggregation Induced Spectral Shifts of Supermolecular Oligofluorensols in Solutions and Films: A Combined Experimental and MD/TD-DFT Study". In: *The Journal of Physical Chemistry. B* 119.32, pp. 10316–10333. DOI: 10.1021/acs.jpcc.5b04558.

- Zanacchi, Francesca Cella, Carlo Manzo, Angel S. Alvarez, Nathan D. Derr, Maria F. Garcia-Parajo, and Melike Lakadamyali (2017). "A DNA origami platform for quantifying protein copy number in super-resolution". In: *Nature Methods* 14.8, pp. 789–792. DOI: 10.1038/nmeth.4342.
- Zarranz, Juan J. et al. (2004). "The new mutation, E46K, of alpha-synuclein causes parkinson and Lewy body dementia". In: *Annals of Neurology* 55.2, pp. 164–173. DOI: 10.1002/ana.10795.
- Zhang, Jiaming, Xiaoping Li, and Jia-Da Li (2019). "The Roles of Post-translational Modifications on alpha-Synuclein in the Pathogenesis of Parkinson's Diseases". In: *Frontiers in Neuroscience* 13. DOI: 10.3389/fnins.2019.00381.